

Disease modeling hypertrophic cardiomyopathy using CRISPR/Cas9 genome editing technology in human pluripotent stem cell-derived cardiomyocytes

Submitted by

Diogo Mosqueira, MEng

School of Medicine

Division of Cancer and Stem Cells

The University of Nottingham

Thesis submitted to The University of Nottingham for the Degree of Doctor in Philosophy

Acknowledgements

First and foremost, I would like to thank Prof. Chris Denning for his insightful and encouraging supervision, in all its different facets, for all the scientific guidance provided during these 3.5 years but for also for his support in helping my future career prospects and for keeping the morale high. I would also like to thank Prof. Arne Hansen, who always had a friendly word and wise advice to provide during my stay in Hamburg, and for his support.

This work was the product of the combined efforts of many extraordinary scientists. I would therefore like to acknowledge them properly. Dr. Ingra Mannhardt has fabricated the Engineered Heart Tissues and provided support during data analysis. Jamie Bhagwan performed the calcium optical mapping work. Maria Muñoz performed manual dissection of hPSC colonies. Maksymilian Prondzynsky and Dr. Lucie Carrier performed the nanoString transcriptomics work. Source Biosciences provided Sequencing services and Nigel Smith performed karyotyping as a core service. I would also like to thank Katarzyna Lis-Slimak for all the help in high-content imaging and Dr. William Skarnes for kindly supplying plasmids used in this work. I would like to deeply thank Dr. James Smith for general support, and for teaching me the tools I needed to succeed in this PhD. I would also like to acknowledge Caroline Reffin and Dr. Karl Firth for introducing me to the lab and for encouraging me to stay for a PhD.

Then, I would like to thank all my wonderful colleagues (in both labs) who made this PhD journey incredibly fun: Jamie Bhagwan, Dr. James Smith, Dr. Elizabeth Scott, Dr. Karl Firth, Jordan Thorpe, Dr. Viola Borgdorff, Dr. Alexander Kondrashov, Dr. James Crutchley, Dr. Luke Flatt, Dr. Gary Duncan, Dr. Harry Hoang, Lazaros Fotopoulos, Dr. Spandan Kalra, Penny Howick, Jayson Bispham, Ralph Hyde, Kate Vo, Dr. Mine Bakar, Zubair Ahmed, Anika Benzin, Maksymilian Prondzynsky, and Dr. Bärbel Ulmer. I would also like to thank the students that I helped supervise or train, as there is always something to learn in teaching: Angharad Evans, Abdul Abakir, Andie Shaw and Ana Lopez.

In addition, I would like to thank all those that discussed my work with me, engaging in enriching discussions which ultimately led to its improvement: Prof. Thomas Eschenhagen, Dr. Vinoj George and Dr. James Smith.

Finally, I would like to thank EPSRC for funding my doctoral studies and subsequent fellowship, and all the Doctoral Training Centre colleagues from Loughborough, Keele and Nottingham, especially Carlos Granja, Kyle Efendi, Matt Dunn and Steven Ruck, as well as other friends made during my stay in the UK, namely João Vasques.

This PhD is the climax of a journey that began 10 years ago (!) with my admission to the University of Porto. I would therefore like to quickly acknowledge all those who helped me during this past decade, such as previous colleagues but mostly previous mentors (that are now friends), especially Prof. Dr. Perpétua Pinto-do-Ó, Prof. Ülo Langel and Dr. Giancarlo Forte, who always believed in me and guided me towards the research excellence that I found in Portugal, Sweden and Japan, respectively.

This degree is the result of a long and hard process that took me away from my home country and family so I would like to thank them for all their unconditional love and devotion, especially my parents and sister for raising me to become a (hopefully) decent human being, whilst showing me the true value of resilience and how fortune favours the brave.

And at last, it was shortly before I embarked on this adventure that I found Sara, my first love. I would like to thank you for supporting our (crazy) adventures with your partnership and dedication, for it would not have been half as fun to do this alone. Whatever the future holds, I am sure we will face it with positivity and both our dreams will come true.

Abstract

Hypertrophic cardiomyopathy (HCM) is a prevalent genetic cardiovascular disease affecting 1:500 individuals whose cardiac function is deteriorated due to thickening of the left ventricle of the heart, mostly owing to mutations in sarcomeric genes. Modeling HCM *in vitro* using human pluripotent stem cell-derived cardiomyocytes (hPSC-CM) offers promise to further investigate the disease mechanisms, towards the development of effective drugs.

Herein, nickase CRISPR/Cas9 genome editing technology was harnessed to introduce the R453C pathological mutation in the *MYH7* sarcomeric gene, in three healthy hPSC lines. Monoclonal hPSC lines generated displayed the mutation in one or both alleles, as confirmed by PCR-genotyping and Sanger sequencing. A monolayer cardiac differentiation protocol was applied to the generated hPSC lines, resulting in >90% cardiomyocyte purities, and expression of mutant allele(s) of the *MYH7* gene was analysed by RT-PCR.

High-content imaging analysis showed that mutant hPSC-CMs displayed higher expression of hypertrophic marker Brain Natriuretic Peptide (BNP), in comparison to isogenic controls. BNP expression was maximised by treatment with hypertrophic inducer Endothelin-1 and rescued by its antagonist Bosentan. Flow cytometry analysis revealed a mild increase in cell volume of mutant cardiomyocytes relative to their wild-type controls.

Functional evaluation of gene-edited lines exposed higher mitochondrial respiration rates relative to the isogenic controls, with the same mitochondrial content, resulting in a trend towards oxidative stress. Further genome engineering to incorporate a calcium indicator in R453C-MYH7 lines enabled confocal line analysis of calcium transients. *MYH7*-mutant hPSC-CMs exhibited higher frequency of irregular events in comparison to the healthy control, faster calcium kinetics, and higher resting cytosolic calcium concentration.

Integration of hPSC-CMs in Engineered Heart Tissues (EHTs) and subsequent analysis of contractile force showed that mutant lines had a hypo-contractile and negative clinotropic phenotype relative to their isogenic controls. Moreover, R453C-MYH7 hEHTs showed a more pronounced negative force-frequency relationship in comparison with the healthy lines. These phenotypes were not rescued by treatment with cardiac myosin activator Omecamtiv Mecarbil, suggesting that targeting other mechanisms indirectly related with the contractile apparatus may be a preferred route to attenuate the observed pathological changes.

Finally, transcriptomic analysis of gene-edited lines showed up-regulation of genes associated with fetal gene program, hypertrophy, fibrosis, apoptosis and autophagy, indicating potential molecular mechanisms associated with the observed phenotypes and HCM progression.

Overall, hPSC-CMs bearing the R453C-MYH7 mutation exhibit the main molecular and functional hallmarks of HCM, providing a physiologically-relevant platform that enables further dissection of disease mechanisms and promotes pharmacological intervention.

Table of Contents

Acknowledgements i
Abstract ii
Table of Contents iii
List of Figures vii
List of Tables ix
Abbreviations x
Gene symbols xiii
Gene nomenclature xiv
1. Introduction 1
1.1 Thesis rationale and objectives 1
1.2 Cardiac diseases 3
1.2.1 Incidence and costs of heart failure 3
1.2.2 Cardiomyopathies 3
1.2.3 Complexity of genotype-phenotype relationships 6
1.2.4 Hypertrophic cardiomyopathy (HCM) 6
1.2.5 Approaches to disease modeling HCM 13
1.3 Human pluripotent stem cell-derived cardiomyocytes 16
1.3.1 Limitations of animal models 16
1.3.2 Derivation, culture and characterisation of hPSC 17
1.3.3 Cardiac differentiation of hPSC 20
1.3.4 Maturation of hPSC-CMs 24
1.4 Genome editing technologies 32
1.4.1 Mechanisms of gene editing 33
1.4.2 Targeted nucleases 35
1.4.3.Gene targeting applications 38
1.5 Phenotyping HCM in hPSC-CMs 40
1.5.1 High content imaging 40
1.5.2 Functional analysis 41
1.6 Hypothesis and major aims of the PhD Project 45
2. Materials and Methods 46
2.1 CRISPR/Cas9 strategy 46
2.1.1 Guide RNA design and synthesis 46

2.1.2 Targeting construct design and synthesis 46
2.1.3 hPSC editing transfection, selection and genotyping....47
2.2 Cell culture 49
2.2.1 hPSC culture....49
2.2.2 Monolayer cardiac differentiation of hPSC 49
2.2.3 hPSC-cardiomyocyte dissociation....49
2.2.4 hPSC-fibroblast culture 50
2.2.5 BNP assay....50
2.3 Molecular Biology....50
2.3.1 RNA extraction, cDNA synthesis and RT-PCR....50
2.3.2 Allele-specific restriction digestion and band densitometry....51
2.3.3 Real-time qPCR....51
2.3.4 Immunocytochemistry (ICC) and image acquisition....52
2.3.5 hPSC karyotyping 52
2.4 Flow cytometry 53
2.4.1 Volumetry 53
2.4.2 Quantification of mitochondrial content and ROS....53
2.4.3 Data analysis 53
2.5 Seahorse analysis of mitochondrial respiration....54
2.6 Human engineered heart tissues....54
2.6.1 hEHT fabrication and maintenance 54
2.6.2 Analysis of contractile force 54
2.6.3 Glucose consumption measurements 56
2.7 Confocal line scans of calcium transients 56
2.7.1 hPSC-CM preparation....56
2.7.2 Image acquisition....56
2.7.3 Data analysis 56
2.8 Transcriptomics analysis 57
2.9 Statistical analysis....57
3. Generation of R453C-MYH7 hPSC lines by CRISPR/Cas9 Genome Editing Technology 58
3.1 Introduction 58
3.1.1 CRISPR/ Cas9 Nickase gene targeting....58
3.1.2 Chapter aims and objectives....59
3.2 Results....61

3.2.1 CRISPR/Cas9 strategy design 61
3.2.2 hPSC transfection and selection 66
3.2.3 Genotypic characterization of targeted clones 66
3.2.4 Selection cassette excision 70
3.2.5 Gene-edited hPSC characterization 70
3.3 Discussion 74
3.3.1 Strengths and drawbacks of plasmid-based strategy 74
3.3.2 Genome-editing efficiency 78
3.3.3 Considerations on generated HCM lines 78
4. High-throughput phenotyping of R453C-MYH7 hPSC-derived cardiomyocytes 80
4.1 Introduction 80
4.1.1 Monolayer cardiac differentiation of hPSC 80
4.1.2 Sarcomeric gene expression in HCM 80
4.1.3 Assessing hypertrophy 81
4.1.4 Multinucleation and polyploidy in HCM 82
4.1.5 Natriuretic peptides as markers and regulators of HCM 83
4.1.6 Sarcomeric disorganisation 84
4.1.7 High-content imaging analysis as a phenotyping tool 85
4.1.8 Chapter aims and objectives 85
4.2 Results 87
4.2.1 Cardiac differentiation of gene-edited hPSC 87
4.2.2 Expression of *MYH7* gene in hPSC-CMs 88
4.2.3 Hypertrophy analysis of gene-edited hPSC-CMs 94
4.2.4 Multinucleation analysis of HCM lines 94
4.2.5 Expression of hypertrophic marker BNP 99
4.2.6. Sarcomeric structure of HCM lines 103
4.3 Discussion 106
4.3.1 General properties of hPSC-CMs 106
4.3.2 *MYH7* gene expression in HCM 107
4.3.3 HCM phenotyping by high-throughput methods 108
5. Functional and Molecular phenotyping of R453C-MYH7 hPSC-derived cardiomyocytes 112
5.1 Introduction 112
5.1.1 Energy depletion model in HCM 112
5.1.2 Contractile force in HCM 119

5.1.3 Calcium transient activity in HCM....125
5.1.4 Autophagy in HCM....130
5.1.5 Chapter aims and objectives....132
5.2 Results....132
5.2.1 Mitochondrial respiration....132
5.2.2 Mitochondria content....133
5.2.3 ROS production....133
5.2.4 Genome engineering of R-GECO in HCM lines....140
5.2.5 Calcium transient activity....140
5.2.6 Contractile force analysis in hEHT....147
5.2.7 Force-frequency relationship in HCM....150
5.2.8 Pharmacological intervention in HCM-hEHTs....152
5.2.9 Transcriptomics of HCM lines....155
5.3 Discussion....159
5.3.1 Cardiac bioenergetics of genome-edited hPSC-CMs....159
5.3.2 Calcium handling in HCM....161
5.3.3 Contractility analysis in hEHTs....162
5.3.4. Transcriptomic analysis....165
5.3.5 Overall considerations....166
6. General Discussion....169
6.1 Validity of generated HCM models....169
6.1.1 Patient-derived vs genome-engineered cells....169
6.1.2 hPSC-CM as model system....170
6.2 Study limitations....172
6.2.1 CRISPR/Cas9 genome editing....172
6.2.2 Phenotypic assays....173
6.3 Proposed model of HCM....176
6.3.1 Disease phenotypes....176
6.3.2 Potential molecular mechanisms and pharmacological intervention....176
6.3.2 Contextualization with literature....180
6.4 Future work....181
References....183
Appendix I – Publication Documents....207
Appendix II – Other scientific contributions....208

List of Figures

Figure 1.1 - PhD project workflow. 2
Figure 1.2 - Echocardiographic features of cardiomyopathies. 5
Figure 1.3 – Schematics of HCM mechanisms. 10
Figure 1.4 - Involvement of sarcomeric gene mutations to HCM. 12
Figure 1.5 - Summary of the developed methods to reprogram, culture and differentiate hPSC into cardiomyocytes. 26
Figure 1.6 - Schematic of in vitro maturation strategies for hPSC-CMs. 30
Figure 1.7 - Mechanisms of gene editing by double strand break repair. 34
Figure 2.1 - EHT fabrication protocol.. 55
Figure 3.1 - CRISPR/Cas9 Nickase gene targeting strategy. 60
Figure 3.2 - Overview of CRISPR/Cas9 strategy design.. 62
Figure 3.3 - CRISPR/Cas9 gRNA and targeting vector plasmid synthesis. 63
Figure 3.4 - Targeting vector synthesis. 65
Figure 3.5 - hPSC transfection and selection. 66
Figure 3.6 - Genotypic characterization of genome-edited hPSC. 68
Figure 3.7 - Off-target analysis of MYH7-R453C genome editing. 69
Figure 3.8 - Selection cassette excision from genome-edited hPSC. 71
Figure 3.9 - Pluripotency marker expression of gene-edited hPSC. 72
Figure 3.10 - Karyotype of genome-edited hPSC lines. 73
Figure 3.11 - Intronic location of the residual footprint left upon resistance cassette excision 77
Figure 4.1 - High-throughput phenotyping of R453C-MYH7 lines generated. 86
Figure 4.2 - Cardiac differentiation of gene-edited hPSC. 87
Figure 4.3 - Determination of hPSC-CM purity by high-content imaging. 89
Figure 4.4 - Expression of MYH7 gene in hPSC-CMs. 90
Figure 4.5 - β-MHC expression in gene-edited hPSC-CMs. 91
Figure 4.6 - Allele-specific expression of the MYH7 gene. 92
Figure 4.7 - Analysis of allelic expression of the MYH7 gene 93
Figure 4.8 - Procedure to estimate cardiomyocyte volume by flow cytometry. 95
Figure 4.9 - Cardiomyocyte volume estimation by flow cytometry. 96
Figure 4.10 - High content imaging algorithm to quantify multinucleation of hPSC-CMs: 97
Figure 4.11 - Multinucleation analysis of gene-edited hPSC-CMs. 98
Figure 4.12 - Expression of hypertrophic marker BNP in hPSC-CMs. 100
Figure 4.13 - High content imaging algorithm to quantify BNP expression by high-content imaging. 101
Figure 4.14 - Quantification of percentage of hPSC-CMs expressing hypertrophic marker BNP in gene-edited cell lines. 102
Figure 4.15 - Sarcomeric structure of gene-edited hPSC-CMs. 104

Figure 4.16 - Estimation of sarcomeric disarray by high-content imaging. 105
Figure 5.1 - Energy depletion model associated with sarcomeric mutations present in HCM. 113
Figure 5.2 - In vitro motility assay 115
Figure 5.3 - Tension/ actin-myosin ATPase assay. 116
Figure 5.4 - Laser trap assay. 121
Figure 5.5 - Illustration of measurement of force generation in EHTs. 122
Figure 5.6 - Excitation–contraction coupling (ECC) in the heart. 126
Figure 5.7 – Autophagy-lysosomal pathway. 131
Figure 5.8 - Functional analysis of mitochondrial respiration in R453C-MYH7 hPSC-CMs using the Seahorse platform. 134
Figure 5.9 Mitochondrial respiration parameters of AT1-R453C-MYH7 cardiomyocytes, measured using Seahorse platform. 135
Figure 5.10 - Mitochondrial respiration parameters of REBL-PAT R453C-MYH7 cardiomyocytes, measured using Seahorse platform. 136
Figure 5.11 - Quantification of mitochondrial content in HCM lines. 137
Figure 5.12 - Quantification of ROS production in HCM AT1 lines by flow cytometry. 138
Figure 5.13 - Quantification of ROS production in HCM REBL-PAT lines by flow cytometry. 139
Figure 5.14 - Gene editing R-GECO calcium indicator into AAVS1 safe locus 141
Figure 5.15 - Determination of successful mono- vs bi-allelic targeting of R-GECO1 in REBL-PAT lines. 142
Figure 5.16 R-GECO protein expression detection by immunocytochemistry.. 143
Figure 5.17 – Optical mapping of calcium transients in R453C-MYH7 REBL-PAT cardiomyocytes. 144
Figure 5.18 - Automated quantification of median peak height of calcium transients 145
Figure 5.19 - Preliminary analysis of Nifedipine blockage of LTCC in REBL-PAT cardiomyocytes. 146
Figure 5.20 - Contractile force analysis in AT1-EHTs. 148
Figure 5.21 - Contractile force analysis in REBL-PAT-EHTs. 149
Figure 5.22 - Glucose consumption of hEHTs. 150
Figure 5.23 - Force-frequency relationship in MYH7-mutant EHTs. 151
Figure 5.24 - Treatment of AT1-EHTs with Omecamtiv Mecarbil. 153
Figure 5.25 - Treatment of REBL-PAT-EHTs with Omecamtiv Mecarbil. 154
Figure 5.26 – Transcriptomics analysis of REBL-PAT hPSC-CMs 156
Figure 5.27 - Transcriptomics analysis of AT1 hPSC-CMs 157
Figure 5.28 - Ratio of MYH7/MYH6 expression in hPSC-CMs 158
Figure 6.1 - In silico evaluation of the likelihood of the R453C-MYH7 SNP to cause damaging phenotypes. 171
Figure 6.2 - Schematic of proposed HCM model. 179

List of Tables

Table 1.1 -Summary of advantages and challenges of different approaches for disease modeling. 15
Table 1.2 - Summary of maturation differences between hPSC-CMs and adult CMs. 28
Table 1.3 – Comparison of genome editing tools 38
Table 1.4- Summary of platforms used to phenotype hPSC-CMs. 44
Table 2.1 - Primers used for the 2-step PCR splice mutagenesis reaction. 46
Table 2.2 - Primers used for genotyping the genome-edited hPSC clones. 48
Table 2.3 - Primers used for RT-PCR reaction to detect MYH7 expression. 51
Table 2.4 – Antibodies used for immunocytochemistry. 52

Abbreviations

Abbreviation	Description
AAV	Adeno-associated virus
ActA	Activin A
ADP	Adenosine diphopshate
AHA	American Heart Association
ALP	Autophagy-lysosomal pathway
ANF	Atrial Natriuretic Factor
AngII	Angiotensin II
ANP	Atrial natriuretic peptide
APs	Action potentials
ATP	Adenosine triphosphate
AVC	Arrhythmogenic ventricular cardiomyopathy
bFGF	Basic fibroblast growth factor
BMP	Bone morphogenetic protein
BNP	Brain natriuretic peptide
BTS	N-Benzyl-p-toluenesulfonamide
Cas	CRISPR-associated
CDI	Cellular Dynamics International
CDS	Cell Dissociation Solution
CFCS	Cardio-facio-cutaneous syndrome
CMs	Cardiomyocytes
CMTs	Cardiac microtissues
CPVT	Catecholaminergic polymorphic ventricular tachycardia
CRISPR	Clustered interspaced short palindromic repeats
cRNA	CRISPR RNA
cTnT/I/C	Cardiac troponin T/ I/ C
Cx43	Connexin 43
DAD	Delayed-after-depolarization
DCM	Dilated cardiomyopathy
DMD	Duchenne muscular dystrophy
DNAse	Deoxyribonuclease
DSB	Double stranded break
E8	Essential 8
EB	Embryoid body
ECAR	Extracellular acidification rate
ECC	Excitation-contraction coupling
ECM	Extracellular matrix
EF	Ejection fraction
EGCg	Epigallocatehin-3-gallate
EHM	Engineered Human Myocardium
EMT	Epithelial to mesenchymal transition
END-2	Endodermal-like cell line
ET1	Endothelin 1
FBS	Fetal Bovine Serum
FHF	First Heart Field
Flp	Flippase
FSC	Forward scatter
GECIs	Genetically-encoded calcium indicators
GF	Growth factor
gRNA	Guide RNA
GSK	Glycogen synthase kinase
HBSS	Hank's Balanced Salt Solution

HCM	Hypertrophic cardiomyopathy
HDAC	Histone deacetylase
HDR	Homologous-directed repair
hEHTs	Human engineered heart tissues
hERG	Human Ether-a-go-go related gene
hESC	Human embryonic stem cells
hESC-CM	Human embryonic stem cell-derived cardiomyocytes
HF	Heart failure
hiPSC	Human induced pluripotent stem cells
hPSC	Human pluripotent stem cells
hPSC-CM	Human pluripotent stem cell-derived cardiomyocytes
ICC	Imunocytochemistry
ICD	Implantable cardioverter-defibrillator
IL-2Rγ	Interleukin-2 receptor γ
Indels	Insertions and/or deletions
INS	Insulin
ISCN	International System for Human Cytogenetic Nomenclature
KO	Knockout
LQTS	Long QT Syndrome
LTCC	L-type Ca^{2+} channel
LV	Left ventricle
LVEF	Left ventricular ejection fraction
LVNC	Left ventricular non-compaction cardiomyopathy
MEA	Multi-electrode arrays
MEF	Mouse embryonic fibroblasts
MHC	Myosin heavy chain
MI	Myocardial infarction
MIC	Mitochondrial cardiomyopathy
miRNA	Micro RNA
MT	Matrigel™
mtDNA	Mitochondrial DNA
MTF	Muscular thin film
mtTFA	Mitochondrial transcription factor A
NAC	N-acetyl-cysteine
NADPH	Nicotinamide adenine dinucleotide phosphate
NCX	Sodium-calcium-exchange pump
NEAA	Non-essential amino acids
NEB	New England Biolabs
NFAT	Nuclear factor of activated T cells
NHEJ	Non-homologous end-joining
NRVM	Neonatal rat ventricular cardiomyocytes
OCR	Oxygen consumption rate
OM	Omecamtiv Mecarbil
OXPHOS	Oxidative phosphorylation
PAM	Protospacer-adjacent motif
PBS	Phosphate Buffer Saline
PCr	Phosphocreatine
PDMS	Polydimethylsiloxane
PEST	Penicillin/ streptomycin
PKA	Protein kinase A
PPARα	Proliferator-activated receptor α
qRT-PCR	Quantitative real-time polymerase chain reaction
RCM	Restrictive cardiomyopathy
RNP	Ribonucleoprotein
ROCK	Rho-associate kinase
ROCKi	ROCK inhibitor
ROS	Reactive oxygen species

RT	Room temperature
SCD	Sudden cardiac death
SERCA	Sarcoplasmic reticulum ATPase
SHF	Second Heart Field
SM	Small molecule
SNP	Single nucleotide polymorphism
SP34	StemPro™34 Serum Free Medium
SpCas9	Streptococcus pyogenes Cas9
SR	Sarcoplasmic reticulum
ssODN	Single stranded oligonucleotide
ssTnI	Slow skeletal troponin I
T3	Tri-iodo-L-thyronine
TALENs	Transcription activator-like effector nuclease
TGF-β	Transforming growth factor-β
TMRM	Tetramethylrhodamine
tracrRNA	Trans-activating RNA
T-tubules	Transverse tubules
UPS	Ubiquitin-proteasome system
VN	Vitronectin-N
WNT	Wingless/ INT protein
WT	Wild-type
ZFN	Zinc finger nucleases
α-MHC	α-myosin heavy chain
β-MHC	β-myosin heavy chain

Gene symbols

Abbreviation	Full name
A1AT	α1-antitrypsin
AAVS1	Adeno-associated virus integration site 1
ABCF1	ATP binding cassette subfamily F member 1
ACE1	Angiotensin-1 converting enzyme 1
ACTA2	Actin alpha 2, smooth muscle, aorta
ACTB	β-actin
ACTC1	Cardiac actin
ANKRD1	Ankyrin Repeat Domain 1
Ask1	Apoptosis signal-regulating kinase 1
ATP2A2	ATPase sarcoplasmic/ endoplasmic reticulum Ca^{2+} transporting 2
BAG3	BCL associated athanogene 3
BAX	BCL2 associated X, apoptosis regulator
BCL2	BCL2, Apoptosis Regulator
BECN1	Beclin-1
BRAF	B-Raf protein
CASP3	Caspase 3
CCR2/5	Co-receptor
CHMP2B	Charged multivesicular body protedin 2B
CLTC	Clathrin heavy chain
COL1A1	Collagen type I alpha 1
COL3A1	Collagen type III alpha 1
COL7A1	Collagen type VII alpha 1
CTGF	Connective tissue growth factor
CX43	Connexin 43
EPG5	Ectopic P-granules autophagy protein 5 homolog
ERBB2	Erb-b2 receptor tyrosine kinase 2
FHL1/2	Four-and-a-half-LIM domains 1/2
FN1	Fibronectin 1
FOXO1	Forkhead box O1
FYCO1	FYVE And Coiled-Coil Domain Containing 1
GAPDH	Glyceraldehyde-3-phopsphate dehydrogenase
GLUT1	Glucose transporter 1
HDAC	Histone deacetylase 6
Isl1	Islet 1
JAK1	Janus kinase 1
JUP	Junctional plakoglobin
KCNH2	hERG (potassium ion channel)
KCNJ2	Potassium Voltage-Gated Channel Subfamily J Member 2
LAMP 1-2	Lysosomal-associated membrane protein 1-2
LMO2	Lim domain only 2
MAP1LC3A	Microtubule associated protein 1 light chain 3 alpha
MAP1LC3B	Microtubule associated protein 1 light chain 3 beta
MEF2	Myocyte enhancer factor 2
MEOX1	Mesenchyme homeobox 1
MTOR	Mechanistic target of rapamycin
MYBPC3	Myosin-binding protein C
MYH6	Myosin heavy chain 6/ α-myosin heavy chain
MYH7	Myosin heavy chain 7/ β-myosin heavy chain
MYL	Myosin light chain
MYL3	Myosin light chain 3
NANOG	Homeobox protein Nanog
NBR1	Neighbour of BRCA1 gene 1

ND1-2	NADH dehydrogenase subunit 1-2
NFKB1	Nuclear factor kappa B subunit 1
Nkx2.5	Homeobox protein Nkx2.5
NPPA/B	Natriuretic peptide A/B
Nppb	Brain natriuretic peptide
NRF1-2	Nuclear respiratory factor 1-2
NRG1	Neuregulin 1
OCT4	Octamer-binding transcription factor 4
PGC1	Peroxisome proliferator-activated receptor gamma coactivator 1-alpha
PGK1	Phosphoglycerate kinase 1
PLN	Phospholamban
PPP1R1A	Protein phosphatase 1, regulatory (inhibitor) subunit 1A (PP-I-1)
RAB7A	RAS oncogene family
RCAN1	Regulator of calcineurin 1
RYR2	Ryanodine receptor 2
SCN5A	Sodium voltage-gated channel alpha subunit 5
SH3TC2	HDAC6
SOX2	Sex determining region Y-box 2
SQSTM1	Sequestosome 1; p62
SRF	Serum response factor
SSEA3/4	Stage-specific embryonic antigen 3/4
STAT1-3	Signal transducer and activator of transcription 1-3
Tbx5	T-box protein 5
TFEB	Transcription factor EB
TNNI3	Cardiac troponin I
TNNT2	Cardiac troponin T
TP53	Tumor protein p53
TPM1	Tropomyosin
TRA-1-60/81	Podocalyxin
TUBB	Tubulin beta class 1
VCP	Valosin containing protein (p97)

Gene nomenclature

According to current guidelines from the Human Genome Nomenclature Committee (http://www.gene.ucl.ac.uk/nomenclature/), abbreviations for human genes are capitalised and italicised, while their respective proteins are capitalised but not italicised. Mouse gene and protein nomenclature follows guidelines from the current Mouse Genome Nomenclature Committee (http://www.informatics.jax.org/mgihome/nomen/), based on which gene abbreviations are written with a capitalised first letter and subsequent lower case letters, all italicised. Abbreviations for mouse proteins have the same gene symbol but are not italicised.

1. Introduction

1.1 Thesis rationale and objectives

Cardiomyopathies constitute a complex and heterogeneous group of cardiac diseases that are responsible for high mortality and morbidity rates associated with heart failure (HF). While several classes have been defined, hypertrophic cardiomyopathy (HCM) is the most prevalent disease form, being the main cause of sudden cardiac death (SCD) in heart patients[1].

HCM aetiology involves a strong genetic contribution, as patients often display mutations in sarcomeric genes such as *MYH7*, with varying degrees of severity and outcome of disease progression that may ultimately result in heart failure[2]. Given the genetic and clinical heterogeneity that characterise HCM, it is not surprising that very few genotype–phenotype relationships have been shown to be reproducible. As the majority of mutations are restricted to each family, studies lack statistical power and robustness to demonstrate correlations between individual mutations and phenotype[3]. The variable expressivity, penetrance and allelic heterogeneity of similar mutations with respect to age at presentation, severity of hypertrophy, and prognosis has further hampered the understanding and treatment of HCM[4].

Current efforts to investigate HCM rely mostly on animal models that lack in similarity and complexity to the human physiology[5], and therefore often cause confounding results that are hard to extrapolate to the human counterpart. Alternatively, the use of human biopsies provides anatomically-relevant sources but are hindered by very limited sample availability[6]. Therefore, creating genetically-tractable human disease models of HCM based on unlimited sources of cardiomyocytes (CMs) will not only enhance the scientific understanding of the disease mechanisms but also foster drug discovery efforts towards its treatment, thus addressing a prevalent pathology. Ultimately, such models have the potential to greatly accelerate the discovery of cost-effective and safe drugs by the pharmaceutical industry sector, resulting in massive savings of lives and funds for national health systems, as well as reducing and/or replacing the number of animals needed for pre-clinical testing.

This PhD project addresses these challenges by aiming to introduce an HCM-associated pathological mutation in the *MYH7* sarcomeric gene in human pluripotent stem cell (hPSC) lines through the CRISPR/Cas9 genome editing technology. For this, an *MYH7*-mutation associated with a poor prognosis and clinical outcome was targeted, namely the R453C amino acid change that stems from the C9123T single nucleotide polymorphism (SNP). The work developed in this topic is described in Chapter 3. Importantly, by introducing the same mutation in several cell lines with distinct genetic backgrounds, the statistical power of the HCM disease model is greatly enhanced (keeping isogenic controls as healthy hPSCs).

Subsequently, efficient cardiac differentiation protocols enabled the production of hPSC-derived cardiomyocytes (hPSC-CMs) that model their diseased counterparts in the human

heart. Thereafter, several high-throughput platforms were used to interrogate cardiac physiology in terms of the development of typical hypertrophy responses, in order to phenotype and validate the generated model, as is described in Chapter 4.

Finally, functional and molecular analysis of the HCM models developed in comparison to their healthy (isogenic) controls was performed in terms of their bioenergetics (assessment of mitochondrial respiration by Seahorse™ platform), calcium handling (by incorporating genetically-encoded calcium indicators, GECIs) and contractile force (via integration in engineered heart tissues, EHTs). Lastly, a medium-scale transcriptomic analysis was performed to identify pathways differentially regulated in the different *MYH7*-mutant variants generated. This work is reported in Chapter 5. The workflow associated with this PhD thesis is illustrated in **Figure 1.1**.

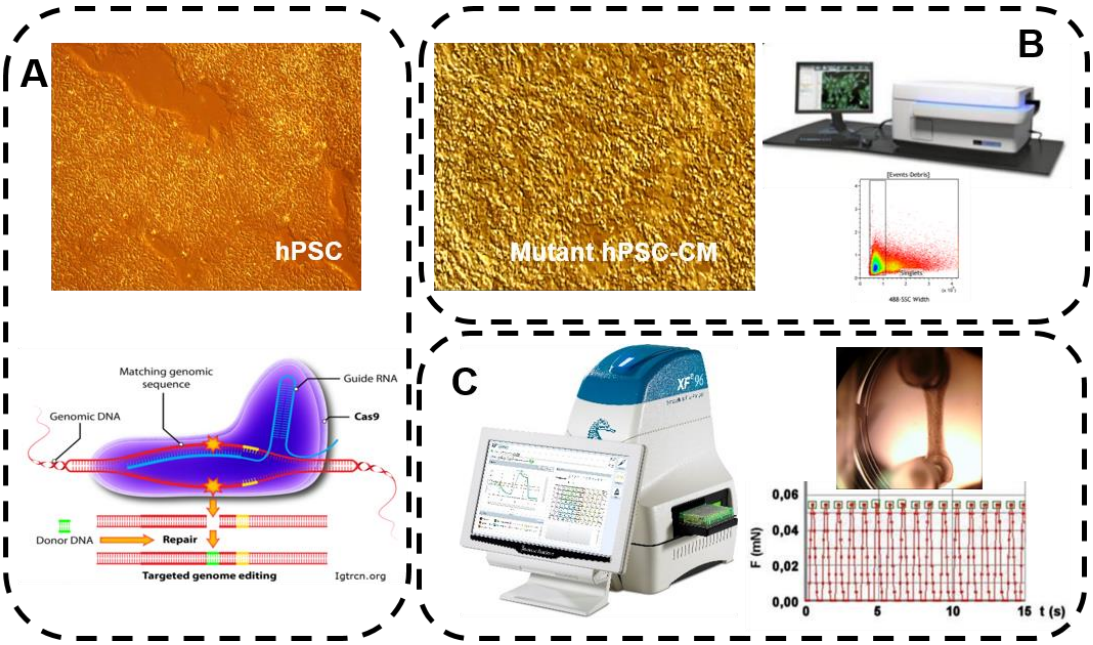


Figure 1.1 PhD project workflow. **A)** CRISPR/Cas9 genome editing technology was used to introduce R453C-MYH7 mutation in healthy hPSC. **B)** Mutant hPSC-CMs generated via a cardiac differentiation protocol were phenotyped in high-throughput platforms such as high-content imaging using a confocal plate reader (Operetta™) and estimation of cardiomyocyte volume by flow cytometry. **C)** Functional and molecular phenotyping of R453C-MYH7 hPSC-CMs was performed to evaluate mitochondrial respiration (Seahorse™ platform), calcium transient analysis, and contractile function in human engineered heart tissues.

The remaining introduction to this thesis concerns clinical and molecular characterization of HCM, the methods associated with hPSC and their cardiac differentiation as well as technologies of genome editing. Subsequently, phenotyping assays recently developed in the field and their application to hPSC-CMs will be discussed. Throughout the thesis, several aspects of HCM disease will be discussed in the respective Results chapters where they were evaluated, and previous reports originated from animal models and tissue biopsies will be described. Finally, the work developed will be put into context with the literature, and its limitations and future perspectives will be discussed.

1.2 Cardiac diseases

1.2.1 Incidence and costs of heart failure

Cardiac diseases represent a major cause of mortality and morbidity worldwide, imposing a heavy economic burden on high- and middle-income countries. In 2012, 2.4% of the US population had heart failure (HF). Prevalence increases with age and mortality rates of Medicare beneficiaries 3 years after an HF hospitalization is reaching 50%[7]. In addition, the World Health Organization has recently estimated that HF affected over 23 million people worldwide, rendering it responsible for 30 percent of all deaths[8]. Moreover, the prevalence of HF is increasing owing to the aging population and improved detection of heart disease, although the age-adjusted incidence of HF seems to have stabilized[9].

The economic burden of HF is divided between direct costs (hospitalization, medications, physician costs, primary healthcare costs and follow-up) and indirect expenses (lost productivity resulting from morbidity and mortality, sickness benefit and welfare support)[10]. While most high-income countries have gathered data of the direct costs of HF (with the UK reporting $1.45 billion in 2012 - which constitutes the highest %GDP spent in healthcare-17.9%), only in the USA have both costs been reported ($20.9 billion in direct and $9.80 billion in indirect costs, in 2012)[10]. Extrapolating this figure to 197 countries where indirect cost figures were missing, it was estimated that the total cost of HF worldwide was $108 billion per *annum*, with direct costs accounting for ~60% ($65 billion) and indirect costs for ~40% ($43 billion) of the overall spend[10].

Furthermore, the American Heart Association (AHA) forecasts an increase in HF prevalence in the US, reaching over 8 million cases in 2030 (~3% of total population), due to the aging and growth of the population[7]. This is predicted to cause a 2.5-fold increase in the direct cost of care from $20.9 billion to $53.1 billion, with total costs expected to amount to $69.8 billion[7]. Extrapolating this data worldwide would result in a forecasted cost of HF reaching the $250 billion figure in 2030.

1.2.2 Cardiomyopathies

Overall, HF occurs when the cardiac function, no longer compensated by endogenous mechanisms, fails to meet the metabolic requirements of the body[11]. It is considered a multifactorial disease, having clinical, environmental and genetic components. In this regard, cardiomyopathies constitute a heterogeneous group of diseases that represent the major causes of mortality and morbidity associated with HF, usually due to failure of myocardial performance, which may be mechanical (e.g. diastolic or systolic dysfunction) or electrical (arrhythmogenic ventricular tachycardia)[12]. Due to its highly heterogeneous nature, definition of cardiomyopathies has been repeatedly revised, with the latest iteration dating from 2006, whereby an expert panel (AHA) proposed that "*cardiomyopathies are a*

heterogeneous group of diseases of the myocardium associated with mechanical and/or electrical dysfunction that usually (but not invariably) exhibit inappropriate ventricular hypertrophy or dilatation and are due to a variety of causes that frequently are genetic. Cardiomyopathies either are confined to the heart or are part of generalized systemic disorders, often leading to cardiovascular death or progressive heart failure–related disability'[12]. Stemming from this definition, primary cardiomyopathies are those solely or predominantly confined to heart muscle, and include 5 main forms: dilated cardiomyopathy (DCM), arrhythmogenic ventricular cardiomyopathy (AVC), restrictive cardiomyopathy (RCM), left ventricular non-compaction cardiomyopathy (LVNC) and hypertrophic cardiomyopathy (HCM)[13]. The clinical characteristics and genetic contribution to each of these classes of cardiomyopathies varies.

DCM is characterized anatomically by dilatation of the left ventricle with normal left ventricular (LV) wall thickness, functionally by progressive contractile failure, and histologically by cardiomyocyte hypertrophy, loss of myofibrils, and interstitial fibrosis[14]. It has a prevalence of 1:2500 individuals and it is the most frequent cause of heart transplantation[12]. About 25-30% of the cases of DCM are identifiable by a defined genetic cause. While more than 20 loci are involved in the progression of this disease, there is a special predominance of Lamin A/C missense mutations (4-8% of genetic-DCM)[15] and Titin truncating mutations (5-12.5% of all cases)[16].

AVC is categorized by the progressive replacement of the ventricular myocardium with fibrous or fat tissue, leading to arrhythmia, HF, and SCD. Histologically, AVC hearts show irregular fibrosis, inflammation, myocyte death, wall thinning, and aneurysm formation[17]. Between 10-20% of AVC patients develop HF due to ventricular dysfunction. AVC has a prevalence ranging from 1 in 1000 to 1 in 5000 and is a familial disease in approximately 50% of cases, whereby the most frequently mutated genes encode proteins involved in the desmosome in the intercalated disk connecting cardiomyocytes, such as deletions in the junctional plakoglobin (*JUP*) gene[18].

RCM is a rare form of cardiomyopathy defined phenotypically by normal (or reduced) sized ventricles with bi-atrial enlargement, and functionally by diastolic dysfunction due to impaired ventricular filling, leading to atrial arrhythmias, despite showing normal LV wall thickness and normal systolic function[19]. RCM causation is partially ascribed to genetic inheritance with most of the identified genes encoding sarcomeric or Z-disk proteins such as *TNNI3, TNNT2, MYH7, ACTC1, TPM1, MYL3*, and *MYL*[19].

LVNC is defined as an uncommon and heterogeneous cardiomyopathy characterized by prominent trabeculations and deep intertrabecular recesses that are most evident in the LV apex and LV myocardium, resulting in 2 distinct layers (compacted and non-compacted), originated from an arrest in the normal embryogenesis[20]. Clinically, LVNC is associated with HF (53% frequency), due to thromboembolism and arrhythmias that often result in SCD[21].

Systolic and diastolic dysfunction are common and, as it occurs in association with many congenital cardiac disorders, it is not clear whether LVNC is a separate cardiomyopathy or a morphological trait shared by phenotypically distinct cardiomyopathies[22]. Nonetheless, the prevalence of LVNC is estimated to range 4.5 to 26 per 10,000 adult patients, with 18-50% of all cases being caused by genetic inheritance, due to mutations mainly in sarcomeric genes (e.g *MYH7, TNNT2* and *ACTC1*)[11].

Finally, HCM is the most prevalent cardiac genetic disease, affecting 1:500 individuals[23]. It is considered the main cause of sudden cardiac death (SCD) (which may be the first manifestation of the disease[1]) in young adults (<35 years old), with up to 20% of the patients developing HF at median age of 48±19 years[24]. In this regard, the implantable cardioverter-defibrillator (ICD) has reported modest rates of prevention of SCD in HCM-bearing children and/or adolescents, from 4%/year in primary prevention, and 11%/ year for secondary prevention after cardiac arrest[25]. Clinical diagnosis relies on 2D echocardiography or cardiac magnetic resonance imaging, by the detection of LV wall thickening[12]. The echocardiographic features of the different cardiomyopathies reviewed in this section are presented in **Figure 1.2**.

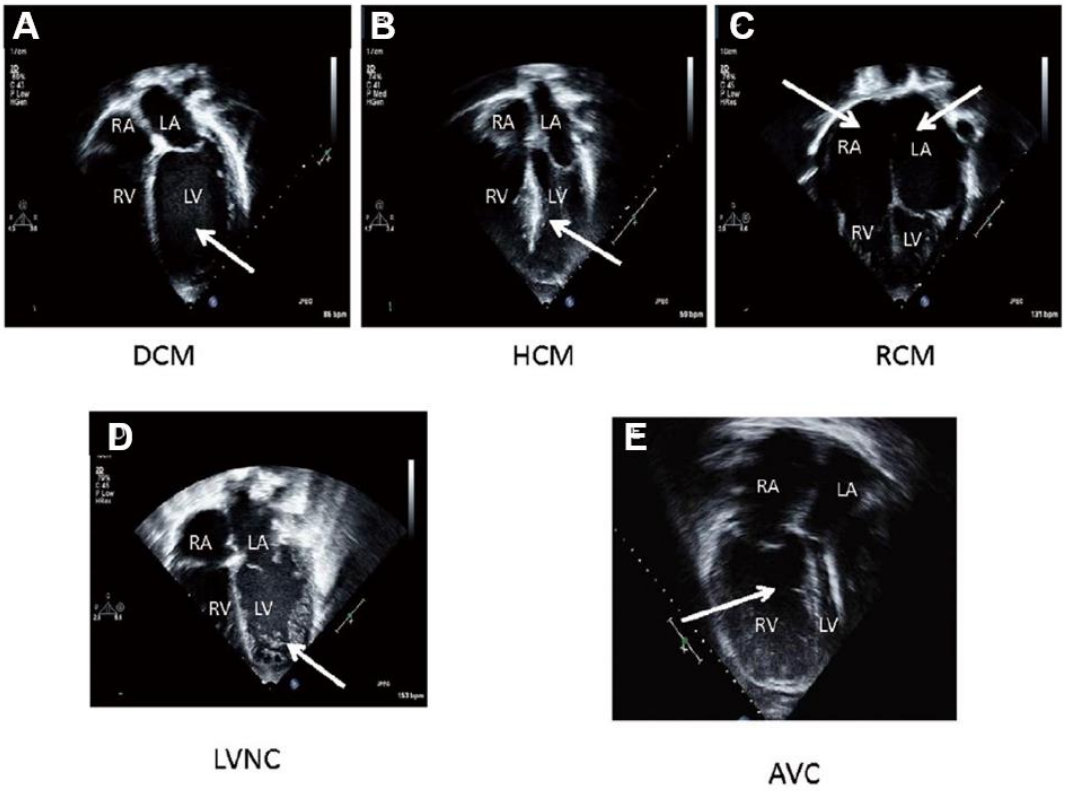


Figure 1.2 - Echocardiographic features of cardiomyopathies. (**A**) 4-chamber view of DCM, highlighting the the dilated left ventricle (arrow). (**B**) 4-chamber view of HCM, illustrating the thickened mid-portion of the interventricular septum (arrow). (**C**) 4-chamber view of RCM, underlining the dilated atria (RA, LA; arrows). (**D**) 4-chamber view of LVNC, emphasizing the hypertrabeculation in the LV (arrow). (**E**) 4-chamber view of AVC detailing the dilated, trabeculated RV (arrow). RA-right atrium; LA-left atrium; RV – right ventricle, LV- left ventricle. Adapted from [13].

1.2.3 Complexity of genotype-phenotype relationships

Despite the existence of different clinical classes of cardiomyopathies, there is extensive overlap between these phenotypes. For instance, HCM, LVNC and AVC may all progress into a dilated ventricle with systolic dysfunction and thus resemble the phenotypic description of DCM, although the primary expression of the disease may differ[12] (e.g. HCM- LV wall thickening, LVNC-trabeculation, AVC-fibrosis). Thus, the dynamic and interchanging clinical manifestations of cardiomyopathies hinder conventional morphological classification (e.g. by echocardiography) and refinement of treatment options.

Another difficulty in segregating and classifying cardiomyopathies lies in the complex genetic contribution of multiple loci and their interactions to the progression of the disease, rather than specific gene mutations correlating with a well-defined phenotype. Typically, each of these phenotypes is associated by one of numerous genetic mutations (**genetic heterogeneity**)[14]. Remarkably, this complexity is reflected in the genetic overlap between different cardiomyopathies, as mutations in genes such as *MYH7, ACTC1* and *TNNT2* have been implicated in HCM, DCM, RCM and LVNC[11]. Importantly, each specific mutation consistently produces the same qualitative phenotype, i.e. a variant causes either HCM or LVNC, but not both. This is clearly demonstrated by *TNNI3* mutation variants: homozygous A2V carriers display DCM[26], R192H causes RCM[27] and R142G is linked to HCM[28] . Nevertheless, such correlations are hampered by the quantitative variability in the cardiomyopathy phenotype, even when the disease gene and allele are the same, which is termed **phenotypic heterogeneity**. Moreover, cardiomyopathies typically exhibit **variable penetrance** (proportion of individuals carrying a pathogenic mutation who display a phenotype) and **variable expressivity** (the severity of the phenotype that develops in a patient with a pathogenic mutation), even in the same family[14].

Importantly, variable penetrance and expressivity imply that factors beyond the single pathogenic mutation (such as genetic and epigenetic backgrounds as well as environmental modifiers) influence the phenotype. In this regard, Ingles et al have recently retrospectively analysed the data derived from 413 HCM patients, and found that 166 (40%) had no sarcomere mutations (non-familial HCM). Interestingly, factors such as older age, male gender, hypertension and non-asymmetric septal morphology were identified as predisposition parameters, although, in all instances, sarcomeric mutation carriers displayed earlier onset and more malignant forms of the disease[29].

1.2.4 Hypertrophic cardiomyopathy (HCM)

In this thesis, an *in vitro* disease model of HCM was developed, so this form of cardiomyopathy will be more extensively reviewed in this section.

1.2.4.1 Clinical and histological characterization

The clinical spectrum of HCM is highly variable and ranges from asymptomatic (i.e. usually undiagnosed) to very severe forms of cardiac dysfunction[30]. Overall, HCM hearts display asymmetric or concentric wall thickening in the absence of an underlying systemic condition such as pressure overload (due to hypertension or aortic valve stenosis)[31]. HCM manifestations may be divided in 3 subtypes[31], characterised by: **i)** progressive LV dilation, thinning and systolic dysfunction (30% of patients); **ii)** LV systolic dysfunction due to outflow tract obstruction (owing to thickening of the interventricular septum- 20% of patients)[32], and **iii)** diastolic HF associated with normal or enhanced ejection fraction (EF) but impaired ventricular relaxation, elevated diastolic pressure, left atrial enlargement and atrial fibrillation (50% of patients). Moreover, in the long-term, 5-10% of HCM patients exhibit severe impairment of contractile performance, leading to sudden ventricular arrhythmia, stroke and progressive diastolic and systolic LV failure[24], also termed end-stage HCM.

Histologically, HCM is associated with interstitial fibrosis (increased collagen content), myocyte enlargement and chaotic spatial arrangement (disarray)[33], as well as thickening of the media of intramural coronary arteries[34]. These features led to the postulation that cardiomyocyte hypertrophy is the adaptive cellular response to an increase in the intrinsic biomechanical stress associated with HCM (due to the impairment of contractile function of the heart).

1.2.4.2 Cellular and molecular mechanisms

Progression of HCM is typically divided in two sequential stages: **i)** compensatory hypertrophy and **ii)** end-stage heart failure. Compensatory hypertrophy relies on changes in gene expression, alterations in cellular morphology, and metabolic shifts in cardiomyocytes, to maintain the cardiac function in response to the increased stress associated with genetic or non-genetic causes[35].

Cardiomyocyte hypertrophy is the most obvious response to altered contractility or physiological stress, as ventricular cardiomyocytes increase in volume to cope with the increased functional demand, thus increasing heart mass as well as LV and interseptum wall thickness[36]. This response relies on increased protein synthesis in cardiomyocytes and higher mobilisation of sarcomeres towards normalisation of the increase in LV tension derived from the initial stress stimulus (mainly HCM mutations changing cardiomyocyte biology). However, (concentric) hypertrophy causes a distortion of the cardiomyocyte alignment which may impair cardiac contractility in the long term, leading to the end-stage HF[37].

HCM triggers **initiation of the fetal gene program**, i.e, induction of genes normally expressed during embryogenesis[35], including those encoding natriuretic factors, β-myosin heavy chain (β-MHC) and α-skeletal actin. Importantly, natriuretic proteins such as Atrial Natriuretic Factor (ANF) and Brain Natriuretic Peptide (BNP) secreted by several cell types in the atria and

ventricles induce diuresis and vasodilation, reducing blood volume and pressure in response to increased wall stress associated with HCM[38,39]. Thus, induced expression of these genes upon HCM triggers a cardioprotective mechanism that attempts to rescue pathological alterations affecting the heart. Moreover, up-regulation of the β-MHC over the α-MHC has been implicated in HCM response, and is regarded as a sensitive marker for early cardiomyopathy[40], as further explored in Chapter 4. This response may indicate an adaptation to an energetic deficit, as the β-MHC displays slower kinetics than α-MHC, thus lower ATPase activity, resulting in more efficient ATP usage[41].

Further adaptive responses to energy imbalances in the myocardium in the context of HCM are based on initial **metabolic shifts** towards the consumption of highly energetic substrates[35]. In the healthy heart, phosphocreatine is the main reserve source of ATP during acute stress. As pathogenesis progresses in cardiomyopathy, the demand for ATP increases, and the levels of phosphocreatine are progressively depleted[42]. Therefore, as a response to cardiac dysfunction stemming from sarcomeric mutations, the initial compensatory stages of HCM rely on free fatty acids, which yield about three times more ATP than glucose, but is more oxygen-demanding, making it a more profitable but less efficient energetic source[43]. However, in end-stage HCM, cardiomyocyte energy substrate utilization shifts to glycolysis[44]; this is a 'cheaper' and quicker means of producing energy, despite yielding lower ATP production, and thus resulting in HF due to inability to supersede the energetic demands the stressed heart requires to function. This is further evidenced by down-regulation of expression and activity of enzymes that metabolize fatty acid use in the failing adult heart, such as acyl-CoA dehydrogenase and peroxisome proliferator-activated receptor-α (PPARα)[45]. Interestingly, this transition from compensatory to maladaptive metabolic shift in HCM is thought to be related to excessive cardiac growth without adequate coronary angiogenesis[46] (also termed microvascular dysfunction, whereby lack of oxygenation of myocardium impairs fatty acid metabolism). This indicates that prolonged adaption to cardiomyopathy is unsustainable due to the compensatory mechanisms elicited in response to the pathological imbalances caused.

Furthermore, increased **myocardial fibrosis** (interstitial and perivascular) has been closely associated with HCM-hearts, as collagen I-III-rich foci are already detected in early stages of cardiomyopathy[35,47]. Remarkably, pathological cues such as cardiac pressure overload, cardiomyocyte apoptosis or mutations in sarcomeric genes were shown to recruit cardiac fibroblasts and myofibroblasts and subsequently hyperactivate them, resulting in the heightened secretion of extracellular matrix (ECM) proteins and other regulatory enzymes and molecules (such as matrix metalloproteinases (MMPs) and micro RNAs- miRNAs)[48]. This leads to the pathophysiological remodelling of the heart ECM, as the presence of collagen-rich regions in the myocardium are not electrically conductive and therefore disrupt the excitation-contraction coupling (ECC) in cardiomyocytes which results in cardiac arrhythmias[49]. In this regard, transforming growth factor-β (TGF-β) has been identified as a

major player in HCM-fibrosis, as its increased secretion from non-myocytes in heterozygous R403Q and R719W-α-MHC mice ($p<0.0001$, vs WT mice) was shown to foster their proliferation (4-fold more BrdU-labeled non-myocytes vs WT mice) and secretion of pro-fibrotic signals in fibroblasts[50]. Remarkably, administration of TGF-β-neutralizing antibodies abrogated non-myocyte proliferation and fibrosis[50], suggesting that prevention and/or modulation of cardiomyopathic fibrosis can represent a promising therapy for HCM.

Interestingly, **disturbed biomechanical stress sensing** may be underlying the mechanisms detailed above[51]. In fact, besides its role and generating contractile force, the sarcomere is a central component of cardiomyocyte signalling pathways, as evidenced by the role of sarcomeric M-bands and the Z-disc in mechanotransducing biomechanical stress[52]. Consistently, mutations in M-band genes such as myomesin-1[53] and Z-disc proteins such as LIM protein[54] have been associated with human HCM. The multitude of downstream pathways and their interactions mediating the hypertrophic response are complex[55,56], but typically include ubiquitous signalling cascades such as calcineurin/ nuclear factor of activated T cells (NFAT)[57], phosphoinositide 3-kinase (PI3K)/ Akt/ glycogen synthase kinase (GSK)[58], and myocyte enhancer factor 2 (MEF2)/ histone deacetylase (HDAC)[59]. Lastly, as explored with further detail in Chapter 5, **impaired calcium cycling** and sensitivity is another hallmark of hypertrophy, as it results in arrhythmias and systolic and diastolic dysfunctions, as increased cytosolic Ca^{2+} concentrations lead to alterations in cardiomyocyte contractility[60].

Collectively, compensatory hypertrophy is activated upon pathological stimuli such as HCM mutations, resulting in ventricular remodelling through alterations in cardiomyocyte volume, interstitial and perivascular fibrosis, induction of fetal gene program, and metabolic switches between fatty acid oxidation and glycolysis. These mechanisms are summarised in **Figure 1.3**. Notably, a sustained hypertrophic response leads to heart failure due to energetic and functional imbalance. It is worth noting that this response is dissimilar to the developmental and/or physiological hypertrophy associated with response to exercise[56], where cardiomyocyte hypertrophy still occurs without promoting cardiac fibrosis and subsequent dysfunction (although some signalling pathways are common between the two mechanisms, such as the calcineurin/NFAT cascade)[55].

1.2.4.3 Sarcomeric genes and phenotypic variability

Cardiac contraction is initiated by the generation of the cardiac impulse by pacemaker cells, without any external stimulation but rather due to electrolyte gradients through the cell membrane. The cardiac impulse is conducted from the sinoatrial node to the atrioventricular node via membrane depolarizarion. After a brief pause at the atrioventricular node, the depolarization current spreads through the ventricular myocardium (cardiac tissue) through the Purkinje network[61], thus pumping blood as a result of heart beat.

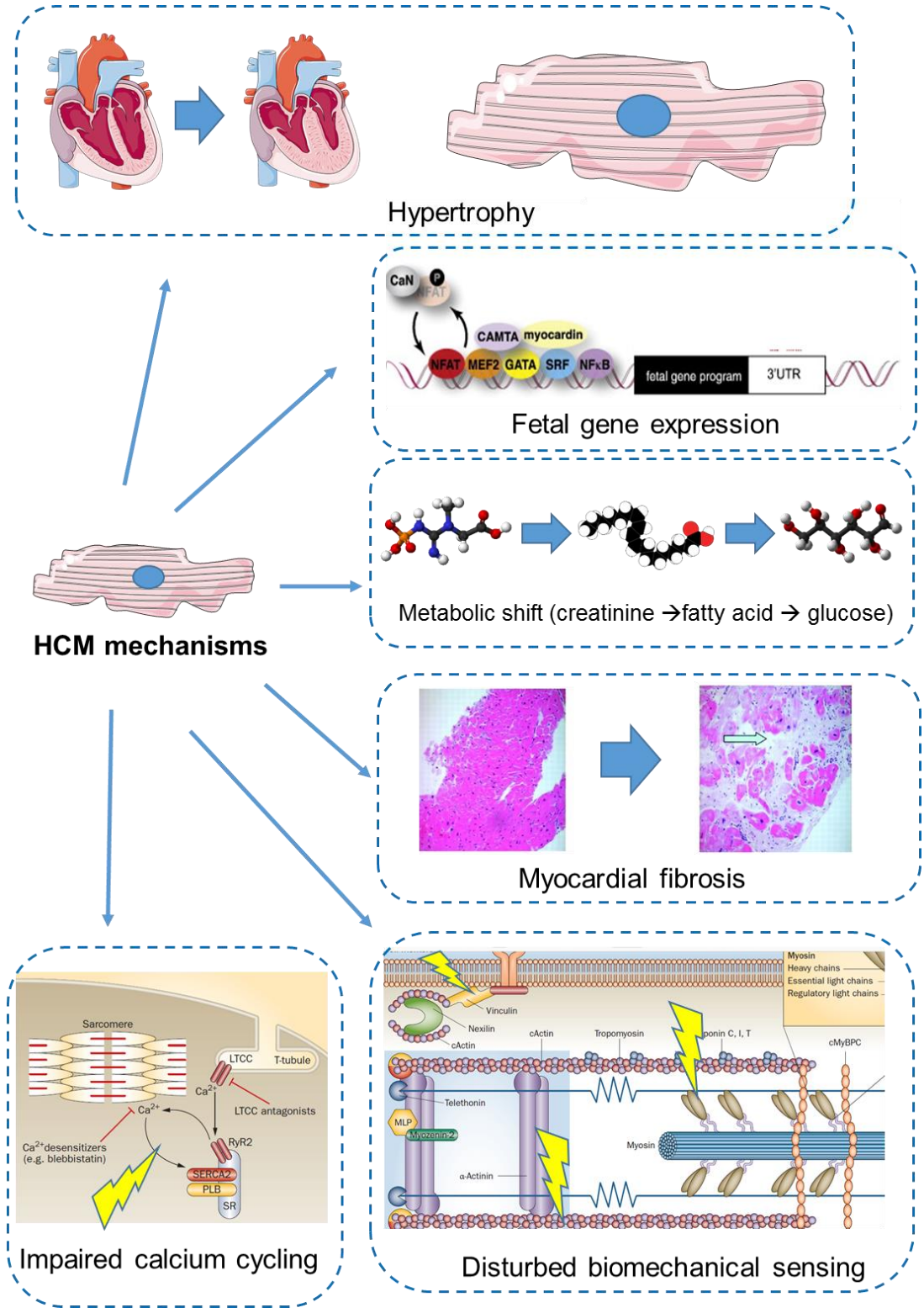


Figure 1.3 – Schematics of HCM mechanisms. Adapted from [39,47,51].

The cardiac tissue is organised in muscle fibres constituted by cardiac muscle cells (cardiomyocytes) in series. CMs are composed of bundles of myofibrils that contain myofilaments displaying repeating units termed sarcomeres, the basic contractile unit of any muscle[62]. The sarcomere encompasses thick and thin filaments – myosin and actin, respectively, that slide past each other when the muscle contracts and relaxes, upon cardiomyocyte depolarisation by an action potential. Additionally, other proteins are involved in the sarcomere contraction such as cardiac troponins (C, I and T), tropomyosins and α/β-myosin heavy chains, constituting the regulatory protein complex that has different roles such as blocking/ exposing sites on the actin molecule in order to mediate the binding to myosin ATPase[63] (**Figure 1.4**). Interactions between myosin and actin constitute the basis for the cardiac contractility, provided there is an energy source (ATP) available and that calcium ions are present in the sarcomeres[64], as explored in Chapter 5. Thereafter, energy production by ATP hydrolysis triggers a conformational change in the actin-myosin complex, thereby shortening the sarcomere, resulting in cardiomyocyte contraction (systole), which ultimately leads to pumping blood into the pulmonary and systemic circulations. Relaxation process (diastole) involves de-activation of the myofilaments by the removal of cytoplasmic calcium[65].

Studies performed in different patient cohorts worldwide support the view that the majority of genes and mutations causing HCM encode proteins associated with the sarcomere and its constituent myofilament elements[66], responsible for regulating cardiomyocyte contraction and ultimately cardiac function. These studies involved the genetic diagnosis of patients and led to the conclusion that mutations in either one of two sarcomeric genes – *MYBPC3* and *MYH7* - were responsible for approximately 60-70% of the causes of autosomal-inherited-HCM, with other less prevalent genes including cardiac troponins T (*TNNT2*) and I (*TNNT3*), and α-tropomyosin (*TPMI1*), each associated with ~5% of HCM cases[67-69] (**Figure 1.4**). In this regard, Lopes et al[3] have analysed the data pooled from different cohorts totalling 2459 patients and corroborated this figure, while the proportion of patients showing mutations in *MYCPB3* is similar to that of *MYH7*. Importantly, approximately 40-60% of the patients showed no mutations in known disease genes, reinforcing the existence of non-familial HCM.

Despite the clinical and phenotypical heterogeneity described in the previous section, mutations in *MYH7* have been overall associated with more severe forms of hypertrophy, greater disease penetrance (reaching 100% in R403Q and R453C-MYH7 mutations[70]), higher risk of SCD and earlier onset, in comparison to those in other sarcomeric genes[2,71]. In fact, data from the most recent meta-analysis review that examined 51 studies totalling 7675 HCM patients showed that *MYH7*-mutant patients exhibit: **i)** earlier mean age of onset of disease (35 vs 39 in *MYBPC3*-mutant patients vs 44 in mutation-negative patients); **ii)** more severe forms of disease, such as higher frequencies of ventricular tachycardia (33% vs 21% in *MYBPC3*-mutant patients vs 17% in mutation negative patients) and conduction system disorders (31% vs 15% in MYBPC3-mutant patients vs 20% in mutation negative patients).

This in turn leads to **iii)** higher risk of SCD (11% vs 5% in *MYBPC3*-mutant patients vs 0.4% in mutation negative patients), resulting in **iv)** higher heart transplantation frequencies (7.7% vs 0.6% in *MYBPC3*-mutant patients vs 2.3% in mutation negative patients)[2].

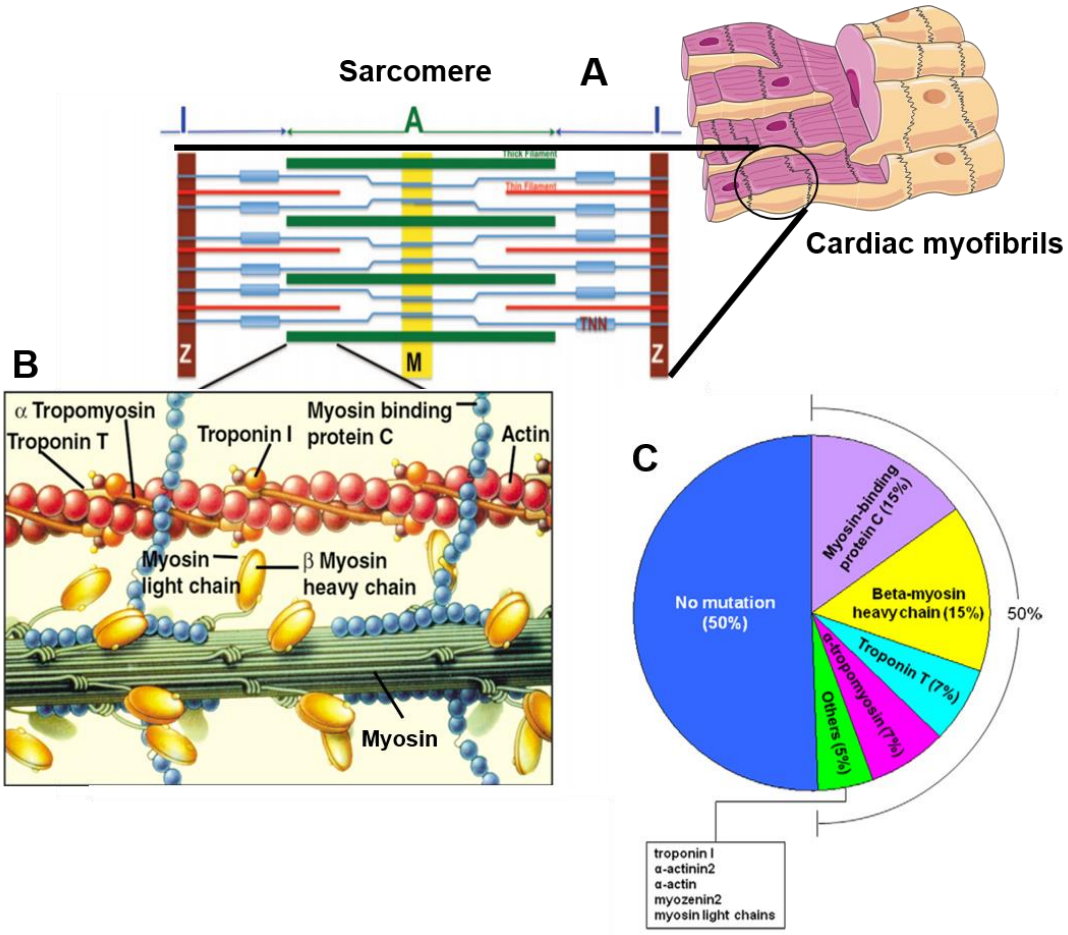


Figure 1.4 - **Involvement of sarcomeric gene mutations to HCM. A)** Cardiomyocytes constituting the cardiac tissue are composed by bundles of myofibrils that contain myofilaments displaying repeating units termed sarcomeres. A sarcomere spans two neighboring Z bands and is constituted by thick myosin (green) and thin actin (red) filaments that slide past each other during contraction-relaxation cycle, as well as **B)** other proteins involved in the regulation of sarcomere contraction such as cardiac troponins (C, I and T), tropomyosins and α/β-myosin heavy chains. **C)** Approximate prevalence of sarcomeric gene mutations in HCM patients. Adapted from [68,69].

1.2.4.4 *MYH7* gene structure and mutagenesis

MYH7 is a large gene located on chromosome 14 in humans, composed of 40 exons that form a 6kb transcript which gives rise to a 1935 amino-acid protein named β-MHC. This protein is divided in three regions: head (exons 3-21), neck (exons 21-25) and tail (exons 25-40), that comprise different functional protein domains such as the ATP binding site in the head region (globular head domain- S1), actin binding site in the neck (S2 domain) and light chain binding site in the tail[72].

To date, over 230 mutations in *MYH7* leading to HCM have been identified in patients, resulting in cardiomyopathies with varying degrees of severity according to the region of the gene mutated. Importantly, clinical data has shown that mutations occur more frequently in the head and neck regions of the gene than in the tail (number of mutations/ number of amino acids of 0.19, 0.20 and 0.04 in head, neck and tail regions, respectively). Moreover, mutations in the head region are more likely to lead to more severe forms of cardiomyopathy than those in other regions (49% of mutations in the head region resulted in malignant clinical phenotypes vs 41% in the neck and 20% in the tail)[73]. In addition, a systematic review of the clinical data gathered between 1966 and 2009 showed that out of a total of 236 exonic mutations in the *MYH7* gene, 207 (87%) caused HCM, 16 (7%) caused DCM, 4(2%) caused RCM and 9 (4%) caused LVNC[73], emphasizing the link between *MYH7* and HCM.

Remarkably, four mutations – R403Q (exon 13)[74], R453C (exon 14)[75], G716R and R719W (exon 19)[76] - have been associated with highly severe forms of early-onset hypertrophic cardiomyopathy with a high incidence of SCD in comparison with other HCM-causing mutations[4]. Despite being particularly rare (~1% prevalence of each mutation in HCM, although early SCD may lead to underestimating this frequency) these mutations are associated with an unusually early onset (<25 years old patients), which highlight their morbidity costs[4]. Considering the structure and function of β-MHC, these mutations are likely interfering with actin binding site, thus perturbing the actin-myosin interaction or altering cross-bridge movement during contraction[73]. The precise mechanisms leading to the disease progression will be addressed in the following Results chapters.

Taken together, HCM is an extremely complex and prevalent disease with multiple clinical manifestations and cellular/molecular mechanisms that arise mainly from mutations in sarcomeric genes, with particular severity in patients bearing *MYH7* mutations.

1.2.5 Approaches to disease modeling HCM

In order to further understand HCM phenotypes and its cellular and molecular mechanisms, several approaches have been undertaken to create disease models. The data acquired from live patients (using non-invasive methods such as echocardiography for monitoring cardiac function[20]) has been complemented by other less complex biological sources that enable more refined analyses of cardiac function. These include: **i)** intact heart muscle strips, **ii)** beating cardiomyocytes, **iii)** myofibrils derived from skinned cells/heart tissue, and **iv)** purified actin/myosin sarcomeric proteins, with progressive decrease in complexity[6]. Although these systems have generated most of the data needed to further the understanding of cardiac diseases such as HCM, they have several limitations. Overall, these comprise the limited sample availability and difficult logistics of sample handling (typically derived from human biopsies). In addition, the simpler systems (isolated cardiac cells and skinned myofibrils) commonly display confounding variables and preparation artefacts. Notably, lower structural

and functional complexity of cell and protein-based models preclude a faithful physiological recapitulation of the human heart[6,77].

Moreover, heterologous expression of mammalian cardiac genes in non-cardiac expression systems (immortalized cell lines such as HEK293) has enabled the characterization of the effect of mutations on individual ion channel function[78]. These analyses have been further enhanced by structural homology modeling and by computational algorithms that integrate individual channel properties into virtual action potentials (APs)[79]. Remarkably, *in silico* modeling of HCM is a developing field, due to the high number of mutations (>1400) identified and the complexity of phenotypes associated with them[80]. Thus, the development of computational models to predict the pathogenicity derived from SNPs has been pursued. For sarcomeric cardiomyopathies, one such algorithm is Poly-Phen2, which predicts the likelihood of a SNP to cause HCM disease phenotypes based on the expected structural and functional change associated with a nucleotide substitution in a given locus (considering physiochemical properties such as hydrophobicity and binding domains), combined with amino acid conservation maps[81]. While the application of the database-driven algorithms to predict primary pathogenicity is a helpful approach to anticipate disease outcomes (with particular usefulness in assisting clinicians decision-making process and prognosing *de novo* mutations), these data do not elucidate potential disease mechanisms. Importantly, sarcomeric proteins are part of a complex multicomponent structure that is hierarchically organised within cardiomyocytes. These in turn interact in the cardiac tissue with other cells to ensure adequate function of the heart as an organ[62]. Therefore, low complexity platforms cannot fully predict the dynamics associated with sarcomere mutations and the consequent disease progression mechanisms.

In this regard, animal models have thus been used as they offer a widely available source of biological material (i.e. the whole heart, cardiac tissue or isolated cardiomyocytes) and, in most cases, tractable genetics enable the establishment of transgenic models to recapitulate genetically-caused disease states. This has resulted in the formation of several cardiomyopathy models in cats, dogs, rodents, zebrafish and *Drosophila* flies[80]. However, the generation of new transgenic models is time-consuming, and the logistics associated with animal house facilities is considerable, especially in the case of large animals[77]. Moreover, species differences between animals and humans comprise the main limitation of these models, as explored in subsequent sections[82].

In order to overcome these limitations (lack of complexity of human cardiac tissues, restricted cardiomyocyte availability, species-differences when using animal models), human pluripotent stem cell cardiomyocytes (hPSC-CMs) have been regarded as a promising alternative due to their capacity to produce virtually unlimited number of human cardiomyocytes[83]. Remarkably, reprogramming of HCM patient-derived somatic cells into a pluripotent state, followed by cardiomyocyte differentiation allows capturing patient genotypes, resulting in

genetically-relevant models for HCM[77]. In addition, gene correction using genome engineering tools can revert (or introduce) the HCM-causing mutation in hPSCs, which offers tremendous potential for disease modeling *in vitro* and, in the long term, gene-therapy[84]. This platform and tools associated with it will be reviewed in the next section. The summary of the different approaches used to model cardiac diseases is presented in **Table 1.1**.

Table 1.1 -Summary of advantages and challenges of different approaches for disease modeling. Adapted from [6,77].

Model	Advantages	Challenges
Live patients (e.g. non-invasive echocardiography)	Whole live-organ analysis	Limited value of data (lack of molecular and in-depth functional characterization)
Intact heart muscle strips (biopsies)	Physiologically-relevant; Pharmacological predictivity	Demanding logistics (requires immediate handling); Limited sample availability
Isolated beating CMs	Amenable to measurements of subcellular functions;	Limited sample availability; lack of proliferative ability in culture; Lack of 3D architecture
Myofibrils from skinned heart tissue/ cells	Direct access to myofilament function; Simple logistics (analysis from frozen samples)	Preparation artefacts; Limited sample availability
Purified actin/ myosin sarcomeric proteins	Direct assessment of actin–myosin interactions	Preparation artefacts; Over-simplistic (non-representative of whole sarcomere interactions)
Animal models	Genetically tractable; Easily available cell and tissue samples; Enables study of whole organ (or organism)	Species-differences (relative to human); Time-consuming genetic manipulation
hPSC-CMs	Unlimited source of CMs; Prolonged experimentation (enables performing chronic studies)	Immaturity; Phenotyping readouts Lack of 3D architecture

1.3 Human pluripotent stem cell-derived cardiomyocytes

Most of the data explored in the previous introduction chapter regarding histological and /or molecular features of HCM is derived from diseased animal models and/or human patient cardiac explants. These sources of cardiomyocytes present a serious limitation to the studies performed; the former due to species differences between animals and humans, from gene expression changes up to variations in cardiac physiology[85], and the latter due to restricted access to human cardiac tissue as well as drawbacks associated with cardiomyocyte culture, such as their lack of proliferative ability[86]. As such, hPSC have been regarded as a promising solution to these limitations, as they can provide potentially unlimited sources of cardiac cells[83]. In this section, the limitations associated with the use animal models for disease modeling will be discussed to pave the way towards the usage of hPSC-CMs.

1.3.1 Limitations of animal models

Human heart tissue derived from non-transplantable or end-stage failing hearts obtained at the time of transplantation likely constitutes the ideal source of cardiomyocytes. However, several issues precludes its use as a reliable cell source[5]. These include the limited availability of donors, high variability in tissue preparation and disease state (entailing factors such as genetics, medication, diet, etc.), and subsequent drawbacks in cardiomyocyte extraction and culture (mainly lack of proliferation in culture as well as de-differentiation). The use of animal-derived cardiomyocytes has thus filled this gap producing extensive knowledge on the molecular pathways associated with human cardiovascular disorders, particularly genetically modified mouse models[82]. This is mainly because the basic principles of cardiac excitation and contraction (reviewed in section 1.2.2) in the animal models mostly used (mouse, rat, rabbit, dog, swine and sheep) are relatively conserved[5]. Moreover, studying these animals poses fewer ethical and logistic barriers in comparison to the human sources mentioned above.

Nevertheless, animal models present striking differences in cardiovascular biology relative to humans, particularly in the mouse. While this species' genome is easily manipulated by gene targeted homologous recombination[87], cardiac physiology is vastly different than that of the human, exhibiting differences such as ~10 times faster beat rates (500bpm vs 60bpm) and 5-10 times shorter electrocardiogram duration (50-100ms vs 450ms)[5]. Moreover, increases in heart rate in mouse are linked with decreased contraction force, while the opposite happens in humans[88] (i.e. human heart display positive force-frequency relationship). Differences in gene expression are also reported such as those pertaining α/β-MHC expression: whereas in humans the α isoform is mainly located to the atria and the β to the ventricles[89], in the mouse the αMHC is expressed in both locations[90]. These differences result in phenotypic variations of cardiac inherited disorders (explored throughout this thesis) as well as changes in drug-induced cardiotoxicity as documented by the 10-fold higher tolerance of mice to 37% of the

drugs than humans[84]. This has resulted in high drug attrition rates (i.e between 1980 and 2009, ~1 in 7 licenced drugs deemed efficacious in Phase III trials had to be withdrawn from the market[91]), as unexpected cardiotoxicity was implicated in 28% drug withdrawals in the USA[92]. Therefore, the use of human models of disease could greatly accelerate the understanding of physiologically relevant molecular mechanisms of disease, promoting the acceleration of drug development efforts and reducing its cost.

1.3.2 Derivation, culture and characterisation of hPSC

The derivation of human embryonic stem cells (hESC) in 1998[93] and the demonstration of human induced pluripotent stem cell (hiPSC) reprogramming from somatic cells by just four genetic factors in 2007[94] constitute two important milestones in modern science and regenerative medicine. Effectively, both technologies resulted in the generation of hPSC that could self-renew indefinitely and generate the three embryonic germ layers and virtually all of the approximately 200 cell types in the body[95]. Remarkably, hPSC can overcome the limitation of animal models and human explants to produce potentially unlimited numbers of cardiomyocytes due to the development of cardiac differentiation protocols (section 1.3.3), with the added value of capturing the genetic background inherent of the initial biological material[83].

The isolation of hESCs from the inner cell mass of the blastocyst[93] has broadened the perspectives of disease modeling and therapeutic intervention but also raised serious ethical concerns due to the requirement of human embryos, prompting efforts to find alternative sources of pluripotent cells. Almost 10 years later, hiPSC were derived by overexpression of key transcription factors (*OCT3/4, cMYC, KLF4, SOX2*) in somatic cells [94]. Initially, hiPSC were produced by the retroviral transfection of human dermal fibroblasts with the four transcription factors, resulting in relatively low efficiencies of 0.02% of transfected cells, and each clone showed approximately 20 retroviral integration sites in total[94]. Thereafter, several methods were developed to enhance reprogramming efficiency and safety such as lentiviruses whereby a single excisable cassette bearing the 4 transcription factors is transfected, resulting in efficiencies of 0.1-1.5% in human skin fibroblasts[96]. However, methods based on integrating viruses carry the risk of insertional mutagenesis, which in turn increases the likelihood of tumorigenesis, as verified by induction of leukemia due to the integration of murine leukemia virus DNA in a promoter of the oncogene *LMO2* as an off-target, in a gene therapy approach designed to correct mutations in interleukin-2 receptor γ chain (IL-2Rγ), associated with X-linked severe combined immunodeficiency[97]. As such, Sendai viruses were engineered to deliver the RNA needed for reprogramming without integration in the genome, showing reprogramming efficiencies of up to 1% in fibroblasts[98]. In addition, non-viral methods to promote transient expression of reprogramming factors resulting in footprint-free hiPSC have been explored, such as mRNA delivery by cationic lipids achieving 1.4% efficiency in human fibroblasts[99], and as OriP/EBNA-based episomal

plasmids. The latter system was used to reprogram several cell types, with efficiencies ranging from approximately 0.01% in fibroblasts to 1.4% in epithelial cells sloughed into urine[100]. Moreover, co-transfection with miR 302/367 factor has shown a 300-400-fold increase in the reprogramming efficiency, indicating that additional factors and small molecules (SMs) such as valproic acid (a histone deacetylase inhibitor) [99] can greatly enhance reprogramming success.

Both hESC and hiPSC express transcription factors (*OCT4, SOX2, NANOG*), cell surface markers such as the embryonic antigens (SSEA-3/4), keratin sulfate-related antigens (TRA-1-60 and TRA-1-81), and display high telomerase activity allowing their indefinite proliferation *in vitro*[95]. hPSC culture methods were initially designed following mouse mESC conditions, i.e. culture of hPSC with mitotically-inactivacted (due to γ-irradiation or mitomycin C treatment) mouse embryonic fibroblasts (MEFs), in an enriched culture medium supplemented with fetal bovine serum (FBS)[101]. Despite supporting the self-renewal of hPSC by the secretion of essential growth factors (GFs, e.g TGFβ), cytokines (e.g Activin A- ActA), and extracellular matrices such as laminins[102], feeder cells such as MEFs present serious drawbacks to the translation of hPSC culture into clinic and to the validity of conclusions drawn from mechanistic studies designed to understand the biology of hPSCs. These are mainly associated with batch-to-batch variations in the expression and secretion of these factors by different feeder cells, thus resulting in undefined media composition that can negatively affect consistent culture of hPSC[103] and introduce confounding variables to the study being performed. Moreover, the serum content and the feeder cells themselves constitute a risk for xenogeneic components and mycoplasma infection which can compromise diverse aspects of cellular physiology such as their growth rate, karyotype and induction of cytokine expression[104].

Thus, feeder-free culture of hPSC was developed to overcome these limitations. Initially, culture of hESC on Matrigel™(MT)-coated tissue culture plates in MEF-conditioned medium ensured long-term stable culture of hPSC[105]. However, this approach still entailed undefined medium formulation and ECM composition, as MT is composed mainly of laminin, collagen IV, heparin sulfate proteoglycans, entactin, and growth factors, exhibiting lot-to-lot variability as it is derived from Engelbreth-Holm-Swarm mouse sarcomas[106]. As such, culture of hPSC into surfaces coated with defined recombinant proteins (e.g. laminin, collagen, fibronectin, vitronectin, E-cadherin) was achieved, resulting in xenogeneic-free substrates despite being expensive and/or labile[107].

Nevertheless, for large-scale expansion of hPSC in chemically-defined and clinically-compliant conditions, biological substrates present drawbacks such as limited scalability and cost. Alternatively, synthetic substrates that support the proliferation of undifferentiated hPSC have been developed. As these are based on peptide or protein-based systems, polymers and polymers in conjunction with biomolecules, batch-to-batch variations are minimized and scalability is ensured, provided that they are amenable to standard sterilization

techniques[107]. For instance, Synthemax™ is a sterilization-compatible vitronectin-based acrylate polymer shown to be effective in the prolonged culture of multiple hESC lines, comprising a scalable and xeno-free system[108].

On the other hand, media reformulation has also led to considerable progress as poorly defined serum, serum replacements and conditioned medium were superseded by more refined media such as StemPro and mTeSR. However, these media often showed considerable batch to batch variability[84]. Development of Essential 8 (E8) medium, where all the protein reagents (including growth factors) are chemically defined has addressed this issue[109] and is becoming the defined medium of choice for many laboratories, despite its high cost at (~USD $450 per litre).

In addition, the passaging method has also been the subject of improvement when culturing hPSC. Initial methods relying on mechanical dissection of individual colonies are incompatible with large experiments and commercial upscaling, so their use is now restricted to particular situations where mono-clogenicity of hPSC colonies needs to be ensured. Clump passaging methods using collagenase, dispase or cell scraping followed but have largely been replaced by small clump passaging with EDTA and lastly by Accutase and Trypsin/ TrypLE enzymes that produce single cells or small clusters (2–5 cells)[110]. Single cell passaging methods enable more accurate cell counting and are compatible with single cell cloning needed for genome editing technologies[84]. However, hPSCs cannot survive as single cells under normal cell culture conditions except when special signalling pathways are manipulated. For example, inhibition of Rho-associated kinase (ROCK) pathway by the SM Y-27632 markedly diminishes dissociation-induced apoptosis in hPSCs (~8.8-fold decrease relative to untreated) and enables the culture of individualized hPSCs in adherent or suspension culture systems[111].

Lastly, large-scale expansion of hPSC for future clinical use requires three-dimensional bioreactors, as surface area limits cell proliferation in adherent cultures. In this regard, Amit and colleagues[112] have developed a simple suspension culture system based on the culture of hESC lines as embryoid bodies in serum-free medium that was able to retain pluripotency and hPSC expansion for 20 passages. More recently, use of defined medium mTeSR has proven to be compatible with a similar suspension culture format, leading to 32-fold expansion of hiPSC[113].

Altogether, since their discovery, culture and expansion of hPSC have been improved to reach GMP-grade clinical standards, enabling the production of the differentiated cell lineages required for disease modeling and even transplantation purposes. As these methods are associated with different costs, a cost-risk analysis should be made individually considering the goal of the study, i.e. whereas cell therapies may require clinical-grade hPSC culture procedures, knowledge-based *in vitro* work is compatible with less stringent and thus

economically-sustainable conditions. The same principle applies to cardiac differentiation protocols, reviewed in the next section.

1.3.3 Cardiac differentiation of hPSC

In order to generate the cardiomyocyte numbers needed for disease modeling and other even more demanding biomedical applications, efficient cardiac differentiation protocols are required. For instance, $1x10^8$ hESC-CMs exhibiting 63% cardiomyocyte purity were required to transplant a guinea pig model of cardiac cryoinjury, resulting in partial remuscularization (8.4±1.5% of the scar are was covered with human cardiomyocytes) and a marked reduction (~9-fold) in ventricular tachycardia relative to non-transplanted animals[114]. Similarly, transplantation of 1 billion hESC-CMs into infarcted hearts of pigtailed macaques led to moderately successful cellular engraftment (about 40% of infarct size), resulting in successful electro-coupling (100% of the animals transplanted)[115]. It then stands to reason that to achieve similar degree of success in larger human hearts, at least 10 billion hPSC-CMs are needed. Regarding *in vitro* analysis of cardiac liabilities, screening of a hundred compounds over 6 x ½ log doses for 10 replicates using existing 96-well calcium imaging systems would require approximately 500 million hPSC-CMs, a number that can amount to 3 billion when using more complex 3D heart tissue models in 24-well scale[84]. As such, generation of highly efficient cardiac differentiation protocols is crucial for these applications, as well as for disease modeling.

1.3.3.1 Recapitulating cardiac development

In order to achieve the cell numbers required for the different applications mentioned above, understanding the biology underlying cardiac development is paramount, as recapitulation of that process *in vitro* using hPSC drives cardiac differentiation. During embryonic development, the heart is one of the first organs to be formed during development in vertebrates. After gastrulation, epithelial-to-mesenchymal (EMT) transition precedes formation of cardiac mesoderm that occurs at the posterior side of the embryo, along with the primitive streak[116].

Mesodermal pre-cardiac cells are multipotent and differentiate into myocardial, endothelial and smooth muscle cells by a phenomenon termed progressive lineage restriction[117]. Myocardial cells then differentiate into chamber-specific cardiomyocytes (atrial and ventricular) and conduction cells[118]. Mesodermal pre-cardiac cells migrate towards the cephalic pole of the embryo to form the first heart field (FHF). Very early in cardiac development, a second population of cardiac cells is present at the medial and ventral parts of the FHF [6]. This group of cells, called the second heart field (SHF), migrates medially and into the pharyngeal regions upon primary heart tube formation. SHF cells differentiate into cardiomyocytes, smooth muscle cells and endothelial cells[119]. The role of the SHF is crucial for the development of the four-chamber heart: cells from the anterior part of the SHF contribute myocardial cells to the right ventricle and to the outflow tract, and smooth muscle

cells to the base of the aorta and the pulmonary artery[120]; cells from the posterior part of the SHF contribute myocardial cells to the walls of the atria and to the atrial septum, and smooth muscle cells to the walls of the systemic and pulmonary veins[121]. The FHF then serves as a scaffold for building most of the heart from the cells of the SHF[122] and gives rise only to the left ventricle and to the most primitive part of the atria. Thereafter, two atrioventricular endocardial cushions appear. Fusion of these endocardial cushions then ensures correct septation of the heart towards the establishment of a 4 chambered organ[123].

Mesoderm formation and cardiogenesis (a process by which progenitor cells of the mesoderm become cardiomyocytes) is controlled by several families of growth factors such as Bone morphogenetic proteins (BMPs) and the wingless/INT proteins (WNT)[124]. In vertebrates, BMP signalling generally promotes cardiogenesis and WNT signaling is involved in cardiac specification, with complex roles as it may inhibit or promote differentiation depending on spatiotemporal context (WNT pathways are active during mesoderm induction and inhibited upon cardiac specification and differentiation)[116].

During the formation of heart fields, expression of transcription factor Nkx2.5, the T-box protein Tbx5, Islet-1 (Isl1), and LIM homeodomain transcription factor in cardiac progenitors is initiated. Finally, Nkx2.5 and Tbx5 associate with members of the GATA family of zinc finger transcription factors (GATA4/5/6) as well as with members of the MEF2 family to trigger expression of cardiac structural genes, such as actin, myosin light and heavy chains and troponins.

In summary, different subtypes of cardiomyocytes can be found in the heart displaying functional heterogeneity (e.g. contraction, generation of electrical impulses, propagation of action potentials) according to their anatomical location[124]. Generally, cardiomyocytes are divided into atrial, ventricular and nodal subtypes. Heart failure mostly affects the left ventricle (as is the case of HCM), so generation of ventricular subtypes of hPSC-CMs is warranted to address disease modeling and transplantation purposes.

1.3.3.2 Cardiac differentiation protocols

Overall, pluripotent stem cells undergo a series of sequential differentiation steps (mesoderm, cardiac mesoderm, cardiac progenitors) spatiotemporally regulated by different growth factor combinations to form beating cardiomyocytes. Thus, the cardiac protocols developed are based on the temporal activation/ inhibition of these signalling pathways to drive cardiac differentiation of hPSC to cardiomyocytes[125]. Despite sharing a common goal, a plethora of different cardiac differentiation protocols was developed and can be divided in 4 main classes: **i)** embryoid body (EB) formation, **ii)** inductive co-culture formation, **iii)** monolayer culture and **iv)** suspension culture[126].

EB-formation methods are based on the suspension culture of hPSC as single cells or small clumps in a medium that drives cardiogenesis and/or does not support pluripotency. EBs can

be formed in many ways granting variable control of EB size and number, such as in ultra-low attachment static suspension cultures, hanging drop method, and forced aggregation in V-shaped 96 well plates or AggreWell™ plates. EBs formed by different approaches undergo cardiogenesis by the temporal-specific treatment with cardiogenic growth factors, SMs and media. Initially, these approaches produced purities of 50% hPSC-CMs and additional enrichment was needed to go beyond 90% purity, such as media re-formulation, optimisation of growth factor concentration and temporal application[126] and by incorporation of selection markers in cardiac promoters (e.g. α-MHC)[127]. Nevertheless, these methods produced cells with properties associated with cardiomyocytes such as expression of sarcomeric genes and translation into myofilament proteins, spontaneous beating and electric field and action potentials typical of early nodal-, atrial-, and ventricular-like cells[128]. Although these methods paved the way for successful generation of cardiomyocytes, they are not amenable to the scaling-up required to produce the billions of cells necessary for transplantation and disease modeling. Moreover, they present other disadvantages such as the requirement of a very strict control of parameters like the EB size and initial number of cells, the heterogeneity of (cardiac) cell types formed within the EB and mostly the lack of resistance of EB-derived cardiomyocytes to dissociation methods into single cells, required for phenotypic analysis.

In a different approach, co-culture of hPSC with a murine visceral endoderm-like cell line (END-2) has resulted in beating areas in 35% of the wells tested, although only 2-5% of the cells were hPSC-CMs[129]. Further refinement of this method by serum and insulin depletion led to a 10-fold increase in the number of beating colonies, formed by 25% cardiomyocytes[130]. Dissection of the interaction between END-2 cells and hPSCs revealed secretion of ActA, BMP and repressors of canonical WNT pathway, thus providing insight into the signals involved in cardiac differentiation, which contributed to refining existing protocols. However, although co-culture requires few cells and is a simple method to generate hPSC-CMs, it is a time-consuming and labour intensive method that results in impure cardiomyocyte populations surrounded by a murine cell line, rendering this protocol unfit for cell-demanding and/or clinical grade applications.

Unlike in EB-methods where complex diffusional barriers add uncertainty to the concentration of growth factors and SM hPSC are exposed to, 2D culture of hPSC forming uniform monolayers provide a more controlled and reproducible differentiation environment. Laflamme et al established the first monolayer protocol for differentiating hESC, based on the treatment of hPSC with a high dose of ActA (100ng/ml) for one day, followed by BMP4 (10ng/ml) for 4 days, in RPMI/B27 medium. This approach resulted in >30% cardiomyocyte purities which could be enhanced by the inclusion of a Percoll gradient centrifugation step to 71-95%[131]. Further improvements to the original methods relied on temporal exclusion of insulin by the use of a insulin-deprived B27 supplement in basal RPMI medium as well as the incorporation of a MT overlay step, based on the fact that ECM proteins play central roles in development and can complement cytokine-based signalling. In this protocol, culture of hPSC onto MT-

coated surfaces in defined commercially available mTESR1 medium until 90% confluence is achieved precedes application of a MT layer dissolved into the same medium[132]. This step emulates the EMT process characteristic of heart development. Subsequent treatment of growth factors ActA, BMP4 and fibroblast growth factor (FGF) in RPMI+B27-insulin medium resulted in cardiomyocytes with high purity (up to 98%) and yield (up to 11 CMs/ input hPSC), from multiple hPSC lines. However, inclusion of MT brought some disadvantages such as undefined composition and high cost (aggravated by the use of recombinant GFs) as it is an animal-based product, thus impeding the clinical application of hPSC-CMs generated by this method.

In order to decrease the variability and costs associated with growth factor-based protocols, several small molecules have been explored for driving cardiac differentiation, such as the use of GSK3β inhibitor ChiR as well as the WNT inhibitors IWR-1-4, resulting in 90% cardiomyocyte purities[133]. Screening of other small molecules resulted in the discovery of KY02111 which acted in synergy with other WNT-inhibitors such as XAV939 to produce 98% pure cardiomyocyte colonies in a serum- and growth factor-depleted medium, thus deeming it a cost-effective protocol[134]. Furthermore, in order to enable the translational application of hPSC-CMs, methods relying solely on chemically defined media and surfaces have been developed. The most defining protocol was developed by Burridge and colleagues whereby several basal media, medium supplements, albumin sources, WNT inhibitors and matrices were screened to establish a highly efficient cardiac differentiation protocol based on the minimum number of components needed for its success[135]. In this method, stable culture of hPSC in E8 medium in vitronectin-coated surfaces precede cardiac differentiation by switching into a basal RPMI-medium supplemented with rice-derived albumin and ascorbic acid. Addition of two small molecules sequentially (firstly ChiR for 2 days followed by WntC59 for another 2 days) resulted in >95% cardiomyocytes with a yield of up to 100 cardiomyocytes for every initial hPSC, in the 11 cell lines tested.

Although cardiac monolayer differentiation protocols are able to generate relatively high numbers of hPSC-CMs, cardiomyocytes suffer inherent heterogeneity (and mixed populations composed by the 3 subtypes), batch variation, limited scalability and inter- and intra-laboratory variability[136], as small-scale 2D cultures are sensitive to fluctuations in physicochemical parameters. Moreover, some of the protocols require hPSC to have been pre-adapted to a particular starting condition as undifferentiated cells (such as stabilised growth characteristics and dissociation method). Nevertheless, automated platforms have been developed to scale up production of monolayer-based cardiac protocols, such as the Tecan Evoware Liquid Handling Platform that can handle ~100 x 92cm^2 Roboflask™ format vessels, resulting in a potential maximum batch production yield of 3 x 10^9 hPSC-CMs in a fully defined and reproducible manner[84].

In order to greatly increase the scalability of existing cardiac differentiation protocols, several 3D suspension bioreactor systems have produced CMs from hPSCs by using anchorage-dependent (i.e., microcarrier-based) and independent (microcarrier-free) systems. MT-coated microcarriers have been used to encapsulate hPSC in 100ml spinner flasks and rocker platforms in an intermittent agitation regime, resulting in up to 60% cardiomyocyte purities by the application of WNT modulation (ChiR+IWP-2) differentiation protocol for 12 days[137]. An example of matrix-independent cardiac differentiation in suspension relied on the formation of hPSC aggregates (80–90×10^6 of cells) in a 100-ml stirred bioreactor. In this approach, approximately 100% of the undifferentiated aggregates generated cardiospheres after 10 days in SM-based WNT-modulation culture. The cardiospheres showed spontaneous contractility and contained highly enriched CMs (up to 90% $cTnT^+$ and MHC^+ cells) with consistent action potential generation supporting electrophysiological functionality[138]. Finally, Breckwoldt and colleagues have recently described a mixed protocol based on the EB-formation by forced aggregation in spinner flasks, following monolayer culture and cardiac differentiation of hPSC[139]. In this work, GF (ActA, BMP4, bFGF)-induced mesoderm induction and SM (DS-I-7)-based cardiac specification of EBs in ultra-low attachment flasks resulted in beating cardiospheres that can then be dissociated using collagenase and plated as single cells or incorporated in 3D EHTs for functional analysis. In this protocol, 48 million cardiomyocytes were reported to be produced from starting 60 million hPSCs, exhibiting purities of 85±4%. The authors claim the method is highly consistent due as the forced aggregation procedure of EB formation generates EBs with homogenous size distribution and cell numbers, which gains considerable importance as spinner flask culture of EBs is highly scalable[139].

A summary of methods for reprogram, culture and differentiate hPSC cardiomyocytes is illustrated in **Figure 1.5**, highlighting those performed in this thesis.

1.3.4 Maturation of hPSC-CMs

Despite the establishment of efficient cardiac differentiation protocols, hPSC-CMs do not exhibit the morphological and functional characteristics of adult cardiomyocytes, resembling the fetal stage of development instead. Therefore, promoting maturity of hPSC-CMs is a current goal of the field as mature human cardiomyocytes may better reflect the physiology of the adult heart (e.g electric and mechanical properties) and therefore be more useful for disease modeling and drug screening approaches and for successful transplantation.

1.3.4.1 Immaturity of hPSC-CMs

Overall, differences between hPSC-CMs and adult CMs range from morphological and gene expression changes up to structural and functional discrepancies[140]. Morphologically, adult CMs are large and cylindrical and display an aspect ratio (length: width) between 5 to 9.5:1[141], whereas hPSC-CMs are round or multi angular and predominantly mono-

nucleated cells with aspect ratios of 2 to 3:1[142]. This reflects on the sarcomeric organisation: while adult CMs show longitudinally oriented sarcomeres with ~2.2μm in length[143], hPSC-CMs exhibit chaotically organised ones showing ~1.6μm length[144]. Ultra-structurally, adult CMs display I-, H-, A- and M-bands whilst hPSC-CMs only show Z-discs and I bands[84]. Moreover, the contractile apparatus also exhibits differences as, during development, several myofibrillar protein isoforms (e.g Troponin I) undergo switching, contributing to the modulation of the contractile function of cardiomyocytes[145]. As such, adult CMs differ from hPSC-CMs as, unlike the latter, they have already undergone the switch. That is the case with: **i)** titin, that shifts from a compliant isoform N2A to a shorter and stiffer form N2B[146]; **ii)** troponin I that changes form a slow skeletal form (ssTnI) to another showing decreased Ca^{2+} sensitivity for tension production (cTnI)[147]; and **iii)** myosin heavy chain (MHC), where the main form expressed in hPSC-CMs is the α-MHC, while β-MHC is primarily expressed in adult CMs, correlating with postnatal heart rate decrease[148].

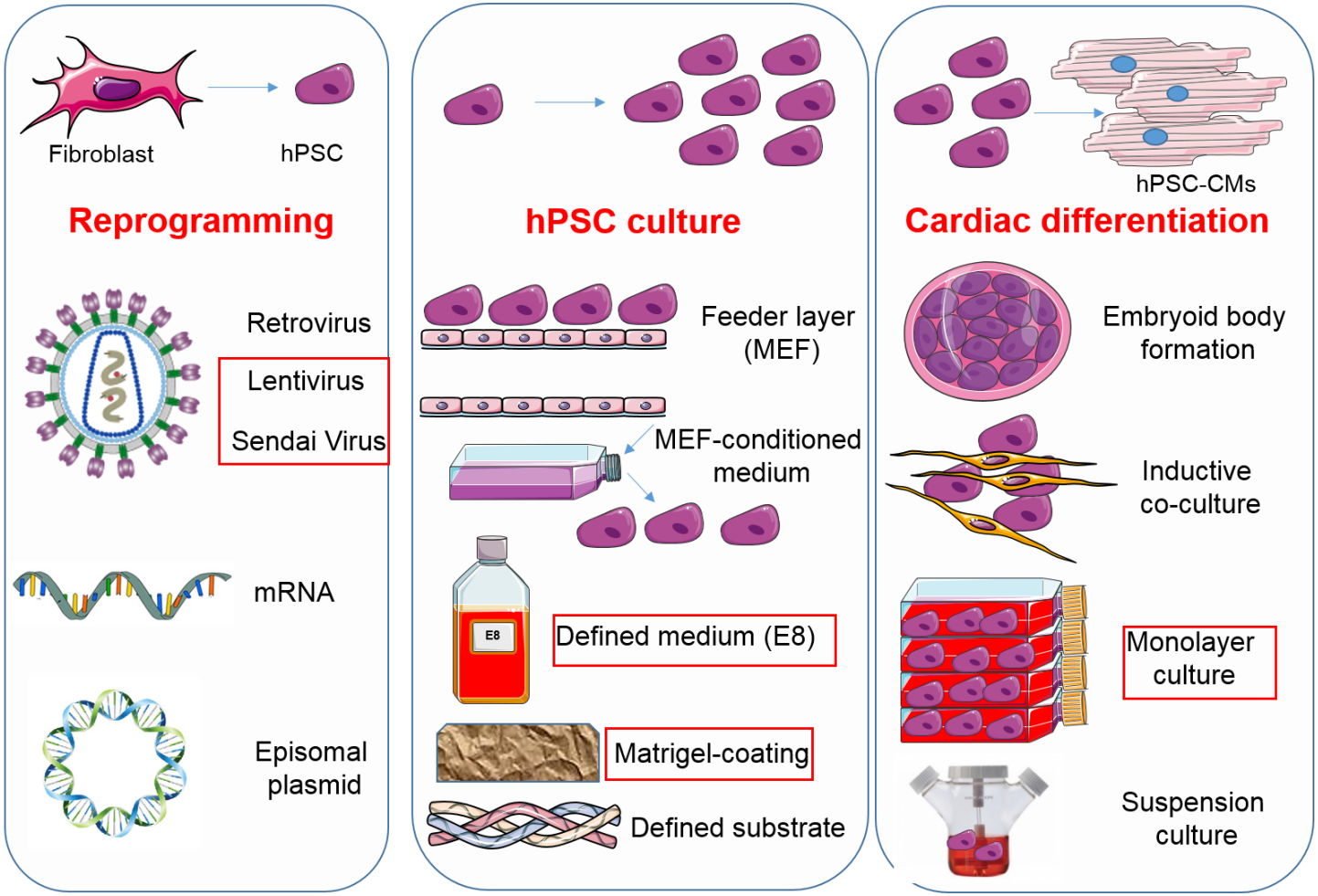


Figure 1.5 - Summary of the developed methods to reprogram, culture and differentiate hPSC into cardiomyocytes. Those used in this thesis are highlighted by red boxes.

Moreover, genes associated with ion transporters or their regulation are predominantly expressed (>2 fold- increase) in adult CMs in comparison with hPSC-CMs, such as sarcolemmal genes (e.g. *KCNH2*) and those involved in the sarcoplasmic reticulum (e.g. phopholamban, *PLN*)[149]. While these changes are reasonably assessable in cardiomyocyte biology, the existence of Transverse tubules (T-tubules) is a hallmark of mature CMs, as these constitute membrane invaginations along the longitudinal axis of adult mammalian ventricular myocytes, and not hPSC-CMs[150]. T-tubule detection is primarily done by electron or fluorescence microscopy and also functionally, as they mediate ECC resulting in synchronous triggering of sarcoplasmic reticulum (SR) calcium release, leading to a coordinated contraction throughout the entire cytoplasm in adult CMs. On the other hand, hPSC-CMs are characterized by heterogeneous calcium dynamics across the cell due to the asynchronous activity of Ca^{2+} transients[150].

The structural and gene expression differences explored result in functional changes. Metabolic differences between adult CMs and hPSC-CMs exist, as although they both rely on oxidative phosphorylation (OXPHOS), adult CMs predominantly metabolise fatty acids whereas hPSC-CMs use glucose and lactate as the main energy sources[151]. Notably, mitochondrial content is also disparate as adult CMs display this organelle throughout the cell constituting 20-40% of the cell volume[152], contrasting with hPSC-CMs where mitochondria occupy a smaller fraction of the cell volume and are mainly perinuclear[153].

Electrophysiological properties are distinct between adult CMs and hPSC-CMs, which is evidenced by the spontaneous beating activity exhibited by the latter in contrast to the quiescence shown by the former[84]. This stems from the high expression of the pacemaker current, I_f, and low expression of inwardly rectifying potassium current, I_{K1} in adult CMs, which stabilises the resting membrane potential to around -85 mV in adult cells whereas this value is -20 to -60 mV in hPSC-CMs[154]. In addition, lower levels of the sodium channel $Na_v1.5$ and the L-type calcium channel (LTCC) in immature cardiomyocytes lead to a 5-fold slower upstroke velocity (50V/s vs 250V/s) relative to adult CMs[155]. Furthermore, location of gap junction proteins (e.g. connexin 43- Cx43) around the cell circumference in hPSC-CMs[156] rather than at the intercalated discs characteristic of adult CMs[157] results in slower conduction velocity (10-20 cm/s vs 30-100 cm/s)[140].

Finally, differences in contractile force between adult CMs and hPSC-CMs amount to several orders of magnitude. At a single cell level, the magnitude of the force generated by hPSC-CMs is typically in the nN range whereas that of adult CMs is in the μN range[140]. This difference is reflected experimentally at the tissue level, as muscle strips of infracted heart muscle showed twitch forces of 40-80 mN/mm^2 [158], which is approximately 600-fold greater than those showed by hPSC-CMs embedded in fibrin-based EHTs (showing forces of 0.08-0.12mN/mm^2)[159]. All of these features are summarized in **Table 1.2**.

Table 1.2 - Summary of maturation differences between hPSC-CMs and adult CMs. Adapted from [140].

Parameters		hPSC-CMs	Adult CMs
Morphology	Cell Shape	Circular	Rod-shaped
	Aspect ratio	2-3 : 1	5-9.5 : 1
	Sarcomere length	~1.6 µm	~ 2.2 µm
Myofibrillar isoform	Titin	N2A	N2B
	Troponin I	ssTnI	cTnI
	MHC	β > α	β >> α
T-tubules		Absent	Present
Mitochondria		Mainly perinuclear, occupies small fraction of cell volume	Regularly distributed; occupies 20-40% of cell volume
Electrophysiological properties	Resting membrane potential	-60 mV	-90mV
	Upstroke velocity	~50 V/s	~ 250 V/s
Conduction velocity		~0.1 m/s	0.3-1.0 m/s
Gap junction distribution		Circumferential	Polarized to intercalated discs
Contractile force		0.8-1.2 mN/mm^2	40-80 mN/mm^2

Altogether, hPSC-CMs are often cited as immature and hence not representative of the adult cardiomyocyte or intact myocardium. However, the same also applies to any *in vitro* system, as the full recreation of the complex 3D structure of the human heart remains elusive[6]. Nevertheless, hPSC-CMs can still be used to model sarcomeric diseases as these cells can phenocopy many aspects of HCM, such as cellular enlargement, contractile arrhythmia calcium dysregulation and sarcomeric disarray[160-162]. In addition, hPSC-CM immaturity may even be advantageous to model early disease stages, which is particularly relevant for HCM patients who typically show an early onset of heart failure[70]. This is when treatment is most likely to be effective, hence will be useful for further mechanistic dissection, development of diagnostics and drug testing

1.3.4.2 Strategies to enhance maturation of hPSC-CMs

The reported differences between adult CMs and hPSC-CMs are likely explained by the fact that human neonatal cardiomyocytes require 6 to 10 years *in vivo* to reach their adult

phenotype in terms of size, shape, molecular composition, metabolism, and physiological function[163], whilst beating cardiomyocytes can be generated from hPSC within 10-15 days of differentiation[125]. Thus, long-term culture of hPSC-CMs to improve maturation has been explored for instance in the work developed by Lundy et al[144] where hPSC-CM cultured for up to 120 days showed a ~3.5 fold increase in cell size and anisotropy, a 10-fold increase in the proportion of multinucleated cells, increase of sarcomeric length from ~1.65μm to over 1.8μm and a qualitative higher density of organised and aligned myofibrils. Functionally, contraction magnitudes were twice as high in late-stage hPSC-CMs, calcium transient kinetics were faster (e.g. ~2.5-fold increase in maximal upstroke and decay velocities and a ~3.5 fold decrease in time to peak), and electrical activity was enhanced, as evidenced by an increase in the maximal upstroke velocity (dV/dt max) from 44 ± 10.8 V/s in early-stage hESC-CMs to 188.7 ± 12.6 V/s in late-stage hESC-CMs, as well as a lower resting membrane potential (- 57.3 ± 1.9 mV vs. - 68.2 ± 2.1 mV), more closely resembling adult CMs. However, long-term culture of hPSC-CMs is incompatible with higher throughput studies and the time scale of drug testing platforms. Therefore, other strategies were developed, based on the provision of biochemical or biophysical cues to the hPSC-CMs to accelerate the maturation state.

Biochemical cues to improve maturation of hPSC-CMs rely mainly on medium additives. As such, treatment of cardiomyocytes with Tri-iodo-L-thyronine (T3)[164] (a hormone involved in human heart development) for one week has resulted increased cardiomyocyte size (60%), anisotropy (~22% lower circularity index), and sarcomere length (from ~1.67 μm to 1.73 μm). Furthermore, contractility analyses performed by culturing individual cardiomyocytes in arrays of microposts showed improvements in the twitch force of T3-treated hPSC-CMs (12.3 ± 0.7 nN/cell vs 7.5 ± 0.4 nN/cell in untreated conditions), although still a few orders of magnitude below adult CMs.T3 treatment has also improved calcium transient kinetics as shown by an increase in maximal upstroke (~2.5-fold) and decay (2-fold) velocities. Lastly, extracellular flux analysis using Seahorse™ platform has resulted in significantly higher ($p<0.05$) mitochondrial respiration rate upon T3-treatment, as evidenced by ~1.5 fold increase in the oxygen consumption rate (OCR) relative to untreated controls. In addition, other documented biochemical cues include miRNAs[165] and the chemical composition of substrates, as shown by the phenylephrine-induced hypertrophic response of neonatal rat ventricular CMs (NRVM) cultured on fibronectin or laminin but not on gelatin[166].

Biophysical cues have also been provided to hPSC-CMs to promote maturation. Beating of adult cardiomyocytes in the atria and ventricles of human heart innervated by the autonomic nervous system is mediated by nodal CMs, which determine pace and contractility[167]. As hPSC-CMs beat spontaneous in culture, it stands to reason that electrical stimulation using an external source could emulate the activity of nodal CMs, thus improving electrical properties of ventricular CMs. This was explored by Radisic et al[168], wherein NRVMs were seeded onto collagen sponges and electrically stimulated for 5 days, resulting in 7-fold higher contraction amplitude vs non-stimulated constructs, evolving progressively with time.

Additionally, electrically stimulated constructs displayed an increase in ultrastructural organisation, as evidenced by higher volume fractions occupied by sarcomeres and mitochondria (32 and 10% in stimulated vs 10 and 8 in unstimulated, respectively), approaching the structure of native heart tissue.

Moreover, mechanical stimulation of hPSC-CMs was investigated, as mechanical cues such as cyclic stretch, mechanical load and substrate stiffness are expected to mimic the native properties of heart tissue that cardiomyocytes experience *in vivo*. In this regard, Mihic and colleagues[169] have seeded hESC-CMs onto gelatin-based scaffolds and exposed them to uniaxial cyclic stretching. Stretched cardiomyocytes displayed more extensive expression of gap junction protein Cx43 throughout the scaffold (double the area), higher expression of cardiac-specific sodium (*SCN5A*) and potassium (*KCNH2* and *KCNJ2*) ion channels, and shorter calcium cycle duration (0.50±0.07s vs. 0.70±0.04s) relative to unstimulated conditions.

Alternatively, 2D substrate stiffness was modulated to resemble that of native heart tissue (in the range of 10-500KPa)[170]. In this regard, NRVMs were cultured on polyacrylamide gels with different elastic modulus (13KPa vs 90KPa) and aspect ratios (2, 4, 7, 10) and traction force microscopy coupled with mathematical modeling were applied to interrogate cardiomyocyte biology. This study showed that sarcomeric content and microtubule polymerisation were higher in 90KPa-seeded cardiomyocytes and peak systolic longitudinal force was higher in those surfaces (0.8-1.2μN) in comparison to 13KPa (0.4-0.5μN), although the maximum values were achieved at different aspect ratios (2:1 for 90KPa surfaces and 7:1 for 13KPa surfaces)[171].

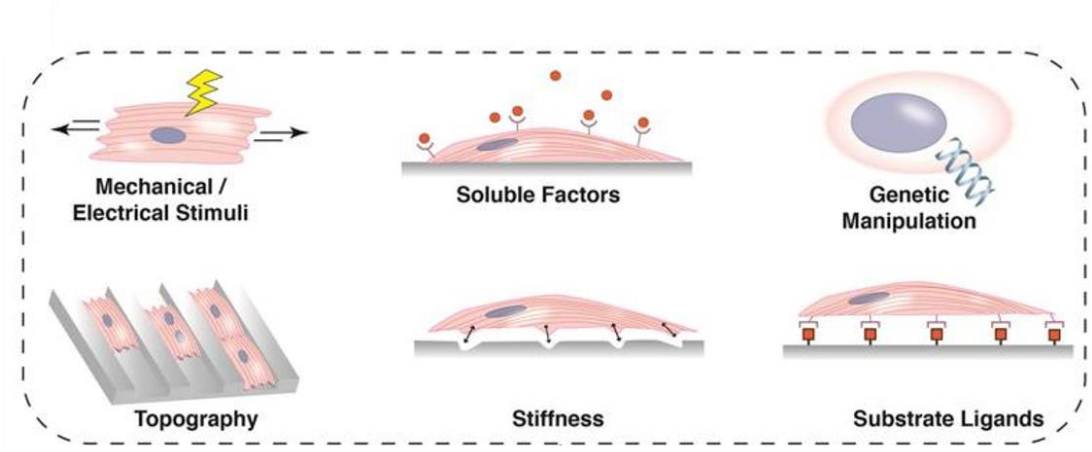


Figure 1.6 - Schematic of *in vitro* maturation strategies for hPSC-CMs. Methods include biophysical stimuli such as mechanical cues, electrical stimulation, optimizing substrate stiffness and topography. Biochemical cues can be presented as soluble factors or substrate ligands within biological or synthetic matrices. Genetic manipulation such as forced expression of missing ion channels has also been adopted as a maturation strategy. Adapted from [84].

In addition, substrate topography and/or patterning was another parameter explored for hPSC-CM maturation, as demonstrated by seeding iPSC-CM onto fibronectin-coated 10μm-wide microgrooved polydimethylsiloxane (PDMS) scaffolds for two weeks, resulting in ameliorated cellular alignment, enhanced calcium transient properties (up to 40% shorter time to peak) and heightened responses to caffeine suggesting improved SR Ca^{2+} cycling[172]. Further development of micropatterning PDMS technology has resulted in the generation of muscular thin films (MTF), which have tunable stiffness and flexibility to mimic healthy as well as diseased myocardium conditions. Shortening of CMs during synchronous contraction causes the MTF to flex and adopt a pseudo 3D conformation, allowing quantification of contractile force by mathematical modeling[173]. *In vitro* maturation strategies are illustrated in **Figure 1.6**.

Nevertheless, 2D systems and MTFs lack the structure and architecture of the adult myocardium, which probably accounts for the modest improvements reported in hPSC-CM maturation. Therefore, integration of hPSC-CMs in 3D systems has been investigated resulting in Engineered Heart Tissues (EHTs)[159] that more closely resemble physiological conditions. EHTs are based on casting cell-hydrogel suspensions in moulds displaying elastic anchors (silicon posts) that guide cardiac tissue organisation in an aligned conformation, thus imposing an auxotonic tension as the CMs perform contractile work against the anchors[84]. hPSC-CMs were shown to align between the silicon posts in hEHTs, showing 3.4-fold improved longitudinal orientation relative to EB-CMs. Sarcomeric distribution in the EHTs was homogeneous throughout the cell but Cx43 is still expressed along the sarcolemma (and not in the intercalated discs, like adult CMs). EHTs display key responses to physiological and pharmacological stimulation, such as increased contractile forces at higher extracellular Ca^{2+} concentrations and upon treatment with β-adrenergic agonist isoprenaline, displaying positive inotropic effect (85% increase in contraction force), as well as shortened contraction and relaxation times (positive clinotropic and lusitropic effect, respectively)[174]. Nevertheless, even if the response of hEHTs to pharmacological stimulation is better than 2D hPSC-CMs, it still falls short of the adult CM activity, indicating incomplete maturation.

Finally, combinatorial strategies based on the promotion of maturation by addressing more than one factor have contributed to incremental advances in achieving maturation of hPSC-CMs. In this regard, cardiac biowires consist of a cell-laden collagen gel around an electrically-conductive surgical suture placed in a PDMS mould. Electrical stimulation of biowires at increasing frequencies (from 1 to 6Hz) enhanced maturation structurally (indicated by myofibrils bearing a higher degree of ultrastructural organisation such as aligned Z-discs displaying up to two I-bands per disc and organised sarcomeres showing up to 0.4-H zones per sarcomere) and functionally, due to higher I_{Kr} (~0.81 vs 0.52pA/pF) and I_{K1} (~1.53 vs 0.94pA/pF) currents upon electrical stimulation[175]. Moreover, Ruan and co-workers have engineered a human cardiac tissue by integrating hiPSC-CMs in a collagen-based scaffold followed by either static stress stimulation or static coupled with electrical stimulation. While

in the former strategy static stress increased force production when compared to unstimulated tissues (0.63±0.10 mN/mm^2 vs 0.055±0.009 mN/mm^2), the combination of static stress and electrical stimulation enhanced this improvement even further (1.34±0.19 mN/mm^2)[176].

More recently, a worldwide collaboration between several laboratories optimized the relative cell composition (CM: non-CM ratio of 1:1), matrix (clinical grade bovine collagen I) and medium formulation (defined and serum-free) to generate a model of defined engineered human myocardium (EHM)[177]. This construct followed a 2-step fabrication process where all the components above are assembled and stabilized for 3 days and subsequently rhythmic contractions by electrical stimulation are applied to promote maturation of hPSC-CMs. Remarkably, this has resulted in EHM-twitch forces in the same order of magnitude of adult non-failing myocardium (6.2±0.8 mN/mm^2 at 1.5 Hz stimulation vs ~25mN/mm^2) and, for the first time, a positive force-frequency relationship (increase in force by 19±5% at 2Hz and 22±5% at 3Hz vs 1Hz). Although this model greatly improved the maturation state of hPSC-CMs, full maturation was still insurmountable, as evidenced by absence of T-tubules and 4-fold lower contraction force in comparison to adult CMs).

While all the approaches explored in this section have met considerable yet relative success, genetic manipulation of hPSC-CMs to promote maturation is fairly unexplored. Nonetheless, adaptation of genome editing technologies towards induction of expression of genes characteristic of adult CMs that are silent in hPSC-CMs (e.g. encoding ion channels such as I_{k1} and Na^{2+}-Ca^{2+} exchangers) should conceivably accelerate efforts[178]. For instance, activation or repression of transcription via nuclease-dead Cas9 and transcriptional Cas9-effector fusion proteins of guideRNA (gRNA)-directed loci should pave the way for genetic manipulation of hPSC-CMs, as discussed in the next section[179].

1.4 Genome editing technologies

As explored above, HCM is mostly caused by genetic alterations in sarcomeric genes of the patient, leading to impaired cardiac function that is characteristic of the disease progression. Therefore, in order to generate new disease models for HCM using hPSC-CMs, the patient genotype must be recapitulated. Thus, two main strategies have arisen to achieve this goal: **i)** reprogram somatic cells from a mutation-carrying patient into hPSCs or **ii)** introduce known pathological mutations in unrelated healthy hPSC line(s).

The main difference between these approaches lies in the preservation of the genetic background of the hPSCs: while that is retained in patient-derived cells, healthy (i.e wild-type) hPSC present an unrelated genetic makeup and can thus mask the contribution of gene modifiers to the progression of the disease. This aspect is particularly relevant in mutations associated with low penetrance, whereby the impact of the genetic background can exceed that caused by the pathogenic mutation[180]. Conversely, when the mutation is known to be highly penetrant, its introduction in several independent healthy hPSC lines may provide

higher statistical power in the phenotypes analysed. This strategy overcomes the limited conclusions typically drawn by studying individual families, where the complexity of HCM precludes the establishment of genotype-phenotype relationships. Given that the R453C-MYH7 mutation is 100% penetrant[70], the latter strategy was the method of choice to develop an hPSC-CM-based HCM model. The technical differences between both methods are explored in more detail in section 3.3.3.

As such, harnessing gene editing technologies to hPSC has been the subject of intensive efforts in the field. In this section, a critical assessment of existing genome editing technologies will be explored, with particular emphasis in the CRISPR/Cas9 tool.

1.4.1 Mechanisms of gene editing

Underlying the field of gene editing is the concept of inducing DNA double strand breaks (DSBs) to stimulate cellular endogenous repair machinery. Breaks in the DNA are repaired through two main pathways – non-homologous end-joining (NHEJ) or homology-directed repair (HDR)[181]. NHEJ is an error-prone mechanism that repairs the DSB without a template through direct re-ligation of the cleaved ends, often resulting in insertions and/or deletions (indels) at the site of the break. Ultimately, this process leads to disruption of the genes by shifting the reading frame of the gene (frameshift mutation) and/or causing full gene knockouts by introducing premature a stop codon[182]. Conversely, HDR is based on the recombination of a donor repair template homologous with the region of the break, leading to restoration of the DNA sequence to its original state[181].

These two pathways can therefore be explored to perform several variants of gene editing, namely: **i)** knockout/ frameshift mutation, **ii)** deletion, **iii)** insertion and **iv)** correction (**Figure 1.7**).

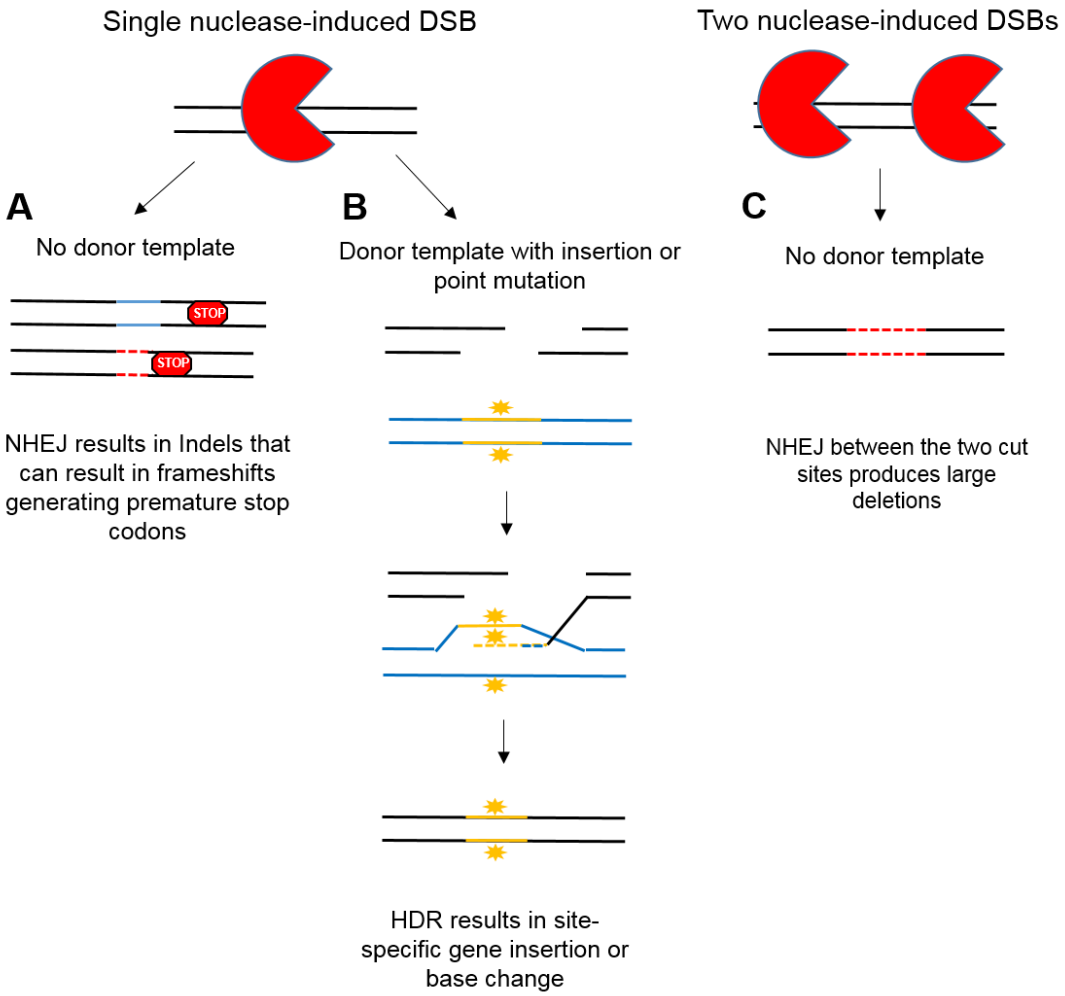


Figure 1.7 - Mechanisms of gene editing by double strand break repair. A) In the absence of a donor template, a single nuclease-induced DSB is repaired by NHEJ resulting in Indels that can cause frameshift mutations thus generating stop codons. **B)** In the presence of a donor template with extended homology arms to the target site, the DSB is repaired by HDR causing insertion of the gene delivered by the donor template, and/or site-specific base changes. **C)** In the case of a DSB caused by two nucleases flanking a gene, large deletions can be specifically generated.

1.4.1.1 Gene knockout/ frameshift mutation

The most basic form of gene editing uses the NHEJ mechanism to introduce indels at the target site, causing frameshifts and/or knockouts. This may be desired in diseases where restoration of the correct reading frame of a gene is beneficial, such as Duchenne muscular dystrophy (DMD)[183]. Furthermore, this method may be employed in particular cases where dominant gain-of-function (or normally functioning) genes are causative of the disease phenotype, as developed by the knockout of the major HIV co-receptor CCR5 to prevent viral infection of T cells[184].

1.4.1.2 Gene deletion

Large segments of DNA of up to several megabases in size may also be excised by NHEJ introducing two DSBs in regions flanking a gene[185]. This strategy is valuable for therapeutic applications that require the removal of a whole genomic component, as attempted by deleting the BCL11A erythroid-specific enhancer region[186].

1.4.1.3 Gene insertion

Unlike the two forms of gene editing described above, gene insertion relies on using a donor DNA template, whereby the genetic insert is flanked by DNA homologous to the break site (i.e homology arms), to enable HDR-mediated DSB repair[187]. For instance, targeted insertion of gene reporters or therapeutic transgenes into safe harbour loci (e.g. AAVS1) precludes risks associated with insertional mutagenesis while enabling ubiquitous gene expression[188].

1.4.1.4 Gene correction

Precise single-base genome editing is also achievable via HDR-mediated repair by supplying an exogenous donor template homologous to the DSB site. With this method, correction of disease-causing mutations can be attained as any sequence differences present in the donor template are incorporated into targeted endogenous locus[188]. Several sources of donor DNA constructs have been used such as plasmids and single stranded oligonucleotides (ssODNs)[189].

1.4.2 Targeted nucleases

In order to harness gene editing technologies, a few natural nucleases were adapted to perform one or several of the functions specified above. These nucleases possess two main properties: **i)** a DNA recognition function that guides them to a specific sequence of the genome and **ii)** a catalytic domain that causes a DNA break leading to gene editing upon repair. Herein, three main classes of nucleases are critically compared: zinc finger nucleases (ZFNs), transcription activator-like effector nucleases (TALENs), and clustered interspaced short palindromic repeats (CRISPR)/ CRISPR-associated Cas9 nucleases[190].

1.4.2.1 Zinc finger nucleases

ZFN are composed by a tandem array of Cys_2-His_2 DNA binding domains of zinc finger proteins and a DNA-cleavage domain of the endonuclease FokI that functions as a dimer, thus requiring the binding of two ZFNs in opposite strands of DNA for causing a DSB[191]. Genome-wide analysis of ZFN-editing revealed a relatively low prevalence of off-target events (*CCR5* vs *CCR2* example below)[192], due to the nuclease's specificity through the long sequence of DNA needed to be recognized (up to 36bp) for its activity. Moreover, modular assembly of ZFN is expensive (approximately USD $25000 each), labour-intensive and time consuming as separate nucleases must be engineered for each individual target, which

compromises its scalability and precludes its use for targeting several loci at once (multiplexing)[193].

1.4.2.2 TALENs

Structurally, TALENs are similar to ZFNs as they comprise a DNA-binding domain fused to a FokI nuclease domain, becoming an active targeted nuclease when bound in pairs to the DNA. However, unlike ZFNs, each DNA-binding domain, formed by multiple units of ~34 amino acids arranged in tandem, enables a 1-to-1 bp correspondence[194], resulting in higher specificity (i.e less off-target activity)[195]. Modular assembly of TALENs is a much more efficient process than that of ZFNs, as the DNA binding domains naturally exist as arrays of repeated motifs, enabling their high-throughput production by the use of construction kits[196], thus reducing costs by 20-fold relative to ZFNs. The main disadvantage of TALENs is the requirement of a preceding T base for target site selection, which may prevent editing specific SNPs involved in genetic diseases[194]. Finally, TALENs large protein size and repetitive nature impairs their *in vivo* delivery, even when using viral systems[197].

1.4.2.3 CRISPR/Cas9

CRISPR/Cas nucleases were derived from an adaptive bacterial immune response mechanism to defend against invading viruses, by the incorporation of foreign nuclei acids into the CRISPR loci. Its subsequent transcription into CRISPR RNAs (cRNAs) together with trans-activating RNA (tracrRNAs) formed complexes with CRISPR-associated (Cas) proteins to form a ribonucleoprotein (RNP) that could cleave nucleic acids via sequence-specific recognition[198]. This naturally occurring gene editing system was then adapted for efficient genetic modification in mammalian cells, by fusing the cRNA and tracrRNA into a single guide RNA (gRNAs) and complexing with Cas9 protein[199]. One of the main advantages of CRISPR/Cas9 nucleases over the other two systems is their ease of assembly, as novel proteins do not need to be engineered for each DNA target site – specificity is solely conferred by altering the gRNA sequence. Furthermore, this system is amenable to multiplexing by the simultaneous use of multiple gRNAs, as they do not couple directly with the Cas9 endonuclease[200].

However, the main limitation of this system is the need for a protospacer-adjacent motif (PAM) located close to the target site, which depends on the species where the Cas9 derived from (e.g the Cas9 from *Streptococcus pyogenes* –SpCas9 - used in this thesis requires the 5'-NGG-3' PAM site for binding and cleavage of target site)[201]. This drawback has been overcome to some extent by the adaptation of Cas9 protein from other species such as *Staphylococcus aureus,* that recognize different PAM sites including NNGRRT or NNGRR(N)[202]. Moreover, several variants of the canonical SpCas9 have been engineered to recognize additional PAM sites including 5'-NGA-3; 5'-NGAG-3', and 5'-NGCG-3,' extending the range of target sequences amenable to CRISPR/Cas9 gene editing[203].

Despite its versatility and efficiency, CRISPR/Cas9 technology possesses several limitations. Besides the requirement of PAM sites in the target region, the main drawback of this nuclease is the considerable incidence of off-target cleavage, which is due to the tolerance of up to five mismatches between the gRNA and the target DNA sequence[204,205]. Notably, frequencies of off-target activity were reported to be similar to on-target events[204], although a whole genome sequencing study showed very rare incidence of off-target events in hPSC using either TALENs or CRISPR/Cas9[206], enabling their use for disease modeling purposes. Despite this, the specificity of CRISPR/Cas9 DNA cleavage is sequence- and locus-dependent as it is reliant on the quantity, position and identity of mismatched bases[205].

Therefore, as the specificity of the used nuclease depends on the target locus, the most faithful evaluation relies on targeting the same gene. In this regard, the *CCR5* locus was edited by the three targeted nuclease classes and specificity was evaluated relative to the highly homologous *CCR2* locus. While on-target efficiencies were similar between ZFNs and TALENs (14% vs 17% mutation frequencies), off-targeting was higher in ZFNs (mutation frequencies of 14% vs 1% in TALENs)[195]. CRISPR/Cas9-based targeting of the same locus resulted in up to 65% on-target efficiency with off-target cleavage rates ranging from 5-20%, depending on the gRNA used[207].

In order to reduce Cas9 off-target activity, online tools were designed (e.g. mit.crispr.edu) considering four main constraints: **i)** potential off-targets should not be followed by a PAM-site, **ii)** global sequence similarity should be minimized (e.g. at least three mismatches), **iii)** at least two of the mismatches should correspond to the PAM-proximal region of the off-target and **iv)** mismatches should lie within 4 bases or ideally consecutive[205]. In addition, gRNAs can be tailored to cause allele-specific gene editing, which is facilitated by the existence of heterozygous SNPs in the target site[208].

In addition, the ratio of Cas9 to sgRNA plasmids should be titrated to optimize on- to off- target event ratio[205]. In this regard, a new approach was designed based on complexing pre-synthesised *in vitro* transcribed gRNAs with recombinant Cas9 protein followed by nucleofection of human cells together with a 100-120bp-long ssODN homologous to the break site[209]. Remarkably, since the recombinant Cas9 protein is active immediately upon entry to the nucleus and is only active for 24 hours (unlike continuously expressed Cas9 plasmid, RNPs are rapidly degraded), off-target effects and toxicities are low, while targeting frequency is high (up to 79% in site-specific mutations). Nevertheless, the main drawback of this approach is transfection efficiency of RNPs into hPSCs, which causes further complications due to the lack of selection procedures of positive colonies.

Another approach to overcome the considerable off-target cleavage activity of CRISPR/Cas9 relied on the inactivation of one of the two catalytic domains of the Cas9 nuclease (the RuvC domain) by a D10A mutation, leaving only one active nuclease site that creates a single-strand break (nick) to the targeted DNA[210]. As will be detailed in Chapter 3, this led to an increase

in specificity by up to 1500-fold relative to nuclease Cas9 in immortalised cell lines, thus reducing off-target activity (depending on the locus targeted).

Finally, a more recent strategy was designed to increase Cas9 specificity by site-specific mutagenesis of residues mediating SpCas9-DNA interactions[211]. This resulted in the engineering of a high fidelity-Cas9 (SpCas9-HF1), characterized by the retention of high on-target activities while reducing nearly all genome-wide off-target effects to undetectable levels (only 2 out of 36 off-targets had barely significant frequencies of indels), in comparison with the standard wtSpCas9.

The main features of the three targeted nucleases are summarized in **Table 1.3**.

Table 1.3 – Comparison of genome editing tools

Parameter	ZFNs	TALENs	CRISPR/Cas9
Specificity	18-36nt	30-36nt	20nt
Sequence requirement	none	5' T	PAM site (NGG, NAG, …)
Assembly/ scalability	Labour-intensive and time consuming	Achievable by construction kits	Simple and straightforward
Off-target activity (context-dependent)	Moderate	Low	Moderate (low if nickase or HF)

1.4.3. Gene targeting applications

Besides creating new human isogenic disease models, gene targeting technologies have been used for, among many other purposes, generating lineage-specific reporter lines (e.g by targeting the safe locus *AAVS1*[212]), engineering immune cells for therapy and also producing cell lines for enhanced synthesis of biomolecules for the pharmaceutical industry[213]. In the field of Regenerative Medicine, a few examples have received special attention due to their clinical potential derived from the correction of disease genes.

First of all, ZFNs were combined with *PiggyBac* technology in a scarless strategy to achieve bi-allelic correction of the Glu342Lys in the α1-antitrypsin gene (*A1AT*) in patient derived hiPSC, thereby restoring the function of *A1AT* in liver cells[214]. Secondly, specific TALENs were designed for correcting genetic defects in the type VII collagen gene (*COL7A1*) involved in a skin disease named Epidermolysis Bullosa[215]. Patient-derived fibroblasts were successfully edited although three off-targets were determined by genome-wide deep sequencing. Recently, a TALEN-based knockout library was designed to target eighty-eight human genes associated with cardiomyopathies[216], by introducing a stop codon in the early

coding region of their target genes. This constitutes a powerful tool to model several variants of congenital heart diseases.

Remarkably, CRISPR/Cas9 has received special attention for gene correction due to their ease of use relative to the other nuclease systems. For instance, a selection-free strategy was applied to DMD patient-derived myogenic cells to remove the duplicated exon 2 of the dystrophin gene, through the targeting of a neighbouring intron with a single gRNA. This resulted in restoration of wild-type dystrophin expression in myotubes derived from corrected myoblasts, without off-target events[217].Furthermore, direct targeting of the β-globin gene involved in β-haemoglobinopathies such as sickle cell anemia and β-thalassemia in human embryos has been pursued[218], even preceding successful correction of the same gene in haemapoietic stem cells[219].

Unlike the work developed in cultured cells, editing of human embryos was plagued by the low efficiency of targeting (only 4 out of 28 embryos: 14.3%), high level of mosaicism and off-target events[218] as well as evidence showing NHEJ as the preferential DNA repair mechanism, resulting in undesired mutations. Although this study was ethically controversial, it showed the limitations and lack of fidelity associated with *in vivo* CRISPR/Cas9 targeting.

However, a milestone in the field was very recently achieved by a highly efficient embryo gene editing of a HCM-causing gene[220]. In this study, correction of the heterozygous 4bp GAGT deletion of the *MYBPC3* gene was successfully accomplished in RNP-targeted embryos. While desired HDR-editing efficiencies in iPSC from patients with the same genotype were moderate (1.7%-11.5%, depending on the ssODN provided), embryo targeting efficiencies were comparatively higher (increasing the percentage of *MYBPC3*$^{WT/WT}$ embryos from 47.4% in untargeted to 66.7% in targeted ones). In addition, mosaicism could be avoided by targeting gametes in the M-phase of cell cycle, with no off-target activity detected by genome-wide deep sequencing. Notably, this exceptionally high targeting efficiency and success of embryo editing was ascribed to a different DNA repair mechanism to that of cultured iPSC, whereby a DSB is repaired using the WT sister chromatid, thus opening the avenue of embryo gene editing in heterozygous loci in the absence of an homologous DNA repair template.

In spite of all these achievements, several challenges for successful clinical application of gene targeting technologies still remain, such as the unpredictability of the effects of gene editing in neighbouring genes and other genetic networks, the size of therapeutic genes to be delivered by vectors, and finally the depth of sequencing required to confirm the absence of off-target activity[221].

1.5 Phenotyping HCM in hPSC-CMs

In vitro assays to phenotype HCM require the integration of hPSC-CMs in platforms to evaluate cardiac cell function. However, the development of phenotyping platforms has not accompanied the success of cardiac differentiation of hPSC to large quantities. In fact, in parallel with insufficient maturation, phenotyping of hPSC-CMs is becoming a bottleneck in the field of disease modeling[84]. Nevertheless, several medium- and high-throughput platforms that measure cardiomyocyte structure, metabolism, electrophysiology, calcium handling and contractility have been developed. These are often complemented by standard molecular tools such as flow cytometry and qPCR analysis[222]. In this thesis, some of these platforms have been used to phenotype HCM in the hPSC-CMs generated, so they will be described in this section and further explored in the corresponding Results chapters.

1.5.1 High content imaging

Several parameters of cardiomyocyte biology can be investigated using high content imaging platforms. Capture of cell number, shape/size and expression of biomarkers correlated with particular biological functions may shed light into cardiac phenotypes. That already is the industry standard for assessing physiology of tumour cells in terms of proliferation, viability, membrane integrity and phagocytosis[223]. Imaging assays are typically performed in 96-, 384- and 1536-well plates, which are compatible with several fully automated image acquisition platforms, such as Opera/Operetta (Perkin Elmer), and CellaVista (Synentec)[224].

Identical platforms were already applied to hPSC-CMs towards the investigation of hypertrophy response (increase in cell area) upon inducers such as endothelin-1 (ET1) and angiotensin II[225]. In addition, staining of relevant cellular structures may provide important phenotyping information. For instance, Pasqualini and colleagues have stained the sarcomeres of commercially-available (Cellular Dynamics International - CDI) hPSC-CMs using an α-actinin antibody, and developed a set of 11 metrics upon image treatment and analysis to score the degree of organisation and alignment that sarcomeres acquire during myofibrillogenesis, which were used evaluate phenotypic maturity[226]. Moreover, staining hPSC-CM with dyes such as tetramethylrhodamine methyl ester (TMRM), caspase-3 or BOBO-1, coupled with Cellomics Arrayscan (ThernoFisher) imaging enabled the assessment of mitochondrial function, apoptosis and cell death, respectively[227]. Lastly, CDI have developed a high-throughput assay to evaluate hypertrophy by the detection of BNP expression in hPSC-CM, through the ImageXpress Micro High Content Screening System (Molecular Devices)[228], with the added benefit of establishing signal threshold controls upon ET1 treatment.

1.5.2 Functional analysis

While imaging platforms provide important information on overall cardiomyocyte biology (e.g. cell area, expression of disease markers, sarcomeric structure), other analyses are required for more in-depth functional evaluation. In this regard, several technologies were developed to assess the main cardiac functions associated with disease modeling and drug discovery: mitochondrial respiration, electrophysiology and calcium, and contractility.

1.5.2.1 Mitochondrial respiration

Besides the application of imaging systems coupled with mitochondria-activated dyes such as TMRM and Mitotracker (Invitrogen), evaluation of mitochondrial function can be determined by calculating glycolysis and oxidative phosphorylation (OXPHOS) rates of hPSC-CMs[84]. Overcoming initial lower-throughput assays, the Seahorse™ Extracellular Flux Analysers (Agilent Technologies) uses 24- or 96-well custom plates to determine *in vitro* oxygen consumption rate (OCR) and extracellular acidification rate (ECAR) to assess OXPHOS and glycolysis[229]. In practice, evaluation of mitochondrial respiration of hPSC-CMs involves measuring basal levels of OCR and ECAR followed by sequential treatment of electron transport chain inhibitors (e.g. oligomycin, rotenone, antimycin-A) or uncouplers (FCCP), as detailed in Chapter 5. This system has been employed in maturation studies, by showing 50% increase in basal and maximal mitochondrial respiration upon T3-treatment[164]. In addition, this platform was used to demonstrate that considerable maturation (e.g. higher oxidative metabolism and myofibril density and alignment) can be induced by culturing hPSC-CMs in galactose/fatty acid-containing medium[230]. Importantly, this platform was also applied to study disease models such as arrhythmogenic right ventricular dysplasia[231] and Barth syndrome[231], typically producing phenocopies of HCM.

1.5.2.3 Electrophysiology and calcium

The gold standard for studying ion channel activity relies on sharp glass electrodes to access the cell interior via conventional patch clamp electrophysiology. Despite providing extensive data on functionality, kinetics, and pharmacology of ion channels, the very low sampling rate of this technique (10-15 data points a day) impairs its use in higher-scale measurements associated with hPSC-CM disease modeling and mostly drug discovery[232]. This limitation fostered the development of higher-throughput systems for measurement of electrophysiology such as planar patch clamp platforms. Importantly, these techniques are less complex and increase data throughput by 10-100 fold, in recombinant cell lines overexpressing single channels[233]. Moreover, these tools are now being applied to hPSC-CMs, resulting in the simultaneous measurement of 16 channels by PatchXpress[234] and CytoPatch2 systems[235]. This gains additional importance as hPSC-CMs are intrinsically fragile, which is further aggravated by the stressful preparation procedures associated with patch clamping. In this regard, Rajamohan and co-workers have developed a protocol than ensured reliable detection of hPSC-CMs, enabling the automated evaluation of sodium, calcium, and

potassium currents as well as dose-responsive curves of their respective channel inhibitors tetrodotoxin, nifedipine, and E-4031[236].

However, the highly intrusive nature of planar patch only enables short term recordings (minutes to hours) from single cells. This is incompatible with applications aimed at evaluating chronic toxicity (requiring measurements over days/ weeks) or when using multi-clusters of cells. For this end, multi-electrode arrays (MEAs) comprise glass slides photo-etched with arrays of microelectrodes that can record field potentials from cell types for hours or even days, by measuring changes in the electrode impedance[84]. MEAs have been used with hPSC-CMs, initially at lower throughputs (single- to 4-well formats) but more recently in the 48-well format[237]. For instance, this platform enabled the evaluation of electrophysiological response of hiPSC-CM carrying *KCNH2* (I_{Kr}) mutations to several drugs such as β-blockers and potassium channel enhancers, resulting in the rescue of arrhythmogenic activity of these cells[232]. However, the reliability of MEAs has been questioned due to reports showing high false-positive rate of pro-arrhythmic recordings[238], possibly due to insufficient cell-electrode contact amounting to inconsistent cell seeding, which leads to reduced signal strength, quality and accuracy of APs acquired[239]. Thus, new improvements towards increasing the consistency and reliability of MEAs are being developed such as their integration with intracellular electrodes[84].

The challenges associated with direct electrophysiological recording (low-throughput and/or harsh and invasive sample preparations) and impedance-based techniques (reliability) have stimulated the development of optical mapping to measure action potentials and calcium wave propagation. This is typically done using voltage[240]- or calcium[241]-sensitive fluorescence dyes such as ANEPPS or Fura2, respectively. Importantly, fluorescence recordings are easily and rapidly acquired with high spatial and temporal resolution from several cells in a single field of view, enabling the analysis of over 440 hESC-CMs in a day[242]. Optical imaging has been applied to hPSC-CMs to measure calcium transients or beat rates, in high-throughput platforms (96- to 384- well formats) such as the CellOPTIQ. In this platform, optical measurements of electrical activity (action potential duration –APD) of commercially-derived hiPSC-CMs in response to channel blockers (E4031, Mexiletine and Nifedipine, targeting the potassium (hERG), Na^{2+} and Ca^{2+} channels, respectively) were performed in a robust and high-throughput manner, showing responses consistent with literature[243]. However, fluorescent dyes are phototoxic, thus limiting their long-term application in live cells[242]. In order to overcome this limitation, genetically-encoded voltage- or calcium- indicators can be used to image action potentials or calcium waves of hPSC-CMs, respectively. This was explored by Leyton-Mange and colleagues[242], by the use of ArcLight voltage-sensor to accurately predict arrhythmic effects, with comparable success to patch clamp measurements. Notably, voltage-sensitive dyes and genetically encoded indicators only provide surrogates of membrane potentials and tend to overestimate action potential duration[242]. Their use will be further explored in Chapter 5.

1.5.2.4 Contractility

Fully functional contractility of cardiac tissue is the ultimate goal of a healthy myocardium in order to pump blood into systemic circulation. In this regard, a plethora of different methods have been developed to measure contractile force in cardiomyocytes including, but not restricted to: atomic force microscopy[244], traction force microscopy (relying on either fluorescent beads embedded in polyacrylamide gels[245,246] or label-free motion vector–based analysis[247]), muscular thin films[248], force transducers[249], microposts[250], and hEHTs[159]. Expectedly, each of these methods involves different sample preparation procedures (such as skinning myofibres for tension measurements in force-transducers vs fibrin encapsulation for hEHT analysis), measure various parameters (direct tension vs optical detection of movement) and report diverse readouts (e.g tension vs force), which makes cross-comparison of contractility properties between platforms rather difficult. Nevertheless, as explored in Chapter 1.3.4, force generation has been measured in hPSC-CMs, in the presence or absence of pharmacology and electrical stimulation. Reported twitch forces for hPSCs-CM range from 2-260nN for single hPSC-CMs[244,246,250] and 0.08–6.2 mN/mm^2 for 3D hPSC-CM derived EHTs[177,251]. However, these values are still at least one order of magnitude lower than adult CMs, which display forces in the microN range when in single cells[172] and 40-80mN/mm^2 range of muscle human strips[158], which reinforce the immaturity state of hPSC-CMs.

However, most of these technologies rely on low- to medium-throughput measurements [84]. Translation into higher throughput has been mostly accomplished by the used of impedance as a surrogate measure of contractility. The fundamental principle of this method is that upon CM contraction and relaxation, nano-scale changes in morphology and membrane structure change the level of impedance between the cell and its underlying surface[252]. Thus, cell-substrate impedance sensing platforms explore these changes by incorporating gold-film electrodes into the bottom of tissue culture plates[253]. Notably, rapid data acquisition frequencies (every 10-12.9 ms/ plate) enables high temporal resolution of subtle changes in CM beat profiles such as arrhythmic events[254]. In this regard, the xCELLigence platform (ACEA Biosciences) has been widely used in hPSC-CMs, showing sensitivity, specificity and accuracy of 90%, 74%, and 82%, respectively, which was overall higher than *in vitro* data for dog (83%, 84% and 82%) and rat (77%, 74%, and 74%) CMs, upon testing a panel of 49 cardioactive compounds[255]. In addition, the CardioExcyte96 (Nanion Technologies) measures both impedance and extracellular field potentials, enabling the simultaneous analysis of hPSC-CM contractility (beat rate, amplitude) and electrophysiology (action potentials)[256]. However, this platform has several disadvantages such as: **i)** high cost (~£100 per 96 well plate), **ii)** the number of functioning wells (which may be as low as 15% of the total capacity of the plate, due to the fragile nature of the gold electrodes), and **iii)** limited throughput of signal recording and data analysis (relying on manual processes)[84]. Therefore, measurement of contractile force in 3D hEHTs has shown to provide a robust

quantification of contractility[159] that is likely a more accurate readout than the indirect method of impedance. In this thesis, the use of 3D hEHTs was the method of choice to evaluate force generation of parental and mutant hPSC-CMs, and will explored in detail in Chapter 5.A summary of the phenotyping platforms described in this section is presented in **Table 1.4**.

Table 1.4- Summary of platforms used to phenotype hPSC-CMs. Adapted from [84].

Parameter	Platform	Readout(s)	Advantages	Challenges
Several (image-based)	High-content imaging (e.g. Operetta™)	Cell shape/size; Expression of relevant markers (hypertrophy); Sarcomeric structure	Very high-throughput (96-well plate format or higher); Automated analysis	Mostly fixed samples; No functional data
Mitochondrial respiration	Seahorse™ Extracellular Flow analyser	Bioenergetics (OXPHOS, OCR/ECAR)	High-throughput (96-well plate)	Expensive; Imprecise normalisation
Electrophysiology	Patch clamp (Manual, automated-e.g. Patchliner™)	Ion channel currents function, kinetics and pharmacology	Rich data sets	Harsh sample preparation methods; Very low throughput (manual)
	MEAs	Field potentials (voltage)	Medium-high throughput (48 well-plate format)	Inconsistent readings (unreliable data)
Calcium	CellOPTIQ	Voltage, calcium and contractility	High-throughput (96-well plates); Enables electric pacing	Requires fluorescent dyes (phototoxicity, signal variability) or GECIs; Labour-intensive data analysis
Contractility	hEHTs	Contractile force; Contraction and relaxation kinetics	Very consistent data; enables pharmacology and histology analysis; Improves maturation state.	Requires high cell numbers (1M/EHT); medium throughput (24-well plate)
	Cardioexcyte™	Impedance (surrogate for contractility) and field potentials (voltage)	High sensitivity, specificity and accuracy	Very expensive (~£100/ 96 well-plate) Labour-intensive data analysis;

1.6 Hypothesis and major aims of the PhD Project

The overarching goal of the PhD project is to **develop and validate an HCM model** by the introduction of the pathological mutation **R453C-MYH7 in hPSC-CMs via CRISPR/Cas9**. The hypotheses underlying the current work are:

1) R453C-MYH7 hPSC-CMs recapitulate HCM hallmarks reported in patients;

2) The use of cells of human origin clarifies previously reported findings using animal models, where data may be misinterpreted due to species-differences;

3) A holistic and comprehensive approach (i.e coupling molecular and functional analyses), provides a deeper understanding of the disease progression than single-phenotyping approaches;

4) The use of isogenic controls represents the best control for the contribution of the pathological mutation to the disease, supplanting previous approaches where unrelated healthy patients/ cell lines were used.

The aims to achieve the goal are:

1) Introduce R453C-MYH7 mutation in hPSC lines using CRISPR/Cas9 genome editing technology

2) Perform molecular and functional phenotyping in order to validate the generated hPSC-CM-derived model

It is expected that the establishment of such a physiologically-relevant HCM model will assist in future approaches aimed at gaining novel mechanistic insight into the disease and designing better pharmacological intervention strategies.

2. Materials and Methods

2.1 CRISPR/Cas9 strategy

2.1.1 Guide RNA design and synthesis

Dual guide RNA/Cas9-Nickase strategy was designed to introduce the *MYH7*-C9123T SNP in three hPSC lines, encoding the R453C-β-MHC modification. The hCas9 D10A plasmid (Addgene #41816), comprising the human codon-optimized *Streptococcus pyogenes* Cas9 nuclease bearing the D10A mutation was used. Candidate sgRNAs were identified by searching for NGG PAM sites in the 150bp up- and downstream of the SNP location, using the available bioinformatics tool website http://crispr.mit.edu/, as previously described[257]. ACCG sequence was added to the 5' end of the gRNA sequences (in a DNA oligonucleotide), and a AAAC sequence to the 3' end of the respective complementary sequences, annealed and cloned into BsaI-digested U6-gRNA vector backbone, using T4 DNA ligase (New England Biolabs, NEB), according to manufacturer's instructions. Thereafter, ligated U6-gRNA vectors were transformed into in TOP10 chemically competent *E.Coli* (Thermo Fisher) and plasmid DNA was extracted by Wizard® *Plus* SV Minipreps DNA Purification System (Promega) and analysed by BsaI-restriction digestion.

2.1.2 Targeting construct design and synthesis

The donor template targeting construct comprised the *MYH7*-C9123T SNP flanked by 1kb homology arms. It was produced by performing a 2-step PCR splice mutagenesis reaction, whereby the 2kb region was amplified using isogenic hPSC genomic DNA in two adjacent 1kb fragments, and the base changes were introduced by the primers used in **Table 2.1**

Table 2.1 - Primers used for the 2-step PCR splice mutagenesis reaction.

Primer name	Primer Sequence (5' → 3')	Reaction Step/ Fragment
MYH7_TC1_Fwd	CAGGGAGAGCTCAGACAAGTTTTCTCT CCAACTTACA	1/1 and 2/1
MYH7_TC2_Rev	TGGCATGGCTGCTTGGTCTCGAGGGT GGCATTGATGCGCGTCACC	1/1
MYH7_TC3_Fwd	CCCTCGAGACCAAGCAGCCATGCCAG TACTTCATAGGAGTCCTGG	1/2
MYH7_TC4_Rev	TTGGGTAAGCTTGTAGTAGGCTCAGCT CTGAGTACAG	1/2 and 2/2
MYH7_TC5_Rev	CCCGCGGCCGCTCCACACCTAGGTCT AAGCAAATAGCTGTTGAAT	2/1
MYH7_TC6_Fwd	GACCTAGGTGTGGAGCGGCCGCGGG AAGGCAGTGGGGACTGTGTG	2/2

Subsequently, the two 1kb fragments were annealed in the 25bp overlapping region and amplified by PCR using Phusion DNA polymerase (NEB), following manufacturer's

instructions. Cycle parameters were: 98°C for 30s for 1 cycle; 98°C for 30s, 64°C for 60-90s, 72°C for 30s for 35 cycles; 72°C for 10 min for 1 cycle. Amplified DNA was thereafter loaded in a 1% agarose (w/v) (Milipore) gel stained with Ethidium Bromide (EtBr, Sigma), run at 100V for 60 min and visualised in Fujifilm LAS-4000 System & Software (GE Healthcare LifeSciences). PCR products were purified from gel using QIAquick Gel Extraction Kit (Qiagen), and Sanger Sequencing reactions were outsourced to Source BioSciences, using primers from **Table 2.2**, up to 500bp up/downstream from the regions of interest.

The generated 2Kb construct was subsequently cloned into pUC57 vector (Eurofins) by HindIII and SacI double digestion and ligation, with bacterial transformation and plasmid DNA purification being performed as above. Afterwards, NotI/AvrII-digested pUC57-R453C-MYH7 insert was cloned into the pR6K-R1R2 backbone, using the same restriction enzymes and ligation procedure. Subsequently, the previously synthesized L1L2 FRT-Blast/Puro plasmids were recombined with the pUC57-MYH7-R453C-pR6K vector previously generated, by a Gateway LR Clonase reaction (Invitrogen), according to the manufacturer's instructions. The final targeting constructs (pUC57-MYH7-R453C-Blast; pUC57-MYH7- R453C-Puro) isogenic to each hPSC line were analysed by diagnostic digestions and confirmed by Sanger Sequencing reactions, as above. All the restriction enzymes were purchased from NEB, and digestions were performed at 37°C for 2h followed by 1h at 37°C in the presence of Calf Intestinal Alkaline Phosphatase (NEB) to avoid linearized plasmid religation. Unless otherwise stated, plasmids were kindly provided by William Skarnes' group (Wellcome Trust Sanger Institute, UK).

2.1.3 hPSC editing transfection, selection and genotyping

hPSC were seeded at approximately 15K/cm^2 24h prior to the transfection (as described below). 1 µg of nickase hCas9 D10A plasmid, 0.5 µg of each gRNA pU6 vector and 1 µg of the pUC57-MYH7-R453C targeting vector corresponding to each hPSC line were complexed in GeneJammer (Agilent Technologies) transfection reagent, diluted 1:10 in OptiMEM reduced-serum medium (Invitrogen). After 15 min incubation at room temperature (RT), the transfection mixture was added to the cells and medium was changed the next day. Transfection efficiency was determined by imaging hPSC transfected with GeneJammer-GFP plasmid (pSIN-IRES-BSD-GFP) in CellaVista Cell Imager (Synentec), followed by automated estimation of GFP positive cells normalized to total cells based on signal area.

48h after transfection, cells were re-seeded sparsely (50 cells/ cm^2) into MT-coated 35mm dishes (Nunc) and antibiotic treatment was performed (0.3-7.5 µg/ml Puromycin, Invitrogen), 5-15 µg/ml Blasticidin, Invitrogen) until colonies appeared. Thereafter, mechanical passaging was performed using a Stem Cell Cutting Tool (Vitrolife) when colonies reached an approximate 0.5–1 mm in diameter, by manually dissecting them into pieces measuring approximately 100-200µm under a stereomicroscope built into a class II safety cabinet

(performed by colleague Maria Muñoz). Individual clones were expanded and subcultured until monolayers were formed and genomic DNA was extracted using DNeasy Blood and Tissue Kit (Qiagen), following manufacturer's instructions. Genotyping PCRs were subsequently performed with 100ng of genomic DNA, using Phusion DNA polymerase (NEB), as above (primer sequences in **Table 2.2**). Afterwards, amplified DNA was loaded in a 1 % agarose gel as above, and PCR products were either purified using a PCR Purification Kit (Qiagen) or directly from gel followed by Sanger Sequencing reactions, as above.

Upon confirmation of positive targeting (HDR introduction of C9123T-*MYH7* SNP) MYH7-mutant hPSC lines were seeded and transfected with 3ug of pCAGGS_FlpO plasmid (wherein Blasticydin or Puromycin resistance markers were cloned by a BmgBI and NsiI double digestion and ligation) followed by antibiotic selection and clone expansion, as above. Genomic DNA was subsequently isolated and PCR and sequencing reactions were performed as above, using primers in **Table 2.2**.

Table 2.2 - Primers used for genotyping the genome-edited hPSC clones.

Primer name	Primer Sequence (5' → 3')	PCR Reaction(s)
***MYH7*_G5_FWD**	CCACTGGGTATGGGAGTCTC	Left homology arm; 5' flank of *MYH7* product
EF1α_REV	GCGATCTCTGGGTTCTACGTTAGTG	Left homology arm; resistance cassette
PolyA_FWD	CATGTCTGGATCCGGGGGTACCGCGTCGAG	Right homology arm; resistance cassette
***MYH7*_G3_REV**	AGGAAGCAGGAGAGAGCATC	Right homology arm; 3' flank of *MYH7* product
***MYH6/7*_uprc_REV**	CCAGCGATGTCCAGGACTCC	Left homology arm, upstream resistance cassette (both alleles)
***MYH6/7*_FWD634**	CCTCATGGGGCTGAACTCA	Sequencing C9123T SNP
***MYH6*_G5_FWD**	CAGACAGAGAGTCCACCACAATCC	*MYH6* off-target analysis
***MYH6*_G3_FWD**	TCAGTTTACCATGAGGATGAC	*MYH6* off-target analysis
***MYH7*_600_FWD**	TCGGGTGAAAGTGGGCAAT	Flipped product
Flp_REV	TTGTACAAGAAAGCTGGGTCT	Flipped product
EF1α_FWD	CGAATCTGGTGGCACCTT	Resistance cassette
PolyA_REV	TGAGTTTGGACAAACCACAAC	Resistance cassette

2.2 Cell culture

2.2.1 hPSC culture

All cell culture experiments were performed in a type II Biological Safety Cabinet, and cells were incubated in a humidified incubator, at 37°C and 5% CO_2 (Heracell). hPSCs were routinely maintained in E8 medium (LifeTechnologies #A1517001) on 1:100 MT (BD #356235)-coated plasticware (Nunc). Cells were passaged every 3 days by washing once with Ca^{2+}/ Mg^{2+}-free Phosphate Buffer Saline (PBS, Gibco #14190-094), followed by incubation with a cell dissociation solution (CDS) made of RPMI 1640 basal medium (Gibco #21875034), cell dissociation buffer (Invitrogen) #1315104) and trypsin-EDTA 0.25% (Gibco #25300054) on a 2:2:1 volume ratio, for 4 minutes at 37°C. Thereafter, CDS was quenched by washing cells with DMEM-F12 (Gibco #11320033) basal medium supplemented with 15% Knockout Serum Replacement (Gibco #10828028), 1% Non-Essential Amino Acids (NEAA, Gibco #11140050), 1% GlutaMAX (Gibco#35050061), 100 µM β-mercaptoethanol (Sigma #63689) and basic Fibroblast Growth Factor (Peprotech 100-18B, 8ng/ml), followed by centrifugation at 160xg for 4 min. Afterwards, hPSC were resuspended in E8 supplemented with 10µM Y-27632 (ROCKi, Tocris Bioscience #1254/10,) and seeded into new MT-coated flasks at approximately 20000 cells/ cm^2. Medium was changed every day. Cell lines were used between passages 20-40.

2.2.2 Monolayer cardiac differentiation of hPSC

hPSC differentiation was performed by seeding vessels at approximately 20-40 thousand cells / cm^2, as described above. Fresh E8 was added the next day and the pre-conditioning step of hPSC was performed the day after, by adding a MT overlay (MT diluted 1:100 in StemPro™34-Serum Free Medium (SP34, Gibco #10639011, supplemented with 1ng/ml BMP4 (R&D #314-BP-050). Approximately 16h later, medium was replaced by SP34 supplemented with 8ng/ml ActA (LifeTechnologies #PHC9564) and 10 ng/ml BMP4. 48h later, medium was changed by RPMI supplemented with B27 without insulin (-INS, LifeTechnologies #A1895601) and KY0211 (R&D #4731) and XAV939 (R&D #3748), both at 100µM. These SM were added again two days later, using RPMI supplemented with B27 with insulin (+INS, LifeTechnologies #0080085-SA) instead. Thereafter, medium was changed every 2-3 days by fresh RPMI+B27+INS until day 15 of differentiation.

2.2.3 hPSC-cardiomyocyte dissociation

hPSC-CMs generated by the monolayer differentiation method were dissociated using a Collagenase II-based protocol, as previously described[139]. Briefly, cells were washed twice with Ca^{2+} and Mg^{2+}-free Hank`s Balanced Salt Solution (HBSS, LifeTechnologies #14175095). Subsequently, cardiomyocytes were incubated with 200U/ml Collagenase II (Worthington

#LS004176) in Ca^{2+}/Mg^{2+}-free HBSS, supplemented with 1mM HEPES (Sigma #H4034), 10μM Y-27632 and 30nM N-Benzyl-p-toluenesulfonamide (BTS, TCI #B3082), all diluted 1:1000, for 3.5h at 37°C at 5% CO_2. Thereafter, dissociated cardiomyocytes were collected from the flasks and washed with RPMI supplemented with 24μg/ml Deoxyribonuclease II (DNAseII – Sigma #D8764), followed by centrifugation at 100xg for 15min. Subsequently, cells were resuspended in warm RPMI and pipetted slowly through a 100μm cell strainer (VWR # 89508-840) into a tube. Cells were then counted using an automated CEDEX HiRes counter (Roche) and centrifuged again as above. Afterwards, cardiomyocytes were resuspended in RPMI+B27+INS for seeding into Vitronectin-N (VN, Lifetech #A14700)-coated vessels, at different densities depending on the assay, or in freezing medium (heat-inactivated FBS, Gibco #16000044) + 10% DMSO - Sigma #D2660) for cryopreservation.

2.2.4 hPSC-fibroblast culture

Derivation of hPSC-fibroblasts was done by adapting a previous method of forced aggregation of hPSC into EB)[258] and immersing them in DMEM basal medium (Gibco #11965092) supplemented with 20% FBS, 1% NEAA, 1% GlutaMAX (all v/v) and 100 μM β-mercaptoethanol (named FM medium). EBs were then passaged by 0.05% Trypsin-EDTA (LifeTechnologies #10462502) for 3 minutes at 37°C, vortexed and plated as single cells in MT-coated surfaces. FM medium was changed every other day and cells were passaged by incubation with Trypsin-EDTA 0.25% for 4min at 37°C, followed by quenching in FM medium and centrifugation at 300xg for 5 min. Afterwards, fibroblasts were resuspended in FM and plated in MT-coated vessels at 6000 cells / cm^2 and fixed the day after, as described below, prior to immunostaining.

2.2.5 BNP assay

BNP assay was performed as previously described[228]. In brief, dissociated hPSC-CMs were seeded at 120K cells/ cm^2 in VN-coated 96 well plates (CellCarrier, Perkin Elmer). One week later, cells with incubated with 10nM Endothelin-1 (ET1) (Sigma #E7764) or 100nM-1μM Bosentan (Sigma #SML1265) for approximately 15h, after which 1μg/ml Brefeldin A (Sigma #B7651) was added to the medium and incubated for another 3h, at 37°C and 5% CO_2. Thereafter, cells were fixed and immunostained as described below.

2.3 Molecular Biology

2.3.1 RNA extraction, cDNA synthesis and RT-PCR

Total RNA was extracted from cell pellets using the RNeasy Mini Kit (Qiagen), and reverse transcribed using SuperScript™III Reverse Transcriptase kit (Invitrogen), according to manufacturer's instructions. RT-PCR reaction was performed using Phusion DNA polymerase

(NEB) and parameters were as described above for standard PCR reaction, using exonic *MYH7* primers displayed in **Table 2.3**. Subsequent PCR and gel electrophoresis were performed as above.

Table 2.3 - Primers used for RT-PCR reaction to detect MYH7 expression.

Primer name	Primer Sequence (5' → 3')	PCR Reaction(s)
***MYH7*_expression_FWD**	CCATTGGGGACCGCAGCAAGA	*MYH7* expression
***MYH7*_expression_REV**	GCGGATTTGCCCAGGTGGTTG	*MYH7* expression
***MYH7*_expression_FWD2**	TCTGTGTCACCGTCAACCCTTACAA	*MYH7* expression (2)
***MYH7*_expression_REV2**	GCATAGTTGGCAAACAGGGTGCTG	*MYH7* expression (2)

2.3.2 Allele-specific restriction digestion and band densitometry

MYH7 expression PCR was performed followed by DNA purification, as described above. Thereafter, 150 ng DNA were incubated with XhoI restriction enzyme (NEB), following manufacturers' instructions, with undigested DNA being used as a control. DNA fragments were then loaded into a 1.2% agarose gel, run for 2h at 75V, followed by image acquisition using EtBr, as previously described. Band densitometry analysis was performed using AIDA Image Analyzer software (Raytest, GmbH), following manufacturer's instructions.

2.3.3 Real-time qPCR

Real-time qPCR reactions were performed via TaqMan® Gene Expression Assays (Applied Biosystems) following manufacturer's instructions. Briefly, Taqman® mastermix (#4369016) including the probe of interest (*MYH7*–Hs01110632_m1, *TNNT2*-Hs00165960_m1, *mt-ND1*-Hs02596873_s1, *mt-ND2*- Hs02596874_g1 or *ACTB*-Hs03023880_g1 was added to a MicroAmp Fast 96 well plate (#4346907). Subsequently, DNA samples (from initial 500 ng of reverse-transcribed RNA for expression studies, or 25ng from isolated DNA for mitochondrial content analysis) were added to the plate which was thereafter sealed with a film (Applied Biosystems #4311971). Amplification was performed in ABI 7500 Real-Time PCR system Applied Biosystems). Normalisation was performed using the cardiac gene *TNNT2* for expression data, or nuclear gene *ACTB* for mitochondrial content analysis, as previously done[259]. The average of WT isogenic cardiomyocytes lines was used for calculating relative quantification, using the ΔΔCT method[260].

2.3.4 Immunocytochemistry (ICC) and image acquisition

Dissociated hPSC-CMs or hPSC were cultured in VN- or MT-coated 96-well plates (CellCarrier, Perkin Elmer #6005550) respectively, at approximately 50K cells/cm^2 as described above. Cells were washed with PBS and fixed in 4% Paraformaldehyde (PFA, Sigma) at RT for 15 min. Afterwards, cells were washed in 0.1% Tween-20 (Fisher Scientific) in PBS, permeabilized with 0.1% Triton-X (Sigma) in PBS for 15 min at RT, and incubated with 4% goat serum (Sigma) in PBS (blocking solution) for 1h at RT, to prevent unspecific antibody binding. Subsequently, primary antibody incubation was performed overnight at 4°C in blocking solution, with the dilutions highlighted in **Table 2.4**. Thereafter, samples were washed 3 times with 0.1% Tween-20 in PBS and incubated with Alexa Fluor secondary antibodies (Life Technologies) in blocking solution for 1h at RT. Afterwards, cells were washed with 0.1% Tween-20 in PBS for (3x 5min), followed by nuclei and/or whole cell counterstaining with 0.5 µg/ml DAPI (Sigma #D9542) or Cell Mask (1:10000, Invitrogen #H32721) in PBS, respectively, for 30 min at RT. Samples were subsequently washed and stored at 4°C in PBS until automated image acquisition was performed in the Operetta high-content imaging system (Perkin Elmer) and analysed using Harmony high-content imaging analysis software, with the developed algorithms for determination of cardiomyocyte purity, multinucleation, BNP expression and sarcomeric disorganisation, as explored in **Chapter 4**.

Table 2.4 – Antibodies used for immunocytochemistry.

Primary antibody (supplier)	Dilution	Secondary antibody	Dilution
OCT4 (Santa Cruz Biotech #sc-5279)	1:200	Alexa Fluor 488	1:1000
SOX2 (R&D Systems #AF2018)	1:200	Alexa Fluor 488	1:1000
NANOG (R&D Systems #AF1997)	1:200	Alexa Fluor 488	1:1000
SSEA4 (Milipore #MAB4304)	1:1000	Alexa Fluor 488	1:1000
SSEA3 (Milipore #MAB1434)	1:200	Alexa Fluor 647	1:1000
α-actinin (Sigma #A7811)	1:800	Alexa Fluor 488	1:400
Cardiac Troponin T (Abcam #45932)	1:500	Alexa Fluor 647	1:400
ProBNP4 (Abcam #13115)	1:500	Alexa Fluor 488	1:400
β-MHC (Sigma #M8421)	1:1000	Alexa Fluor 488	1:400

2.3.5 hPSC karyotyping

hPSC were karyotyped as previously described[261], in a service provided by the Cytogenetics Department of Nottingham City Hospital (Nigel Smith). In brief, exponentially growing hPSC cultures (at least 1x10^6 cells) were treated with 100 ng/ml KaryoMAX™

Colcemid solution (Gibco #15210040) for 1h and harvested by CDS-passaging. Pelleted cells (200×g for 4 min) were resuspended in 0.6% sodium citrate (Fisher) and incubated at RT for 20 min. Cells were then centrifuged (400×g for 4 min) and fixed by resuspension in 16.7% glacial acetic acid (Fisher) in methanol (Fisher) before washing with two further changes of fixative. Chromosome spreads were prepared by dropping cells onto glass slides, which were air dried and heated to 70°C overnight. Chromosomes were G-banded by trypsin treatment and staining with Leishman's. For each culture, at least 30 metaphase spreads were examined; full analysis involving band by band comparison between chromosome homologues was performed on three spreads and presence of gross abnormalities visually examined in 30 spreads, in accordance with ISCN Human Cytogenetic Nomenclature international guidelines[262].

2.4 Flow cytometry

2.4.1 Volumetry

Flow volumetry analysis was performed by adapting an existing method[263] to hPSC-CMs. In order to establish a calibration curve relating forward light scattered and cell size, calibration beads of known dimensions (2-14.3μm, Spherotech #PPS-6K) were analysed using Astrios Cell Sorter flow cytometer (Beckman Coulter), after removing debris and duplets/triplets. Thereafter, dissociated hPSC-CMs were analysed in the same manner and estimation of cardiomyocyte volume was performed using the calibration curve and formula of volume of a perfect sphere ($V = \frac{\pi}{6} \times diameter^3$). Violin plots were made using Stata SE14 (StataCorp LLC).

2.4.2 Quantification of mitochondrial content and ROS

Mitochondria of dissociated hPSC-CMs were stained using 100nM MitoTracker green FM (Life Technologies #M7514). Intracellular ROS production by hPSC-CMs was investigated by staining with 2.5μM CellROX green (Life Technologies #C10444) or 5μM MitoSox Red (Life Technologies #M36008). Live cells were incubated with the dyes (made in Ca^{2+}/Mg^{2+} -rich HBSS (Gibco #14025) for 30 minutes at 37°C and 5% CO_2, followed by a PBS wash and centrifugation/ resuspension in PBS. Samples were then stored on ice before being run on Astrios flow cytometer.

2.4.3 Data analysis

Flow cytometry data was analysed in Kaluza software (Beckman Coulter), after removing cell debris and duplets/ triplets and using unstained samples as controls. Mean signal fluorescence intensities were used to compare mitochondrial content and ROS production in hPSC-CMs relative to wild-type (WT) isogenic controls, over 5-7 experimental replicates.

2.5 Seahorse analysis of mitochondrial respiration

The Seahorse XF96 extracellular flux analyser was used to assess mitochondrial respiration, as previously described[164]. Briefly, dissociated hPSC-CM were seeded into VN-coated XF96 well plates, at a density of approximately 5000 cells/mm^2. Cardiomyocytes were cultured for one week and medium was exchanged for XF base medium (Agilent Technologies #102353), supplemented with 10mM glucose (Sigma #G7528), 1mM sodium pyruvate (Sigma #S8636) and 2mM L-glutamine (Life Technologies #25030-081) 1h prior to the assay. Selective inhibitors were sequentially injected during the measurements (1.5μM oligomycin, 0.4μM FCCP, 1 μM rotenone, all from Agilent Technologies), following manufacturer's instructions. The OCR values were further normalized to the number of cells present in each well, quantified by 1:400 Hoechst in PBS staining (Hoechst 33342; Sigma) using fluorescence at 355 nm excitation and 460 nm emission in an automated imaging platform (CellaVista, Synentec).

2.6 Human engineered heart tissues

2.6.1 hEHT fabrication and maintenance

hEHTs were fabricated as previously described[139,264] (**Figure 2.1**), by collaborator Dr. Ingra Mannhardt (Medical University Hamburg). In brief, teflon spacers (EHT Technologies) were inserted in 2% ultra-pure agarose (Invitrogen #15510-027) solution pipetted into 24-well plates (Nunc) before gellification. Thereafter, spacers were removed and silicon racks (EHT Technologies) were placed in the aperture left by the agarose casting molds. Subsequently, freshly dissociated hPSC-CMs were resuspended in DMEM medium (Biochrom, F0415), supplemented with 10% heat-inactivated fetal calf-serum (Biochrom #S0615), 1% penicillin/ streptomycin (PEST, Gibco), 2mM L-glutamine, 1% heat-inactivated horse serum (Gibco #26050088), 10% MT, 0.1% Y-27632 and 5mg/ml fibrinogen (Sigma #F8630). The CM-fibrinogen mix was then quickly mixed with 3U thrombin (Sigma #T7513) and pipetted into the aperture between the silicon posts. Forming hEHTs were then incubated for 2h at 37°C and 5-7% CO_2 and subsequently moved to new 24-well plates filled with DMEM medium supplemented with 10% horse serum, 10 μg/ml insulin (Sigma #I9278), 33 μg/ml aprotinin (Sigma #A1153) and 1% (v/v) PEST, termed EHT medium. Each hEHT consisted of 1 million hPSC-CMs and was fed every other day for 2-3 weeks until fully mature.

2.6.2 Analysis of contractile force

Contractile force was analysed as previously described[159]. Briefly, 2-3 week-old hEHTs were immersed in modified Tyrode's solution (120 mM NaCl, 5.4 mM KCl, 1 mM $MgCl_2$, 1–1.8 mM $CaCl_2$, 0.4 mM NaH_2PO_4, 22.6 mM $NaHCO_3$, 5 mM glucose, 0.05 mM Na_2EDTA, and 25

mM HEPES) pre-equilibrated overnight (37°C, 7% CO_2, 40% O_2), and the 24 well-plate was placed inside a transparent chamber to maintain homeostatic temperature (37°C) and CO_2 (5%). Automated video-optical recordings of silicon post deflection were enabled by a video camera (Basler A6021-2) placed above the chamber, with a separate computer running a customized software (CMTV GmbH) to track hEHT movement and determine contractile force based on the known mechanical properties of the silicon. When indicated, EHTs were

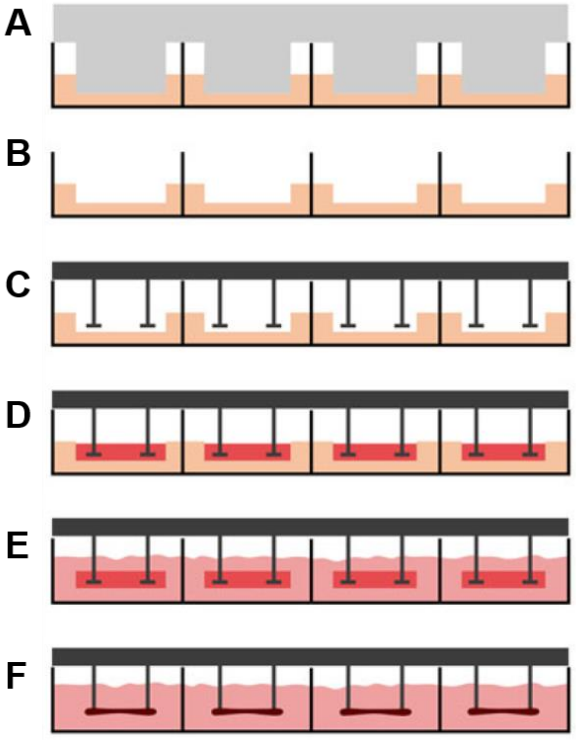


Figure 2.1 - EHT fabrication protocol. A) Teflon spacer in liquid agarose **B)** casting molds after solidification; **C)** silicone racks with two posts in each casting mold **D)** master mix of cells, fibrinogen, and thrombin inside casting molds, **E)** cells in a block of fibrin transferred to fresh medium after polymerization **F)** EHTs after 2 weeks of development. Adapted from [253].

electrically paced (2V, 1-2.5 Hz, impulse duration 4 ms) with carbon electrodes using a Grass S88X stimulator (Astro-Med). The contraction peaks were analysed in terms of frequency (beat rate), force, and contraction (T_1) and relaxation time (T_2) at 80% of peak height (Figure 5.20, Chapter 5). For Omecamtiv Mecarbil (OM) treatment experiments, baseline measurements were firstly recorded from electrically-paced hEHTs (1.75Hz for AT1 lines and 1.5Hz for REBL-PATs), followed by treatment with 1 μM OM for 30min and subsequent measurements. Absolute values of contractile force, T_1 and T_2 were reported for baseline characterization of hEHTs, and relative quantification was performed upon OM treatment by plotting changes from baseline (untreated conditions).

2.6.3 Glucose consumption measurements

Quantification of glucose consumption by EHTs was performed by determining concentrations of glucose in EHT medium 24h following medium change, using a blood glucose monitor (Accu-Chek). As the initial glucose in the medium is 120 mg/dl, measured values represent available glucose, and thus the difference between these two values indicates the glucose consumed, which was divided by the number of beats of unstimulated hEHTs for 24h to determine glucose consumption per beat.

2.7 Confocal line scans of calcium transients

2.7.1 hPSC-CM preparation

Targeted GECI hPSC-CMs were differentiated as previously described, cultured in RPMI+B27+INS without phenol red (Gibco #11835030) and dissociated on day 15, by colleague Jamie Bhagwan. hPSC-CMs were seeded at a density of 150,000 cells per well in VN-coated 35mm-diameter MatTek dishes (Nunc). CMs were assayed no earlier than day 24 and no later than day 30 of differentiation.

2.7.2 Image acquisition

Intracellular calcium transient measurements were made using an LSM 880C confocal microscope (Carl Zeiss) on line-scan mode, as previously described[265], by colleague Jamie Bhagwan. Briefly, CMs were located using a 40x oil objective and a longitudinal line was drawn across a single CM. Line-scan images were taken every 75 milliseconds for a total of 4000 cycles resulting in a 5 minute scan. CMs were kept at 37°C and 5% CO_2 throughout data acquisition.

2.7.3 Data analysis

Confocal line scan images were analysed in Fiji software (National Institute of Health) by colleague Jamie Bhagwan. The average fluorescence intensity of each line was calculated over time to generate a confocal line-scan trace. Using the 'multi kymograph' Fiji plugin, a corresponding kymograph image was produced. In order to calculate beat rate and arrhythmic events, data was fed into pClamp software (Molecular Devices). Baselines were adjusted to account for photobleaching, and calcium transients were counted and analysed using the 'event detection' function. Inter-event interval, T_{rise}, T_{decay} and peak height amplitude for each calcium transient event were calculated in event detection mode. In order to determine abnormal DAD-like calcium transients, median peak height analysis was performed using Excel (Microsoft), wherein the median peak height for a line-scan image was calculated, and any calcium transient events that were below 75% of the peak height were considered 'abnormal', including those that did not return to baseline and gave a 'double peak'.

2.8 Transcriptomics analysis

Gene expression analysis was performed by collaborator Maksymilian Prondzynski and Dr. Lucie Carrier (Medical University Hamburg) using nanoString nCounter Elements technology. Briefly, 50ng of RNA extracted from hPSC-CMs (as above) was hybridized with a customized nanoString Gene Expression CodeSet. Analysis was done using the nCounter Sprint Profiler, following manufacturer's instructions. The mRNA levels were normalized to five housekeeping genes (*ABCF1, CLTC, GAPDH, PGK1, and TUBB*) and expressed as fold change in mutant lines over isogenic control hPSC-CMs.

2.9 Statistical analysis

Values presented in text and figures are as mean ± standard error of the mean (unless stated otherwise) of at least three independent experiments, as indicated in the figure legends. Statistical analysis was performed by using Graph Pad Prism (v7, La Jolla, CA, USA) software, evaluated by unpaired one-way ANOVA test by using Dunnett's post hoc test for correction of multiple comparisons (relative to WT isogenic lines or untreated conditions for each line), and differences were considered significant when *$p < 0.05$, **$p < 0.01$, ***$p < 0.005$ and **** $p < 0.0001$.

3. Generation of R453C-MYH7 hPSC lines by CRISPR/Cas9 Genome Editing Technology

3.1 Introduction

As reviewed in Chapter 1.2, HCM is a prevalent and complex cardiac disease frequently caused by mutations in genes encoding sarcomeric proteins. Given the genetic and clinical heterogeneity that characterises HCM, it is not surprising that very few genotype–phenotype relationships have been shown to be reproducible. As the majority of mutations are restricted to each family, studies lack statistical power and robustness to demonstrate correlations between individual mutations and phenotype[3]. The variable expressivity, penetrance and allelic heterogeneity of similar mutations with respect to age at presentation, severity of hypertrophy, and prognosis has further hampered the understanding and treatment of HCM[4]. Therefore, by introducing the same SNP in three different hPSC lines using the same genome editing strategy, a greater insight can be gained on the disease phenotype and especially the degree of penetrance of the mutation.

Among the sarcomeric genes mutated in HCM patients, *MYH7* is prevalent (20-50% of genotyped cases)[67]. Despite clinical and phenotypic heterogeneity, *MYH7* mutations are associated with more severe forms of hypertrophy relative to when other sarcomeric genes are altered. This includes higher frequencies of ventricular tachycardia, greater disease penetrance, higher risk of sudden cardiac death and earlier onset[2,75]. In fact, unlike most sarcomeric gene mutations, the R453C-MYH7 SNP has shown 100% penetrance[70], which justifies a focused investigation to understand how the pathogenic change leads to sudden cardiac death in young patients[24]. However, there is limited data available from cardiac explants and mouse models bearing the R453C-MYH7 mutation, the latter often causing confounding results due to species-differences[266]. Existing HCM models using hPSC-CMs have not targeted this mutation [161,162] and lack proper isogenic controls wherein the patient genetic background is preserved.

Therefore, in order to overcome the limitations presented by these cell sources, human models of R453C-MYH7 HCM were created by harnessing CRISPR/Cas9 genome editing technology in hPSC. These models are expected to generate physiologically-relevant knowledge on the disease progression, so that drug discovery efforts can be better guided towards treatment of the disease.

3.1.1 CRISPR/ Cas9 Nickase gene targeting

Genome editing technologies are based on several targeted nucleases such as ZFNs, TALENs and CRISPR/Cas9, as reviewed in Chapter 1.4.2. Due to its versatility and ease of

assembly and high efficiency, CRISPR/Cas9 proved to be advantageous to the others[267]. However, the main concern associated with this endonuclease is its off-target cleavage activity, due to its tolerance of up to 5 mismatches between the gRNA and the target site. In order to overcome this limitation, a nickase Cas9 protein was developed by inactivating one of its catalytic domains[210], leading to the requirement of two gRNAs to cause single stranded nicks in the target DNA. By targeting proximal and opposite strands in the target gene, a double nick is created, resulting in reduced off-target activity to an almost undetectable level (increase in specificity in up to 1500-fold vs Cas9 nuclease). This is due to the fact that only nicks that are in close proximity produce DSB that are subsequently repaired by the HDR pathway using the donor homologous template (distant single nicks are quickly repaired through the HDR pathway using the intact complementary DNA strand as the template)[268].

3.1.2 Chapter aims and objectives

In this thesis, the nickase Cas9 was used to introduce the R453C-MYH7 mutation in three hPSC lines by resorting to bioinformatics tools to design the gRNAs that provided the best specificity[257]. In this chapter, the generation of R453C-MYH7 hPSC lines (HUES7-hESC, AT1-iPSC and REBL PAT-iPSC) is described as well as their characterization and validation.

A schematic representation of CRISPR/Cas9-mediated genome editing is depicted in **Figure 3.1**.

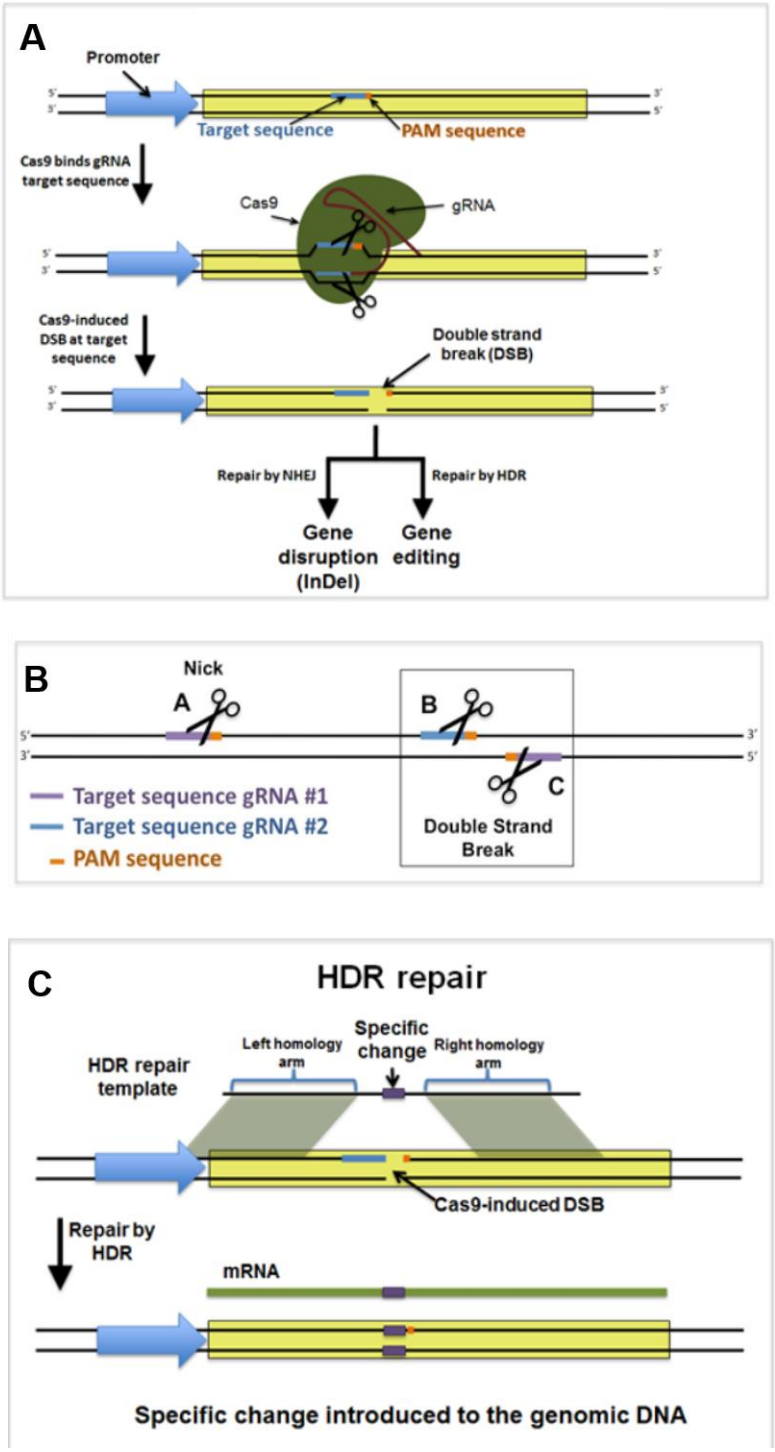


Figure 3.1 - CRISPR/Cas9 Nickase gene targeting strategy. **A)** Introduction of DSB by gRNA-directed Cas9 endonuclease via PAM site recognition leads to DNA repair processes which are the basis of gene-editing. **B)** In the nickase Cas9-based approach, DSB are only inserted upon double nicking opposite strands are that are in close proximity. **C)** HDR repair of inserted DSB in the presence of a homology template containing the specific genetic change allows sequence-specific genome editing of the locus of interest. Adapted from addgene.org/crispr/guide.

3.2 Results

3.2.1 CRISPR/Cas9 strategy design

In order to generate a new R453C-MYH7 HCM disease model, a CRISPR/Cas9 strategy was designed (**Figure 3.2**). The R453 amino acid is encoded in exon 14 of the *MYH7* gene (**Fig3.2A**), and Sanger sequencing hPSC genomic DNA showed no SNPs in the PAM sites targeted by the highest score gRNAs (within 30 bp of the R453 site, highlighted), rendering them suitable for CRISPR/Cas9 gene editing (**Fig3.2B**).

The strategy designed was based on a dual guide RNA/Cas9 nickase approach involving the co-transfection of four DNA plasmids (**Fig3.2C**): **i)** hCas9 D10A nickase, **ii)** oligonucleotide sequence of 2 gRNAs separately cloned into pU6 vectors, and **iii)** donor template targeting vector containing the R453C SNP flanked by 1Kb homology arms and a resistance cassette for positive selection, cloned into a pUC57 vector.

Following transfection of these 4 plasmids using a commercially available polycationic polymer (GeneJammer), hPSC were selected by antibiotic treatment as a puromycin or blasticydin resistance cassette was inserted in the targeting vector, in an intron immediately downstream of the R453C mutation. Genotyping of positive colonies was then performed and upon resistance cassette excision, the gene-edited hPSC lines were characterized in terms of pluripotency and karyotypic stability (**Fig 3.2D**). The next section will detail the strategy design and will focus on the synthesis of the required plasmids.

3.2.1.1 Guide RNA design and synthesis

Synthesis of the four plasmids needed for gene targeting is outlined in **Figure 3.3**. hCas9 nickase plasmid was commercially available (**Fig3.3A**).

Two gRNA combinations were used in this thesis so as to generate a double stranded break with a 5' overhang (**Fig3.3B**). Both the combinations used (gRNA66+gRNA46 and RNA66+gRNA39) were predicted to only have one off-target gene, the highly homologous *MYH6* locus. Guide RNA synthesis was then based on cloning the gRNA oligo sequences provided by the MIT CRISPR tool into a pU6 backbone, by annealing the forward and reverse sequences of each of the gRNAs flanked by BsaI restriction sites. Cloning success was verified by diagnostic enzymatic digestion with NdeI (unique cutter) and EcoRI (lost upon gRNA oligo cloning) and confirmed for the 3 gRNA plasmids by Sanger sequencing.

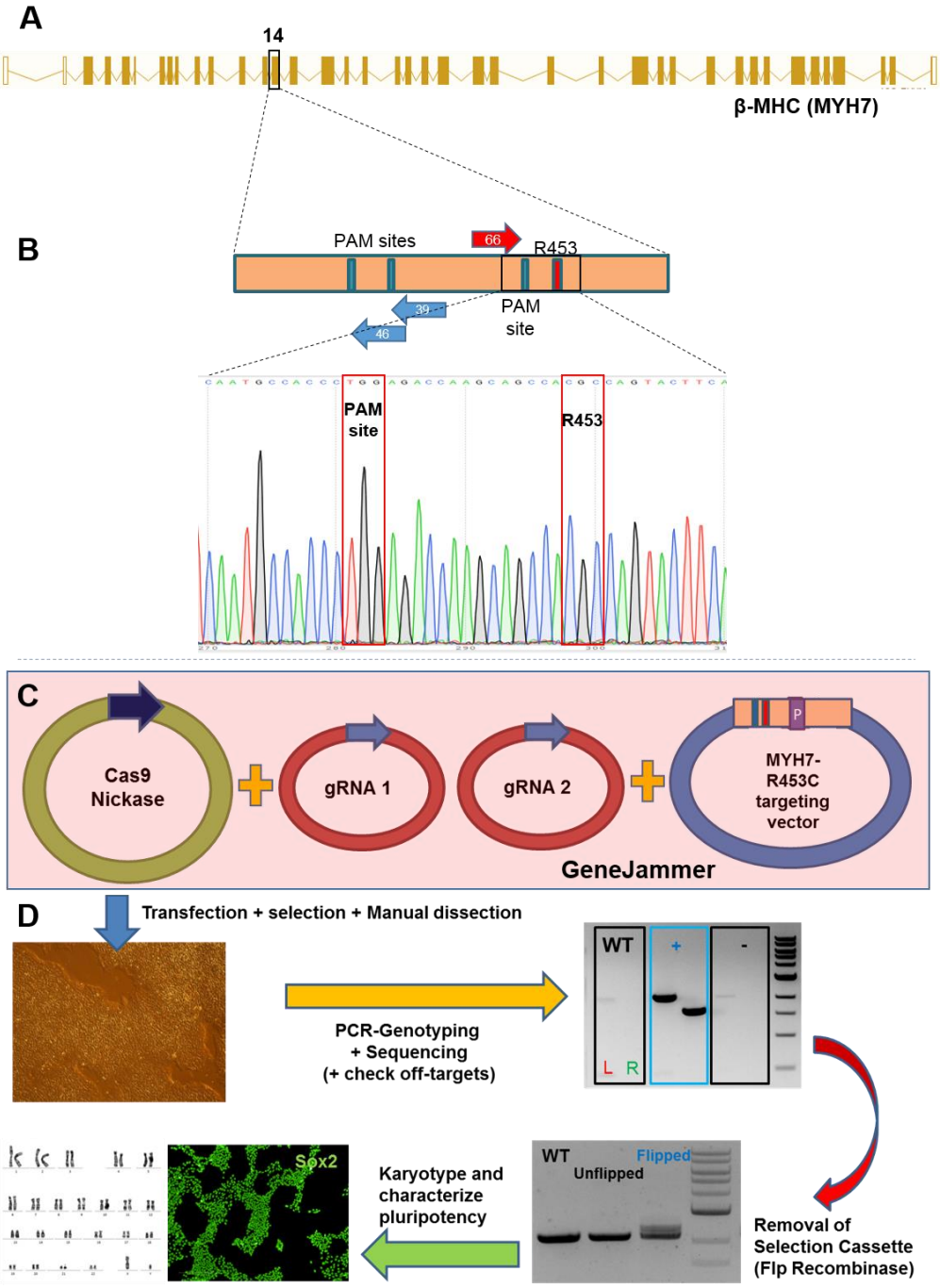


Figure 3.2 - Overview of CRISPR/Cas9 strategy design. A) Structure of the *MYH7* gene highlighting exon 14 (target site). **B)** Sequencing *MYH7* gene showed no SNPs on the mapped aminoacid R453 region as well as on the PAM sites displaying the highest scores (indicated) on the CRISPR design tool. **C)** The gene-editing strategy consisted in transfecting hPSC with 4 plasmids: i) Cas9 nickase, ii) guide RNA pair and iii) targeting vector in order to repair the dsDNA break via homologous directed repair. **D)** Transfected cells were then selected via antibiotic resistance, genotyped and characterized upon removal of selection cassette.

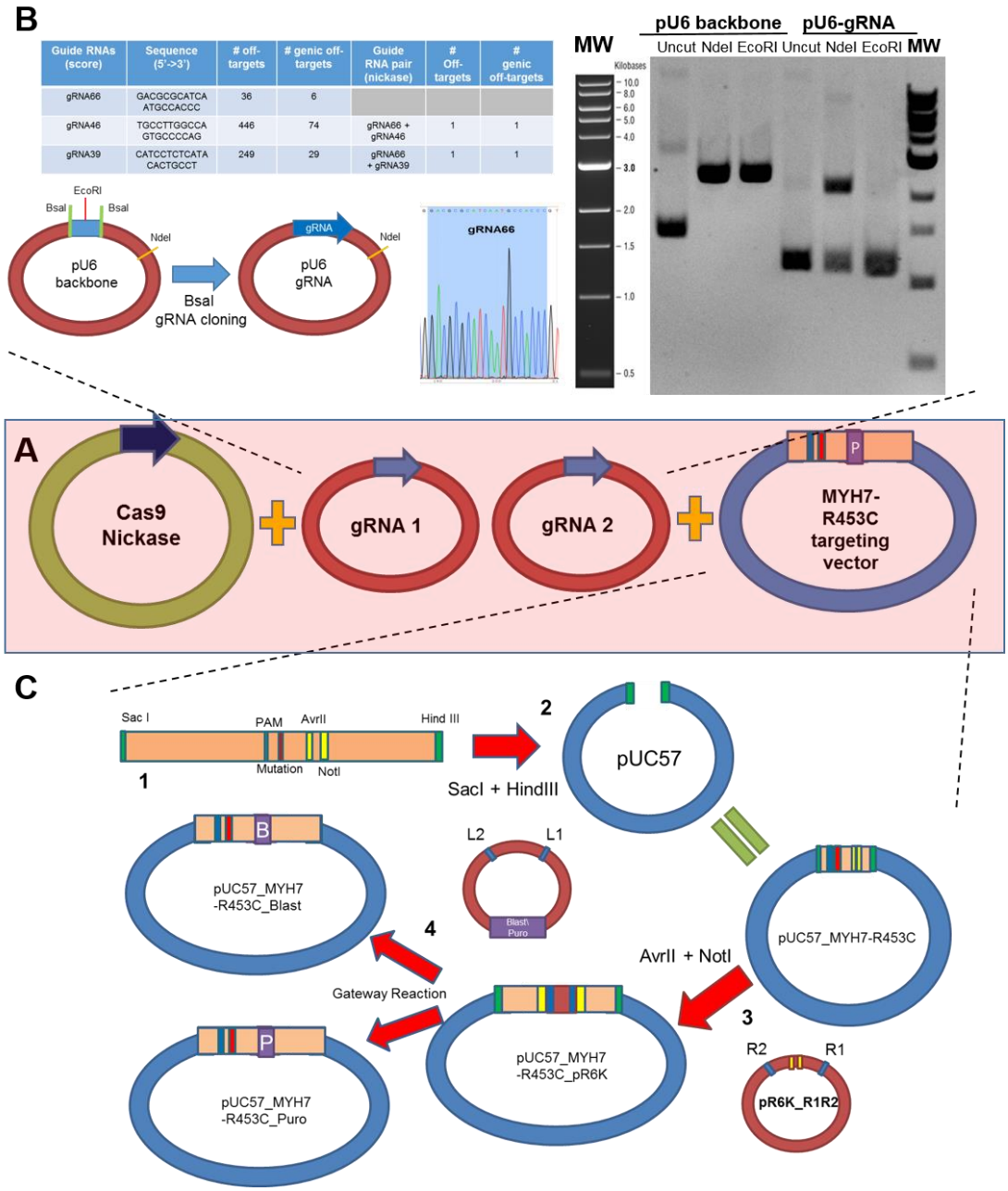


Figure 3.3 - CRISPR/Cas9 gRNA and targeting vector plasmid synthesis. A) Unlike the Cas9 nickase that was commercially available, the remaining plasmids were manually synthesized. **B)** gRNA oligonucleotide DNA sequences were cloned into a pU6 backbone plasmid via BsaI restriction site ligation. Plasmid sequence was then confirmed by diagnostic enzymatic restriction digestions and Sanger sequencing. **C)** Targeting vector synthesis was based on amplification of the 2Kb sequence containing the R453C and PAM site mutations by PCR-splice mutagenesis followed by several cloning steps so as to produce the final plasmid containing antibiotic resistance cassette for selection (detailed in Figure 3)

3.2.1.2 Targeting vector synthesis

Targeting vector synthesis is outlined in **Figure 3.3C** and it relied on cloning the R453C SNP flanked by 1Kb homology arms into a pUC57 vector containing a resistance cassette, by four main steps: **1)** PCR splice mutagenesis, **2)** cloning into pUC57 vector, **3)** subcloning the pR6K vector and **4)** Gateway reaction to insert a resistance cassette.

The details of this procedure are depicted in **Figure 3.4**. Firstly, PCR-splice mutagenesis was performed using genomic DNA from the hPSC lines to be targeted, to introduce the MYH7-R453C SNP (CGC→TGC) and also the PAM site silent mutation (TGG→TCG, to prevent Cas9 from cutting the donor construct). Moreover, in order to enable subsequent cloning steps, additional AvrII and NotI restriction sites were also inserted in an intron immediately downstream the R453C-SNP (allowing enough space to preserve splice donor/ acceptor sites and expected branching points[269]). As such, the 2Kb genomic DNA template was amplified in two separate fragments and the mutations were inserted by the sequences of the primers used (**Fig 3.4A**). Thereafter, the HindIII and SacI sites edging the DNA fragment enabled successful cloning into pUC57 vector, as verified by diagnostic restriction digestion using the same enzymes, and further validation by sequencing showing the R453C-SNP (**Fig3.4B**).

In order to confer antibiotic resistance required for positive selection of targeted hPSCs, an initial cloning step was performed to introduce the R1 and R2 sites for the subsequent recombination with the L1/L2 sites present in the vectors bearing the resistance cassettes. This was achieved by AvrII and NotI-mediated recombination between the pUC57-MYH7-R453C vectors with the pR6K insert bearing the R1/R2 sites (**Fig3.4C**), and verified by diagnostic digestions. Finally, the L1/L2 plasmids bearing either the blasticydin or puromycin resistance cassettes were recombined with the pUC57-MYH7-R453C-pR6K plasmids through a Gateway recombination reaction (**Fig3.4D**), resulting in the final targeting vectors displaying the R453C-SNP and antibiotic resistance cassette. The final validation of the donor templates was done by diagnostic digestion using the unique cutter HindIII and the multi-cutter BsaI enzymes (used to distinguish between blasticydin and puromycin vectors), followed by Sanger sequencing.

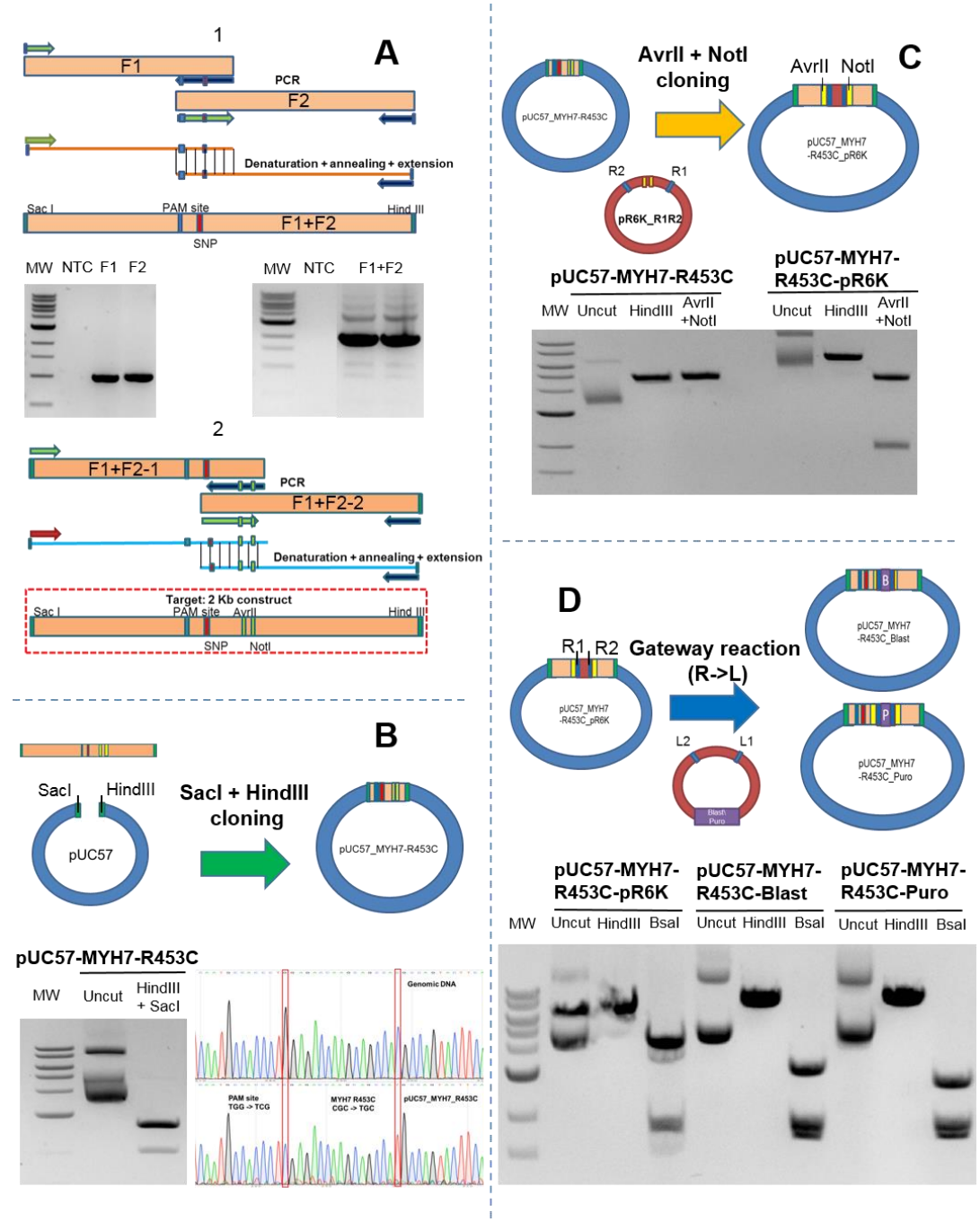


Figure 3.4 - Targeting vector synthesis. A) A 2-step PCR-splice mutagenesis procedure was used to introduce the R453C and the silent PAM site mutations as well as the restriction sites needed for cloning (SacI, HindIII, AvrII and NotI). Starting with genomic DNA from each hPSC line to be targeted, each product was divided into 2 fragments resulting in a 2Kb construct where the SNP is flanked by 1Kb homology arms. **B)** The DNA insert produced in A was cloned into a pUC57 vector via SacI and HindIII restriction site ligation. Sequencing data shows that the PAM site silent mutation and the R453C-MYH7 SNP were inserted. **C)** In order to enable the recombination needed to introduce the antibiotic resistance cassettes in the targeting vector, an initial cloning step was performed to introduce the R1 and R2 sites, via AvrII and NotI restriction site ligation. **D)** The Blasticydin or Puromycin resistance cassettes were introduced in an intron downstream of the R453C mutation by a Gateway reaction (where L1/L2 sites were recombined with R1/R2 sites). Diagnostic digestions were performed in each step to confirm that the plasmids generated were correct, followed by validation by sequencing. MW – Molecular weight marker; NTC- non template control.

3.2.2 hPSC transfection and selection

Having generated the tools needed to edit the hPSC, the next step was transfection and positive selection. hPSC transfection was done by complexing the four plasmids with the commercially available GeneJammer transfection reagent (polyamine polymer). Transfection efficiency was roughly estimated by transfecting separate hPSC with a GFP plasmid and then assessing the number of cells expressing GFP 24h later (**Fig3.5A-D**). Using the Cellavista automated platform, the approximate transfection efficiency was 25%, based on the GFP signal area normalized to total area occupied by cells. Transfected hPSC were then selected using blasticydin or puromycin treatment until colony formation was detected (**Fig3.5E**). Colonies were then isolated by manual dissection (forming monoclonal hPSC) and genotyped, and positive clones were expanded to a monolayer format (**Fig3.5F**).

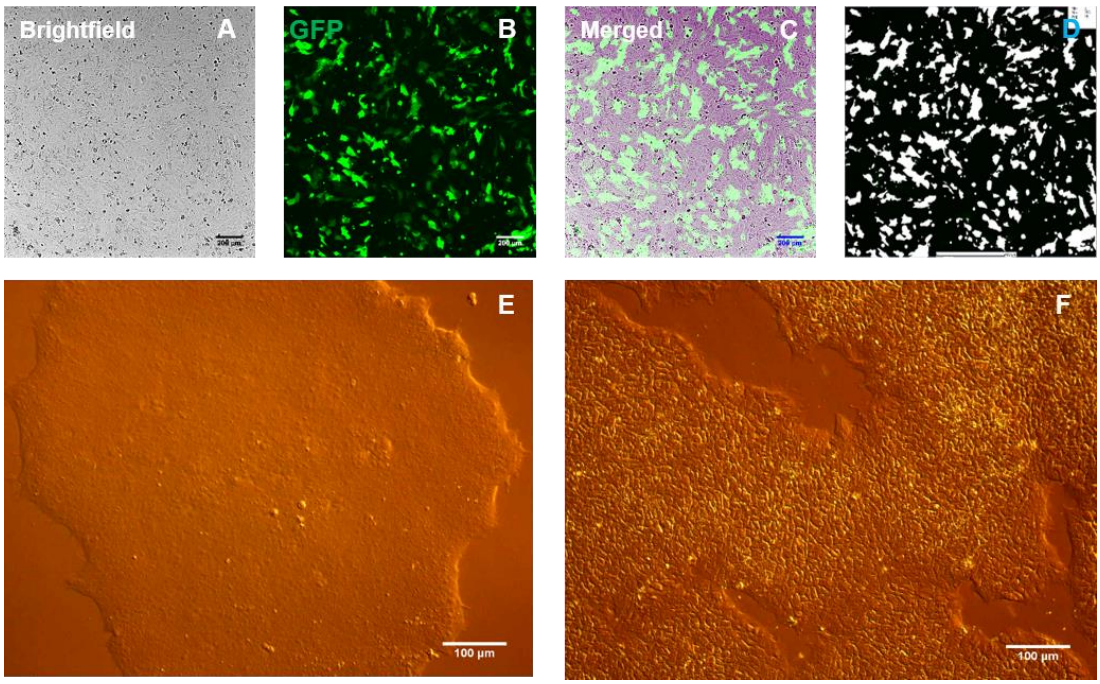


Figure 3.5 - hPSC transfection and selection. **A-D)** GeneJammer-mediated transfection efficiency was estimated using a GFP plasmid resulting in ~25% as calculated by CellaVista software, based on area of fluorescent cells normalized to total cell area. **E)** Selection of positive clones was achieved using antibiotic selection leading to colony formation and subsequent **F)** cell expansion into monolayer format. Scale bars: A-D: 200µm, E,F: 100µm.

3.2.3 Genotypic characterization of targeted clones

In order to ensure that targeted colonies displayed the desired R453C-MYH7 change, genotyping was performed by several PCR reactions and confirmed by sequencing (**Figure 3.6**). PCR reactions 1-3 were designed to target both MYH7 alleles individually, by the use of primers that recognized sequences outside the region covered by the targeting vector. Expectedly, at least one of the alleles of positively targeted hPSC contained a resistance cassette, as the cells were resistant to antibiotic treatment.

PCR reactions 1 and 2 were aimed at left and right homology arms respectively, and the reactions were only successful in positive clones (**Fig3.6B1-2**), in contrast to untargeted (WT) hPSC. Further sequencing of the left homology arm confirmed the R453C-MYH7 genotype (**Fig3.6B1**'). PCR reaction 3 was only successful in the non-cassette allele, as the resistance cassette sequence is composed by long and highly repetitive regions that are not amplified in a PCR reaction not optimized for that purpose (**Fig3.6B3**). Interestingly, one of the AT1 colonies did not show untargeted DNA product suggesting that bi-allelic gene editing occurred. As both the MYH7 alleles of this colony display the resistance cassette, the *MYH7* expression is abrogated, as validated in Chapter 4. Finally, PCR reaction 4 was designed to amplify both alleles (**Fig3.6B4**) and sequencing of the amplified product enabled confirmation of the heterozygous vs homozygous genotype of positive colonies detected (**Fig3.6B4'**).

Next, undesired indel activity and *MYH6* off-targeting was investigated (**Figure 3.7**). By amplifying the non-cassette allele (PCR reaction 3), some colonies showed bands with larger sizes than expected (**Fig3.7A**), in comparison to the untargeted controls (WT). Moreover, further inspection (sequencing) of PCR products from colonies where no band size differences were initially verified led to the detection of reads with multiple peaks (similar to those in **Fig3.7C'**). These events likely derive from NHEJ repair mechanism that results in indels and frameshifts in the non-cassette *MYH7* allele and as such, colonies displaying NHEJ were excluding for downstream disease modeling experiments as the genotype is not characteristic of human forms of the disease.

Overall, targeting efficiencies are reported in **Fig3.7B**, across the three hPSC lines targeted, with monoallelic targeting rates ranging from 27.1% to 42.5% and bi-allelic between 4.3% and 11.8%. These efficiencies are high relative to those of selection-free methods previously reported (HDR-editing efficiencies between 0.2 and 15% in hPSCs[270]). However, unwanted editing events were detected such as the prevalence of indels in the non-cassette allele of positive clones (around 40%).

Finally, editing of the *MYH6* gene (the only off-target predicted by the MIT CRISPR Design software) was investigated by PCR, showing no evidence of indels in the positive colonies analysed (**Fig3.7C**). However, the existence of multiple peaks in *MYH6* DNA sequence in one of the AT1 R453C-MYH7 homozygous colonies (**Fig3.7C'**) point towards frameshift mutations in this locus, indicating off-target activity of *MYH7*-directed CRISPR/Cas9 nickase.

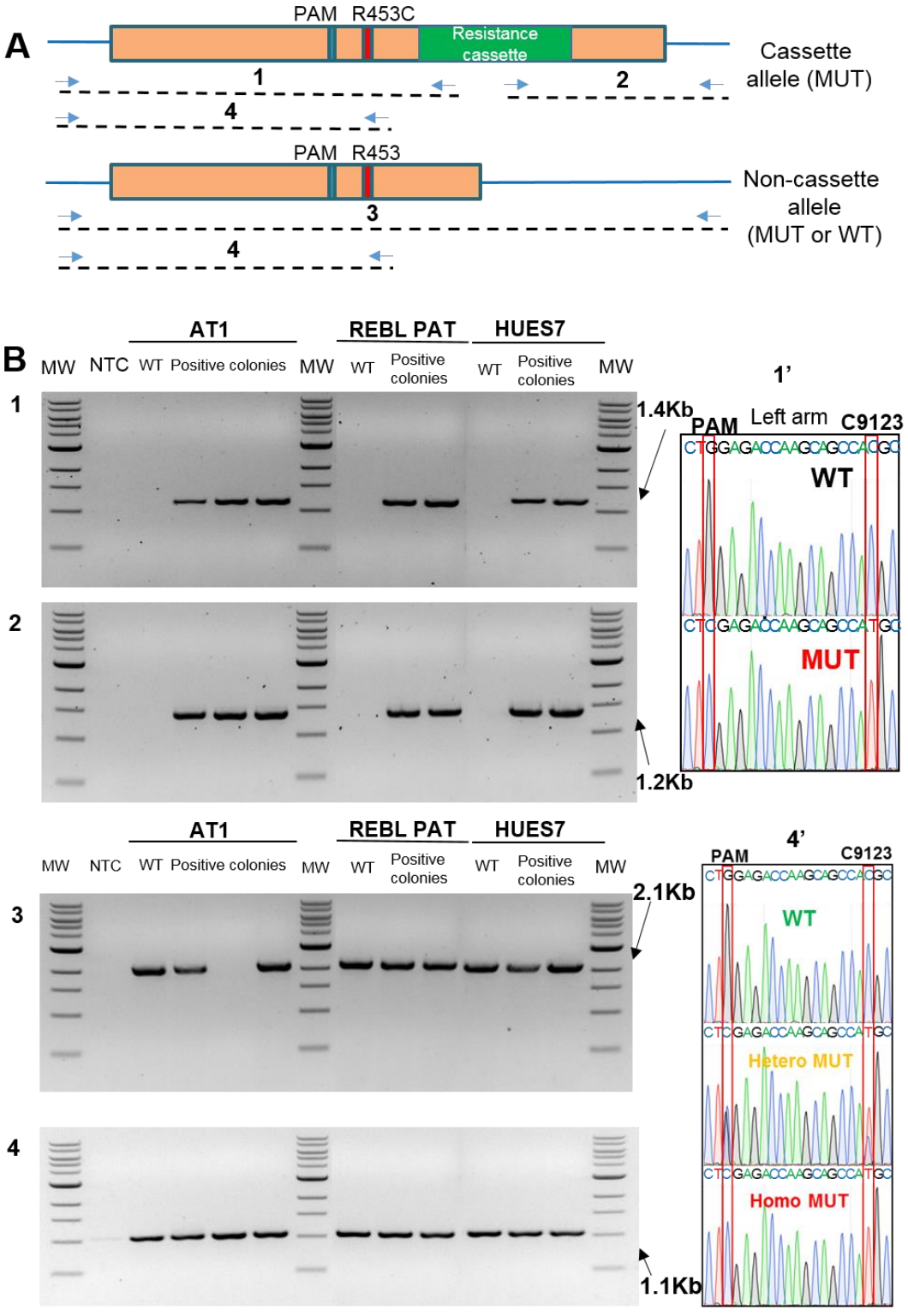
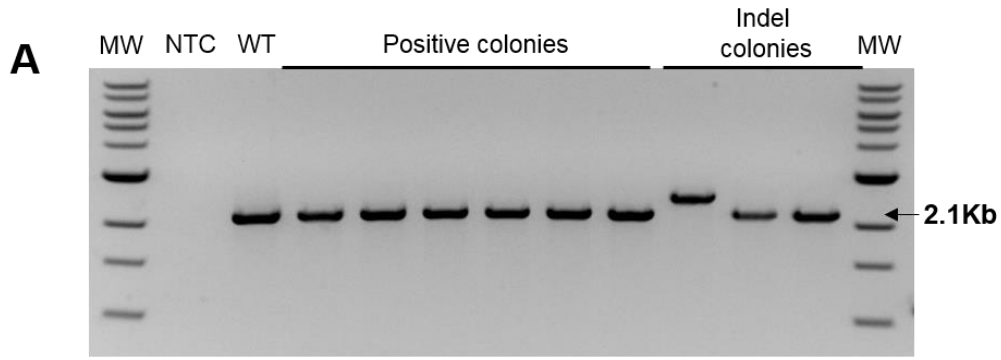


Figure 3.6 - Genotypic characterization of genome-edited hPSC. A) Schematic of the *MYH7* gene post gene targeting as well as the PCRs used to genotype picked colonies (numbered, with corresponding gels in B) – at least one of the alleles was expected to have a resistance cassette in positive colonies. **B)** DNA electrophoresis gels showing the results of the PCR amplification of: **1)** Left homology arm (cassette allele); **2)** right homology arm (cassette allele), **3)** Non-cassette allele, **4)** both alleles. **1')** Sequencing left homology arm confirms introduction of the R453C SNP in the cassette allele. **4')** Sequencing both alleles shows heterozygous and homozygous colonies for the 3 hPSC lines targeted. MW – Molecular weight marker; NTC- non template control.



B

hPSC line	Positive colonies (% picked)	Bi-allelic (% positive)	Indels /Frameshifts (% analysed)
HUES7	23/85 (27.1%)	1/23 (4.3%)	4/10 (40%)
AT1	17/40 (42.5%)	2/17 (11.8%)	4/10 (40%)
REBL PAT	11/30 (36.7%)	1/11 (9.1%)	4/10 (40%)

Previous selection-free methods in hiPSC: **0.2-15% efficiency [270]**

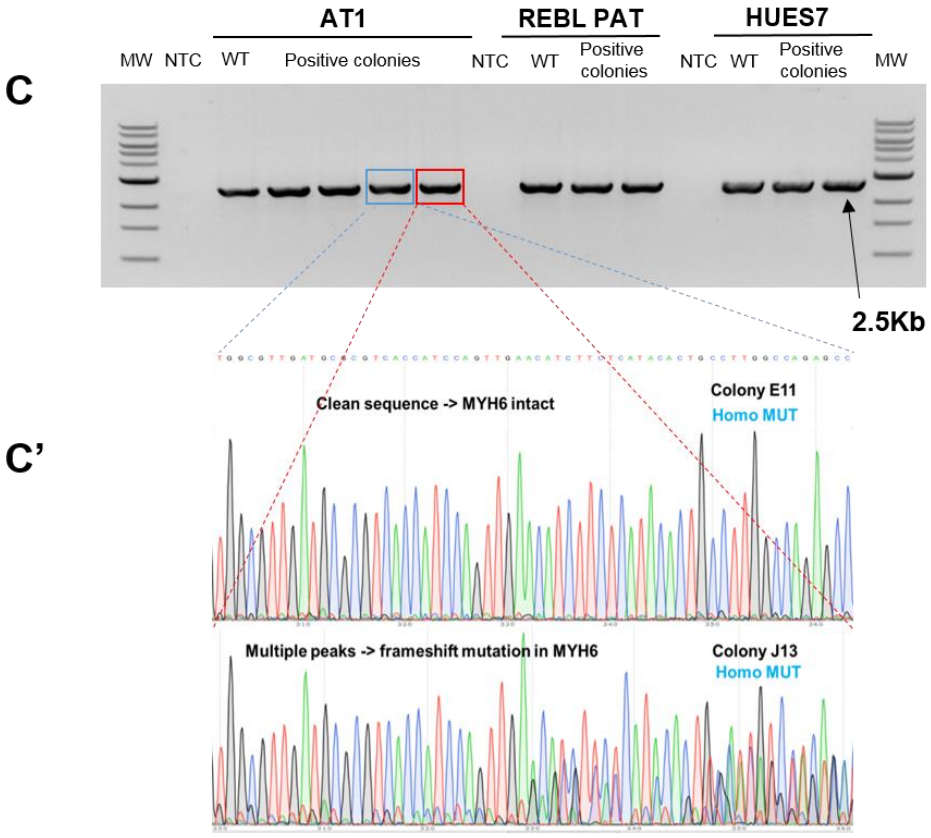


Figure 3.7 - Off-target analysis of MYH7-R453C genome editing. A) PCR amplification of non-cassette allele of the *MYH7* gene (PCR reaction 3 in Figure 3.6A) showed larger bands than expected in some colonies, indicating occurrence of indels and/or unsidered frameshifts. **B)** Quantification of editing efficiencies in the 3 hPSC lines targeted. **C)** PCR amplification of *MYH6* off-target gene does not indicate Indel events. However, sequencing data shows that one of the colonies (in red) had a frameshift mutation in the MYH6 gene, due to the existence of multiple peaks by sequencing **C')**. MW – Molecular weight marker; NTC- non template control.

3.2.4 Selection cassette excision

Having confirmed that the *MYH7* locus was successfully targeted in hPSC, the final step was to remove the resistance cassette in the intron downstream the R453C site, as it is conceivable that this cassette may interfere with gene expression, despite being in an intron. Therefore, R453C-MYH7 hPSC were transfected with a FlpO plasmid that could recognize FRT sites present in the resistance cassette, thus excising it from the *MYH7* locus while leaving a 280bp footprint in the intron (**Fig3.8A**). For this goal, antibiotic selection was done as before, using a different antibiotic than the one applied in the first transfection.

Genotyping of colonies generated was performed by three PCR reactions (**Fig3.8B**). PCR reaction 1 resulted in products of different sizes depending on whether the resistance cassette had been excised (flipped), showing that the DNA fragment had been correctly removed in transfected colonies (**Fig3.8C1**), as further confirmed by sequencing. PCR reaction 2 targeted the resistance cassette *per se*, and was negative for flipped colonies in contrast to unfilpped ones (**Fig.3.8C2**) PCR reaction 3 enabled amplification of both alleles, revealing double bands in colonies where a resistance cassette had previously been inserted in one of them (**Fig3.8C3**) (as expected, the bi-allelic resistance cassette colony showed only 1 band upon flippase).

3.2.5 Gene-edited hPSC characterization

As targeted hPSC lines have undergone several population doublings and single cell culture until colony formation during the 2 step gene editing procedure, characterization of pluripotency and genetic stability was performed.

3.2.5.1 Expression of pluripotency markers

Expression of pluripotency markers *OCT4, SOX2, NANOG, SSEA4* and *SSEA3* was evaluated by immunostaining (**Figure 3.9**). A very high percentage (>90%) of the hPSCs bearing the generated genotypes express the 5 markers analysed, in contrast to fibroblasts, which showed no expression of either of these markers.

3.2.5.2 Karyotype

It has been reported that hESC lines cultured for a long time may show chromosomal gains such as 12, 17, 20 and X, suggesting growth advantages of certain populations[271], especially when cultured as single cells. hPSC were therefore karyotyped showing that all of the generated hPSC were genetically stable, except for the HUES7 *MYH7*$^{MUT/MUT}$ that had an additional DNA fragment in the seventh chromosome (**Figure 3.10**).

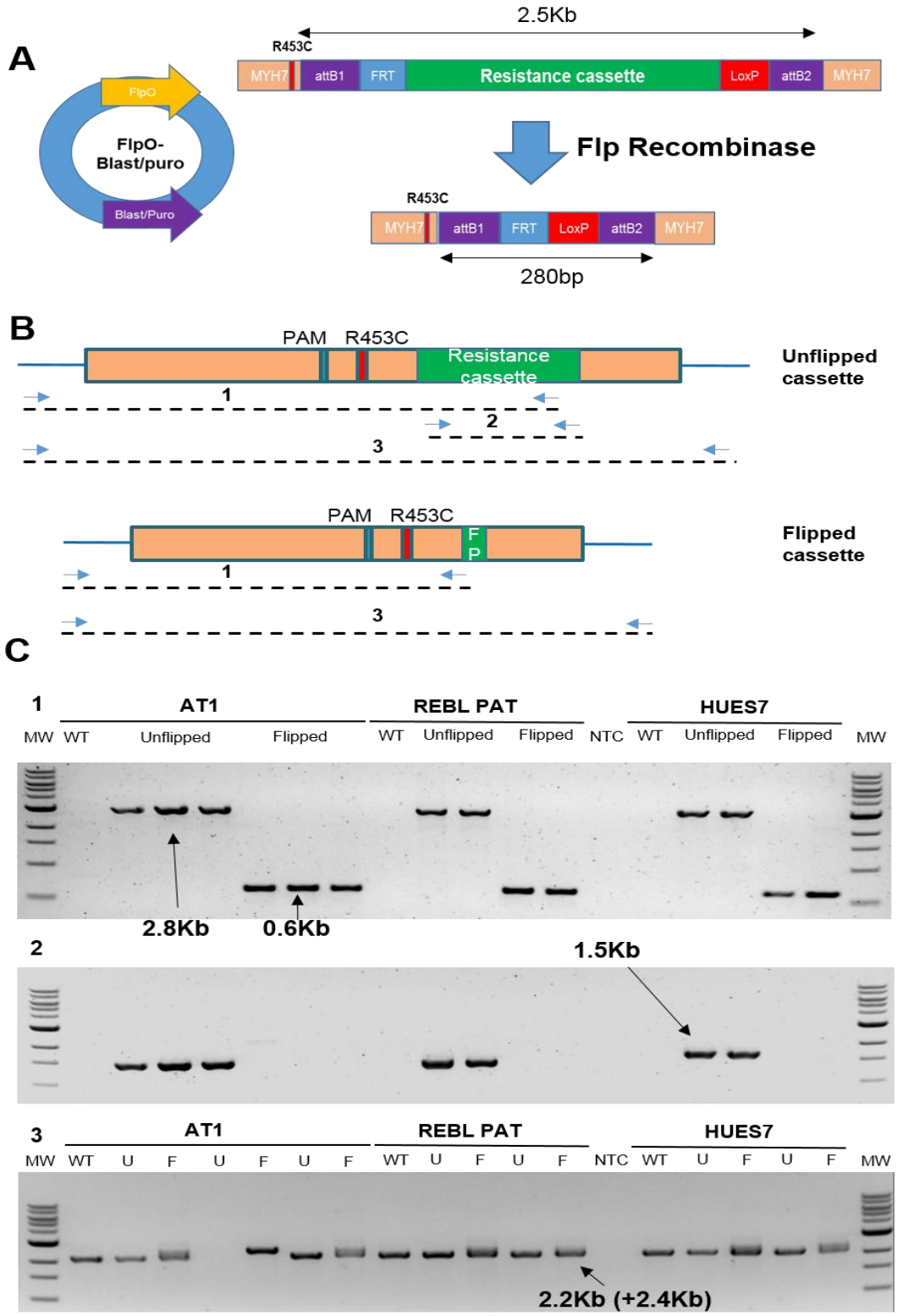
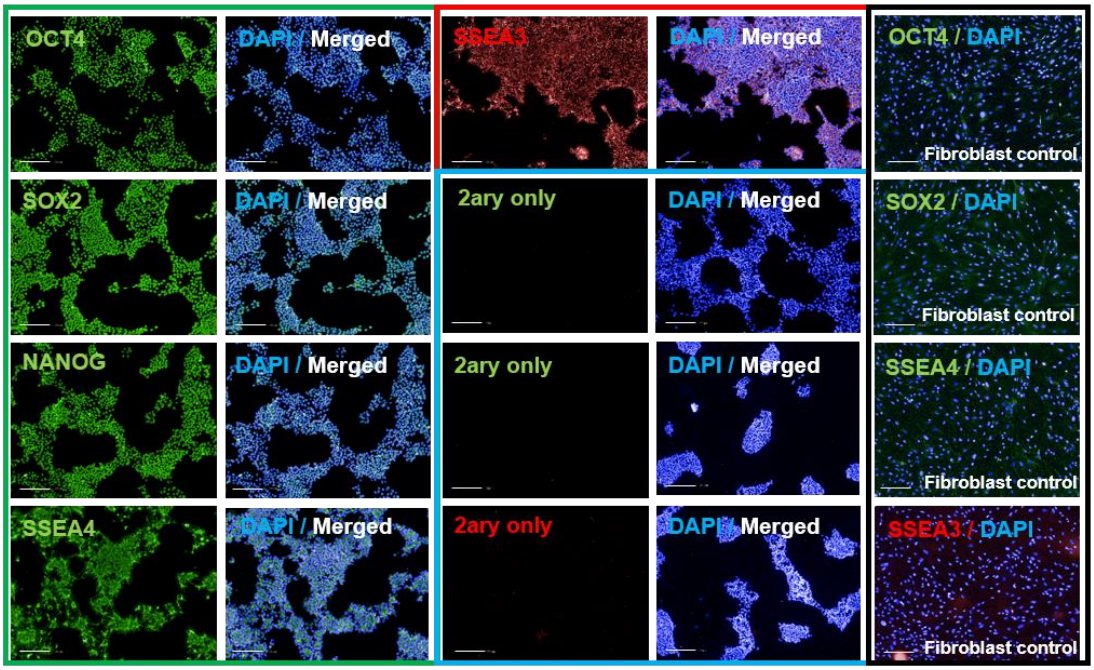


Figure 3.8 - Selection cassette excision from genome-edited hPSC. A) FlpO plasmid used to excise the selection cassette by recognizing FRT sequences. **B)** Schematic of the *MYH7* gene upon R453C CRISPR-targeting, before and after the excision of the selection cassette, as well as the PCRs performed to genotype colonies (numbered). **C)** DNA electrophoresis gels showing the PCR results: **1)** Flipped colonies have a smaller product (~0.6Kb) than the unflipped ones (~2.8Kb); **2)** colonies lose resistance cassette DNA upon cassette excision; **3)** removal of resistance cassette leaves a 280bp (intronic) footprint in the MYH7 gene, as shown by the double band when amplifying both alleles of targeted colonies (U-unflipped, F-flipped, MW – Molecular weight marker; NTC- non template control).

A

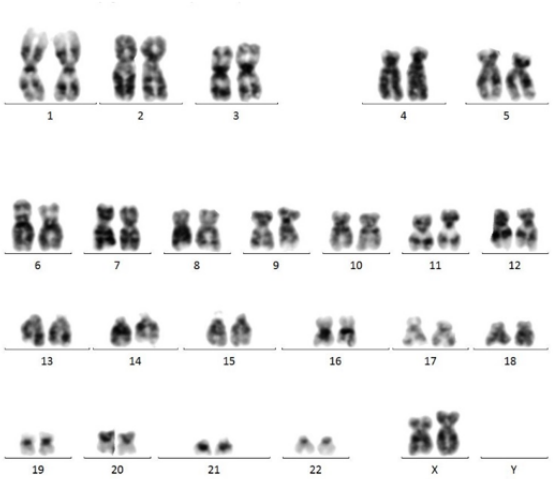


B

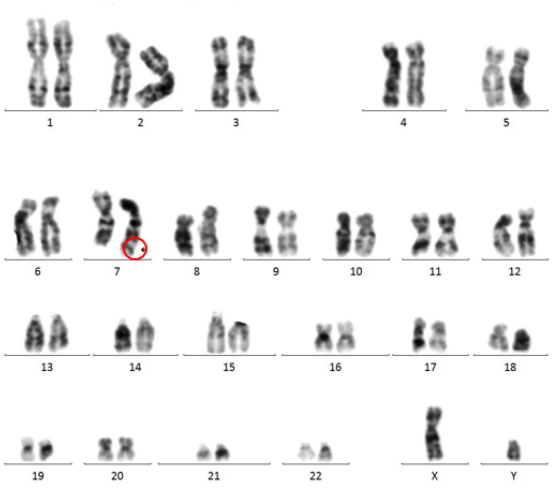
Cell line	% OCT4⁺	% SOX2⁺	% NANOG⁺	% SSEA4⁺	% SSEA3⁺
AT1 MYH7$^{WT/WT}$	99.8 ± 0.0	99.8 ± 0.0	99.7 ± 0.0	97.8 ± 0.3	98.5 ± 0.7
AT1 MYH7$^{WT/MUT}$	98.6 ± 0.8	98.9 ± 0.4	98.8 ± 0.1	96.4 ± 0.7	98.2 ± 0.6
AT1 MYH7$^{MUT/MUT}$	99.5 ± 0.3	99.7 ± 0.1	98.7 ± 0.6	97.1 ± 0.4	97.6 ± 2.0
AT1 MYH7$^{-/-}$	99.3 ± 0.4	99.3 ± 0.2	97.8 ± 1.5	94.9 ± 2.4	90.8 ± 4.7
AT1 MYH7$^{MUT/MUT}$ + MYH6$^{WT/fs}$	99.2 ± 0.2	99.3 ± 0.2	98.7 ± 0.5	97.3 ± 0.3	98.6 ± 0.4
REBL PAT MYH7$^{WT/WT}$	99.7 ± 0.0	99.7 ± 0.1	98.8 ± 0.3	95.6 ± 1.1	95.8 ± 3.1
REBL PAT MYH7$^{WT/MUT}$	99.7 ± 0.1	99.7 ± 0.1	98.7 ± 0.5	91.9 ± 0.8	97.2 ± 0.8
REBL PAT MYH7$^{MUT/MUT}$	98.9 ± 1.2	99.7 ± 0.1	99.3 ± 0.4	92.2 ± 1.8	97.4 ± 2.5
HUES7-MYH7$^{WT/WT}$	98.4 ± 1.2	99.7 ± 0.2	96.9 ± 0.9	87.0 ± 4.7	81.9 ± 3.2
HUES7 MYH7$^{WT/MUT}$	93.6 ± 4.2	99.7 ± 0.1	98.6 ± 0.3	95.4 ± 1.1	94.0 ± 3.3
HUES7 MYH7$^{MUT/MUT}$	98.5 ± 0.5	98.9 ± 1.5	90.7 ± 2.1	90.4 ± 1.1	93.5 ± 2.0

Figure 3.9 - Pluripotency marker expression of gene-edited hPSC. A) Representative fluorescent micrographs of genome-edited hPSC lines stained for pluripotency markers OCT4, SOX2, NANOG, SSEA4 and SSEA3. **B)** Quantification of pluripotency marker expression shows that a high percentage (90^{+}%) of cells maintain pluripotency upon genome editing of the MYH7 locus. Scale bar =200 µm.

A



B



C

hPSC line	Karyotype
AT1 MYH7$^{WT/WT}$	46,XX[28] 45,XX,-18[1] 45,XX,-21[1]
AT1 MYH7$^{WT/MUT}$	46,XX[28] 45,XX,-20[1] 45,XX,-21[1]
AT1 MYH7$^{MUT/MUT}$	46,XX[24] 45,XX,-22[2] 45,XX,-2[1] 45,XX,-9[1] 45,XX,-20[1] 45,XX,-21[1]
AT1 MYH7$^{-/-}$	46,XX[24] 45,XX,-22[2] 45,XX,-2[1] 45,XX,-9[1] 45,XX,-20[1] 45,XX,-21[1]
AT1 MYH7$^{MUT/MUT}$ + MYH6$^{WT/fs}$	46,XX[23] 45,XX,-12[2] 45,XX,-8[1] 45,XX,-17[1] 45,XX,-11[1] 45,XX,-20[1] 45,XX,-19[1]
REBL PAT MYH7$^{WT/WT}$	46,XY[30]
REBL PAT MYH7$^{WT/MUT}$	46,XY[30]
REBL PAT MYH7$^{MUT/MUT}$	46,XY[30]
HUES7 MYH7$^{WT/WT}$	46,XY[22] 45,XY[1]
HUES7 MYH7$^{WT/MUT}$	46,XY[26] 45,XY,-8[1] 45,XY,-19[1] 45,XY,-21[1] 45,XY,+mar[1]
HUES7 MYH7$^{MUT/MUT}$	46,XY,add(7)(q3)[25] 46,XY,add(7)(q3)[25],16[2] 46,XY,add(7)(q3)[25],-20[2] 46,XY,-4,add(7)(q3)[25]

Figure 3.10 - Karyotype of genome-edited hPSC lines. Representative karyogram of a **A)** genetically stable hPSC line and that of the **B)** HUES7 *MYH7*$^{MUT/MUT}$ indicating the additional genetic material on the seventh chromosome. **C)** Table showing that all the generated lines display genomic integrity, except for the HUES7$^{MUT/MUT}$ line (highlighted in red). Karyotyping service performed by Nigel Smith (Cytogenetics Department, Nottingham City Hospital).

3.3 Discussion

3.3.1 Strengths and drawbacks of plasmid-based strategy

In this chapter, the strategy for introducing the R453C-MYH7 SNP in hPSC was described as well as the synthesis of the DNA constructs required for CRISPR/Cas9 targeting (gRNAs and donor repair templates). hPSC were successfully targeted, resulting in several variants of the R453C-MYH7 genotype, and characterized in terms of pluripotency and karyotype.

The plasmid-based CRISPR/Cas9 system used herein has several advantages over other methods such as RNP-based editing. First of all, cloning of these plasmids is straightforward, in comparison to more intricate reactions needed to assemble the components of the editing strategy, such as *in vitro* transcription and purification needed to produce gRNAs in the RNP-based editing. Moreover, plasmid DNA cloning enables additional versatility in terms of the DNA elements that can be co-introduced with the desired SNP, such as **i)** selection cassettes to enhance editing efficiency, **ii)** additional silent mutations with downstream applications such as allele-specific genotyping and **iii)** longer homology arms, which enhance recombination efficiency as explored below.

Typically, selection-free methods such as RNP-based strategies usually result in lower editing efficiencies, requiring genotypic analysis of more clones, which may be further aggravated by the use of short homology arms in some *loci*. Furthermore, transfection of DNA-RNA-protein complexes is harder to optimize than that of simple DNA plasmids, as the protein buffer composition must be kept stable throughout the transfection procedure. In addition, performing PCR-splice mutagenesis to introduce the R453C change in the MYH7 locus using genomic DNA derived from each hPSC line preserves their genetic background thus narrowing down any observed phenotypes to the penetrance of the mutation (and not to SNPs between lines). However, as the half-life of the plasmid DNA is longer than that of the RNP (as protein complexes get degraded rapidly), the integrity of the targeted locus was often compromised as shown by the high proportion of indel activity (40%) in clones edited by the plasmid strategy herein. Moreover, additional off-target activity is also more likely to occur in the former, which was nevertheless minimized by the use of nickase Cas9.

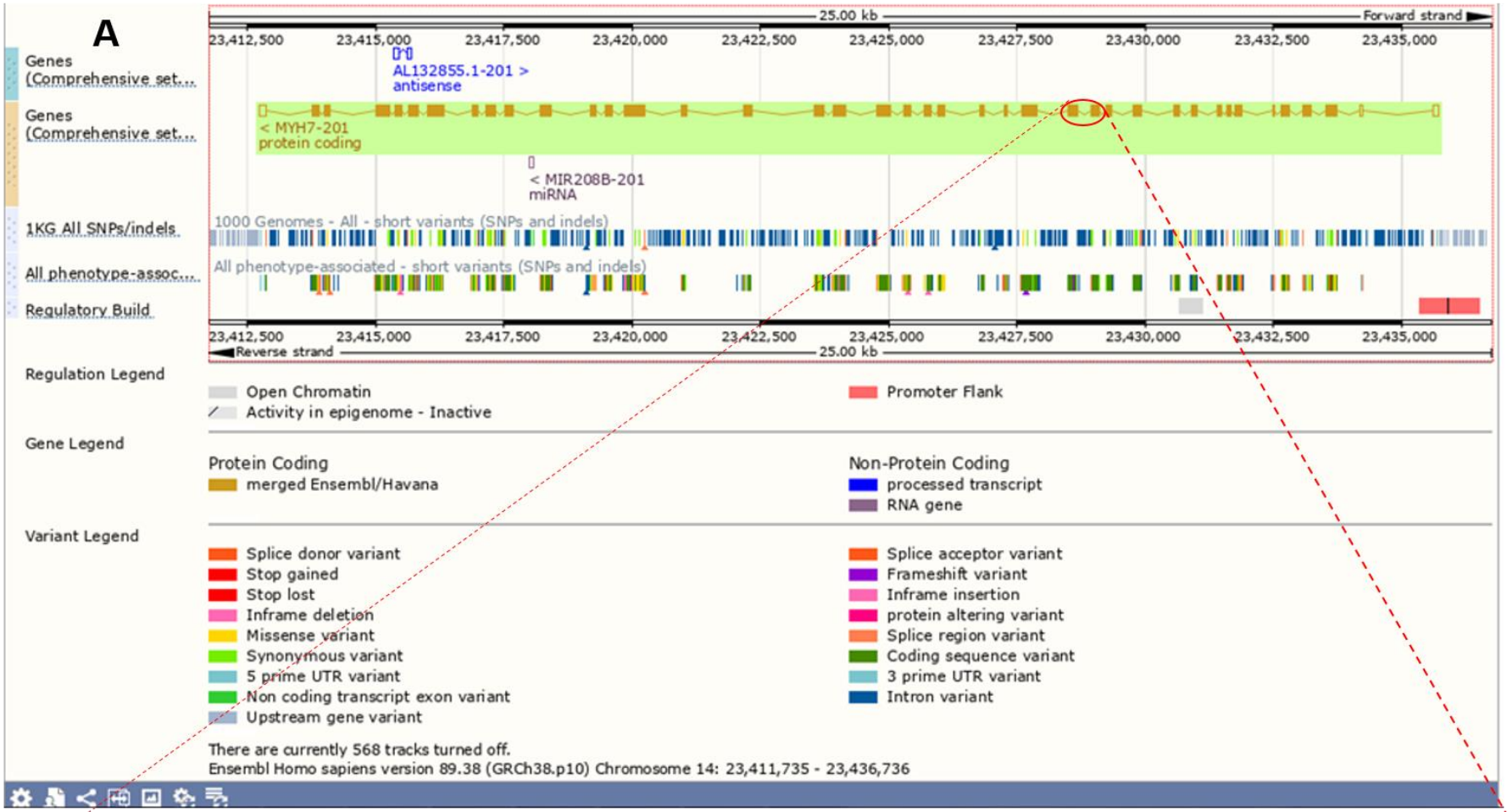
The size of the homology arms needed for successful HDR-recombination depends on the complexity of the sequence surrounding the SNP of interest. In more intricate *loci* where long repetitive elements surround the target SNP, as well as when there is a high degree of homology between the gene of interest and its off-targets, long homology arms ensure successful recombination with the donor template. This was indeed the case with targeting exon 14 of the *MYH7* gene: due to the high homology degree (>90% sequence alignment) with *MYH6* gene, shorter homology arms (100-150bp) characteristic or RNP-strategies would likely result in less successful HDR of the *MYH7* gene and potentially more off-target activity, in contrast to the 1Kb homology arms in the plasmid-based strategy.

While the observed transfection efficiencies were seemingly low (~25%), due to the use of a sub-optimal commercially available transfection reagent (GeneJammer), antibiotic selection was used to positively select edited colonies, overcoming that limitation. An alternative method to surpass low transfection efficiency is to co-express the Cas9 nickase and the gRNA construct in the same plasmid, so that both components are delivered to transfected cells simultaneously[200], as was recently shown by the successful generation of major histocompatibility complex II-knockout murine tumor cell lines[272].

Conferring antibiotic resistance to targeted hPSC clones led to efficient targeting, and the subsequent removal of the selection cassette eliminates undesired activation of endogenous genes. However, even though the exonic ORF was precisely corrected, a 280bp footprint is left in the intron upon cassette excision, with unknown effects in regulation of genetic networks. As explored in Chapter 4, *MYH7* expression was only restored upon the excision of the selection cassette, whereas the presence of the full cassette completely abrogated gene expression (resulting in a relevant MYH7-knockout line). This was corroborated in other loci, as was shown by lack of gene expression in selection-cassette targeted *KCNH2* hPSC-CMs[84].

Nevertheless, the two attB sites that compose the footprint have shown not to interfere with transcription or translation in several expression systems including mammalian cells[273], although this is dependent on the region where they lie (i.e. in case of disrupting splice junctions, regulation of gene expression may be affected). Thus, careful consideration was given to the location of the footprint in the intron during the initial strategy design. In most genes, donor and acceptor splice sites are located immediately adjacent to the exons they flank. Moreover, during the pre-mRNA synthesis, formation of intermediate structures requires 5-8 nucleotide sequences termed branching points that usually lie between 10 to 50 bp up/downstream the splice acceptor/donor sites, respectively[269]. In the strategy designed, the footprint starts 73bp downstream of the splice donor site and ends 192bp upstream of the splice acceptor site of the next exon, thus it is highly likely not interfering with RNA splicing processes and ultimately gene expression. Moreover, intronic location of the footprint is free of any gene-regulatory elements as well as annotated phenotype-associated variants (**Figure 3.11A-B**). Overall, the risk associated with the footprint inserted in the intron downstream of the R453C-MYH7 SNP is much reduced.

Alternatively, more recent footprint-free strategies exist such as the RNP-based method (described above), as well as the seamless excision of resistance cassette through transposase acting on flanking *PiggyBac* transposons[274]. However, this method has its own disadvantages such as the requirement of a TTAA site naturally occurring (or forcefully engineered) in the target locus. In addition, it also consists of a 2 step procedure resulting in additional population doublings which may lead to chromosomal instability (as seen in one of the HUES7 lines).


A
Genes (Comprehensive set...
Genes (Comprehensive set...
1KG All SNPs/indels
All phenotype-assoc...
Regulatory Build
25.00 kb
Forward strand
23,412,500
23,415,000
23,417,500
23,420,000
23,422,500
23,425,000
23,427,500
23,430,000
23,432,500
23,435,000
AL132855.1-201 > antisense
< MYH7-201 protein coding
< MIR208B-201 miRNA
1000 Genomes - All - short variants (SNPs and indels)
All phenotype-associated - short variants (SNPs and indels)
Reverse strand
Regulation Legend
Open Chromatin
Activity in epigenome - Inactive
Promoter Flank
Gene Legend
Protein Coding
merged Ensembl/Havana
Non-Protein Coding
processed transcript
RNA gene
Variant Legend
Splice donor variant
Stop gained
Stop lost
Inframe deletion
Missense variant
Synonymous variant
5 prime UTR variant
Non coding transcript exon variant
Upstream gene variant
Splice acceptor variant
Frameshift variant
Inframe insertion
protein altering variant
Splice region variant
Coding sequence variant
3 prime UTR variant
Intron variant
There are currently 568 tracks turned off.
Ensembl Homo sapiens version 89.38 (GRCh38.p10) Chromosome 14: 23,411,735 - 23,436,736

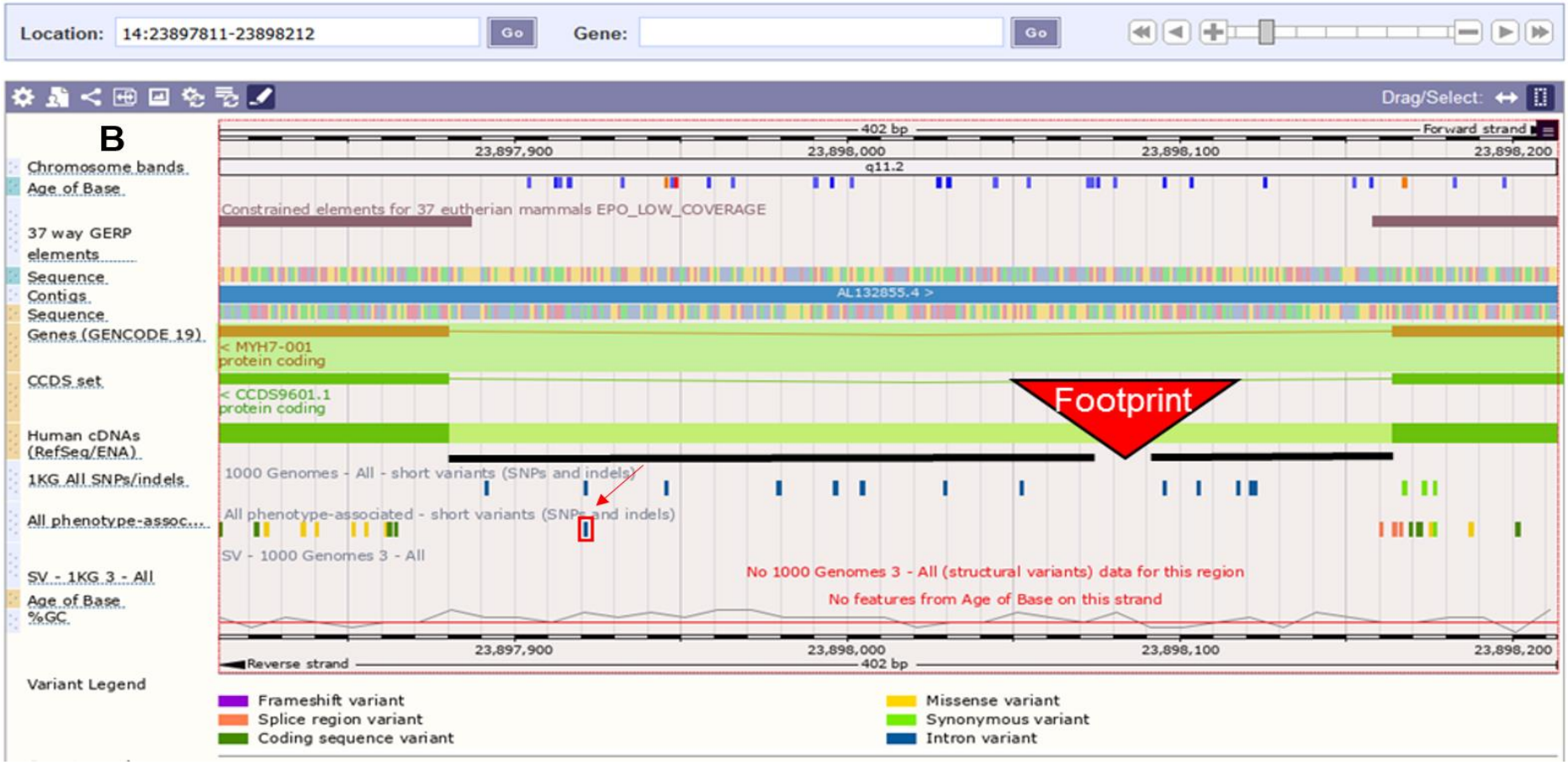


Figure 3.11 - Intronic location of the residual footprint left upon resistance cassette excision. **A)** The footprint located in the intron between exons 14 and 15 does not interfere with any annotated regulatory regions such as promoters and epigenetic modifiers (highlighted in 3.11B). **B)** Predicted splice donor and acceptor sites (located immediately down/up stream of the flanking exons, respectively) are unaffected by the footprint, as well as any known phenotype-associated intronic variants (highlighted in red box). Adapted from Ensembl genome browser.

3.3.2 Genome-editing efficiency

Selection-free methods have reported to generate HDR-editing efficiencies between 0.2 and 15% in hPSCs[270], with bi-allelic targeting being even more challenging. Herein, the targeting efficiencies achieved were approximately 35% for mono-allelic editing and 8.5% for bi-allelic targeting across three hPSC lines, while approximately 40% of positive colonies analysed also had indels in the *MYH7* locus. Thus, the editing efficiencies attained were high due to the selection procedure, but NHEJ activity was also enhanced as seen by the high frequency of indels in targeted hPSC. This urges caution as coupling successful introduction of the R453C-SNP in one allele with disruption of the other allele is undesired, justifying the allele-specific PCR-genotyping performed, so that the generated HCM models fully recapitulate physiological genotypes without any additional gene frameshifts that disrupt expression and may cause knockouts.

Moreover, chromatin packing is a known determinant of CRISPR/Cas9 editing efficiency due to lower DNA accessibility[275]. Notably, as shown in Chapter 4, the *MYH7* gene is only expressed in hPSC-cardiomyocytes and not in hPSCs, suggesting that densely packed chromatin may have hampered even higher editing efficiencies.

Lastly, in a recent study, pre-optimization of gRNAs using a lentiviral vector-based reporter assay led to Cas9 nickase efficiencies in iPSCs of 50% in monoallelic targeting, 40% bi-allelic and 10% Indels[276]. Although this is a model synthetic gene assay and not a true endogenous locus-directed targeting, it is conceivable that performing such a pre-optimization would have also led to higher targeting efficiencies in the *MYH7* locus.

3.3.3 Considerations on generated HCM lines

Disease modelling efforts rely on phenocopying pathological hallmarks *in vitro*. In cases where the disease progression is related to a strong genetic component, recapitulation of patient genotypes is a key goal. As explored in section 1.4, this is usually achieved by either reprogramming patient-derived somatic cells into a pluripotent state, followed by the correction of the causative mutation, or by introducing the pathological change in otherwise healthy (i.e WT) hPSC lines. While both strategies ensure isogenic controls are generated towards a more refined analysis of disease phenotypes, they show relative merits and disadvantages.

Using mutation-corrected patient-derived cells ensures the genetic background is preserved, which may be important to study gene modifiers, that can aggravate or attenuate the disease progression[36]. However, the establishment of genotype-phenotype relationships is usually restricted to individual patients or families, given the phenotypic complexity of HCM[14]. Alternatively, provided there is enough evidence indicating the causation of the genetic mutation, introduction of the pathological change (“knock-in”) in several unrelated healthy hPSC lines provides a more statistically robust platform to model the disease. In addition, the

role of gene modifiers may also be studied by looking at the relationship between disparate genetic backgrounds/ transcriptomes[6] and the resulting clinical outcome, which is masked by restricting the study to closely related family members.

From a technical perspective, gene-editing patient-derived hPSCs encompasses an additional methodological step - reprogramming of several somatic cell lines, whereas gene-editing healthy hPSC takes advantage of previously characterised lines. In addition, gene targeting is more efficient in healhy hPSC lines as both alleles are equal (hence gRNA design is simplified). This also facilitates the generation of homozygous mutants, as shown herein. Conversely, patient-derived hPSC bear heterozygous mutations that require allele-specific gRNA design and targeting, typically less efficient and requiring time-consuming optimisation steps[208].

Using the plasmid-based CRISPR/Cas9 genome editing system, a total of 8 new cell lines were generated from the three initially healthy (WT) independent hPSC lines. The trio MYH7-WT, heterozygous MYH7-R453C and homozygous MYH7-R453C across three completely unrelated cell lines provides a compelling platform for modeling HCM in the hPSC-derived cardiomyocytes, as it enables more robust genotype-phenotype correlations.

While HCM is closely linked to the heterozygote MYH7-R453C mutation, having a homozygote variant may also provide greater insight on the molecular mechanisms of the disease, possibly acting in a surrogate “dose-response” manner. However, due to the genomic instability of the homozygous HUES7 line, only the iPSC lines will be functionally phenotyped (Chapter 5) while the hESC line will be used as a validation tool for most of the molecular analyses (Chapter 4).

The MYH7 knockout line is also a useful control for modeling HCM as it provides a complete abrogation of the β-MHC protein, elucidating its activity in human hPSC-cardiomyocytes. Finally, the MYH7-R453C homozygous line with the MYH6 frameshift mutation (off-target) is also an interesting line to phenotype, as cases where a hybrid α/β-MHC protein formed by non-homologous pairing between *MYH6* and *MYH7* genes followed by an unequal crossover have also been reported in patients[277].

4. High-throughput phenotyping of R453C-MYH7 hPSC-derived cardiomyocytes

4.1 Introduction

4.1.1 Monolayer cardiac differentiation of hPSC

Modeling cardiac pathologies relies on recapitulating clinical phenotypes *in vitro*. In order to investigate those phenotypes, the relevant cell type must be generated. As mutations in the *MYH7* gene are mostly associated with cardiomyocyte alterations, an efficient cardiac differentiation protocol must be applied to the gene-edited hPSC previously developed. As explored in Chapter 1.3.3, many protocols exist that aim to recreate the developmental cues exerted in the embryo. In this thesis, a monolayer-based cardiac differentiation protocol was used in order to produce the large numbers of cardiomyocytes required for phenotyping HCM *in vitro*. The protocol used can be considered a hybrid between several published methodologies as it involved: **i)** stable culture of hPSC adhered onto MT in E8 medium [109] **ii)** MT overlay step to promote EMT[132], **iii)** mesoderm induction via activation of WNT signaling by GFs (ActA and BMP-4)[131] and **iv)** cardiac specification via SM inhibition of the WNT pathway (via KY02111 and XAV939)[134] – **Figure 4.2A**. The herein protocol has previously shown to consistently produce >90% α-actinin^{+} cardiomyocyte cultures in 12 days, across over 10 hPSC lines (including the three starting hPSC lines used in this work). Moreover, cardiomyocytes produced were reported to be prevalently ventricular (~80% MLC2v^{+}) and their proportion increases with time in culture (George and Hoang, in submission). Further dissociation of beating sheets using a collagenase-based protocol[139] enabled subsequent phenotypic analysis at single cell and dense monolayer level.

4.1.2 Sarcomeric gene expression in HCM

As explored in the Introduction, the cellular response to cardiac hypertrophy is multifaceted, involving changes in gene expression that reflect differences in contractility and myocyte morphology. In this regard, a switch from fast α-MHC towards slow β-MHC expression upon heart failure has been well documented in rats (decrease in α-MHC protein from 93-97% to 22-71% and increase in β-MHC from 3-6% to 29-78%)[278]. The same is true in the human myocardium, but on a much smaller magnitude, as the protein fraction of α-MHC over both myosin heavy chains decreases from 7.2±3.2% to 0.075±0.24%, determined by western blot[279]. This change results in slower cross-bridging kinetics as seen by the reduction of unloaded shortening velocities from 0.72 +/- 0.09 Lmax/sec in human healthy cardiac muscle fibers to 0.41 +/- 0.06 Lmax/sec in myopathic muscles[41].

Furthermore, changes in the expression of sarcomeric genes in septal myectomy specimens derived from HCM patients have also been reported, such as in those bearing one of several variants of *MYBPC3 or MYH7* mutations[280]. Firstly, the ratio of mutant/wild type transcripts was ~1:5 in truncating *MYBPC3* mutations but ~1:1 in missense *MYBPC3* mutations. Interestingly, unlike in healthy hearts, HCM patient biopsies showed variable *MYBPC3 and MYH7* transcript abundances, and mutations in one of the sarcomeric genes caused changes in the transcription of the other one (e.g *MYBPC3* mutations caused up to ~7-fold increase in *MYH7* transcription). Remarkably, HCM hearts from *MYH7* mutant patients showed an average ~57% increase in the MYBPC3 protein level in comparison to healthy hearts, depending on the mutation site. These observations strongly indicate that HCM causes changes in sarcomeric gene expression and that variations in the expression of a single gene can cause drastic alterations in the expression of other genes in HCM hearts. Finally, heterozygous missense mutations in sarcomeric genes have been shown to affect the ratio of mutant to wild-type allele expression, ranging from 30%-84% in *MYBPC3* mutant hearts[280] to ~25-70% in MYH7 mutant ventricles[281], depending on the mutation site. Collectively, these findings highlight the complexity of the regulation of sarcomeric gene expression networks in HCM, justifying a similar analysis in the gene edited hPSC-CM models developed in this thesis.

4.1.3 Assessing hypertrophy

One of the hallmarks of HCM is the increased cardiomyocyte size, also termed hypertrophy. As *in vitro* models of HCM rely on 2D culture of cardiomyocytes, cell area analysis of gene-edited hPSC-CMs is warranted. However, several culture conditions were reported to affect cell area, such as substrate properties, time in culture and serum supplementation. NRVMs cultured in collagen-coated polyacrylamide gels showed different aspect ratios depending on the stiffness of the surface (from ~1.35 in 3KPa surfaces up to 4.3 in 22-50Kpa substrates)[282]. In addition, Engler and colleagues[170] reported variations in cell area ranging from ~800 μm^2 up to ~1600 μm^2 in 10-day-old quail embryonic myocardium cardiomyocytes seeded onto collagen I-coated polyacrylamide gels with different stiffness. Importantly, in hPSC-CMs, serum supplementation has shown to be a major determinant of cell area, resulting in increases of up to ~3-fold versus cardiomyocytes without exposure to serum[283]. This finding is of utmost importance, as healthy hPSC-CM cultured in 5 or 20% serum conditions have shown cell areas even greater than those of HCM patient-derived hiPSC-CMs, strongly indicating that serum supplementation is masking the hypertrophic readout in the form of cell area.

Consequently, while changes in cell area in cardiomyocytes derived from HCM patients have previously been reported[284] and are therefore accepted in the field, measurement of cell volume offers a better strategy to estimate hypertrophy *in vitro* as the artefacts resulting from 2D culture conditions in cell area readouts are minimized. This is because changes in cell

area may affect the length/width of a cardiomyocyte while adjusting thickness (and thus maintaining the overall volume), whereas variations in volume are more representative of a true *in vivo* hypertrophic state. While volumetric analysis is possible using histological methods[285] or scanning ion conductance microscopy[286] such procedures are time-consuming and not amenable to a high-throughput format. As such, a flow cytometry method was developed by Tzur et al[263] based on different light scattering properties according to the cell size, in several immortalised murine and human cell lines. In this thesis, this method was adapted to hPSC-CMs, by comparing their forward scatter signal of emitted light to that of (calibration) beads of known size, resulting in estimations of cardiomyocyte volume measurements that could be compared between the different gene edited lines.

4.1.4 Multinucleation and polyploidy in HCM

An increase in the proportion of multinucleated cardiomyocytes in hypertrophied hearts has been the subject of investigation for several decades. The first report dates from 1973, consisting on the quantification of the number of nuclei per myocyte in autopsied human hearts by light microscopical morphometry of sliced cardiac tissues, showing that the percentage of bi-nucleated cardiomyocytes increased from 13.5% in normal hearts to 28.7% in severely hypertrophic hearts[287]. About 20 years later, Vliegen and colleagues have performed a similar study by dividing human hearts according to indexed weight between normal, moderate and severely hypertrophied[288]. Based on regression analysis, it was reported that a doubling of indexed heart weight was associated with an increase in multinucleation by 7% - as the mean number of nuclei per myocyte increased from 1.16±0.05 in normal hearts to 1.32±0.10 in severely hypertrophied hearts. However, a contradictory report has been published afterwards showing no statistically significant difference in the fraction of mono-nucleated and bi-nucleated cardiomyocytes in healthy vs hypertrophied hearts (74±8% and 25.5±8% vs 75±8% and 24±7, respectively)[289]. It should be noted, however, that in all these studies, HCM was classified based on the weight of hearts post-mortem, and no genetic profiling was performed, which may lead to pooling hearts bearing different forms of HCM and thus including confounding variables. Conversely, a disease model based on iPSC-CM bearing R663H-MYH7 mutation showed an increased frequency of multinucleation (48.3±8.7%) relative to their healthy iPSC-CMs (22.1±3.4%)[161], from manual nuclei/cell count in fluorescent micrographs.

Furthermore, increase of polyploidy (number of chromosome pairs) in HCM hearts has been reported (from 4-10c in healthy hearts to 15-20c in diseased hearts, where c is the haploid DNA content), as assessed by DNA cytophotometry[290]. Moreover, increase in multinucleation and polyploidy in response to pathological cues other than HCM has been thoroughly described, as in the outcome of myocardial infarction (MI) [291]. Thus, despite not being able to proliferate at a rate required for cell renewal (turnover rates have been reported to be below 1% in human adults[292]), cardiomyocytes can still synthesize DNA and undergo

mitosis under pathological conditions, suggesting that this may constitute an adaptive response to additional metabolic and/or biophysical stress, such as HCM or MI[293]. In this regard, Anatskaya and Vinogradov have employed a comparative genome-scale analysis approach to identify ploidy-responsive genes in the human heart, showing that there is a shift in the expression of several genes involved in cardiac contraction (from fast α to slow β-MHC), and ATP-synthesis (e.g.acetyl-coenzyme A synthetase 2), enhancing stress protection by driving CMs to energy saving mode[294]. However, this response may only provide short-term benefit but may prove to be a liability as polyploid cells have shown to have less stable genomes[295].

Overall, evaluation of multinucleation in HCM warrants further investigation in developed *in vitro* models due to its potential role as part of an adaptive response to the disease progression.

4.1.5 Natriuretic peptides as markers and regulators of HCM

Phenotyping HCM in hPSC-CMs and the manifold effects of several compounds requires the validation of high throughput platforms. Thus, establishing simple and quick assays to quantify hypertrophy is of paramount importance, especially when several cell lines and treatments amount to tens of different conditions to investigate. As previously discussed, the myocardium adapts to increased workloads through the hypertrophy of individual muscle cells (i.e increase in cardiomyocyte volume and protein content)[296]. Moreover, expression of various genes is triggered upon hypertrophic response, such as those encoding natriuretic peptides that play a major role in regulating cardiovascular homeostasis[297], like ANP and BNP. Consequently, plasma ANP/BNP levels are used as a clinical diagnostics tool as these were shown to be found to be increased to levels more than 100-fold above normal in the failing heart[298].

Remarkably, besides serving as surrogate markers for cardiac hypertrophy, ANP and BNP were found to regulate cardiovascular homeostasis upon hypertrophy, which was further corroborated by the expression of their receptors in non-myocyte and myocyte cell types in the heart[299]. For instance, treatment of neonatal rat cardiac fibroblasts with ANP resulted in ~20% lower rates of bFGF-induced [^{3}H] thymidine incorporation, indicating inhibition of cell proliferation[300]. In addition, genetic mice models of *Nppb* (encoding BNP) knockout resulted in a 3-fold increase in interstitial fibrosis in the heart upon ventricular pressure overload[301], establishing BNP as an anti-fibrotic factor. Additionally, BNP was shown to be produced in adult canine cardiac fibroblasts (at 11.2±1.0 pg/10^5 cells per 48 h) and acted to supress collagen production (as [^{3}H] proline incorporation into the cells was 29% lower in BNP-supplemented cultures) and increase metalloproteinase activity (30% higher MMP-2 abundance)[302]. Interestingly, cardiomyocytes were shown to react to BNP signalling upon cardiac hypertrophy by the expression of several genes encoding contractile (e.g. cardiac actin) and non-contractile components (e.g ANP), thus coordinating a response to the

pathological aggression, leading to changes in cardiomyocyte cell size, and actin cytoskeleton rearrangement[297].

Furthermore, mechanical loading was shown to promote BNP expression in ventricular cardiomyocytes in various rat models of acute or chronic stretch of the ventricular wall[303]. This stretch-induced BNP expression is mediated by non-cardiomyocytes (e.g. endothelial cells) that mechanotransduce the physical stimulus into a biochemical response by the secretion of chemical mediators. For instance, when bovine endothelial cells are stretched, Endothelin-1 (ET1) is rapidly released into the medium (within 20 minutes)[304]. ET1 was also detected in medium conditioned by rat non-cardiomyocytes and its effects on co-cultured rat cardiomyocytes (increase of ANP and BNP production by ~3-fold) were blocked by ET1 receptor antagonist Bosentan[305]. More recently, ET1 treatment of iPSC-CM was reported to increase BNP expression by ~12-fold relative to untreated cultures[228]. Notably, cardiomyocytes secrete BNP into the extracellular medium[306], thus contributing to the cross-talk with non-cardiomyocytes, based on paracrine and autocrine BNP-mediated signalling mechanisms.

Taken together, the existing literature clearly demonstrates that expression of BNP in cardiomyocytes is triggered under hypertrophic conditions via mechanically-induced production of chemical mediators such as ET1 (or even BNP itself), from non-cardiomyocytes present in the *milieu*.

4.1.6 Sarcomeric disorganisation

As discussed above, expression of sarcomeric genes is severely affected during HCM, causing changes in cardiomyocyte contractility[41]. Thus, evaluation of sarcomeric structure of HCM cardiomyocytes provides insight into the underlying phenotypic alterations in cardiac contractility. In that regard, Tanaka et al[160] have investigated myofibrillar disarray in hiPSC-CMs derived from three HCM patients showing an increased percentage of cardiomyocytes exhibiting disorganised sarcomeres (~9%) in comparison to healthy cardiomyocytes (~5%), which was further aggravated by treatment with ET1 (reaching ~20%). Likewise, electron microscopy analysis of R723G-MYH7 skinned myofibres revealed Z-disc irregularities and considerable reduction in the myofibril density (~26% lower) compared to healthy tissues, coincident with reduced active force (23.8±1.7 kN/m^2 vs 34.7±3.8 kN/m^2 in healthy controls)[307]. These examples not only show that changes in sarcomeric structure are closely associated with HCM phenotypes but may also be intrinsically connected with cardiac contractility alterations. However, electron microscopy analysis is not feasible when evaluation of multiple genetic variants is required, justifying the high content imaging procedure performed in this thesis.

4.1.7 High-content imaging analysis as a phenotyping tool

In this chapter, several hallmarks of HCM were reviewed as well as assays to evaluate them. An initial phase of phenotypic screening the gene-edited lines developed would be useful to tailor more focused (functional) experiments downstream and could accelerate the efforts towards a deeper understanding of this genetic cardiac disease. As such, high-throughput methods to investigate the hypertrophic response of hPSC-CMs to the introduction of the R453C-MYH7 mutation were developed (**Figure 4.1**). High-content imaging platforms offer the possibility of investigating tens of conditions/ cell lines in the same 96-multiwell plate, compatible with Operetta™ confocal plate imaging systems[84,308].

Assays based on immunofluorescent labelling of hPSC-CMs can therefore be developed to determine changes in several parameters of HCM, as previously developed in the BNP quantification assay[228]. Therefore, several high content imaging assays were developed for the purpose of phenotyping HCM in this thesis, namely: **i)** cardiomyocyte purity, **ii)** multi-nucleation analysis, **iii)** adaptation of the BNP assay, and **iv)** analysis of sarcomeric structure. The algorithms designed for each of these assays are presented in the Results section of this chapter, and were optimized to include enough sensitivity in order to distinguish between the measured classes in each assay (e.g. multinucleated vs mono-nucleated cells, or BNP negative vs BNP positive cardiomyocytes). Thus, signal thresholding to relevant controls (often fibroblasts) was performed so as to confer to the assays additional robustness.

However, it should be noted that these assays provide higher sampling power at the cost of resolution. That is effectively the case when analysing complex structural analysis, such as sarcomeric structure, without resorting to powerful electron microscopy techniques. Finally, flow cytometry analysis is useful to estimate (rather than accurately measure) cardiomyocyte volume associated with each genotype. The limitations inherent to these approaches should therefore be considered and will be explored in the Discussion section of this chapter.

4.1.8 Chapter aims and objectives

In the previous chapter, generation of R453C-MYH7 mutant hPSC lines by CRISPR/Cas9 gene-editing was described. This chapter is focused on generating cardiomyocytes from each of these lines and to perform molecular phenotyping associated with structural aspects of HCM, mainly in terms of **i)** *MYH7* expression, **ii)** hypertrophy, **iii)** multi-nucleation, **iv)** BNP hypertrophic marker expression, and **v)** sarcomeric structure.

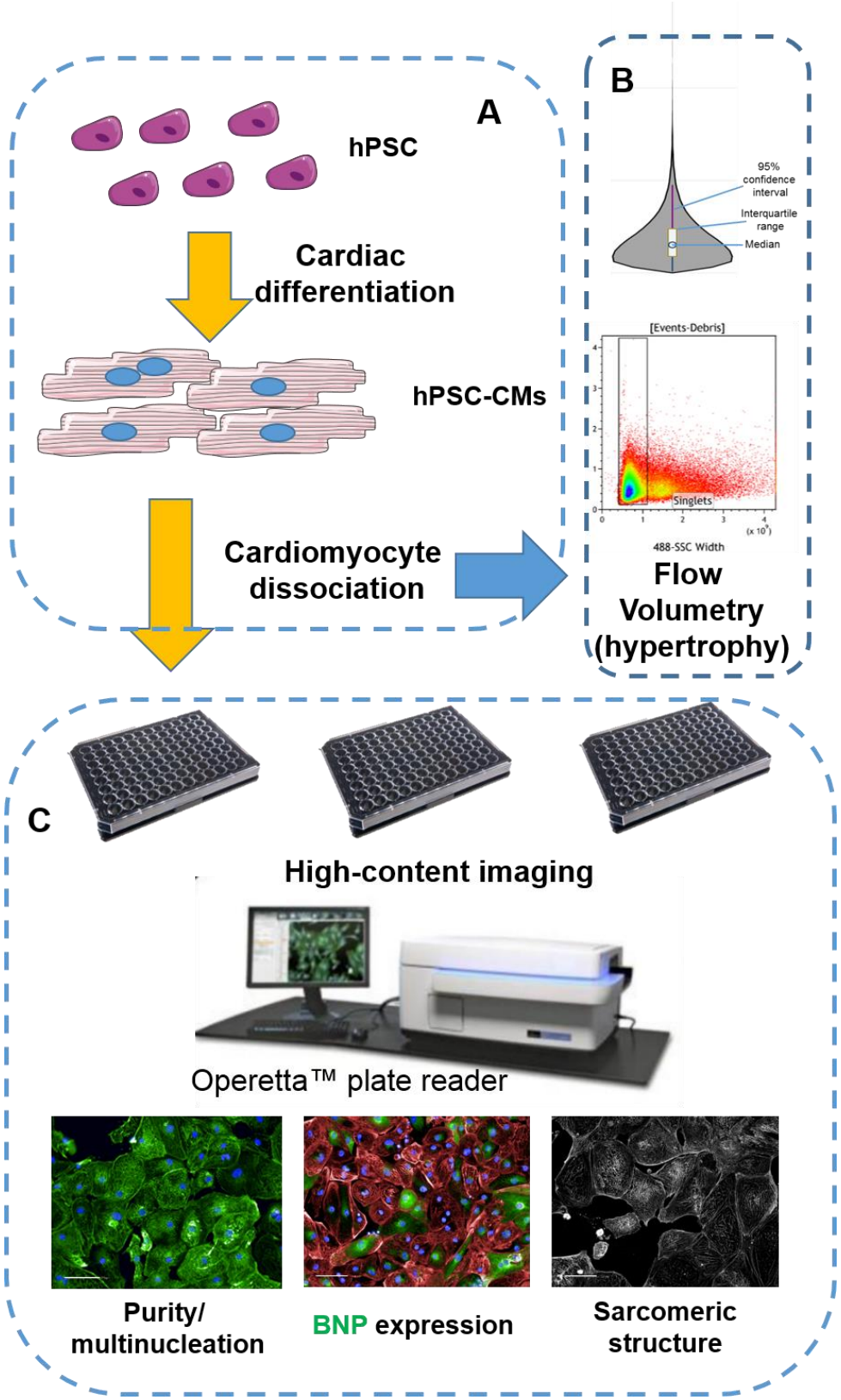


Figure 4.1 - High-throughput phenotyping of R453C-MYH7 lines generated. A) hPSC were differentiated into cardiomyocytes using a monolayer method. **B)** hPSC-CMs were dissociated and estimation of cardiomyocyte volume was performed by flow cytometry to assess hypertrophy (reported as violin plots). **C)** hPSC-CMs were seeded in 96-well plates and immunocytochemistry was done to quantify: **i)** purity, **ii)** multinucleation, **iii)** BNP expression, and **iv)** sarcomeric structure.

4.2 Results

4.2.1 Cardiac differentiation of gene-edited hPSC

As HCM is a cardiac disease, generation of the relevant cardiac muscle cell type is mandatory in order to establish *in vitro* disease models. A monolayer-based cardiac differentiation protocol was applied to the gene-edited hPSC lines in order to produce cardiomyocytes (**Fig 4.2A**). This protocol was designed to recapitulate developmental stages of cardiogenesis by modulating the WNT signalling pathway, in order to drive hPSCs through mesodermal lineages and subsequent specification in cardiac progenitors, resulting in terminally differentiated cardiomyocytes. Expression of cardiac-specific sarcomeric protein α-actinin was confirmed in hPSC-CMs by immunocytochemistry (**Fig 4.2B**), in contrast to a negative cell-type control (fibroblasts).

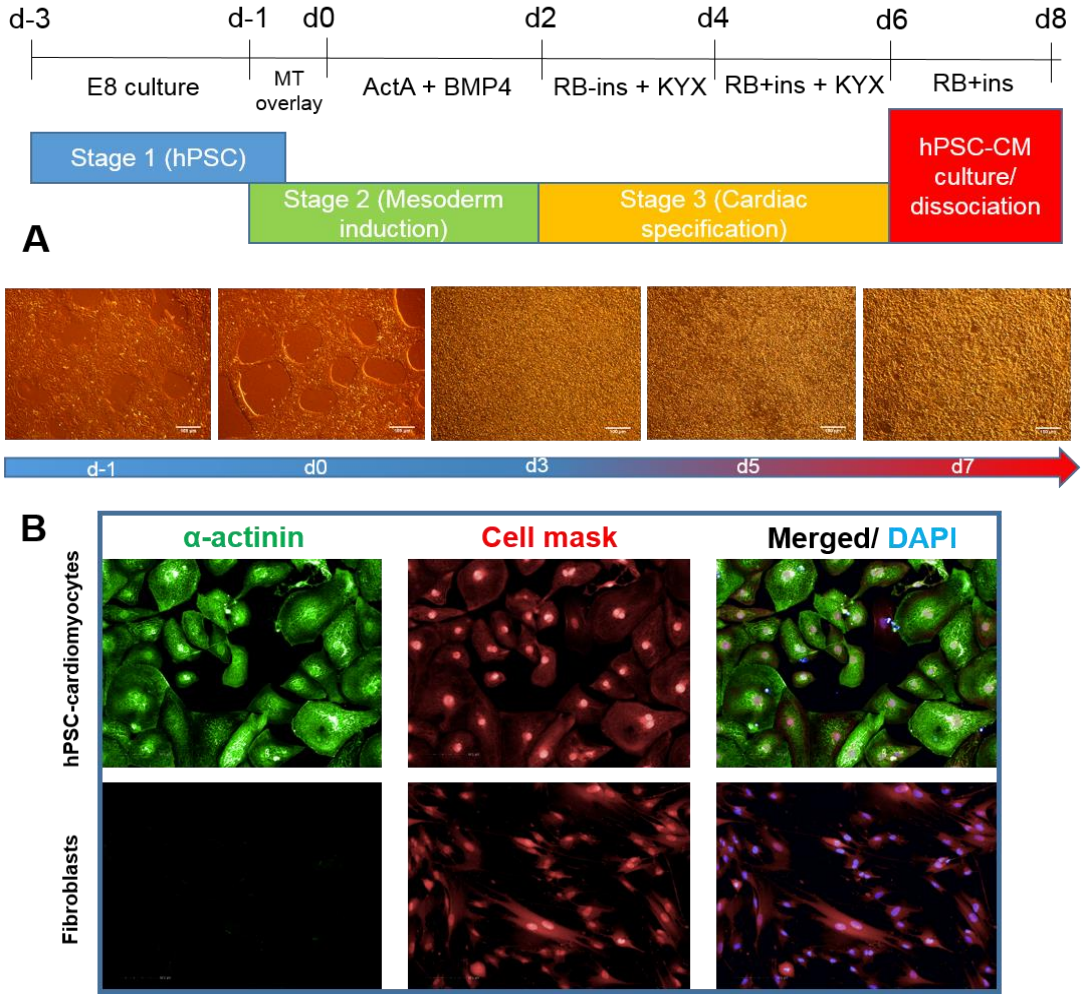


Figure 4.2 - Cardiac differentiation of gene-edited hPSC. A) Monolayer cardiac differentiation protocol overview. A matrigel overlay was applied to E8-cultured hPSCs, followed by Wnt pathway activation (Stage 2) and inhibition (Stage 3), resulting in beating sheets of hPSC-CMs 8-12 days after the differentiation started. **B)** Representative fluorescence micrographs of cardiac α-actinin imunostained hPSC-cardiomyocytes and fibroblast controls, using a cell mask and DAPI as counterstains. Scale bar=100μm

An imaging algorithm was then developed to quantify the percentage of cardiomyocytes in the differentiated hPSC culture (cardiomyocyte purity), by identifying cell nuclei and cytoplasm, quantifying α-actinin signal intensity in the cell and determining positive staining in comparison to fibroblasts as negative controls (**Fig4.3A**). Applying the cardiac differentiation protocol to the gene-edited hPSC resulted in cardiomyocyte cultures showing >90% purities (**Fig4.3B**), thus enabling phenotyping of the cardiac disease that constitutes the focus of this thesis.

4.2.2 Expression of *MYH7* gene in hPSC-CMs

In order to characterise hPSC-CMs produced from the gene-edited lines, expression of the *MYH7* gene was evaluated. Semi-quantitative RT-PCR analysis showed that all the gene-edited hPSC-CMs where the selection cassette has been excised expressed *MYH7* gene, contrasting with the line which had drug resistance cassettes in both alleles of the *MYH7* locus, resulting in MYH7 knockout (**Fig4.4A**). In addition, undifferentiated hPSC did not show expression of this cardiac gene.

In order to check if the 280bp residual footprint left in the intron of the *MYH7* locus due to the targeting strategy affected gene expression, a more rigorous quantitative TaqMan® qRT-PCR was performed. Although this experiment needs additional repeats, *MYH7* expression showed an increased trend between gene-edited and untargeted (WT) lines (except for the MYH7$^{-/-}$ line), achieving statistical significance in AT1 R453C-heterozygous cardiomyocytes (**Fig 4.4B)**. Further analysis of *MYH7* expression at the protein level was performed by immunostaining hPSC-CMs, corroborating RT-PCR data as all the gene-edited hPSC-CMs displayed β-MHC signal, except for the knockout line (**Fig4.5**).

Next, allele-specific expression of the targeted locus was analysed. While the preferred method to perform this analysis is typically qRT-PCR, the complete homology between *MYH7* and *MYH6* genes in the region of the inserted SNPs prevents its application (**Fig 4.6A**). Thus, a unique restriction site (XhoI) was identified in the mutant, but not the unedited wild-type, allele (**Fig 4.6B**), resulting from the PAM site silent mutation previously inserted, thus enabling allele-specific expression analysis by band densitometry. XhoI-digestion of RT-PCR amplified *MYH7* gene resulted in complete cleavage of products from homozygous R453C-MYH7 hPSC-CMs, and no digestion of wild-type hPSC-CM *MYH7* product (**Fig4.7A**), validating the sensitivity of this method. Estimation of partially-digested products from heterozygous R453C-MYH7 hPSC-CMs by band densitometry resulted in ratios of MUT/WT allele ranging from 25% in HUES7 cardiomyocytes up to 60% in AT1 cardiomyocytes (**Fig4.7B**).

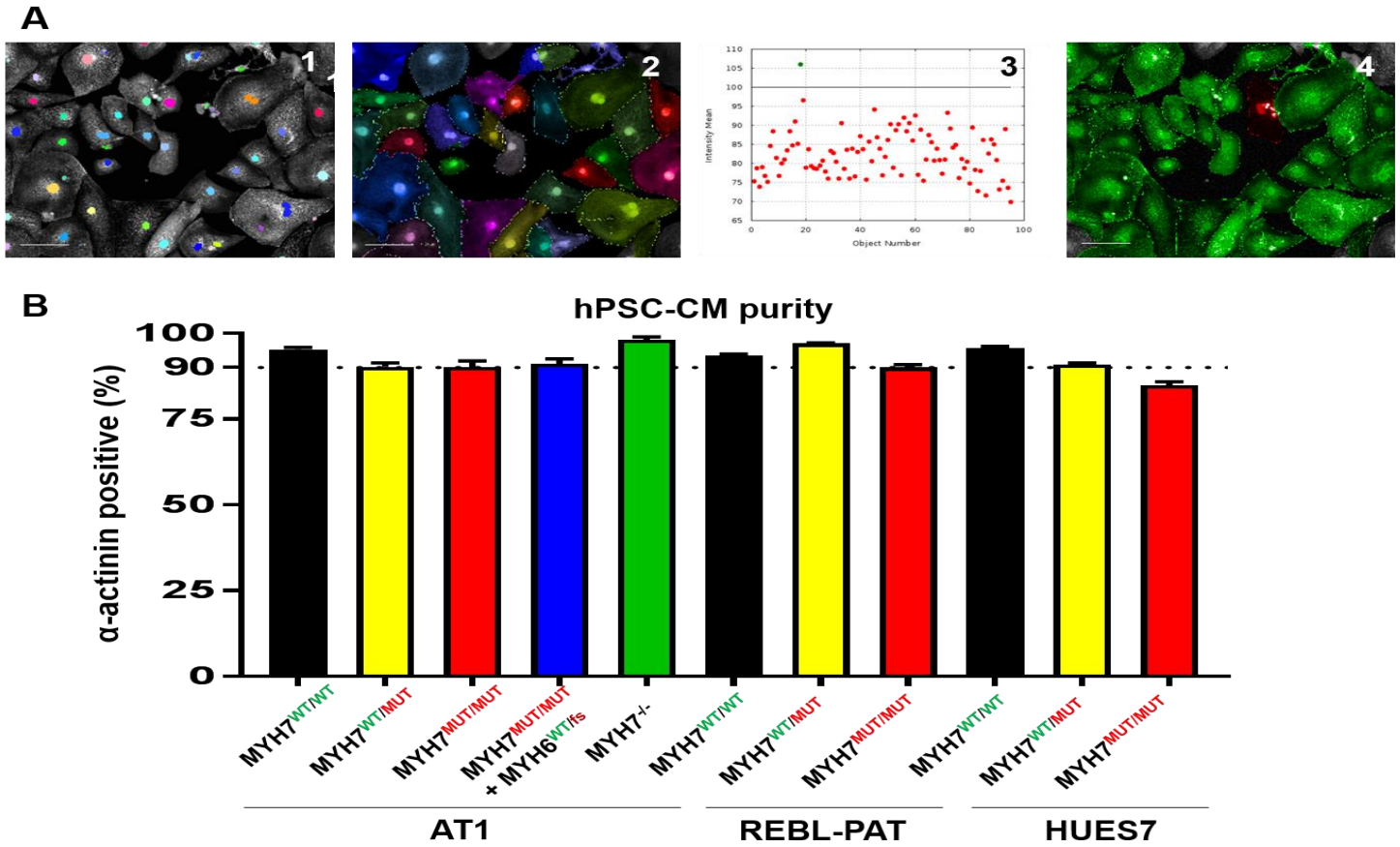


Figure 4.3 - Determination of hPSC-CM purity by high-content imaging. **A)** Algorithm to quantify purity of imunostained hPSC-CMs (using field-of-view from Figure 4.2B): 1) find nuclei using DAPI stain; 2) find cytoplasm using cell mask stain and measure α-actinin signal intensity ; 3) apply a previously determined signal threshold using stained fibroblasts (negative control); 4) count cardiomyocytes (green) and non-cardiomyocytes (red). **B)** Purity of gene-edited hPSC-CM lines showed successful differentiation with >90% α-actinin^{+} cells, N=8, scale bar = 100µm.

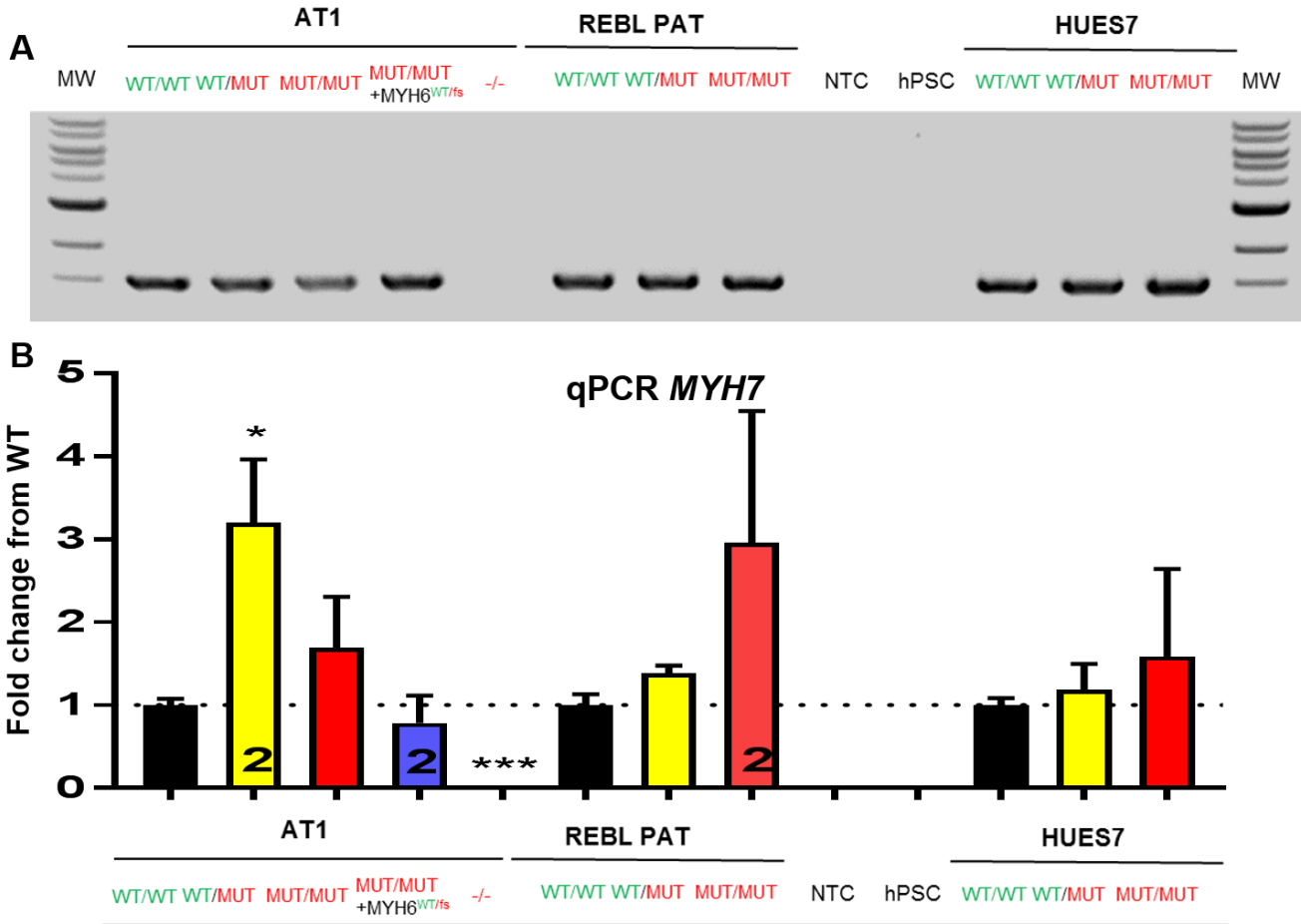


Figure 4.4 - Expression of MYH7 gene in hPSC-CMs. A) RT-PCR analysis showing expression of *MYH7* gene in gene-edited hPSC-CMs, except for the MYH7 knockout AT1 line. **B)** qRT-PCR analysis showed in increasing trend in MYH7 expression in gene-edited lines relative to isogenic controls, achieving statistical significance in AT1 lines. (N=3, unless stated otherwise, *p<0.05, ***p<0.001).

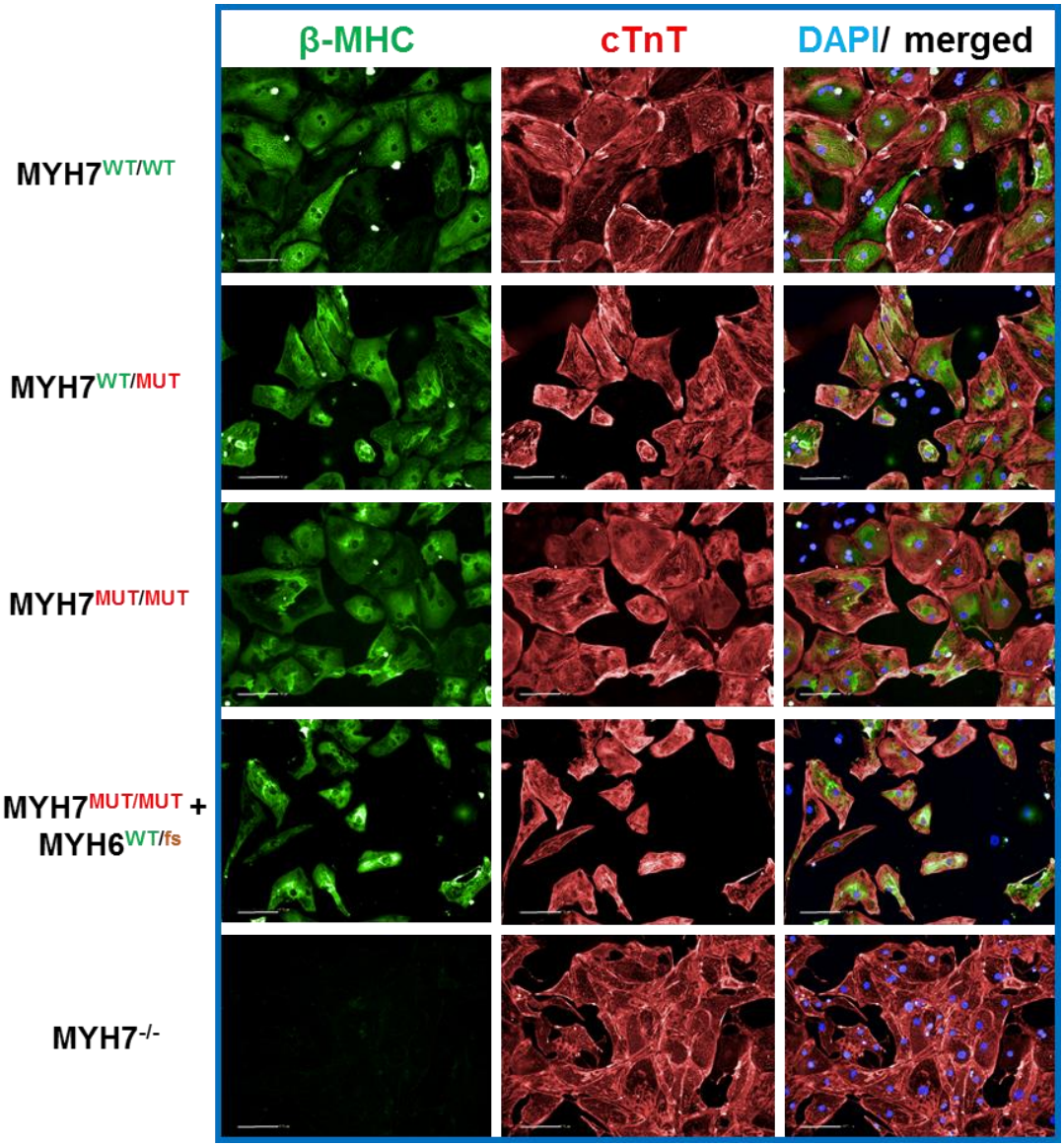


Figure 4.5 - β-MHC expression in gene-edited hPSC-CMs. Representative fluorescence micrographs of AT1-CMs co-stained for β-MHC, cardiac troponin T and DAPI, confirming protein expression of the MYH7 gene in cardiomyocytes, with the exception of the knockout line. Scale bar = 100µm.

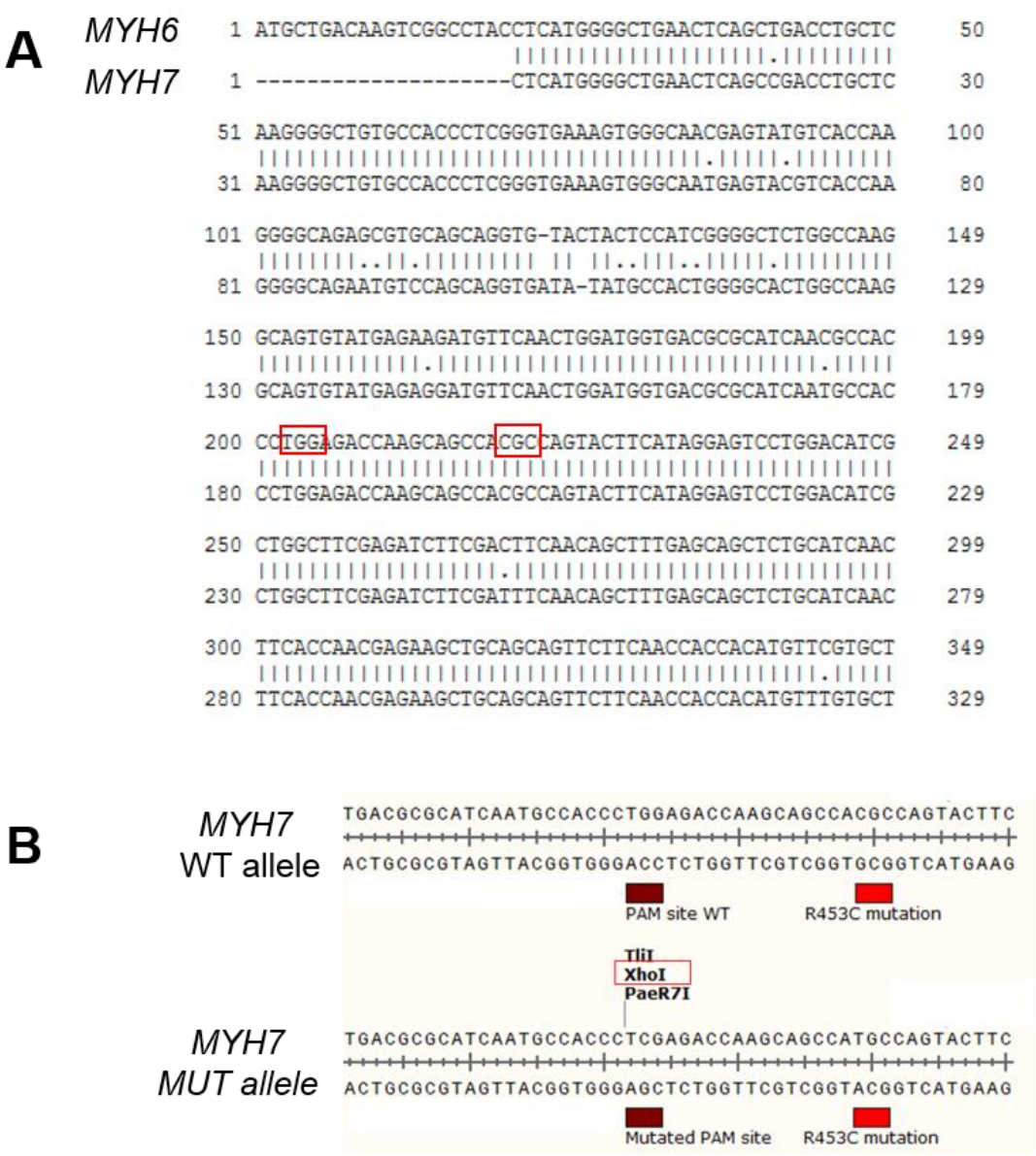


Figure 4.6 - Allele-specific expression of the MYH7 gene. A) Sequence alignment between *MYH6* and *MYH7* genes shows perfect homology in mutation sites (highlighted), **B)** making XhoI digestion as the preferred method to distinguish between WT and mutant alleles.

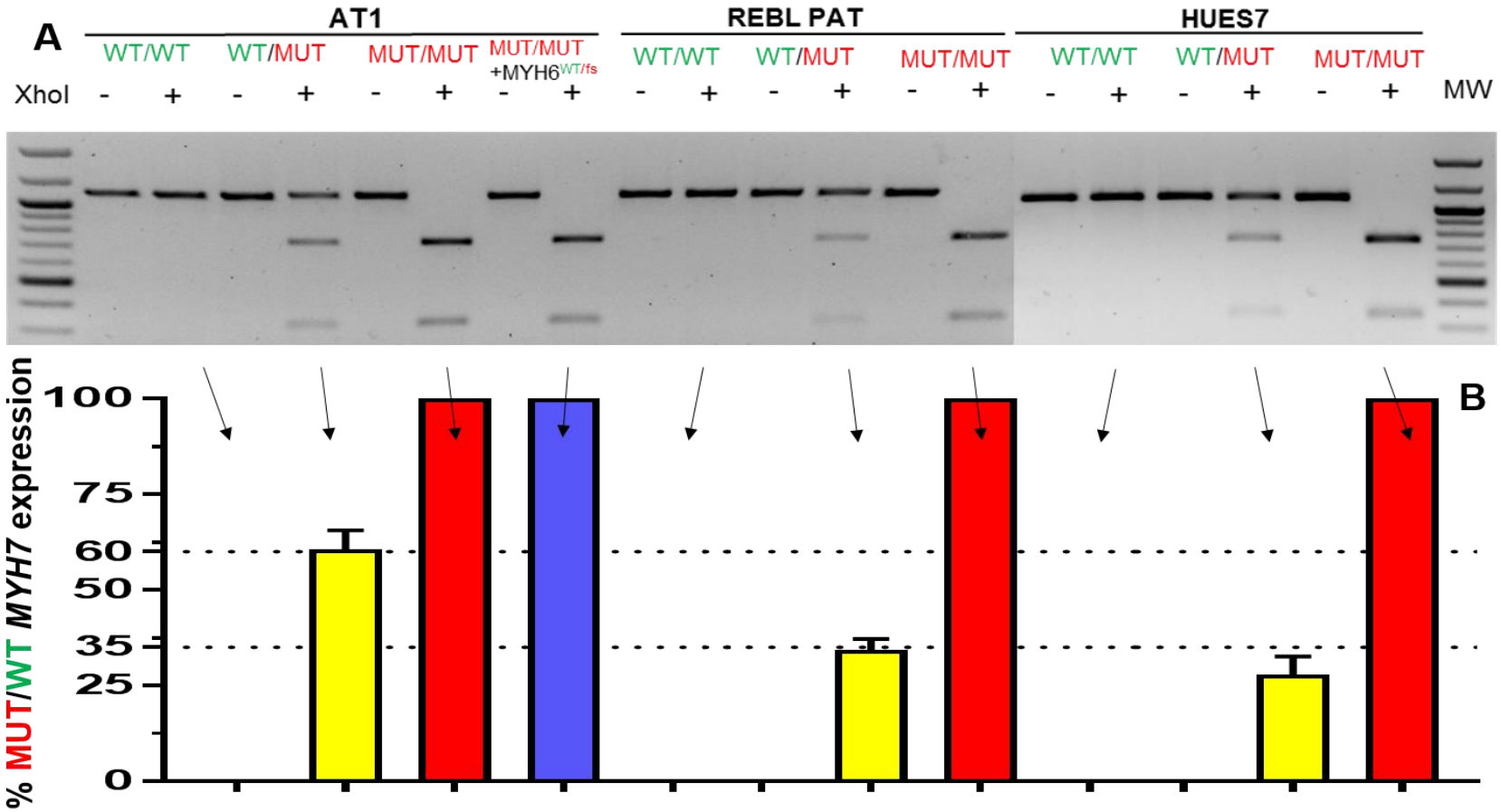


Figure 4.7 - Analysis of allelic expression of the *MYH7* gene A) XhoI-digestion of RT-PCR amplified MYH7 gene resulted in no digestion in WT hPSC-CMs, complete digestion in MYH7-R543C homozygous mutants, and partial digestion in products derived from heterozygous cell lines. **B)** Band densitometry analysis of A) shows that the ratio between MUT and WT MYH7 alleles in heterozygote lines range from 25% in HUES7 lines up to 60% in AT1 lines (N=4).

4.2.3 Hypertrophy analysis of gene-edited hPSC-CMs

Estimation of cell volume as a measurement of hypertrophy was performed by flow cytometry. Forward scatter (FSC) of calibration beads with known sizes was determined in order to establish a calibration curve (**Figure 4.8)**. Thereafter, hPSC-CM size was determined and cardiomyocyte volume was calculated using the formula of a perfect sphere (as an approximation of dissociated cardiomyocytes in suspension). Violin plots of cardiomyocyte volume (**Figure 4.9)** show an increase in the cell volume median of gene-edited lines (approximately 34-51% higher in AT1, 14-35% higher in REBL-PAT and 12% higher in heterozygous R453C-MYH7 HUES7) and first quartile metric (22-51% higher in AT1, 15-28% in REBL PAT and 13% in HUES7) in comparison to their respective isogenic controls, with the exception of the karyotypically abnormal HUES7 R453C-MYH7 homozygote line.

4.2.4 Multinucleation analysis of HCM lines

Evaluation of multinucleation in gene-edited hPSC-CMs was performed by high-content imaging, as it is a hallmark of HCM. A simple imaging algorithm was developed to enable distinction between mono-, bi- and multi-nucleated cardiomyocytes, based on the relative proximity of DAPI-stained nuclei (**Fig4.10)**. Interestingly, only the heterozygote R453C-MYH7 lines showed an increase in bi- and multi-nucleated cardiomyocytes relative to their respective isogenic control (**Fig 4.11**), across all the three initial cell lines edited. *MYH7*- mutant lines showed an increase in the percentage of bi- and multi-nucleated cardiomyocytes of 2.1% and 3.6%, 1.9% and 1.3%, and 1.1% and 1.9% in comparison to their isogenic AT1, REBL PAT and HUES7 lines, respectively (**Fig4.11B**).

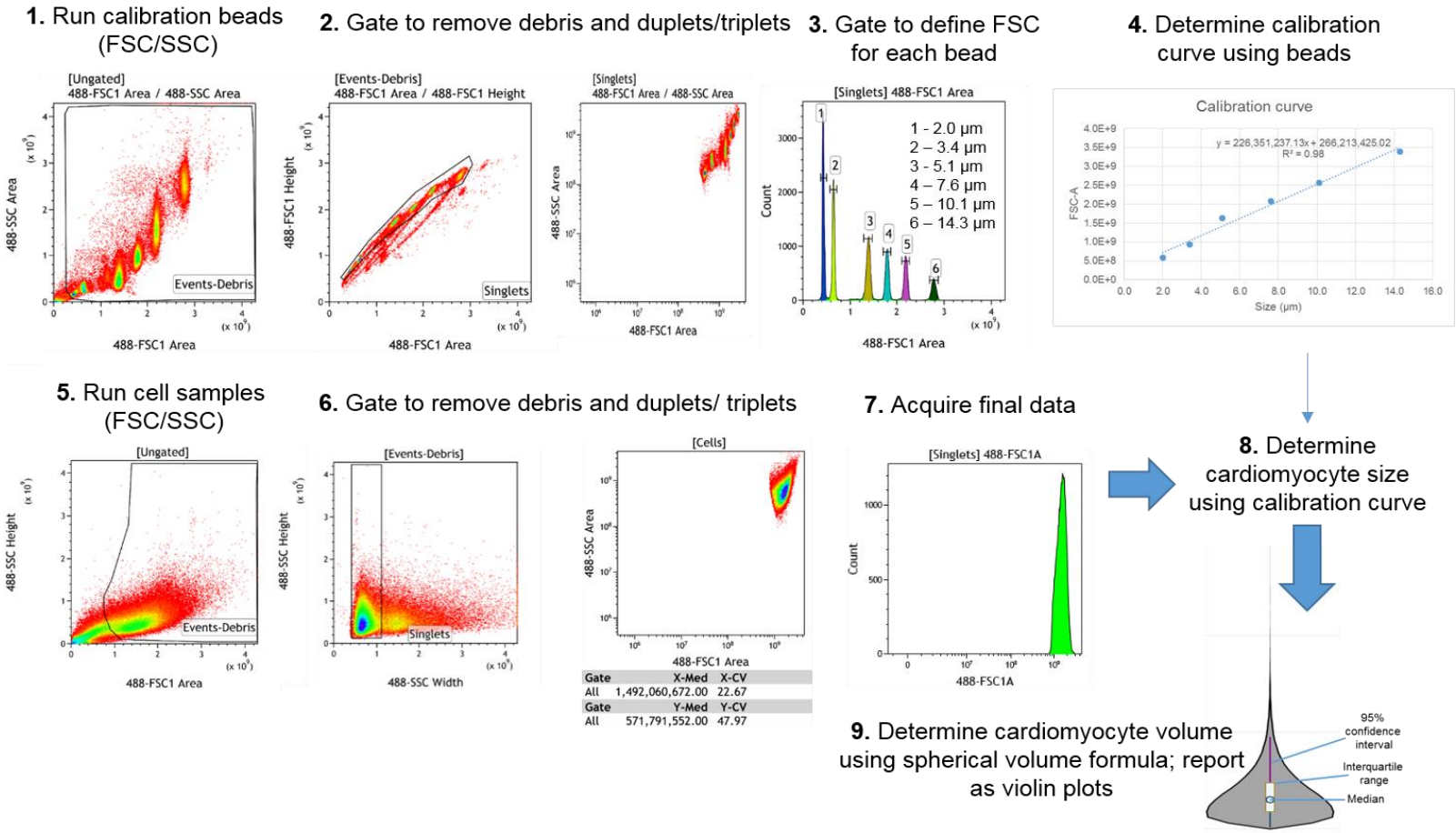


Figure 4.8 - Procedure to estimate cardiomyocyte volume by flow cytometry. Using beads of known sizes in the expected range of cells, a calibration curve was determined by measuring forward scatter (FSC). FSC of cell samples was then measured and sizes were estimated using the calibration curve. Cardiomyocyte volume was then calculated by applying the formula of a volume of a perfect sphere which is an approximation for dissociated cardiomyocytes in suspension. Data was reported as violin plots to better represent spread of cardiomyocyte volumes per genotype.

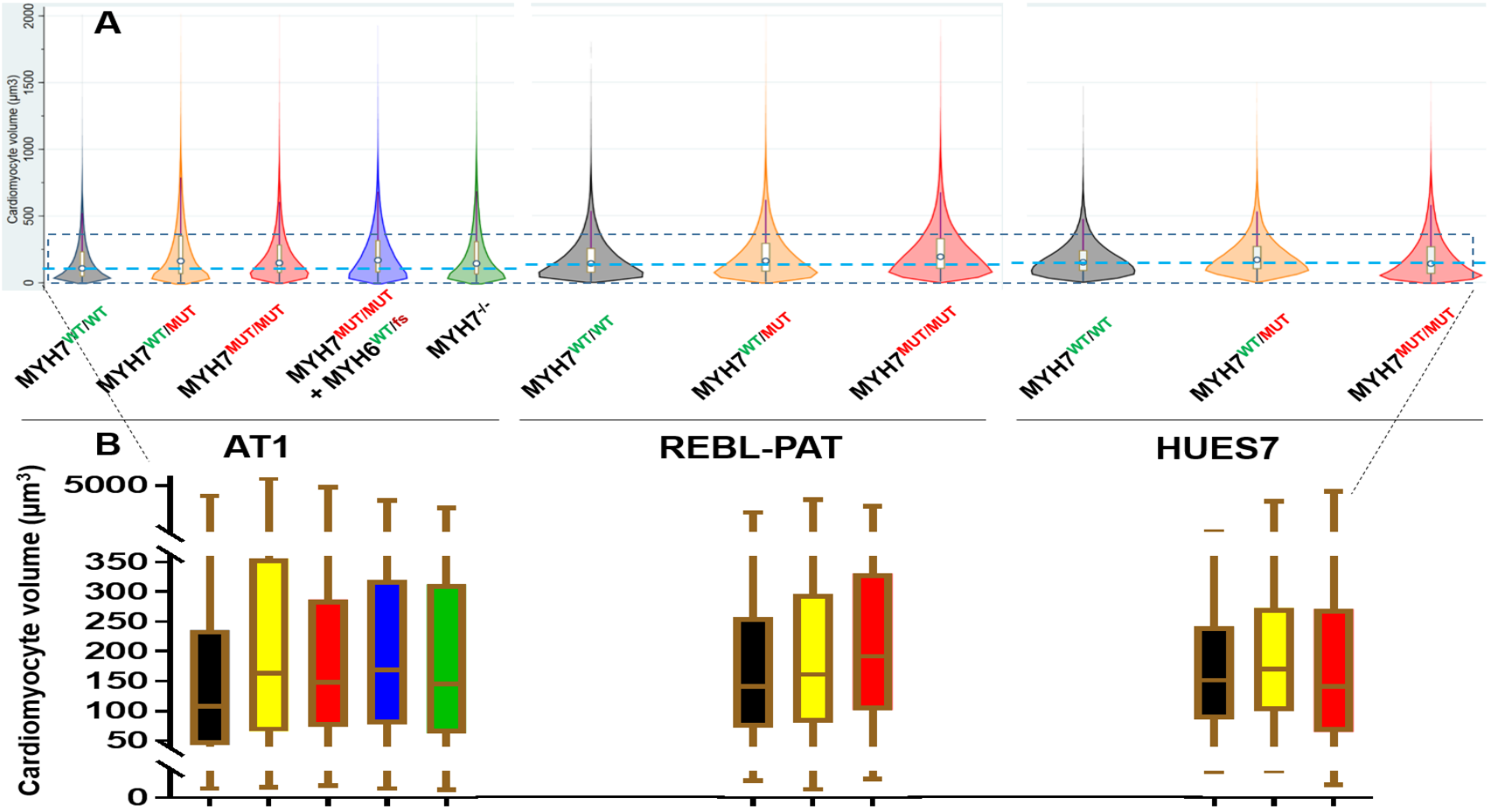


Figure 4.9 - Cardiomyocyte volume estimation by flow cytometry. **A)** Violin plots showing cardiomyocyte volume of AT1 lines (N=9), RPAT lines (N=6) and HUES7 lines (N=3). Dotted line indicates median of cardiomyocyte volume of isogenic controls. **B)** Box and whiskers plots detailing interquartile range of cardiomyocyte volume highlights higher median and first quartile metrics in gene-edited lines relative to their isogenic controls.

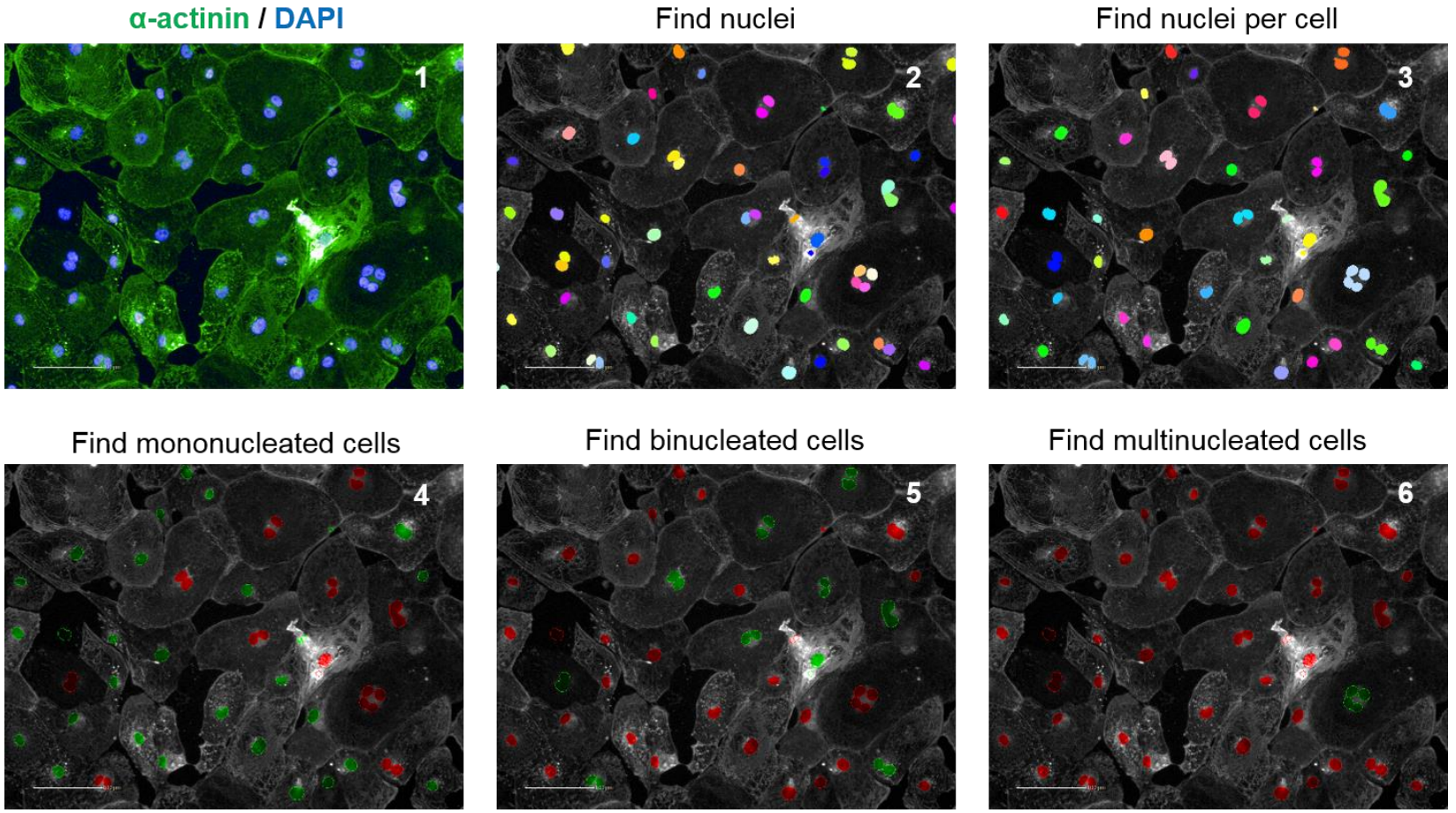


Figure 4.10 - High content imaging algorithm to quantify multinucleation of hPSC-CMs: 1) Input image of α-actinin/DAPI imunostained hPSC-CMs; **2)** find nuclei; **3)** find nuclei per cell by clustering nuclei within the same cell (empirically determined distance); **4)** bin cells according to the number of nuclei as mononucleated; **5)** binucleated and **6)** multinucleated (highlighted in green, respectively). Scale bar =100µm.

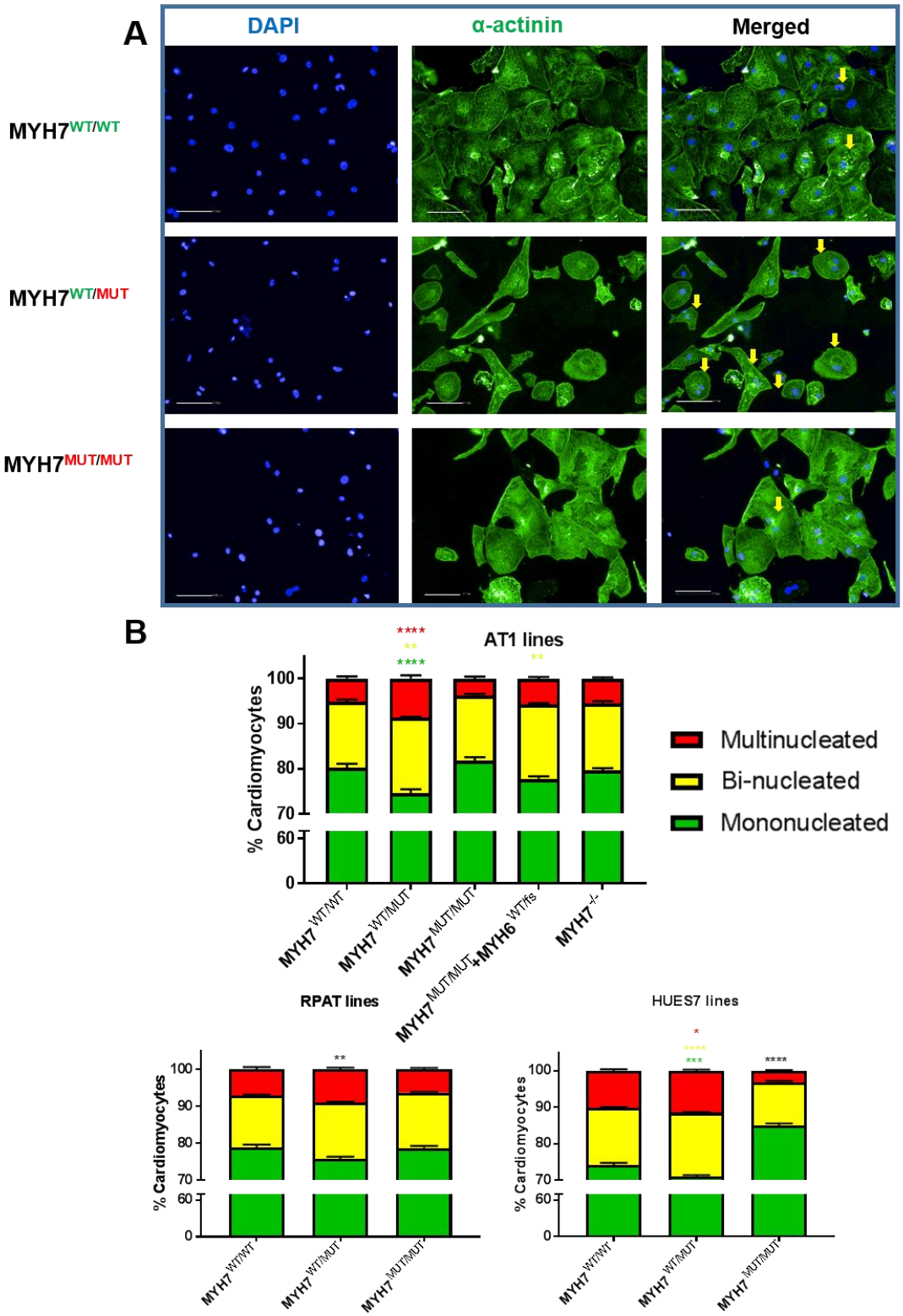


Figure 4.11 - Multinucleation analysis of gene-edited hPSC-CMs. A) Representative fluorescent micrographs of gene-edited hPSC-CMs imunostained for cardiac marker α-actinin and DAPI with bi/multinucleated cardiomyocytes highlighted by the yellow arrows. Scale bar=100 μm **B)** Automated quantification of multinucleation of hPSC-CMs showed that all the heterozygote lines had a higher proportion of bi- and multinucleated cells in comparison to their isogenic controls (N=8, * p<0.05; ** p<0.01; ***p<0.005; ****p<0.0001, between each group and its isogenic control, color-coded according to the category compared - black asterisks indicate changes in all three categories).

4.2.5 Expression of hypertrophic marker BNP

As the phenotypes shown above only address morphological changes associated with HCM, a more detailed molecular analysis is warranted. As discussed in the introduction, BNP expression has been used as a typical biomarker for hypertrophy. By blocking its secretion from hPSC-CMs using BrefeldinA, analysis of immunostained BNP signal was performed by high content imaging, as previously reported[228]. Broadly, a higher percentage of R453C-MYH7 hPSC-CMs showed positive BNP signal in comparison to their relative isogenic controls (**Fig 4.12A**), a phenotype that was rescued by treatment with the ET1 receptor antagonist bosentan (100nM for AT1 lines and 1μM for REBL PAT lines, **Fig 4.12B**). In all the cell lines analysed, treatment with ET1 (10nM) maximized BNP expression, acting as a molecular aggravator of hypertrophy that provides sensitivity to this assay (**Fig4.12C**).

In order to quantify BNP expression by high content imaging, an image algorithm was developed (**Fig 4.13**). This was based on the measurement of BNP signal in the perinuclear region of cardiomyocytes and binning signal intensities according to established thresholds. Boundaries were set by using unstimulated BNP-negative wild-type cardiomyocytes as a negative threshold, and positive signal was divided in two groups according to intensity, with ET1-treated cardiomyocytes belonging to highest signal intensity category.

Across the 3 lines (AT1, REBL PAT and HUES7), the percentage of hPSC-CMs expressing medium or high levels of BNP signal progressively increased from unedited parental cells to heterozygotes, with the highest levels seen in homozygotes (**Fig4.14A**). Thus, relative to unedited hPSC-CMs, fold increases for BNP medium and high- expressing heterozygotes were AT1 ~3.3-fold, REBL-PAT ~1.8-fold, HUES7 ~1.5fold, while for homozygotes were AT1 ~4-fold, REBL PAT ~2.3-fold, HUES7~1.9fold). The homozygotes showed statistically significant higher levels than heterozygotes ($p<0.05$). Interestingly, the homozygote R453C-MYH7+MYH6$^{fs/wt}$ line and the MYH7$^{-/-}$ line did not show a statistically significant increase in BNP expression, suggesting that the observed phenotype could be dependent on specific R453C-MYH7 mutations.

The observed phenotype could be reversed by treatment with ET1 receptor antagonist Bosentan (**Fig4.14B**), decreasing BNP levels presented by mutant lines to those of their respective untreated wild type controls ($p<0.05$ in AT1 heterozygote, $p<0.001$ in AT1 homozygote, $p<0.01$ in REBL-PAT heterozygote, $p<0.05$ in REBL-PAT homozygote between bosentan treatment and respective vehicle controls), except for the HUES7 line where the treatment did not result in statistically significant differences.

Relative to untreated hPSC-CMs, addition of ET1 caused significant increases in BNP expression in all lines (resulting in ~90% of BNP^{+} cardiomyocytes, **Fig4.14C**), which is expected according to its documented effect in stimulating BNP expression in cardiomyocytes upon cardiac hypertrophy[305].

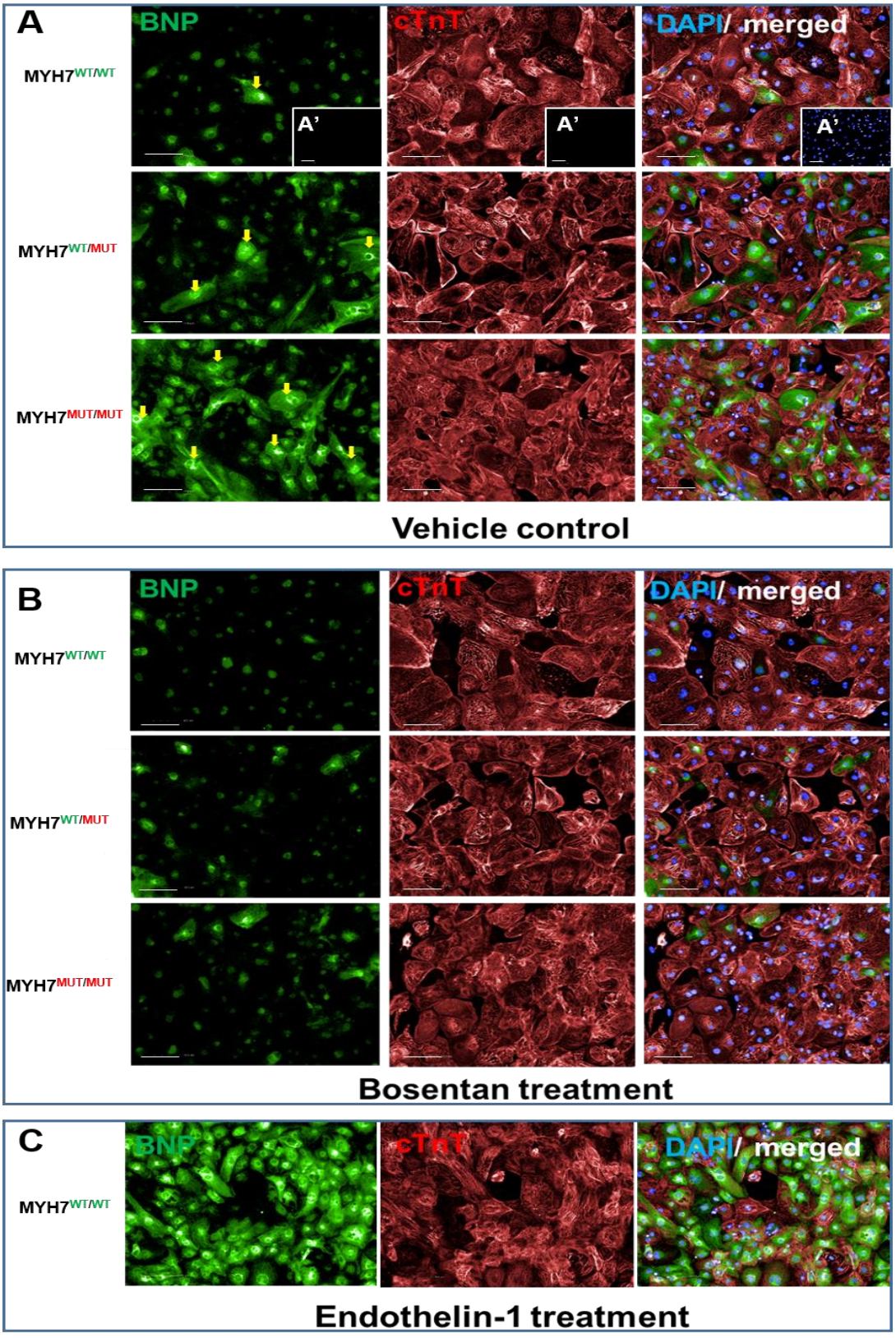


Figure 4.12 - Expression of hypertrophic marker BNP in hPSC-CMs. Representative fluorescence micrographs of BNP/cTnT/DAPI co-imunostained gene-edited hPSC-CMs treated with **A)** 0.1% DMSO (vehicle control), **B)** bosentan (100nM for AT1-cardiomyocyes and 1μM for REBL PAT-CMs) and **C)** Endothelin-1 (10nM), as well as **A')** stained fibroblasts as a negative control. Examples of BNP positive cells are highlighted by the yellow arrows. Scale bar=100μm.

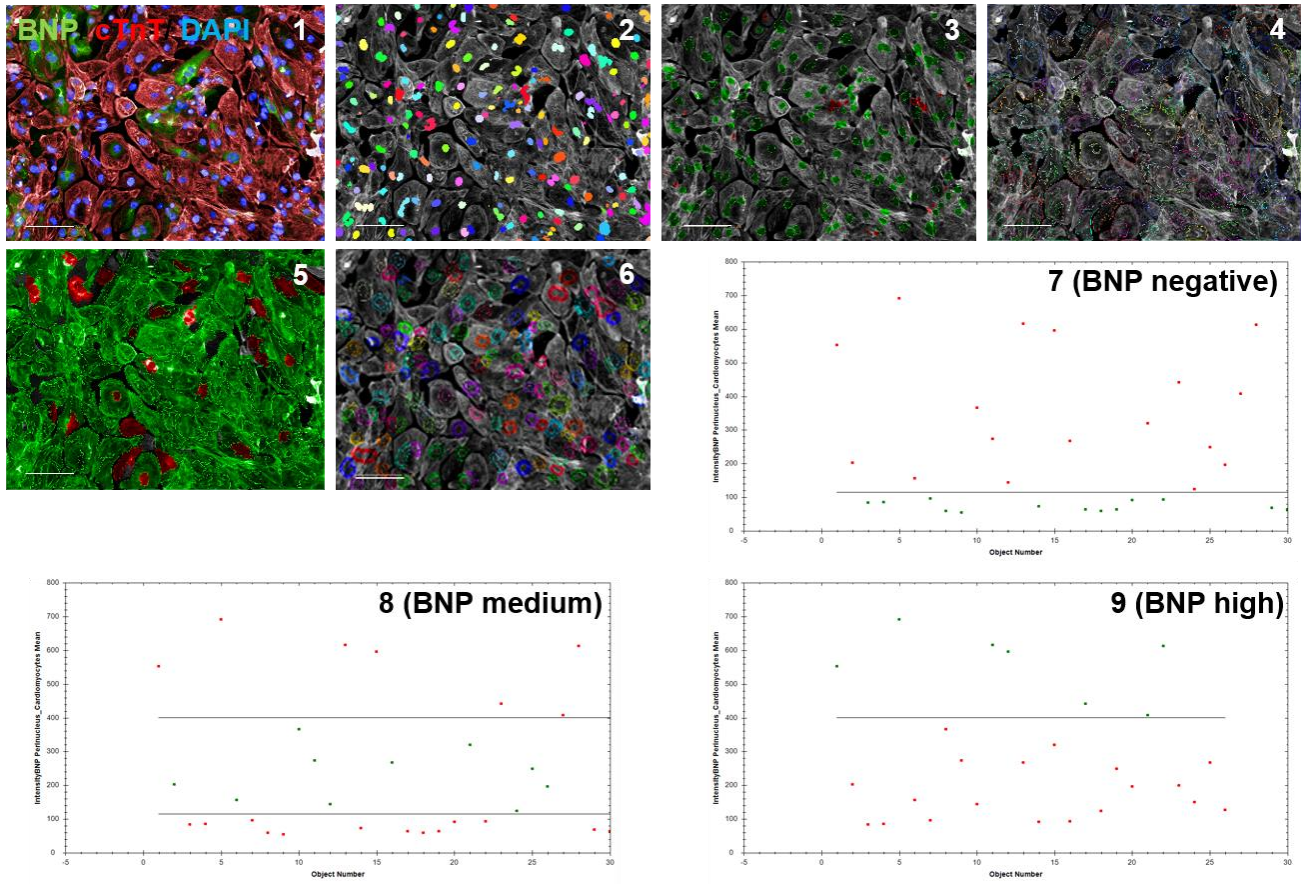


Figure 4.13 - High content imaging algorithm to quantify BNP expression by high-content imaging. 1) Input image of co-imunostained hPSC-CMs for BNP, cardiac marker cTnT and nuclei (DAPI); **2)** Find nuclei using DAPI channel; **3)** Remove DAPI-labelled cell clumps and debris (in red); **4)** Find cytoplasm using cTnT channel; **5)** Select cardiomyocytes based on cTnT signal intensity (thresholded to stained fibroblasts); **6)** Define perinuclear region; **7)** Quantify BNP intensity in the perinuclear region of cardiomyocytes and bin them according to BNP signal thresholds as negative, **8)** medium and **9)** high.

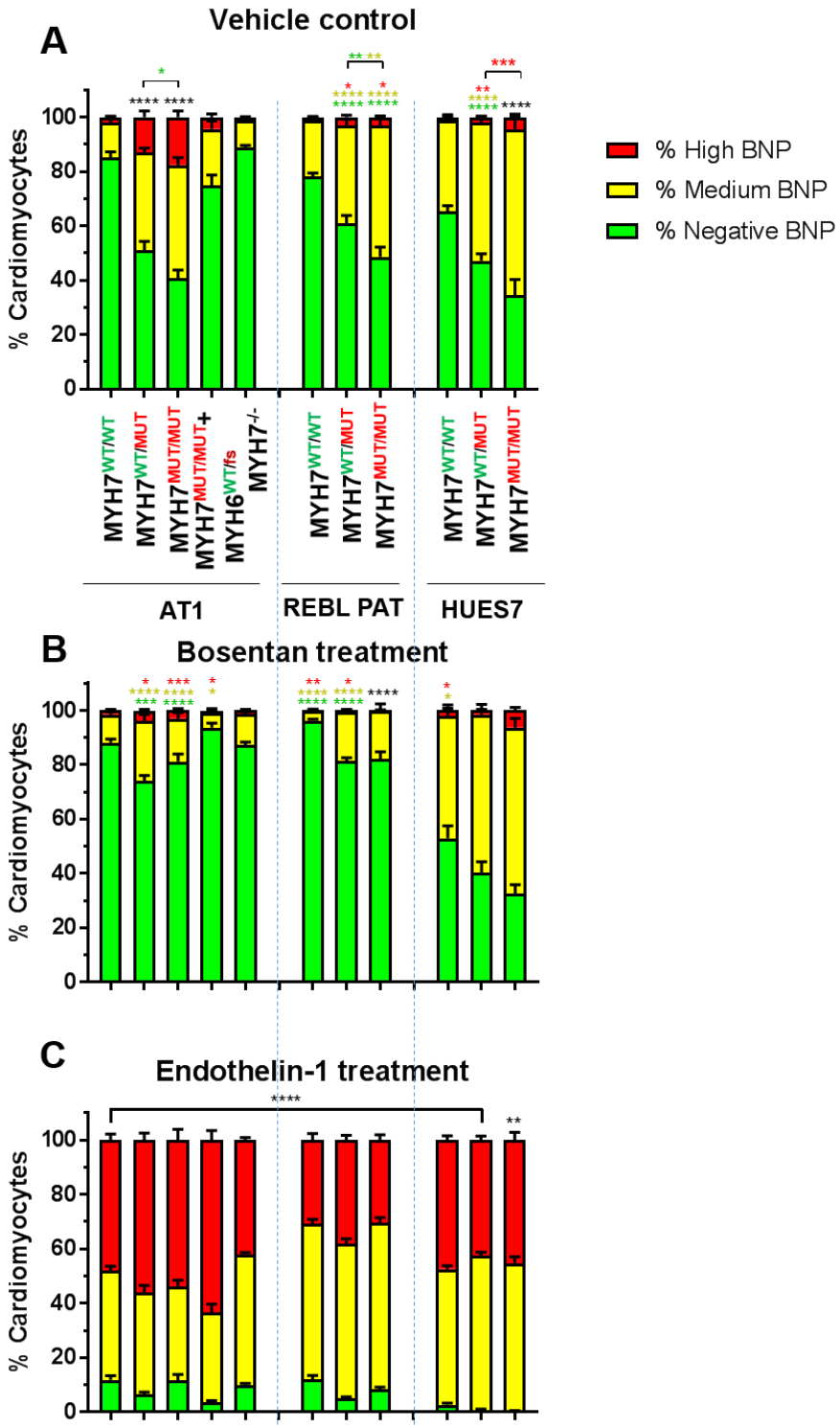


Figure 4.14 - Quantification of percentage of hPSC-CMs expressing hypertrophic marker BNP in gene-edited cell lines. **A)** Heterozygote and homozygote lines displayed higher BNP expression than their respective isogenic controls. **B)** Bosentan treatment rescued BNP levels of mutant lines to their isogenic controls, with the exception of HUES7 hPSC-CMs. **C)** ET-1 treatment maximized BNP expression in all lines. Data plotted as mean +/- SEM, N=6. * p<0.05; ** p<0.01; ***p<0.005; ****p<0.0001, between gene-edited lines and respective isogenic controls in A (unless indicated by the capped lines), and between treatments and respective vehicle controls in B and C for each genotype, color-coded according to the category compared (black asterisks indicate changes in all three categories).

4.2.6. Sarcomeric structure of HCM lines

β-MHC is a critical component of the sarcomere in cardiomyocytes, which plays a central role in contraction. Therefore, assessment of the impact of the R453C-MYH7 mutation in sarcomeric structure was performed by high content imaging. On a broader scale, immunostaining sarcomeric marker α-actinin reveals qualitative differences between R453C-MYH7 AT1 lines and their healthy isogenic controls, as evidenced by the seemingly higher frequency of cardiomyocytes bearing more diffuse sarcomeres and/or showing disarrayed patterns (**Fig 4.15A,** highlighted by yellow arrows). In addition, a more detailed analysis of cardiomyocytes co-stained for two sarcomeric markers (α-actinin and cardiac Troponin T) emphasizes those differences with more clarity, which become particularly evident when comparing the $MYH7^{-/-}$ line to the healthy isogenic control (**Fig. 4.15B**).

In order to estimate these differences in a quantitative manner and eliminate subjectivity, an image algorithm was developed by analysing the morphological and texture properties of cardiomyocytes. This automated method (named PhenoLOGIC™ Machine Learning imaging algorithm) employed the sharpened signal of sarcomeric structures labelled with α-actinin, using a sliding parabola mathematical correction (**Fig 4.16A**), to increase image quality and detection of subtle image features.

After manually training the algorithm to distinguish between cardiomyocytes displaying organised vs disarrayed sarcomeres, cardiomyocyte analysis by high content imaging showed increased prevalence of sarcomeric disarray in diseased AT1 lines relative to their healthy isogenic control (WT: 14.0±2.6%, heterozygous: 46.2±2.4%- $p<0.0001$, homozygous: 31.9±3.3%-$p<0.01$, homozygous + MYH6 frameshift: 35.3±2.6%$p<0.001$, knockout: 56.4±4.3%-$p<0.0001$, **Fig 4.16B**).

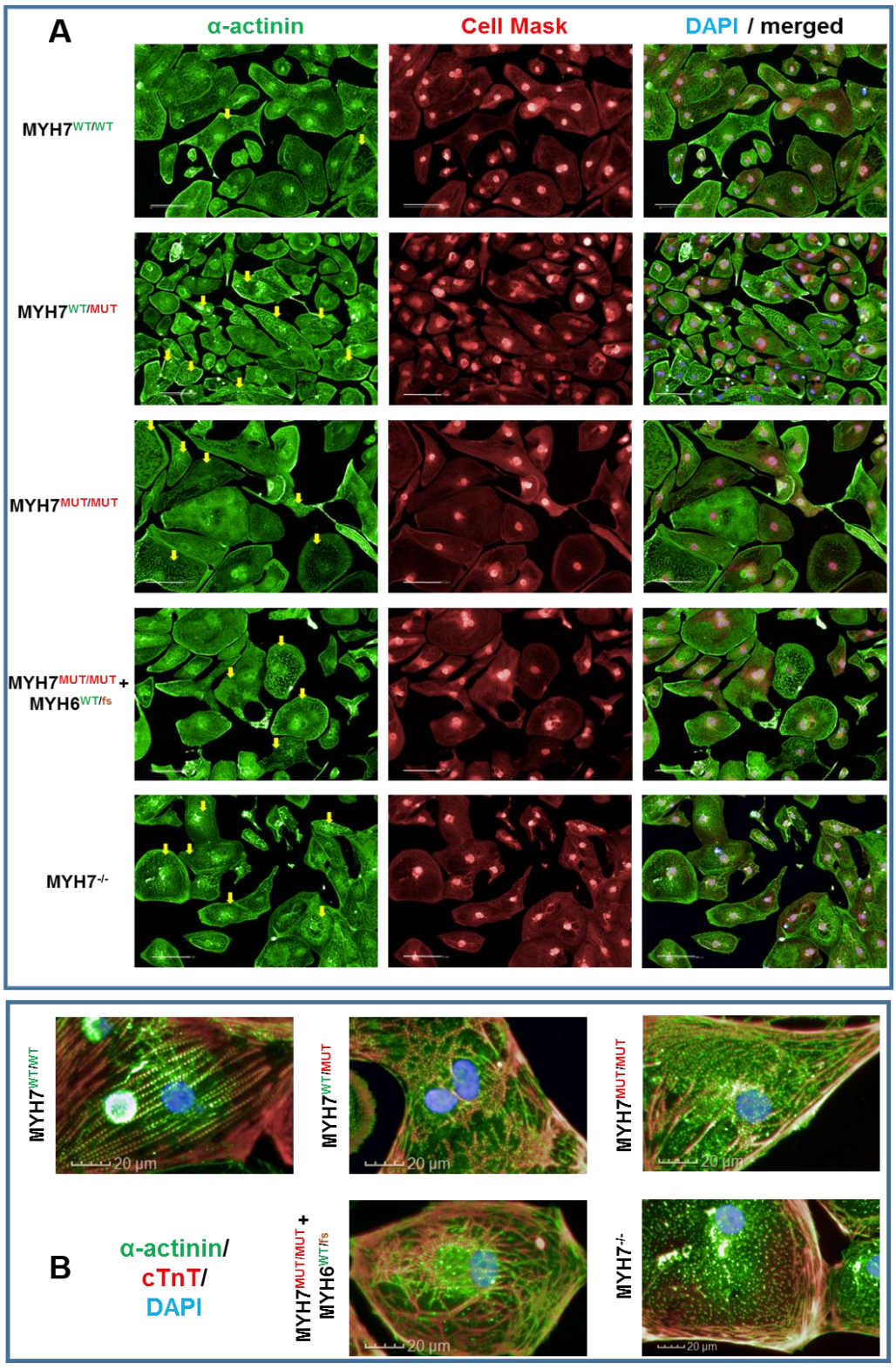
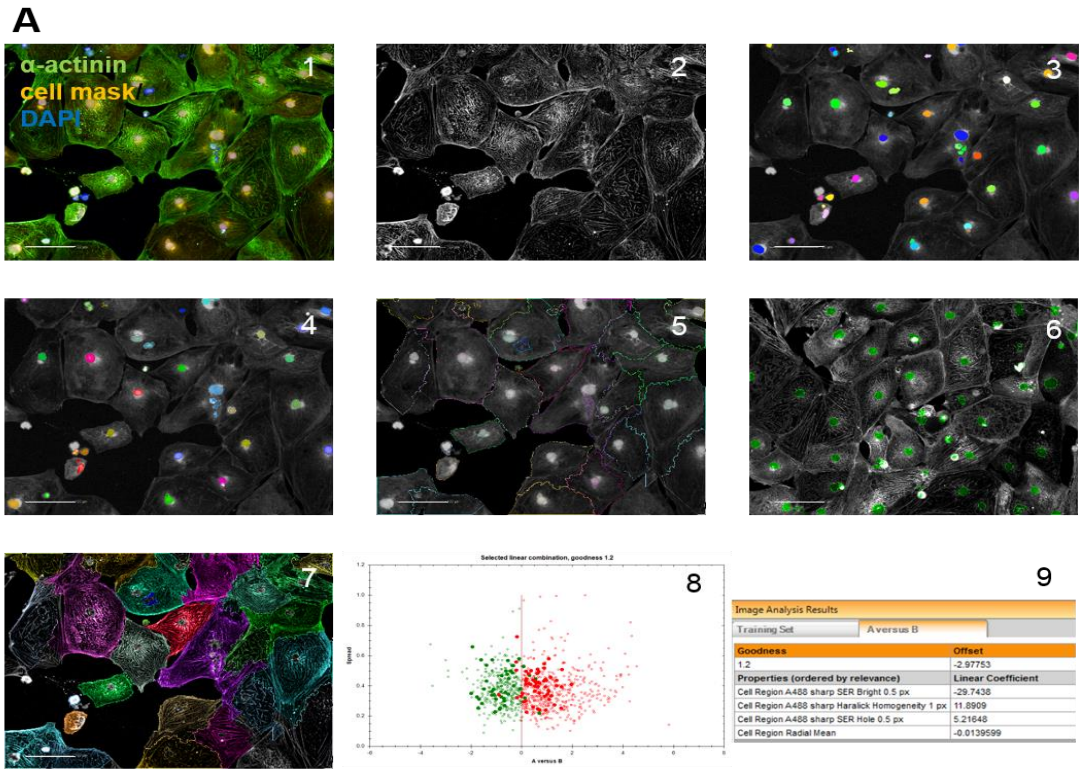


Figure 4.15 - Sarcomeric structure of gene-edited hPSC-CMs. **A)** Representative fluorescence micrographs of hPSC-CMs stained for sarcomeric marker α-actinin show several disarrayed cardiomyocytes in diseased AT1 lines (indicated by yellow arrows). Scale bar =100µm. **B)** Higher magnification micrographs of representative cardiomyocytes co-stained for two sarcomeric markers (α-actinin and Troponin T) highlight differences in sarcomeric banding pattern, as diseased lines show disorganised sarcomeres in contrast to the oriented ones in the healthy isogenic control line. Scale bar=20µm.



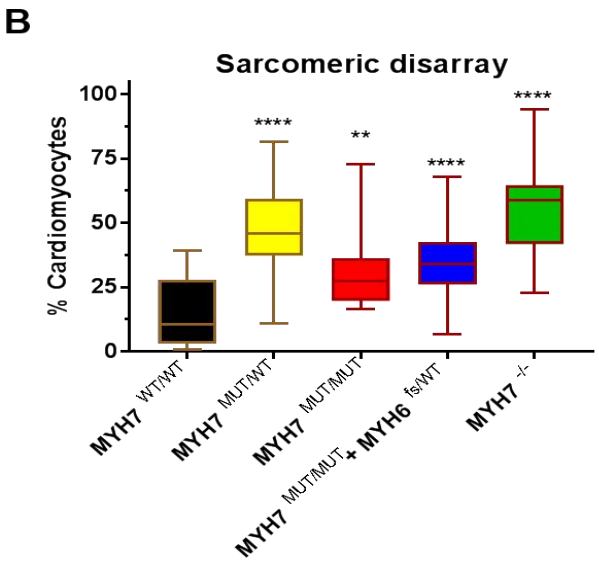


Figure 4.16 - **Estimation of sarcomeric disarray by high-content imaging. A)** algorithm to estimate percentage of cardiomyocytes showing disarrayed sarcomeres. 1) input image of imunostained hPSC-CMs for sarcomeric marker α-actinin using cell mask and DAPI as counterstains; 2) sharpen the signal derived from the sarcomeric staining to achieve higher resolution, using sliding parabola correction; 3) find nuclei of stained cells; 4) modify nuclei to account for multinucleated cells; 5) find cytoplasm using Cell mask counterstain channel 6) select cardiomyocytes based on α-actinin signal intensity relative to cell type control (fibroblasts); 7) calculate morphology and texture properties of cardiomyocytes in the cytoplasm, using sharpened α-actinin signal; 8) train software to distinguish between a cardiomyocyte displaying an organised (in green) vs disarrayed (red) sarcomere; 9) parameters of training indicate goodness of fit factor as well as the main texture/morphological properties that differ between organised vs disarrayed sarcomeres. **B**) Percentage of cardiomyocytes exhibiting disarrayed sarcomeres in gene-edited AT1 hPSC-CMs.

4.3 Discussion

In this chapter, cardiac differentiation of the gene edited hPSC lines was described as well as the characterization of the cardiomyocytes in terms of purity, *MYH7* expression, multi-nucleation, cell volume, BNP expression and sarcomeric structure. These analyses enabled high-throughput analysis of the HCM lines, which in many cases showed statistically significant changes in phenotypes associated with cardiomyocyte biology. It therefore stood to reason that these changes may be indicative of functional and underlying molecular mechanistic differences involved in this disease, which will be explored in the subsequent Chapter.

4.3.1 General properties of hPSC-CMs

The monolayer cardiac differentiation protocol used herein produced cultures exhibiting over 90% α-actinin^{+} cardiomyocytes. While this number indicates high enough purities to perform subsequent phenotyping experiments, morphological cellular heterogeneity is observed, with particular impact in more complex imaging-based readouts, such as sarcomeric disorganisation by high-content analysis. In this regard, selection methods exist to enrich for cardiomyocyte populations over contaminating (predominantly) fibroblasts. One of those methods relies on metabolic differences between those cell types, as while fibroblasts solely use glucose as their energy source, hPSC-CMs can utilise both lactate and glucose. Therefore, by culturing mixed populations in medium containing 4mM lactate and deprived of glucose, hPSC-CM purities of 99% were achieved[309]. Nevertheless, this selection method may be imposing unwanted effects such as selective death of particular cardiomyocyte subpopulations which could be valuable to disease modelling in order to get a more representative physiology. This is particularly important in this disease model as CMs bearing different genotypes exhibited metabolic differences (Chapter 5), which could be overlooked by the application of selection protocols.

Although the differentiation protocol used was shown to produce mostly (up to 80%) ventricular cells (George and Hoang, in submission), atrial and even nodal subtypes are likely to be present in the cardiomyocyte cultures, as previously shown [161,225,232]. This can represent a limitation to the study, as the *MYH7* gene is mostly expressed in ventricular cardiomyocytes, causing functional consequences when mutant. Methods to purify specific cardiac subtypes were not available when this work was being undertaken but are starting to emerge [310-312] and so this issue could be addressed now. Nevertheless, there could be advantages to have the heterogeneity of non-selected populations. Ventricular, atrial and nodal subtypes are all present in the heart. Therefore, by including them in these experiments, a more physiologically (albeit uncontrolled) representative analysis of HCM is being performed.

Finally, the incomplete maturation of hPSC-CMs generated, a defining drawback shared by the whole field, may be biasing interpretation of the data[84]. The phenotypes of fetal cardiomyocytes may be different than those exhibited by fully mature adult cardiomyocytes constituting the patient's heart. While improvements are being made, for example by growth factor supplementation of culture medium[313], a protocol to produce fully mature hPSC-CMs still remains elusive. Nonetheless, isogenic wild-type variants of each line provide the most relevant control to the inserted mutation. In this approach, the comparison of any observed effects in edited lines to their healthy counterparts will provide greater insight of the phenotypes, with translatable potential towards adult cardiomyocyte equivalents.

4.3.2 *MYH7* gene expression in HCM

In contrast to undifferentiated hPSC, the differentiated hPSC-CMs expressed the *MYH7* gene. However, the caveat to this was that expression of the edited alleles only occurred after Flp-mediated excision of the drug selection cassette. Although targeted insertion of selection cassettes has been shown to disrupt expression of other genes prior to their excision [84,314], this observation was surprising in the case of the edited *MYH7* lines in this thesis. The insertion site had been specifically selected to reside in an intron, well away from any annotated sequences known to be involved in splicing, promoter/enhancer activity or regulation via non-coding RNA (**Figure 3.11**).

In each of the isogenic sets of hPSC-CMs from which the cassette had been excised, qRT-PCR data appeared to show an increasing trend in *MYH7* expression in heterozygote and homozygote line relative to the parental (WT/WT). Further repeats are required to determine whether these changes reach levels of statistical significance. Moreover, human HCM is associated with a shift in the expression of myosin heavy chains, with α-MHC expression decreasing in favour of increasing β-MHC levels. Therefore, it is hard to determine whether any changes in MYH7 expression are due to the residual footprint, or reflecting a phenotype of the HCM. Thus, future studies will perform qPCR for *MYH7* and *MYH6* on the isogenic sets to ascertain if the potentially increased upregulation of *MYH7* isoform is accompanied by a decrease in *MYH6* expression in the edited lines. Finally, the expression of *MYH7* was extinguished in the homozygote knockout created in the AT1 line.

Notably, ratios of mutant: wild-type *MYH7* expression range from 25% in HUES7-CMs to 60% in AT1-CMs. While these ratios are within the range reported for other *MYH7* mutations[281], the difference observed between lines may derive from the contribution of the genetic background inherent to each cell line targeted (presumably operating through known regulatory mechanisms such as environmental-derived pathways and/or epigenetics). While the impact of epigenetics may have been minimized in hiPSC (erased during reprogramming), the postulated existence of residual epigenetic memory (e.g. predominant hypomethylation of

CpG islands[315]) may conceivably interfere with gene expression at a differentiated state[316].

Remarkably, Tripathi and colleagues have shown that increased fraction of mutant *MYH7* levels over total mRNA and protein content is correlated with more severe forms of HCM (such as ~2-fold increase interseptum thickness and age of onset of cardiac events)[281]. Moreover, the postulated existence of gene modifiers (e.g. polymorphisms in angiotensin-1 converting enzyme 1 -ACE-1) that increase the expression of mutant alleles may lead to the development of more severe clinical phenotypes in some patients [317]. In addition, the impact of other factors in modulating the expression of gene modifiers and mutant genes themselves (age, previous cardiac interventions) may also underlie progressive aggravation of HCM[317], adding an additional layer of complexity to this disease.

Many mutations in cardiac-associated genes lead to a differential penetrance in the patients. Remarkably, the phenotypes observed in the analyses performed in this Chapter were present in all the 3 isogenic cell lines. This is likely due to two main reasons: **i)** mutations in *MYH7* gene are more penetrant than mutations in other sarcomeric genes (as verified in clinical phenotyping data[318] and particularly established in the R403Q-MYH7 SNP showing 100% penetrance[319]; and **ii)** most HCM mutations are associated with a dominant-negative mode of action, i.e. patients heterozygous for a sarcomeric gene mutation produce thick filaments containing both normal and mutant myosin connected in series and thus mutant myosin heads exert a poison peptide effect by affecting the whole contractile apparatus[320]. As such, changes in the fraction of mutant transcripts may play a secondary role in the phenotypes developed, which are mainly dependent on the highly prevalent R453C-MYH7 mutation, as discussed below.

In addition, as it was previously shown (section 4.1.2) that mutations in one sarcomeric gene interfere with the expression of other genes[307], a more detailed investigation of the expression of other sarcomeric genes in the generated hPSC-CMs by larger scale transcriptomics studies should provide insight in terms of the regulation of gene networks in HCM.

4.3.3 HCM phenotyping by high-throughput methods

Application of high-throughput phenotyping methods to the gene-edited lines has resulted in valuable data towards further understanding of HCM disease. Firstly, volumetric analysis showed an increase in the volume of R453C-MYH7 cardiomyocytes in comparison to their isogenic controls. The most predominant effect was detected in AT1 lines, as the median and first quartile metrics of heterozygote R453C-MYH7 cardiomyocyte volume were approximately 50% higher than their wild type counterparts. To the best of my knowledge, this is the first time CM volume has been estimated by flow cytometry, so it is difficult to draw a comparison between the observed values and those reported using other methods, which is further

hampered by reporting differences as fold changes instead of absolute values[284]. Nevertheless, the large sampling capacity of this technique (50 thousands cells were sampled in 3-9 experimental replicates) offers confidence in the reported data, supported by the unbiased nature of the analysis, unlike measurements of cell area that often tend to misrepresent the heterogeneity of cardiomyocyte morphology in 2D culture.

Multi-nucleation analysis revealed that heterozygote R453C-MYH7 lines had an increased proportion of bi- and multinucleated cardiomyocytes relative to their healthy controls. This observation is of utmost importance given that HCM patient genotypes are mostly represented by the heterozygote variants. Although ploidy was not analysed in these cells, multinucleated cardiomyocytes are by definition polyploid, thus activation of ploidy-activated genes is potentially initiated in R453C-MYH7 cardiomyocytes. Importantly, 187 genes were reported to be triggered during polyploidy as a response to stress[294], such as the replacement of energy intensive contractile proteins (α-MHC) with more economic ones (β-MHC), towards the development of an adaptive response based on shifting the heart to “energy-saving” mode. Thus, this finding warrants further investigation, so that a comprehensive transcriptomics analysis will be performed to further interrogate this data to understand whether an adaptive response relying on the activation of ploidy-responsive genes is developed upon HCM induction. Notably, the HUES7 R453C-MYH7 homozygote line showed a very different distribution of multinucleation in comparison with all the other lines, exhibiting over 85% mononucleated cardiomyocytes. While the reason for this difference is not known, it could be accounted for by the fact that this is a hESC line, whereas the other lines investigated were of hiPSC origin. Alternatively, it may be due to the karyotypic abnormality harboured specifically in the homozygote edited line, where an addition of the long arm of chromosome 7 (7q32) may alter cell division and/or karyokinesis. Nevertheless, the gain of chromosome 7 was surprising given that in most cases changes in hPSCs are associated with part or whole gains of 1, 12 and/or 17 or of the specific 20q11.21 minimal amplicon[321].

The BNP assay results showed that the introduction of the R453C-MYH7 mutation increases expression of the hypertrophic marker BNP, without any biochemical stimulation. As expected, ET1 treatment of hPSC-CMs greatly increased BNP expression, in accordance with a previous report[228]). Treatment with ET1 receptor antagonist bosentan reverted BNP levels in mutant cardiomyocytes to those of their isogenic control. These findings indicate the existence of an autocrine regulatory mechanism of BNP expression mediated by ET1 associated signalling pathways in hPSC-CMs. These data suggest that BNP expression in HCM cardiomyocytes recapitulates the pathophysiological adaptive response of the heart: mechanical-induced secretion of ET1 by endothelial cells and cardiac fibroblasts upon ventricular wall stress trigger BNP expression in several cardiac cell types, leading to changes in cardiomyocyte cell size and actin cytoskeleton rearrangement[297]. It is worth noting that despite being present in all the three isogenic cell lines analysed, the magnitude of the observed phenotype varies (AT1>REBL-PAT>HUES7), as evidenced by a 10-fold higher bosentan concentration needed

to rescue BNP levels in REBL PAT lines in comparison to AT1 lines, and the lack of response of HUES7 lines to the treatment. In addition, although the use of bosentan as a therapeutic agent may be promising, reports of the anti-fibrotic effect of BNP (as reviewed in section 4.1.5) as shown by a 3-fold increase in cardiac interstitial fibrosis in BNP-knockout mice[301] warrant further caution in the inhibition of this pathway.

Analysis of the sarcomeric structure showed an up to 4-fold increase in the prevalence of disarrayed sarcomeres in diseased AT1 cardiomyocytes in comparison to the wild type controls, with the MYH7 knockout showing the most severe phenotype by the appearance of diffuse/granulated sarcomeres. This difference is in the same range with that reported by Tanaka et al in *MYBPC3* mutant HCM hiPSC-CMs[160]. This observation is expected as *MYH7* encodes a protein that plays a central role in regulating cardiomyocyte contraction, which is the primary function of sarcomeres. Functional analysis would provide insight on whether these structural changes are reflected in alterations in cardiomyocyte contractility and was undertaken in Chapter 5.

Notably, the PhenoLOGIC™ Machine Learning imaging algorithm used to measure sarcomeric disarray was the most challenging to develop of those described in this thesis. This was because the image analysis must consistently display three main properties: **i)** well distributed cardiomyocytes, without forming any clumps and preferably extensively spread in the surface; **ii)** good signal intensity and signal-to-noise ratio in order to provide better sharpened images (thus higher resolution) and distinction between individual cells and background (improved image segmentation); **iii)** clear differences between conditions/ cell lines in order to facilitate the manual training. Between these three constraints, the first two are easily controlled by the establishment of robust protocols of cardiomyocyte dissociation and culture (although cardiomyocyte heterogeneity constitutes a limitation to the first point), but the third relies heavily on the panel of genotypes and/or conditions to analyse.

In this regard, the AT1 lines have shown greater resolving power due to the higher number of its genotypes, with the MYH7$^{-/-}$ showing very clear changes in sarcomeric structures, which could then be used to train the algorithm in comparison to wild type cardiomyocytes. Consequently, HUES7 and REBL-PAT cardiomyocytes could not be analysed using this algorithm due to the existence of a lower number of genotypes, specifically the absence of the MYH7$^{-/-}$ variant, which caused difficulties when training the software. Alternative proprietary image analysis algorithms have been developed to analyse a broader number of properties of sarcomeric structure, relying on complex mathematical modelling of the images acquired[226]. It is conceivable that applying such an algorithm to the hPSC lines in this thesis could overcome issues encountered using the *Harmony* High Content Analysis Software (Perkin Elmer).

Collectively, the high-throughput phenotyping described in this Chapter allowed an unbiased, automated and comprehensive analysis of several hallmarks of HCM, shedding light on

functional changes in cardiomyocyte biology. Although these type of methods do not offer the same resolution as others that could address the same readouts (e.g. histology for volumetric analysis, and electron microscopy for sarcomeric structure), the high sampling capacity of the Operetta™ confocal plate reader coupled to imaging algorithms proved its usefulness by the high number of parameters and conditions analysed using a single image or variations in the immunostained proteins within the same multi-well plate. These results gave confidence to progress to the next stage of the thesis, which was in-depth functional analysis of the isogenic sets of *MYH7*-mutant hPSC-CMs generated, and is the subject of the next Chapter.

5. Functional and Molecular phenotyping of R453C-MYH7 hPSC-derived cardiomyocytes

5.1 Introduction

5.1.1 Energy depletion model in HCM

As reviewed in the Introduction, cardiomyocyte contraction is initiated by an increase in the cytoplasmic Ca^{2+} concentration, derived from voltage-gated Ca^{2+} channels upon membrane depolarization, and from the sarcoplasmic reticulum[322]. Increase in intracellular Ca^{2+} triggers binding of the actin filaments to the myosin ATPase, located on the myosin head. Thereafter, energy production by ATP hydrolysis triggers a conformational change in the actin-myosin complex, thereby shortening the sarcomere. Calcium efflux mediated by sodium-calcium-exchange pump then restores the intracellular Ca^{2+} concentration and the sarcomere relaxes, completing the contraction-relaxation cycle[64]. Collectively, this is a highly energy-demanding process sustaining cardiac contractile (systolic) and relaxation (diastolic) functions throughout the lifetime of an individual. In fact, the heart is the highest oxygen-consuming organ in the body, requiring approximately 8–15 ml O_2/min/100 g tissue at a resting pulse rate, which can increase to more than 70 ml O_2/min/100 g myocardial tissue during vigorous exercise, which is in turn significantly more than that consumed by the brain (approximately 3 ml O_2/min/100g tissue)[323]. Moreover, 90% of ATP used in the heart comes from mitochondrial oxidative phosphorylation[324]. This energy is mainly consumed by the myosin ATPase (70%), while the remainder is mainly used for re-uptaking Ca^{2+} into the sarcoplasmic reticulum through the SERCA and to maintain an ion gradient imbalance across the membrane, required for depolarization to occur in each heartbeat[325].

As revised in Chapter 1.2, HCM is a very complex disease characterized by phenotypic heterogeneity[14] and variable genetic predictivity. Only ~50% of HCM patients have mutations in genes known to cause the disease and the cause in the remaining patients is not known. Thus, a model to unify the several phenotypes and outcomes of HCM has been proposed, based on energy depletion in the myocardium[325].

According to the energy depletion model, cardiac dysfunction in HCM is due to an inefficient sarcomeric ATP utilization, which is caused by the incorporation of mutant contractile proteins in the sarcomere. As detailed below, HCM mutations in β-MHC modify the cycling rate of myosin heads[326], which gains further relevance in patients heterozygous for HCM mutations that have wild-type myosin heads combined with mutant ones. Therefore, upon the actin-myosin interaction, mutant heads will be removed at a different rate than wild-type ones, leading to forced detachment of some of the crossbridges before the contraction is finished. This results in ATP inefficiency, as ATP is hydrolysed without generating force in the slow-

detaching myosin heads[327]. Consequently, this increased cost of force production imposes a metabolic stress as mitochondrial respiration needs to be enhanced to cope with increased energetic demands, resulting in the production of reactive oxygen species (ROS).

Furthermore, if energy supply cannot match demand, Ca^{2+} re-uptake into the sarcoplasmic reticulum after contraction is compromised, resulting in prolonged cytosolic Ca^{2+} transients which cause ventricular arrhythmias and changes in downstream Ca^{2+} -dependent signalling pathways coordinating the hypertrophic response[325]. This model is represented in **Figure 5.1**. Finally, severe energy deficit will also disrupt transmembrane ion transporters needed to establish membrane chemical and electrical gradients required for normal electrophysiological activity. Importantly, all these processes are aggravated in circumstances where an additional workload is placed upon the heart, with direct implications in sports-related SCD[325]. Data supporting this model and its implications are explored in the next section.

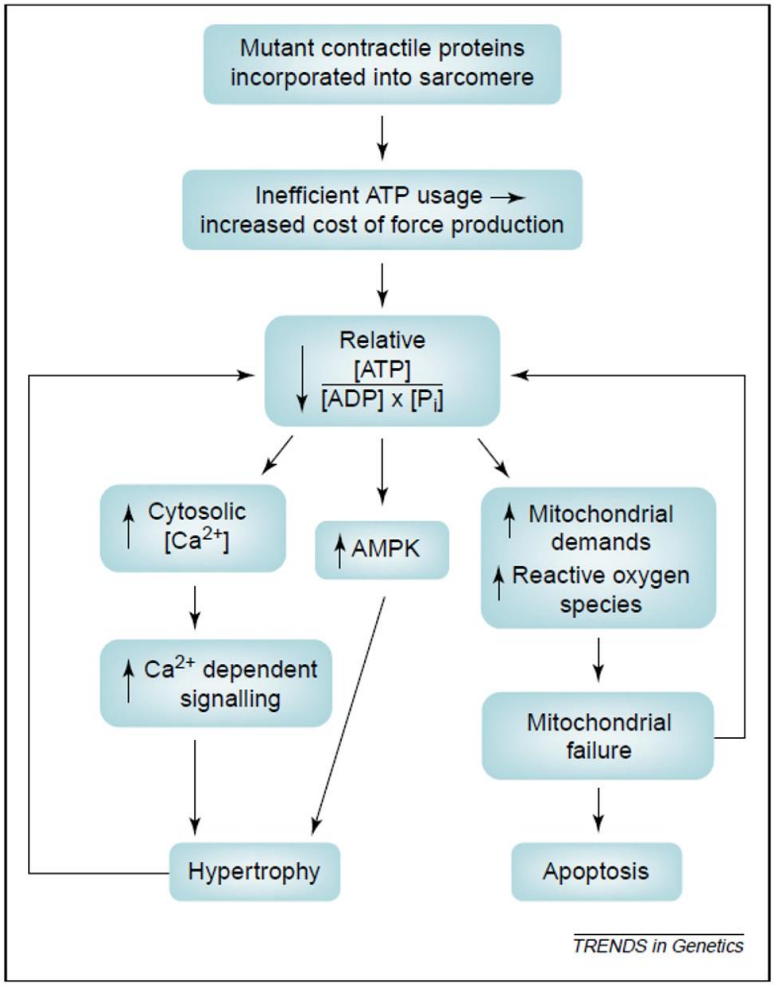


Figure 5.1 - Energy depletion model associated with sarcomeric mutations present in HCM. Increased cost of force production due to inefficient ATP usage in the sarcomere results in energetic deficit in critical compartments of the cardiomyocyte, leading to failure to maintain free energy levels sufficient for contraction and critical homeostatic functions, such as Ca^{2+} re-uptake. Increased cytosolic calcium leads to activation of Ca^{2+}-dependent signaling pathways and functionally to arrhythmias. Compensatory response by increased mitochondrial activity imposes a metabolic stress that leads to generation of reactive oxygen species that in turn promote apoptosis. Adapted from [311].

5.1.1.1 Mitochondrial activity

Supporting the energy depletion model are several studies ranging from different animal models to human cardiac explants and even live HCM patients.

Firstly, phosphorus-31 magnetic resonance spectroscopy ($_{31}$P-MRS) was used to determine the phosphocreatine (PCr) to ATP ratio (PCr/ATP), which is an indicator of the energetic state of cardiac muscle[328]. Using this non-invasive technique, HCM patients bearing mutations in one HCM gene (encoding β-MHC, cTnT or MyBPC) showed ~30% lower PCr/ATP ratios relative to healthy controls, demonstrating energetic deficit in HCM hearts, regardless of the mutation presented[329]. Remarkably, even mutation carriers that had not developed HCM also exhibited lower ratios, suggesting that energetic imbalances are an early feature of the disease. Moreover, application of the same technique to explanted hearts of transgenic mice models of HCM corroborated these results, as mice with a R403Q-MYH7 mutation showed ~22% lower PCr/ATP ratios[330] relative to healthy controls, and those bearing the R92Q-cTnT SNP had ~8% lower ratios[331] compared to WT, the latter showing a more modest effect possibly because the affected protein does not directly interact with the ATP hydrolysis site in the myosin head. However, these data provide only a global indication of the energetic status of the heart with regards to the creatine kinase shuttle, without providing any insight in terms of the kinetics of actin-myosin sliding involved in the contraction-relaxation cycle.

In addition, mitochondrial oxidative capacity was reported to be preserved[332] or even enhanced in human hypertrophied hearts, as shown by the increased (~2-fold higher vs controls) oxygen consumption in mitochondria isolated from cardiac tissues, in the presence of ADP and different sugar sources[333]. However, it has also been shown that there is a progressive impairment of fatty acid oxidation that precedes end-stage heart failure in rodent models[334,335], as there is no corresponding increase in glucose oxidation. As fatty acids are typically more energetic than single glucose molecules this indicates that the hypertrophic heart cannot cope with prolonged demanding OXPHOS requirements associated with hypertrophy, resulting in HF.

5.1.1.2 Kinetics of actin-myosin interaction

Addressing the limitations of whole cell/tissue energetic analysis, *in vitro* motility assays were developed based on the movement of fluorescently-labeled actin filaments over a layer of randomly-oriented myosin molecules immunoadsorbed to an antibody-coated surface (**Figure 5.2**). Videoenhanced fluorescence microscopy can then be harnessed to record the distance travelled by actin filaments in a given time interval in order to measure the maximum velocity[336]. In addition, tethering a ulta-compliant microneedle to actin filaments enables measurement of average force per crossbridge.

In order to complement this analysis, acto-myosin ATPase assays have been developed to estimate the kinetic parameters of actin-myosin sliding in cardiac myofibrils, generating tension due to ATP hydrolysis[249]. This assay relies on tethering skinned myofibres between a motor and a force transducer followed by immersion in buffers with different calcium concentrations[337] (**Figure 5.3**). Placing myofibers in high calcium medium triggers contraction and tension is developed exponentially with a rate constant that reflects thin filament activation upon Ca^{2+} binding (k_{ACT}), the rate of strong myosin binding to actin (crossbridge formation), the subsequent force-generating crossbridge isomerization and initial cross-bridge turnover. Conversely, placing the muscle strip in low calcium medium initiates a slow relaxation phase, whereby force decay occurs under isometric conditions with a rate constant (slow k_{REL}) reflecting the rate of cross-bridge detachment, independent of Ca^{2+} dissociation from troponin C. It is worth noting that myofibrils are the smallest subunit of the cardiomyocyte contractile apparatus and consist of sarcomeres (single contractile units) in series[62].

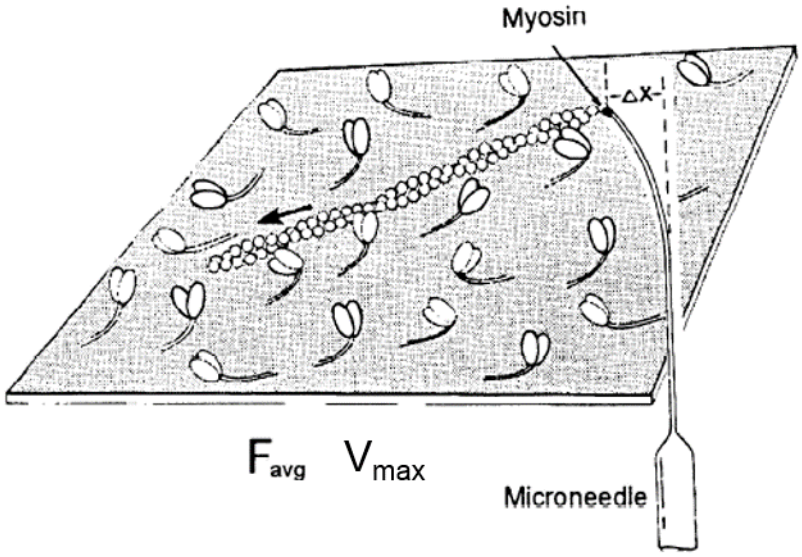


Figure 5.2 - In vitro motility assay – Myosin molecules are adhered randomly into a nitrocellulose-coated coverslip. In the presence of ATP, velocity (V_{max}) of single, fluorescently labelled actin filaments may be determined. By attaching an actin filament to an ultracompliant glass microneedle, average force per cross-bridge (F_{avg}) can be estimated. Adapted from [322].

However, studies performed using these techniques have produced conflicting results. Initial reports based on heterologously expressed rat R403Q-α-MHC showed a 4-fold decrease in ATPase activity and a 5-fold reduction in *in vitro* motility compared with wild type controls[338]. However, the same mutation in whole cardiac myosin isolated from mouse explants led to 60% higher velocity by the *in vitro* motility assay, and a 2.3-fold higher actin-activated ATPase activity than a wild-type myosin[339]. These discrepancies extended to myosins derived from human biopsies, as whereas Cuda et al showed that β-MHC mutant myosins had consistently lower sliding velocities (0.112-0.292 μm/s) than healthy ones (0.48 μm/s)[340], Palmiter and

colleagues reported the opposite in R403Q and L908V-β-MHC (30% higher velocities)[341]. These differences highlight the main drawback of these methods: preparation of protein sources. Firstly, tissue biopsies allow limited concentrations of myosins, which may be further affected by freezing and tissue handling procedures which also cause additional protein degradation. Alternatively, proteins derived from recombinant *in vitro* expression systems may show changes in structure due to the isolation/ purification protocol, with functional consequences for the endpoint assay. Importantly, these assays do not fully represent the complex environment characteristic of a highly organized sarcomere composed by a plethora of different regulatory proteins, as isolated proteins are investigated under unloaded conditions. Nevertheless, this experimental setup was recently optimized for hiPSC-CMs that had undergone maturation by long-time culture onto nanostructured patterns[342], showing that kinetics of contractility of these constructs more closely resemble those of fetal cardiomyocytes than adult ones.

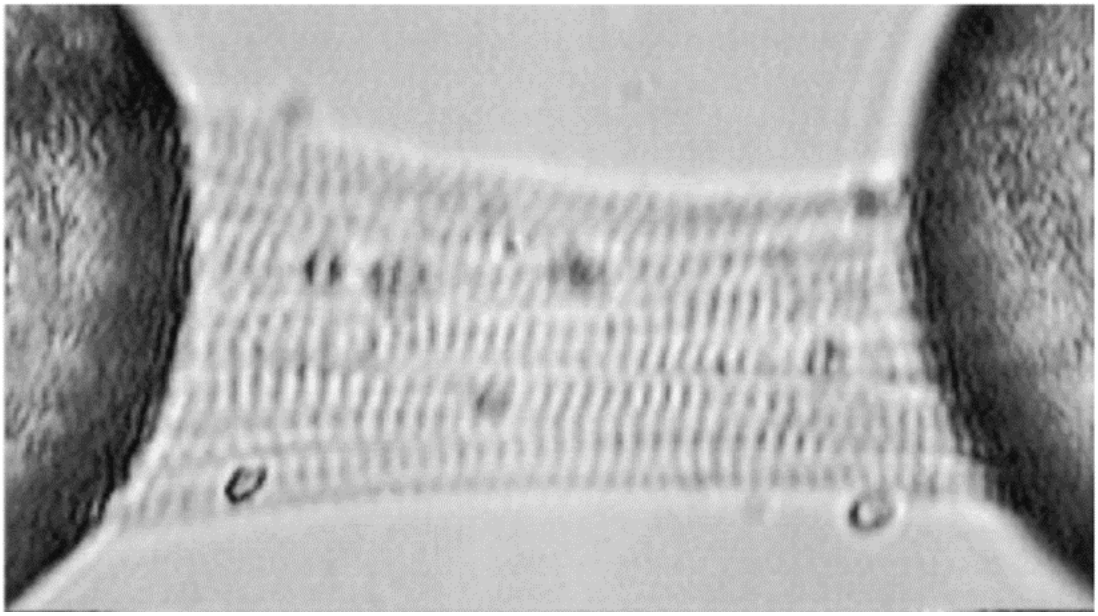


Figure 5.3 - Tension/ actin-myosin ATPase assay. Cardiac skinned preparation glued between a force transducer and a piezoelectric motor. By rapidly (~10 ms) switching from low to high [Ca^{2+}] solutions in the presence of ATP, contraction pulls the transducer thus enabling the measurement of force generated. Re-immersion into low [Ca^{2+}] solutions triggers relaxation. Measurement of the kinetics of these processes enables determination of parameters associated with actin-myosin interaction (detailed in text). Adapted from [350].

Providing additional support to the energy depletion model is the observation that diseases that limit myocardial energy production result in phenocopies of HCM, without any sarcomeric gene mutations. These syndromes include abnormalities in mitochondrial transfer RNA mutations[343], disorders of oxidative phosphorylation[344], combined respiratory-chain deficiencies[345] and defects in fatty-acid metabolism (e.g. CD36 deficiency)[346]. Moreover, experimental disruption of energy production in mouse models was shown to recapitulate HCM phenotype, as reported by the knockout of adenine nucleotide translocator-1, involved

in exporting ATP from the mitochondria[347]. Finally, patients showing both sarcomeric and mitochondrial mutations (e.g. R249Q-MYH7 plus A4300G-tRNAIle) exhibit more severe hypertrophy and myocardial dysfunctional phenotypes (~72% higher intraventricular septum thickness) than those bearing only mutations in one of such genes[348].

Investigation of digenic models reinforces the longstanding notion of genetic background contribution to HCM clinical outcome. This concept was also explored in the analysis of a cardiac explant from a patient bearing a homozygous R403W-MYH7 mutation and a heterozygote V896M-MYBPC3 mutation, which resulted in impairment of the ejection fraction (33% lower than healthy individuals)[349]. *In vitro* motility assays showed 18% higher sliding velocity relative to control, and ATPase assays revealed a dramatic increase in the maximal actin-activated ATPase activity (114% higher than healthy). Finally, the diseased cardiac myosin heads showed an increased affinity for actin in comparison to healthy controls (87% higher K_m), reinforcing the postulated differences in actin-myosin interactions between HCM patients and healthy individuals. These results indicate a disproportionate enhancement of energy consumption without the associated improvements in the mechanical function, thus suggesting inefficient ATP utilisation, which is a hallmark of the energy depletion model.

5.1.1.3 Mitochondrial content

It is well known that exercise causes increased mitochondrial content in all skeletal muscle fibre types, thus improving muscle capacity for ATP production[350]. In the heart, however, changes in energy production upon exercise have shown contradictory results, with some studies showing increases in myocardial mass rather than mitochondrial content (fatty acid oxidation is unchanged suggesting the absence of metabolic remodelling)[351]. In the context of heart failure, no conclusive evidence has shown increase in mitochondrial content, as no changes in mitochondrial transcription factor A (mtTFA), mtDNA content and mRNA for all mitochondrial-encoded subunits of the electron transport chain were detected in explanted failing hearts when compared to donor hearts[352]. Contrastingly, hearts derived from mitochondrial cardiomyopathic (MIC) patients (a form of HCM associated with mutations in mtDNA) showed striking phenotypes in terms of mitochondrial proliferation, as shown by ~15-fold increase of expression of key regulators of mitochondrial biogenesis (*PGC1, NRF1, NRF2, and TFAM*), 3-fold increase in mtDNA content per cell, and induction of genes involved in fatty acid metabolism (10-fold increase in PPAR-α) and glucose transport (6-fold increase in *GLUT1*), when compared to healthy samples[353].

Taken together, in spite of the inherent methodological caveats, these investigations corroborate the energy depletion model of HCM: a higher energetic demand due to inefficient ATP utilisation in the sarcomere is not accompanied by an increase of the mitochondrial content/biogenesis. Subsequently, metabolic reduction in fatty acid oxidation leads to disruption of energy supply, which ultimately results in sudden cardiac death as the energetic needs associated with cardiac contractions are not met.

5.1.1.4 Oxidative stress

Besides providing energy for cardiac contraction and relaxation, mitochondria generate ROS as a by-product of aerobic OXPHOS[354]. ROS are well known to cause detrimental effects to lipids (peroxidation results in damage to the cell membrane and organelles[355]), DNA (leading to mutagenesis induced by strand breaks[356]), proteins (resulting in inactivation and/or denaturation of enzymes[357]), and other alterations in chromatin structure affecting gene expression[358].

Interestingly, ROS were shown to mediate the hypertrophic effects of sympathetic angiotensin system as reported by Dai and colleagues[359]. Angiotensin II (AngII)-treated mice showed increased production of ROS (2-fold and 50% increase in relative fluorescence intensities of MitoSox and DCDFA, respectively) in comparison to untreated animals. This resulted in mitochondrial damage in cardiomyocytes (~4-fold increase in protein carbonylation and mtDNA deletions vs untreated), and double the proportion of abnormal mitochondria and autophagosomes/autolysosomes. In addition, mitochondrial biogenesis was promoted upon AngII treatment (~80% increase in expression of *PGC-1α*). Ultimately, the treatment resulted in a cardiac hypertrophic phenotype (35% increase in heart weight, 70% in left ventricle mass index), that was attenuated in transgenic mice overexpressing catalase (antioxidant enzyme), indicating that ROS production in mitochondria was responsible for triggering HCM.

Moreover, ROS were reported to activate redox-sensitive proteins such as the kinase Ask-1 that was shown to promote the cardiac hypertrophy phenotype in mice, resulting in cardiomyocyte apoptosis upon AngII treatment. This response did not occur in Ask-$1^{-/-}$ transgenic mice[360], which also exhibited attenuated ventricular remodeling in response to pressure overload (14% increase in intraventricular septum wall thickness vs 32% in wild type mice). These findings illustrate the contribution of ROS to the progression of HCM by causing mitochondrial damage and cardiomyocyte apoptosis.

In human failing hearts, NADPH-induced superoxide (O_2^-) production was slightly higher than healthy hearts (30%), but dramatically increased in MIC hearts (~2.7 increase). Notably, the more pronounced increase was accompanied by higher expression and activity levels of antioxidant enzymes superoxide dismutase (~15-fold) and glutathione peroxidase (~5-fold) in MIC hearts. The fact that this change in gene expression was not sufficient to attenuate ROS production points out the lack of an efficient adaptive response of the human heart to increased ROS generation, which can aggravate energy-depletion phenotypes.

Collectively, the energy depletion model has therapeutic implications, as interventions that improve cardiac bioenergetics can conceivably prevent the onset of the hypertrophic phenotype due to energetic disruption. Thus, a randomized study in which HCM patients were treated with the metabolic modulator perhexiline, known to shift myocardial substrate utilization from fatty acids to lactate was performed, resulted in 36% higher PCr/ATP ratios

relative to placebo-treated patients. Restoration of energetic state to healthy levels was associated with improvements in exercise capacity (increase in V_{O2} from 22.2±0.2 mL/kg/min to 24.3±0.2 in treated patients versus 23.6±0.3 to 22.3±0.2 mL/kg/min in placebo conditions[361].

Moreover, the worldwide administration of beta-blockers to heart disease patients is in part justified in light of ROS-mediated apoptosis due to stimulation of beta-adrenergic receptors (βARs), as shown in NRVM[362]. In addition drugs such as carvedilol have been shown in clinical trials to be superior to other beta-blockers for the treatment of congestive heart failure, potentially due to its more pronounced antioxidant effects[363]. Thus, development of mitochondrial-targeted antioxidants for prevention and treatment of hypertensive cardiomyopathy is now a major research driver[51].

5.1.2 Contractile force in HCM

As explored in the introduction, several methods to measure contractility of hPSC-CMs have been developed. Among these methods, tension models and hEHTs have been preferentially used to model HCM, and so will be reviewed in this section.

5.1.2.1 Contractility in HCM

One of the most frequently used methods to measure contractility of cardiomyocytes relies on tethering skinned myofibres between a force transducer and a piezoelectric motor followed by the fast switch of the construct between buffers with different calcium concentrations[364], as described in the previous section. Measurement of isometric tension in cardiac strips from explanted hearts enables comparison of force generation in different conditions (HCM patients with different genotypes vs healthy controls).

The first reports of tension measurements were done using *soleus* muscle fibres instead of cardiac explants due to easier sample accessibility and identical β-MHC expression in slow-twitch skeletal (*soleus*) muscle to ventricular myocardial β-MHC in HCM patients[365]. Lankford et al have reported lower isometric force generation values in fibres isolated from patients bearing G741R-MYH7 or R403Q-MYH7 mutations (42% and 56% lower than healthy controls, respectively) while no changes were detected in G256E-MYH7 mutation bearers[366].

However, the suitability of *soleus* muscle samples for tension measurements was recently questioned due to differences in the forces reported in comparison to skinned cardiac biopsies derived from the same patient. This was the case in the R723G-MYH7 mutation, that was previously documented to cause a severely malignant phenotype in patients, as shown by sudden cardiac death at a mean age of 42 years old in one third of a patient cohort, with approximately 23% of the remaining individuals developing progressive heart failure, leading to death or heart transplant[367]. In this regard, Kraft et al reported a ~30% decrease in the

maximum force in R723G-MYH7 cardiomyocytes whereas *soleus* muscle fibres showed 22.8% higher maximum forces[307]. This difference was ascribed to a lower density of myofibrils in cardiac tissues as well as reduced phosphorylation of troponin I and T, myosin-binding-protein C, and myosin-light-chain 2 in R723G-MYH7-myocardium compared to donor, highlighting variations in potential regulatory functions between the two tissue types. A follow-up study from the same group using only cardiac explants from patients bearing different mutations in *MYH7* or *MYBPC3* genes has consistently revealed lower tension forces in HCM samples (21+ 1 kN/m^2) versus healthy controls (36+ 2 kN/m^2), with *MYH7*-mutant samples showing the lowest values with particular emphasis when normalised to myofibril density (73+ 3.7 vs 113+ 5.0 kN/m^2)[368]. Lastly, as mentioned in the previous section, this technology was recently applied to hPSC-CMs, as E848G-MYH7 samples developed ~66% lower maximal isometric tension forces than healthy controls[342].

Furthermore, measurements of generated tension in this system can be complemented by simultaneous ATPase activity assays to estimate energetic costs of contraction, enabling determination of sarcomeric ATP usage efficiency. This was done in [369], showing that tension cost, i.e. ATPase activity during force development, was significantly higher in *MYBPC3* mutant (p=0.01) and *MYH7* mutant patient cardiac muscle strips (p<0.0001) compared with sarcomere mutation-negative HCM patients, at saturating Ca^{2+} concentrations. This data corroborates the energy depletion model by supporting the premise that sarcomeric ATP usage is inefficient in HCM hearts. This report was also validated in multicellular cardiac myofibrils of human R403Q-β-MHC, as they show lower tension generation 11.4±1.1 kN/m^2 relative to non-sarcomeric-mutant HCM patients (24.4±1.6 kN/m^2), as well as maximum ATPase activity (4.4±0.5 and 6.6± 1.2μmol/l/s, respectively), resulting in higher tension cost (2.9±0.2 and 1.8±0.1 μmol/l/s/kN/m^2, respectively)[370]. Interestingly, this difference was not observed in single myofibrils derived from the same tissues, reinforcing the notion that sample preparation may affect the endpoint assay and that a more complex 3D structure can provide a more realistic and physiologically-relevant insight.

In contrast, single molecular analysis of actin-myosin interaction was developed using a laser trap assay (**Figure 5.4**). This method consists coating silica beads with myosin molecules in a surface and optically trapping actin filaments attached to beads. Through the use of an electronic feedback system, the direct measurement of force and displacement that results from the interaction of a single myosin molecule with a single suspended actin filament is enabled[371]. However, data generated from this assay in β-MHC mutant samples has often been contradicted by other reports or techniques. This was reported in [339] where the same group has shown significant differences between myosin extracted from cardiac explants in mice bearing the R403Q-MYH7 mutation vs wild type ones when performing *in vitro* motility assays (2.3-fold higher actin-activated ATPase activity, 2.2-fold greater average force

generation, and 1.6-fold faster actin filament sliding in the motility assay), but no changes in force and displacement in the same samples when using the optical trap assay.

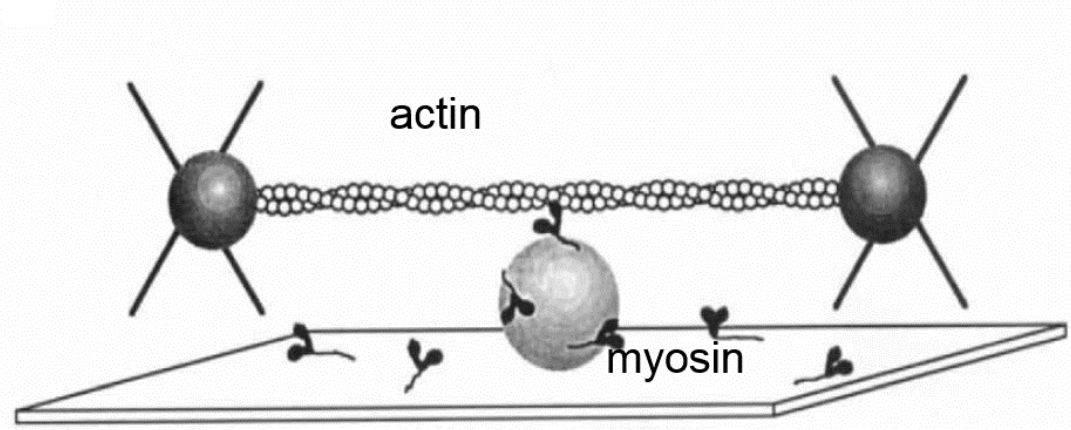


Figure 5.4 - Laser trap assay. Two optical traps are focused on beads attached to a single actin filament. The filament is stretched and lowered onto a silica bead that is fixed to a microscope coverslip and sparsely coated with myosin. The actin-myosin interaction mediated by laser trapping displaces the bead proportionally to the force generated, so that by measuring the bead displacement, estimation of force is enabled. Adapted from [357].

This discrepancy between techniques was extended to human R453C-MYH7 samples. Whereas Sommese et al[372] reported a 30% decrease in the maximum ATPase and *in vitro* velocity, coupled by a 50% increase in the force generated (measured by the optical trap assay), Bloemink et al[373] reported only a few differences in kinetic parameters of actin-myosin interaction, in transient kinetic assays (35% decrease in the rate constants for ATP binding to the motor domain and 3-fold decrease in the ATP hydrolysis step/recovery stroke).

Taken together, comparing data from single molecule mechanics to multicellular myofibrils suggest that the more reductionist models tend to generate less robust conclusions due to the lack of physiological relevance of the model. In this regard 3D hEHTs offer the additional complexity needed to perform analysis of contractile force at the tissue level.

5.1.2.2 Engineered Heart Tissue technology

In most of the methods to analyse cardiac contractility described and analysed in the previous section, the 3D architecture characteristic of a cardiac tissue structure is not recapitulated, resulting in discrepant results when using methods with varying degree of organisation (single molecules vs multicellular constructs). To address this limitation, 3D approaches to incorporate hPSC-CMs have been investigated including cardiac microtissues (CMTs)[374] and EHTs[375]. Briefly, CMTs are based on the incorporation of cardiomyocytes in fibrin/collagen gels tethered to PDMS cantilevers, with direct force reporting being done via a microelectromechanical sensor coupled to the cantilevers.

EHTs were originally described as force-generating cardiac tissue-like structures that constitute a complex and highly functional cardiac construct[375]. EHT fabrication involves encapsulating CMs in fibrin gels between two silicon posts that guide cardiac tissue organization in an aligned conformation (as shown in the Methods section, **Figure 2.1**). The CMs perform contractile work against the silicon posts, thus developing an auxotonic tension that resembles physiological conditions[376] and was shown to enhance hPSC-CM maturation (as reviewed in the introduction). Importantly, functional evaluation of CM contractility can be monitored indirectly in the EHTs by video-optically analysing the deflection of the silicon posts with known mechanical properties (**Figure 5.5**). Notably, EHTs can be loaded with calcium- or voltage-sensitive dyes, enabling functional analysis of calcium transients and electrophysiology[377]. While EHT fabrication requires labour-intensive sample preparation and a lengthy maturation period (at least 2 weeks), data reliability is relatively high in comparison to actin-myosin sliding assays, as shown by typically reproducible results at N=4–8 [378].

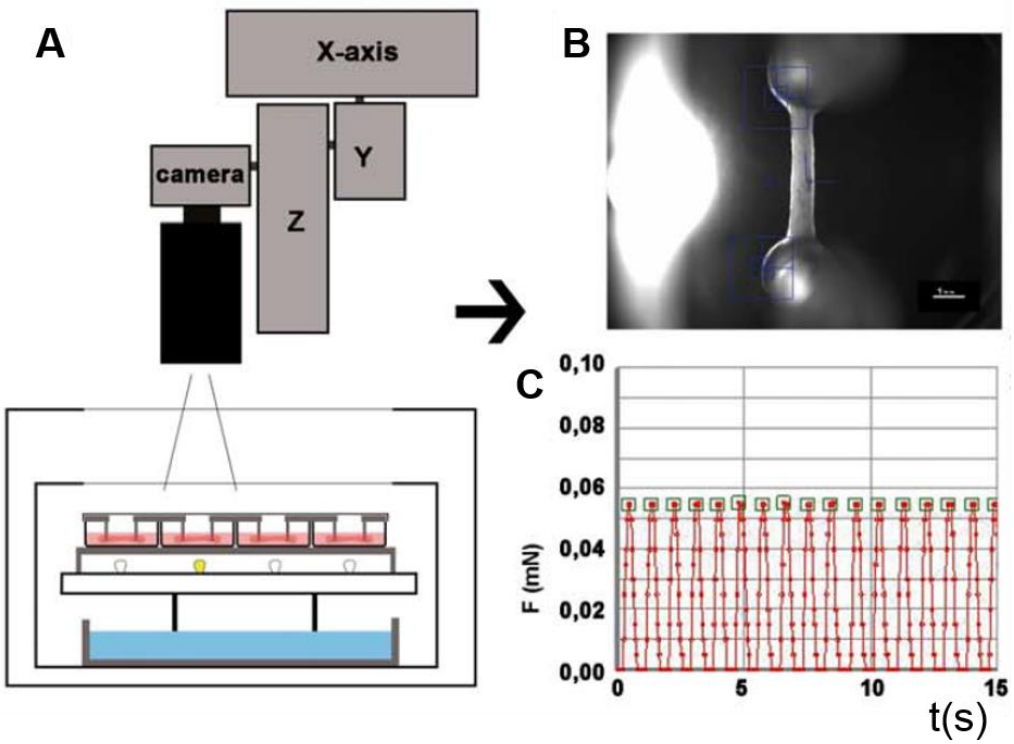


Figure 5.5 - Illustration of measurement of force generation in EHTs. **A)** EHTs in 24 well plates are analyzed by automated video-optical recording, whereby a camera is placed above the incubator and directed to each well by x-y-z-coordinate motor system; **B)** Movies are recorded, automated figure recognition module identifies top and bottom end of each EHT (blue squares). **C)** Based on post deflection, post geometry and elastic propensity, force development is calculated and recorded over time. Contraction peaks are automatically recognized (green squares) and parameters of contraction are calculated. Adapted from [366].

Each of these 3D systems has their own advantages and disadvantages. EHTs are produced in centimetre-scale requiring 0.5-1 million CMs per tissue, which is costly at current

commercial rates of USD$1000/million cells, whereas CMTs operate in a 96-well format, enabling the fabrication of 100-200 CMTs per 1 million cells. However, while the EHT platform enables measurements over several weeks (allowing monitoring chronic effects of drug treatments), long-term evaluation of CMTs is hampered by the difficulties associated with their manual handling. Importantly, both systems enable establishment of dynamic loads by changing the mechanical properties of the silicon posts (EHTs) and cantilevers (CMTs), which can be tuned to mimic heart pathologies[84].

While initial EHT fabrication relied on animal sources such as chicken, mouse and rat, human EHTs (hEHT) using hPSC-CMs are now routinely fabricated[174]. Moreover, tissue fabrication using highly pure cardiomyocyte populations resulted in highly functional (contractile-wise) and drug-responsive constructs, which refuted the initially postulated requirement of native cell types (e.g. cardiac fibroblasts and endothelial cells) to fully recapitulate the heart contractile physiology.

Pharmacological response of EHTs was validated by the screening of more than 50 compounds in ratEHTs[378], as well as hEHTs made from hESC-CMs and commercially available hiPSC-CMs, showing the expected prolongation of relaxation in response to blockers of the hERG-channel (e.g., E-4031, procainamide, sertindole, quinidine)[376]. Thus, the use of hEHTs as a test-bed for drug screening is currently underway, filling the needs of the pharmaceutical industry by providing a humanised platform of the cardiac tissue that partially recapitulates the complexity of the human heart[174].

Besides their use for drug screening purposes, EHTs have been used for disease modeling approaches. The first report consisted in transducing rat cardiomyocytes with adeno-associated virus (AAV) encoding SNPs identified in HCM patients, in the four-and-a-half-LIM domains 1 (*FHL1*) gene[379]. Contractile force analysis of EHTs fabricated using these cells resulted in hyper- and hypocontractile phenotypes depending on the mutation (K455fs-FHL1 showed a 27% increase in force while C276S-FHL1 genotype was associated with a 23% lower force). Evaluation of the beating kinetics of these tissues showed prolonged contraction and relaxation times in both variants (~18% and ~30% longer, respectively)[379]. Similarly, *FHL2* mutations engineered by the same method showing an identical hypercontractile phenotype in rat EHTs (27% higher force in T171M-FHL2 and V187L-FHL2 relative to WT) with a significant increase ($p<0.05$) in the contraction and relaxation times of the first mutation[380]. The same approach was applied to *ANKRD1* variants in rat, showing a stronger phenotype in the T123M-ANKRD1 EHTs (~50% higher contractile force, contraction velocity and relaxation velocity vs wild type) but not discernible phenotypes in the P52A and I280V genotypes[381]. These studies demonstrate varying contractile effects derived from different mutations in the same locus, reinforcing the concept that phenotypes are mutation-specific. This is because changes in amino acid residues associated with different physio-chemical

properties lead to disruption of protein interactions to a variable degree, resulting in phenotypic heterogeneity associated with HCM.

Moreover, fabrication of EHTs from knock-in mice showing heterozygote or homozygote mutations in the *MYBPC3* gene showed ~2.2 fold higher contractile force under electrical pacing, while the homozygous variant exhibited more severe phenotypes such as faster contraction and relaxation times ($p<0.05$). In addition, mutant EHTs had different response to drugs in comparison to WT controls, as evidenced by a blunted response to isoprenaline and EMD57033 (calcium sensitizer) in terms of contractile force[382]. A further iteration of this study relied on additional genetic variants in the *MYBPC3* gene, through the use of AAV in mouse cardiac cells to introduce truncated mutations in this locus[383]. This approach resulted in *MYBPC3*-knockouts that showed ~50% higher maximum contraction force in EHTs. This phenotype was rescued by the restoration of WT-*MYBPC3* expression via AAV-mediated gene transfer, indicating that sarcomeric gene haploinsufficiency is a mechanism associated with the observed phenotypes.

While all these disease modeling examples portrayed EHTs made from animal cells, recent reports have showed human EHT made from cardiomyocytes bearing specific HCM-causing mutations. Firstly, Cashman et al made collagenI/ MT-based EHTs using iPSC-CMs derived from patients exhibiting cardio-facio-cutaneous syndrome (CFCS), which results in cardiac abnormalities including HCM in 40% of the patients. Most patients show mutations in the *BRAF* gene, encoding a kinase involved in the ubiquitous RAS/MAPK pathway. By mixing *BRAF*-mutant iPSC-CMs and $CD90^+$ cardiac stromal cells in a 1:3 ratio, EHT analysis showed a very faint phenotype in terms of contractile force parameters, as some of the initial differences (e.g. ~25% higher maximum force vs unrelated WT patients) dissipated after time (11 days), suggesting the existence of transient effects among more permanent ones (as 25% faster contraction and relaxation times were preserved over time)[384]. In addition, this report points out the importance of refining healthy controls to isogenic pairs, as it is well known that genetic background contributes to the observed phenotypes and clinical outcomes. In this regard, Stillitano et al have used TALENs to correct the R14 deletion of the phospholamban (*PLN)* gene in order to restore the hypocontractile phenotype (40% lower contractile force) exhibited in mutant collagenI/ MT tissues made from iPSC-CMs[385]. However, this report shows only very preliminary characterization of the phenotype which is aggravated by the high variability shown in the tissues. Further, more comprehensive reports of HCM mutations should provide additional insight into the functional and molecular mechanisms underlying hyper- and hypocontractile phenotypes shown using EHTs.

5.1.2.3 Clinical echocardiography and pharmacological intervention

Primarily, indirect investigation of HCM was done directly in patients through echocardiographic tools such as Doppler Tissue Imaging. Clinical data showed that patients bearing mutations in β-MHC locus exhibited marginally higher (13.5%) left ventricular ejection

fractions (LVEF) in comparison to healthy subjects. However, the increased or preserved LVEF in HCM patients can be explained by the concentric nature of the hypertrophy (thickening of the LV walls without increase in heart size), that leads to a smaller LV (end-diastolic volume). Thus, the contractile work required for the myocardium to pump the blood into systemic circulation is reduced (causing similar of higher LVEF)[386], which has been interpreted as a compensatory mechanism to hypocontractile phenotype of cardiomyocytes[36]. Moreover, early diastolic myocardial velocities were significantly lower ($p<0.02$) in HCM patients vs healthy controls[387].

Although these results encompass a low number of patients (<20), attributing parameters obtained by echo-cardiographic measurements to risk-stratify patients (hyper- vs hypo-contractile phenotype with or without affecting diastolic function) can be very useful to more specifically tailor drug treatment regimens to HCM patients. In this regard, 2 drugs have recently been developed towards restoring contractility of the myocardium to normal levels. The small molecule MYK-461 showed to reduce cardiac myofibril contractility by inducing a 90% decrease in the ATPase activity in mice models of β-MHC-mutant HCM[388]. Administration of this compound to these mice showed a trend towards superseding the development of hypertrophy and fibrosis although differences were not always statistically significant. Conversely, Omecamtiv Mecarbil (OM) increases cardiac contractility by accelerating the transition rate of the myosin from the weakly bound to the strongly bound, force-generating state. This resulted in increased cardiac contractility in several pre-clinical and clinical trials already undertaken, by causing a concentration-dependent increase in systolic ejection time, stroke volume and fractional shortening [389].

5.1.3 Calcium transient activity in HCM

Due to its central role in regulating excitation-contraction coupling, calcium homeostasis has been shown to play a central role in the development of HCM. Calcium release from the SR or influx from L-type Ca^{2+} channel (LTCC) triggers actin-myosin interactions that are central to cardiac contraction. Free calcium binds to cardiac troponin C (cTnC) that is part of the regulatory complex attached to the thin filaments. This induces a conformational change in the regulatory complex such that Troponin I (cTnI) exposes a site on the actin molecule that is able to bind to the myosin ATPase located on the myosin head[64]. Calcium efflux mediated by reuptake into the SR via an ATPase (SERCA) as well as into the extracellular space through a sodium-calcium-exchange (NCX) pump then restores the intracellular Ca^{2+} concentration and the sarcomere relaxes, completing the contraction-relaxation cycle[322] (**Figure 5.6**).

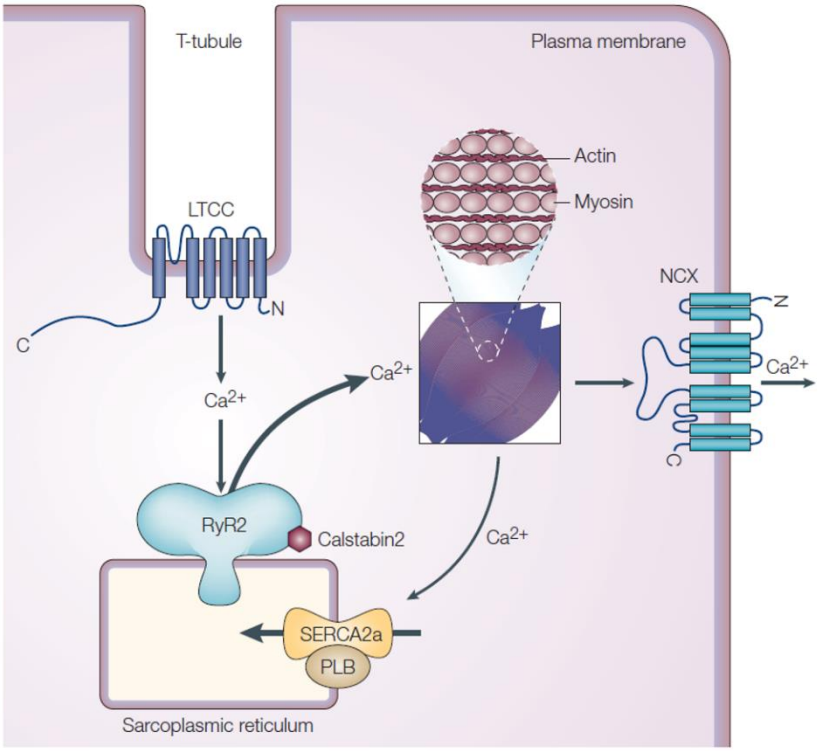


Figure 5.6 - Excitation–contraction coupling (ECC) in the heart. Excitation–contraction coupling in the heart involves membrane depolarization, which activates voltage-gated L-type Ca^{2+} channels (LTCC). Further Ca^{2+} release from the sarcoplasmic reticulum (SR) through ryanodine receptors (RyR2) induces contraction by regulating actin-myosin interactions. To enable relaxation, intracellular Ca^{2+} is re-uptaken back into the SR via SR Ca $^{2+}$-ATPase (SERCA2a), which is regulated by phospholamban (PLB), or extruded from the cell via the Na^{+}/Ca^{2+}-exchanger (NCX), via ATP-dependent mechanisms. Adapted from [58].

Regulation of Ca^{2+} in the heart in terms of magnitude and timing determine the strength of contraction. This process is known to be controlled by phosphorylation of both Ca^{2+}-handling pumps and ion channels[60]. For instance, stimulation of beta-adrenergic receptors by catecholamines triggers signalling cascades which result in subsequent protein kinase A (PKA) activation, which phosphorylates LTCCs and SR receptors phospholamban and ryanodine receptor 2 (*RYR2*)[390]. These events enhance calcium influx from the extracellular space and release from the SR, respectively, leading to enhancement of calcium contractility. Conversely, the unphosphorylated form of PLN regulates Ca^{2+} reuptake into the SR by SERCA2a[391]. Thus, the regulation of the phosphorylation state of Ca^{2+} pumps and receptors by several protein kinases controls ECC and therefore cardiac contractility. Consequently, dysregulation of calcium cycling and/or altered expression, phosphorylation and/or mutation of key proteins involved in the contraction cycle result in pathological states such as HCM[51]. Remarkably, abnormalities in calcium fluxes may result in prolonged calcium transients triggering delayed-after-depolarizations (DADs) or spontaneous calcium oscillations[392] which constitute cardiac arrhythmias that are common in exercise-induced SCD (such as patients displaying catecholaminergic polymorphic ventricular tachycardia (CPVT) due to

mutations in *RYR2* gene[393]). Moreover, alterations in the calcium sensitivity of myofilaments due to missense mutations are the typically observed in HCM patients.

5.1.3.1 Myofilament calcium sensitivity and arrhythmias

Data from transgenic mouse models have clearly linked mutations in sarcomeric genes resulting in HCM with impaired calcium handling properties. Knollmann and colleagues have studied isolated cardiomyocytes, perfused hearts and whole mice bearing the human I79N-cTnT mutation, showing shortened ventricular action potentials, only at 70% repolarization (APD70, 14±1.2ms in I79N-cTnT, vs 23±2.2ms in control. Notably, Ca^{2+} transients of electrically-stimulated ventricular I79N- cTnT myocytes were measured using a fluorescent calcium indicator dye (Fura-2-AM) and showed reduced intensity (fluorescent amplitude F340/F410, I79N-cTnT 0.44±0.06 vs control 0.85±0.07) and slow decay kinetics (I79N-Tg 374±28 ms vs control 191±11 ms), consistent with increased Ca^{2+} sensitivity of I79N mutant fibers[392]. Moreover, the same group has later demonstrated that ventricular tachycardia could be induced by calcium-sensitizing agents (such as EMD57033) and prevented by the calcium desensitizer blebbistatin in the same animal model, indicating that myofilament calcium sensitization was underlying arrhythmias[394].

The tension models described in the previous sections to estimate cardiac bioenergetics and contractile forces have also been applied to investigate calcium sensitivity of myofilaments in HCM, by changing the Ca^{2+} concentration of the buffer solutions where the myofibres are immersed[364]. The work developed by Kraft et al in skinned myofibres from human cardiac explants bearing the R723G-MYH7 mutation has shown a modest increase in calcium sensitivity relative to healthy controls (pCa50 of 5.56±0.01 vs 5.51±0.02), provided that a hyperphosphorylation state of several sarcomeric proteins (cTnI/T, MYBPC and MYL2) is maintained by PKA-mediated activity[307]. However, in a subsequent study, no differences in myofilament calcium sensitivity were detected in PKA-treated myofibres derived from patients bearing *MYH7* or *MYBPC3* mutations relative to controls, despite displaying lower contractile forces[368]. This observation questions the involvement of calcium sensitivity to the development of a hypocontractile hypertrophic phenotype. This concept was further emphasized in the work performed by Kirschner and colleagues that showed a high variability in the pCa_{50} between individual fibres, although there was a clear trend towards lower pCas50 (lower calcium sensitivity) in R723G-MYH7 and R719W-MYH7 *soleus* muscle fibers and a higher calcium sensitivity of I736T-MYH7 ones[395]. Although technical limitations cannot be ruled out (sample preparation constraints) in explaining this result, individual fibre variation in the same muscle is likely to cause imbalances in force generation thus causing contractile dysfunction and disarray in the myocardium. In addition, this finding reinforces the phenotypic variability associated with HCM as different mutations in the same gene have cause opposite effects. Lastly, analysis of an additional mutation E848G-MYH7 in hiPSC-CM myofibrils showed a decreased reduction of tension generation in the mutant line (28%) versus the

healthy line (50%) in lower calcium conditions, indicating higher myofilament Ca^{2+} sensitivity[342].

Alternative methods to measure arrhythmic events in calcium transients rely on confocal line-scans of cardiomyocytes treated with fluorometric dyes. Lan et al have used this method to investigate Ca^{2+}-transient irregularities in Fluo-4-labeled R663H-MYH7-hPSC-CMs[161]. Remarkably, unlike healthy controls, mutant cardiomyocytes displayed multiple events and tachyarrhythmia-like waveforms leading to a ~3-fold increase in the percentage of cells displaying irregular Ca^{2+} transients and putative DADs, which were further aggravated in high calcium concentrations and upon positive inotropic stress. Similar abnormal calcium handling was also verified in another model of Rho2-AM-labeled R442G-MYH7-hPSC-CMs, as 20% of the cells exhibited irregular Ca^{2+} transients (vs virtually none in healthy controls). Moreover, mutant cardiomyocytes showed a 21% increase in the resting Ca^{2+} concentration and 50% lower Ca^{2+} release from the SR upon caffeine treatment relative to wild type controls, likely due to lower *RYR2* and *SERCA2A* expression levels[162]. These findings may be explained by the energy depletion model, as energy deficit in HCM cardiomyocytes leads to increased cytosolic Ca^{2+}, due to the disruption of highly energetic processes such as Ca^{2+} reuptake into the SR and extrusion via LTCC.

Moreover, calcium transient analysis was also performed in Fura2-labeled EHTs by measuring the F340/F380 ratio of calcium-labeled tissues using a fluorescent microscope. This analysis is based on the ratiometric nature of the dye: calcium-bound Fura-2 has peak excitation at 340 nm and emits at 510 nm whereas Ca^{2+}-free Fura-2 has peak excitation at 380 nm and also emits at 510 nm. Thus, by plotting the ratio of fluorescence obtained by UV-excitation at 340 vs 380nm wavelengths, calcium transients can be analysed. This system was initially applied to EHTs made from different animal sources, showing varying sensitivity to external Ca^{2+} (EC_{50}: 0.15, 0.39, and 1.05 mM Ca^{2+}) of rat, mouse, and human EHTs, respectively[377]. Furthermore, using this method, EHTs made from *Mybpc3*-mutant mice were shown to display two fold-higher sensitivity to calcium, as evidenced by lower EC_{50}s of force generation than WT (0.34mM for homozygous, 0.48mM for heterozygote vs 0.66mM for WT)[382]. This data was further corroborated by the tension model showing lower 30% EC_{50} of AAV-induced *Mybpc3*-knockout rat EHTs relative to WT controls[383].

Collectively, changes in myofilament calcium sensitivity are involved in some HCM phenotypes, depending on the mutation site and locus affected. For this, pharmacological intervention is available in order to decrease or increase calcium sensitivity to healthy values. In this regard, Levosimendan was shown to interfere with the interaction between cTnC and cTnI towards increasing myofilament calcium sensitivity, despite having secondary effects such as phosphodiesterase 3 inhibition[396]. Importantly, calcium sensitizers like Levosimendan improve contractility without a proportional increase in the myocardium energy consumption[397], as, upon treatment, ECC can occur at lower (previously inert) calcium

concentrations. Levosimendan clinical efficacy was already demonstrated in clinical trials, as 24h administration led to a 40% increase in cardiac output relative to placebo controls[398]. Conversely, green tea-derived epigallocatechin-3-gallate (EGCg) interacts with cTnC causing calcium desensitizing effects, as shown by lower pCa_{50} relative to untreated (5.2 vs 5.82) in tension models using skinned mouse myofibres[399]. Furthermore, treatment of a transgenic mouse model bearing the R193H-cTnI mutation with EGCg showed improvement in diastolic function (decrease in isovolumetric relaxation time towards healthy levels) due to mild decreases in sarcomere relaxation time (~12%) and calcium decay rate (~10%), without changes in the systolic function[400].

5.1.3.2 Genetically-encoded calcium indicators (GECIs)

Most of the data obtained by optical mapping of calcium transients relies on staining cardiomyocytes with fluorescent dyes. Although they offer a practical solution to visualize the propagation of calcium waves, fluorescent dyes are inherently phototoxic, which can cause temporal degradation of sample and signal quality over time, thereby limiting recording times[401]. Thus, genetically-encoded calcium indicators (GECIs) were developed resulting in sustained detection of calcium transients[401]. Different GECI versions were developed featuring various spectral properties of excitation/ emission, different calcium binding affinities and kinetics, resulting in intensiometric (e.g. R-GECO1) and ratiometric indicators (e.g. GEM-GECO)[401]. As described above, the latter enables the distinction between bound and free calcium in the cell and provides the advantages of being quantitative and less prone to artefacts. However, both fluorometric dyes and GECIs contribute to cytosolic Ca^{2+} buffering capacity, by sequestering Ca^{2+} ions and preventing their interaction with sarcomeric proteins in the excitation-contraction cycle. The extent of Ca^{2+} buffering in NRVM was quantified in [402], showing values averaging 2 µmol/L, which is at least 50x lower than the value reported in physiological cytoplasm (≥100 µmol/L)[403] and at least one order of magnitude lower than small fluorescent dyes.

Overall, GECIs offer several advantages over conventional fluorescent dyes such as: **i)** almost no unintended compartmentalization; **ii)** homogeneous expression in cells, enabling imaging at the tissue/organ level; **iii)** cell-type–specific Ca^{2+} mapping through promoter-driven expression; **iv)** subcellular targeting by the expression of fusion proteins; and **v)** the possibility for extended imaging over days and weeks, enabling the investigation of chronic treatments[404].

Delivery of the DNA vector bearing the calcium indicator into cardiomyocytes has been optimized. Biological transfection reagents (such as lipofection) are notoriously inefficient in terminally differentiating (non-dividing) cells such as cardiomyocytes[405]. Thus, viral transduction methods have been used such as lentivirus, achieving a high transduction efficiency (>97%), although protein expression only reached detectable levels after 1 week[406]. Adenoviruses have then been engineered for this purpose resulting in protein

expression of the genetically encoded fusion proteins or biosensors to optically detectable levels within 24 hours, with sustained levels during 1 week[407]. However, use of viral methods may result in patchy transduction patterns as not all of the cells are successfully transfected and may have different copies of the vector, which may confound the subsequent calcium transient analysis.

Nevertheless, a considerable number of approaches have employed viral-mediated gene transfer of GECIs into cardiomyocytes to analyse calcium handling properties, as reviewed in[404]. In addition, the same principle can be applied to voltage indicators, which has resulted in models bearing dual genetically encoded calcium and voltage sensors. For instance, Song et al have transfected the intensiometric R-GECO1 and the genetically encoded voltage indicator ArcLight into Timothy syndrome patient-derived hPSC-CMs using lentivirus transduction[408]. LQTS-diseased cardiomyocytes showed irregular calcium transients and significantly prolonged action potentials relative to healthy controls ($p<0.01$), which were rescued by roscovitine treatment. Moreover, Shinnawi and colleagues have engineered a similar lentiviral-based transduction system to deliver GCaMP5G to hiPSC-CMs, which proved to be superior to the fluorescent dye Rhod-3-AM in detecting calcium transients (~5-fold increase in signal to noise ratio and ~13-fold higher photostability), although the transient kinetics were slightly slower than those of the dye (calcium rise time of 277±32ms vs 218±23ms) in line scan recordings[409]. Finally, the authors applied this tool to model CPVT2 hiPSC-CMs bearing a homozygous mutation in the calsequestrin gene (D307H), showing arrythmogenic activity in 20% of the cells which was exacerbated with isoprenaline treatment. Taken together, GECIs are a useful system to add to the disease modeling toolbox.

5.1.4 Autophagy in HCM

As previously discussed in this thesis, HCM-associated missense mutations can often lead to dominant-negative consequences of sarcomeric proteins (poison peptide), whereas truncating mutations (more common in *MYBPC3* gene) often led to haploinsufficiency. Thus, cardiac remodelling processes triggered upon HCM (initiated during the compensatory phase) may alter the regulation of protein synthesis and degradation, potentially leading to the accumulation of toxic proteins[410]. In order to ensure that these aberrant proteins are either repaired of removed from the cytoplasm, two main cellular mechanisms are activated, the ubiquitin-proteasome system (UPS)[411] and autophagy-lysosomal pathway (ALP)[412].

Remarkably, these protein homeostatic pathways that ensure adequate protein turnover in the cell have shown to be involved in the context of HCM[413], thus rendering them therapeutic candidates. UPS-mediated protein degradation relies on ubiquitination of target proteins followed by proteolysis by the 26S protesome, in an ATP-dependent multistage process[414]. In a gene transfer model of rat cardiomyocytes, truncated cardiac MyBP-C proteins were shown to be unstable and not fully incorporated into the sarcomere (analysed by

immunofluorescence), which resulted in their degradation by the UPS[415]. Importantly, prolonged degradation of mutant MyBP-C led to impairment of UPS function. A similar effect was seen by missense mutations E334K-MYBPC3 in the same model, leading to accumulation of pro-apoptotic proteins (~50% higher *Bax* expression relative to WT control)[416]. Corroborating these findings, data from tissue biopsies of HCM patients (mostly bearing *MYBPC3* mutations) showed a reduction in the proteasome activity in comparison to nonfailing hearts ($p<0.01$)[417]. Thus, it has been postulated that UPS impairment in HCM interferes with homeostatic protein turnover and elimination of poison peptides, resulting in accumulation of aberrant and misfolded proteins, as well as common targets of the UPS system such as pro-apoptotic and pro-hypertrophic proteins, ultimately leading to proteotoxicity that exacerbates disease phenotypes[410].

While the UPS plays a major role in degrading the majority of proteins (including sarcomeric ones), the ALP is involved in the removal and recycling of long-lived proteins and aggregates as well as whole organelles such as mitochondria. Mechanistically, the ALP is based on the engulfment of proteins or organelles into vesicles named autophagosomes that subsequently fuse with lysosomes to degrade the incorporated constituents via proteolytic activity[412,418] (**Figure 5.7**).

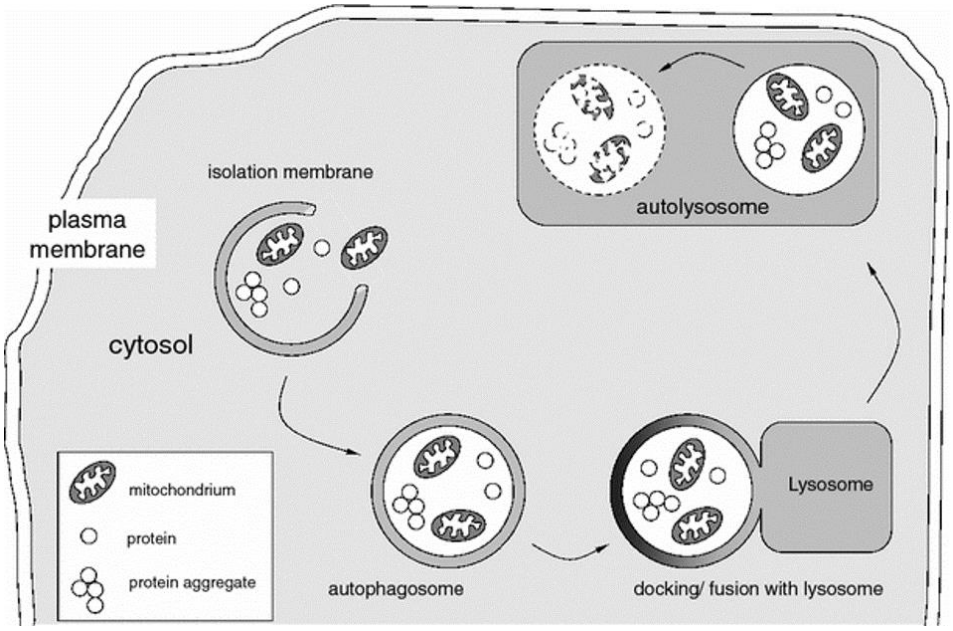


Figure 5.7 – Autophagy-lysosomal pathway. Mitochondria and misfolded proteins or protein aggregates are engulfed by autophagosomes which then fuse with lysosomes to form autolysosomes where the cargo is degraded by enzymatic action. Adapted from [409].

While the role of autophagy in HCM progression is not as explored as that of UPS (as the latter is the main degradation system for sarcomeric proteins), electron microscopy analysis of an endomyocardial biopsy derived from an HCM patient in transition to heart failure has

shown large areas containing autophagic vacuoles which engulfed mitochondria[419]. Moreover, autophagosomes also included glycogen granules and tubulofilamentous inclusions which where concomitant with myofibrillar loss in cardiomyocytes, indicating whole myofilament degradation by ALP. Remarkably, these observations were corroborated in a separate report performed in a cardiac tissue biopsy from an HCM patient showing very high blood plasma levels of BNP (600 pg/ml)[420]. However, none of these studies employed genetic profiling to determine HCM-causation.

Furthermore, truncating mutations in the lysosomal-associated membrane protein 2 (*LAMP2*) lead to compromised autophagy, as this protein is required for the maturation of autophagosomes and fusion with lysosomes[421]. Interestingly, this results in Danon disease, which causes a phenocopy of HCM including extensive cardiomyocyte vacuolation and myofibrillar disruption[422], therefore highlighting the link between autophagy and HCM.

Taken together, both UPS and ALP mechanisms are related to HCM disease progression. Thus, changes in gene expression coordinating autophagic response were also explored in this chapter, in order to further elucidate molecular mechanisms associated with HCM.

5.1.5 Chapter aims and objectives

The previous chapter was focused on the use of high-throughput platforms to interrogate the HCM phenotype in gene-edited cardiomyocytes. Several clear changes were observed in diseased cell lines such as increase in multinucleation, BNP expression, volume and sarcomeric disorganisation. In this chapter, further phenotypic analysis was carried out by performing functional assays dedicated to probing cardiac functions such as contractility, calcium handling and metabolism. Finally, a medium-scale gene expression study was performed to identify putative molecular mechanisms involved in the observed HCM phenotypes in the gene-edited lines generated.

5.2 Results

5.2.1 Mitochondrial respiration

In order to test if the energy depletion model is applicable to the R453C-MYH7 gene edited lines generated, mitochondrial function was assessed by measuring OXPHOS of hPSC-CMs in a Seahorse platform. As shown in the schematic in **Fig5.8A**, this platform measures oxygen consumption rates (OCR) of confluent monolayers of cells, first in basal conditions and thereafter upon sequential addition of electron transport chain inhibitors. Thus, the treatment sequence, with the 5 measurable outputs in ***bold***, is 1) ***basal*** recording; 2) oligomycin, which is an ATP synthase inhibitor to provide information on ***ATP production*** and ***proton leak***; 3) FCCP, which is an uncoupler and reports on ***maximal respiration***; 4) rotenone, an inhibitor of complex 1 of the electron transport chain to give data on ***spare capacity***.

This sequence was used to derive the mitochondrial respiration profiles of cardiomyocytes produced from the parental and engineered MYH7 hPSC lines (**Fig 5.8B,C**). AT1 lines showed the most pronounced differences, with a significant increases of 2.5-3-fold in the basal respiration (**Fig. 5.9A**) and of ~1.75-2.75-fold in the maximal respiration (**Fig. 5.9B**) of all four of the gene-edited hPSC-CMs relative to WT controls. This reflected in ~3-fold higher ATP production rates in mutant lines (**Fig5.9C**) as well an overall similar increase in spare capacity (**Fig5.9D**). Finally, the lines showing the most extensive mutation loads also showed significantly increased non-mitochondrial respiration rates ($p<0.05$). Notably, there was a general association between increase in mutation load and basal respiration and/or maximal respiration rates (i.e. order of WT < heterozygote < homozygote < KO < homozygote+MYH6-FS), supporting the energy depletion model.

For REBL-PAT, both heterozygote and homozygote R453C-MYH7 hPSC-CMs exhibited increased maximal respiration rates vs WT controls, albeit to a lesser but significant level of 40% (**Fig. 5.10B**). Although there were similar trends to AT1 lines in terms of the remaining parameters of mitochondrial respiration, these did not achieve statistical significance, with the exception of higher spare capacity of homozygous line ($p<0.05$), **Fig5.10A-E**.

5.2.2 Mitochondria content

To further understand whether increased mitochondrial respiration capacities in gene-edited lines were reflected by an increased mitochondrial content, the ratio between mitochondrial vs nuclear DNA was quantified by qPCR, as described in iPSC models of genetic insulin resistance [259]. Interestingly, edited lines showed a decreasing trend for mitochondrial:nuclear DNA ratio in both mitochondrial-specific probes (NADH dehydrogenase 1 and 2, ND1-2) relative to their isogenic controls (**Fig5.11A,C**), reaching significance ($p<0.05$) for the mostly compromised AT1 lines. In addition, flow cytometry analysis of Mitotracker®-labeled cardiomyocytes corroborated these data as evidenced by the lack of statistically significant differences in signal intensities between healthy and diseased lines (**Fig 5.11B,D**), showing a negative trend in the AT1 MYH7$^{-/-}$ line.

5.2.3 ROS production

Next, in order to ascertain if the observed increases in mitochondrial respiration without changes in mitochondrial content led to the generation of ROS, flow cytometry analysis of CellROX and MitoSox-labelled cardiomyocytes was performed. Overall, in AT1 lines there were no statistically significant differences in ROS production between diseased and healthy lines, despite an increasing trend of CellROX signal intensity between *MYH7* homozygous and MYH7 knockout relative to the WT control (**Fig 5.12A,B**). This was also true for the REBL-PAT lines except for the homozygous line showing statistically significant increase in CellROX signal intensity ($p<0.01$) (**Fig5.13A,B**).

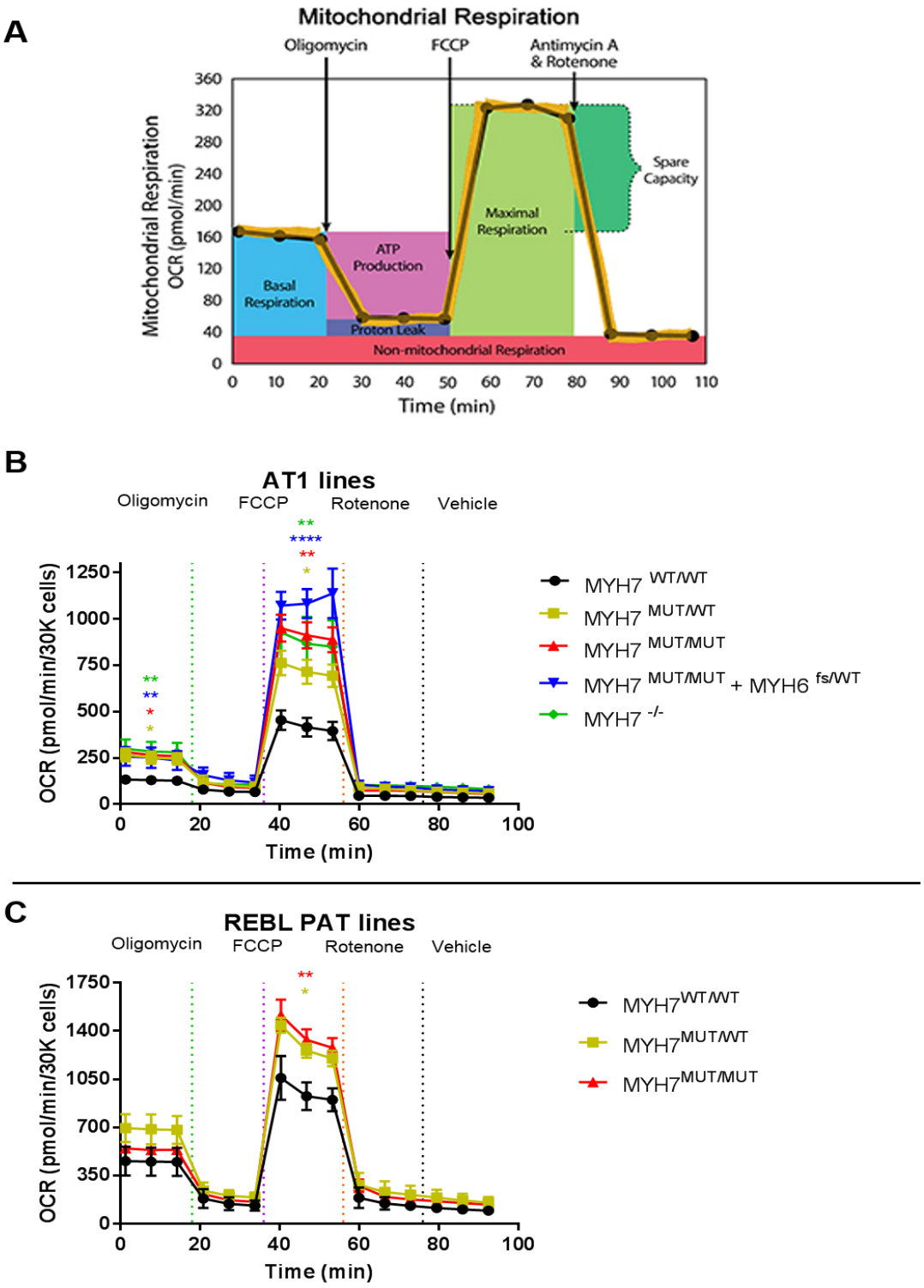


Figure 5.8 - Functional analysis of mitochondrial respiration in R453C-MYH7 hPSC-CMs using the Seahorse platform. A) test profile of the key parameters of mitochondrial respiration. Sequential compound injections enable measurement of basal respiration, ATP production, proton leak, maximal respiration, spare respiratory capacity, and non-mitochondrial respiration (adapted from manufacturers' user guide). Mitochondrial respiration profile of **B)** AT1 and **C)** REBL-PAT lines show increased basal respiration and maximal respiration rates in all edited lines relative to the isogenic controls. * p<0.05; ** p<0.01; ***p<0.005; ****p<0.0001, of the corresponding parameter between mutant lines and healthy controls, N=5)

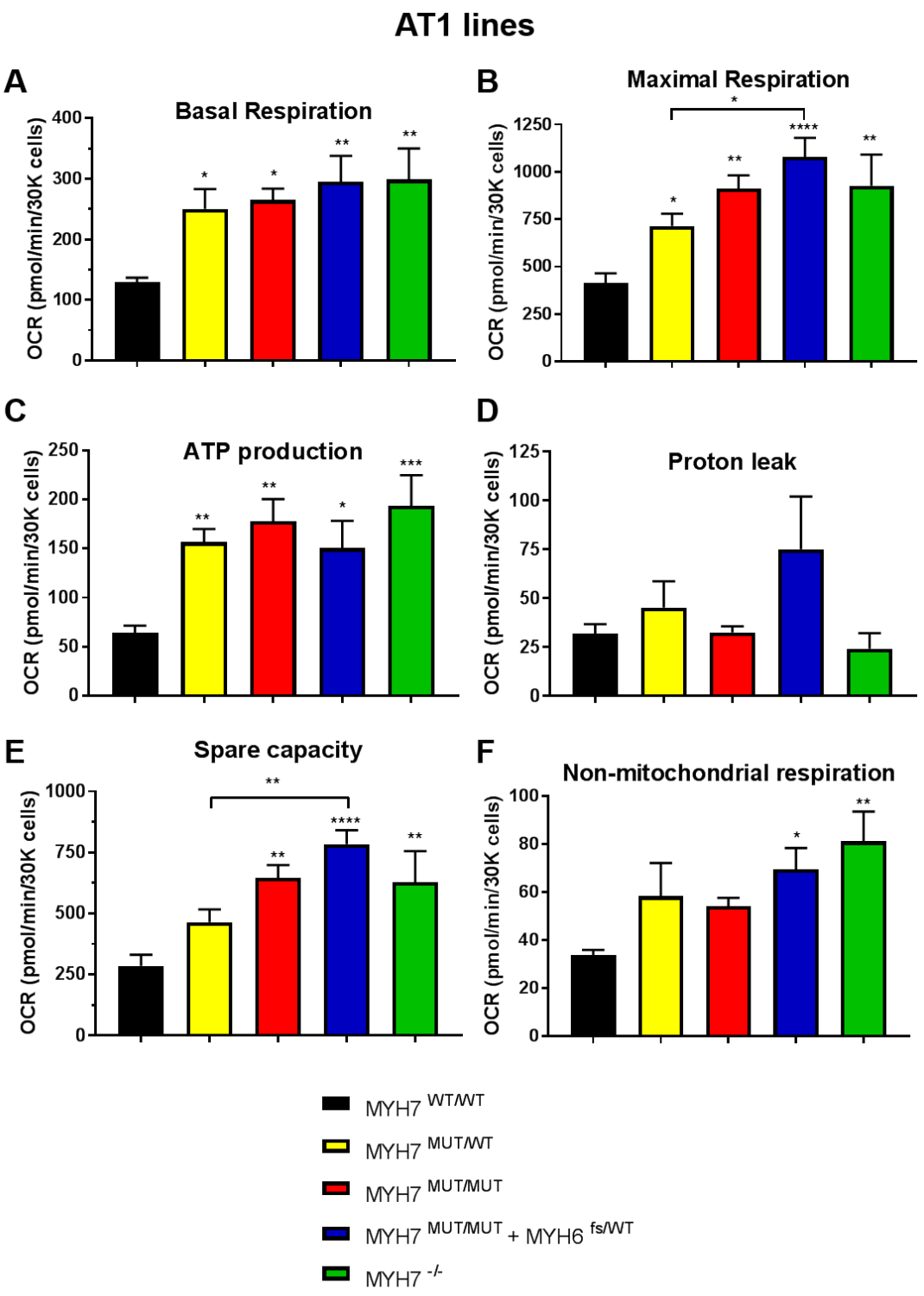


Figure 5.9 Mitochondrial respiration parameters of AT1-R453C-MYH7 cardiomyocytes, measured using Seahorse platform. AT1 lines showed differences in both **A)** basal respiration (~2.5-3-fold increase) and **B)** maximal respiration rates (~1.75-2.75-fold increase) between gene edited cardiomyocytes and isogenic controls, which reflected in ~3-fold higher ATP production rates **(C)** and spare capacity **(E)**. There were no changes associated with **D)** proton leakage and only two of the lines showed **F)** significantly increased non-mitochondrial respiration rates * p<0.05; ** p<0.01; ***p<0.005; ****p<0.0001, of the corresponding parameter between mutant lines and healthy controls, unless otherwise indicated by capped lines; N=5.

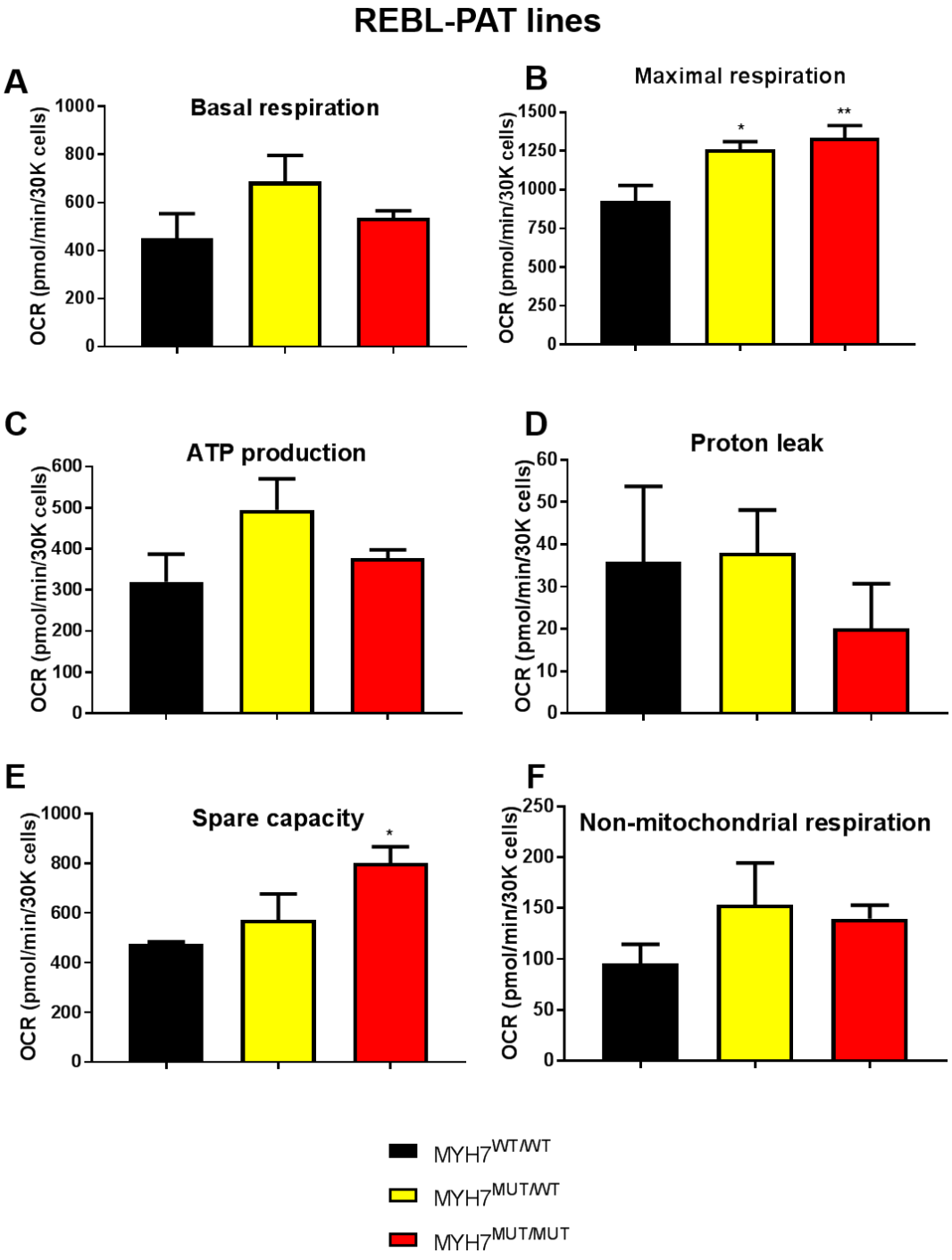


Figure 5.10 - Mitochondrial respiration parameters of REBL-PAT R453C-MYH7 cardiomyocytes, measured using Seahorse platform. REBL-PAT lines displayed higher **B)** maximal respiration rates relative healthy (WT) controls (~40% increase). Although there were similar trends to AT1 lines in terms of the remaining parameters of mitochondrial respiration, these did not achieve statistical significance, with the exception of **E)** higher spare capacity of homozygous line. * $p<0.05$; ** $p<0.01$; of the corresponding parameter between mutant lines and healthy controls; N=5.

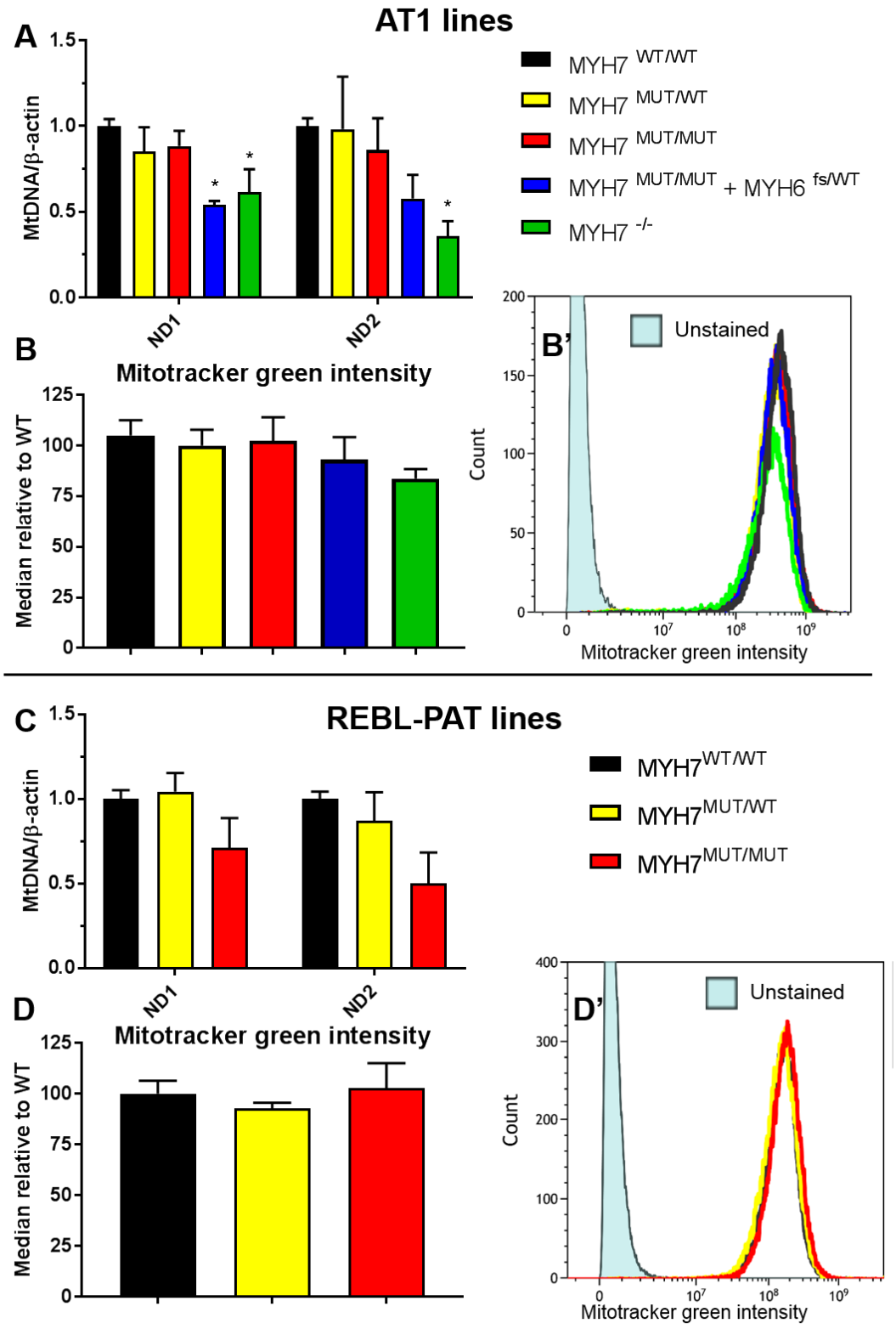


Figure 5.11 - Quantification of mitochondrial content in HCM lines. qPCR analysis of the ratio of mitochondrial (*NT1-2*) /nuclear (*ACTB*) DNA showed a decreasing trend of mitochondrial content in both **A)** AT1 and **C)** REBL-PAT lines, with some of the AT1 lines showing statistically significant differences (N=3 for all lines). **B,D)** Flow cytometry analysis of Mitotracker®-labelled cardiomyocytes of each lines did not show any differences in mitochondrial content between lines (**B',D'** showing representative histograms of signal intensity for AT1 (N=5) and REBL PAT lines (N=7), respectively). * $p<0.05$ between diseased lines and healthy control.

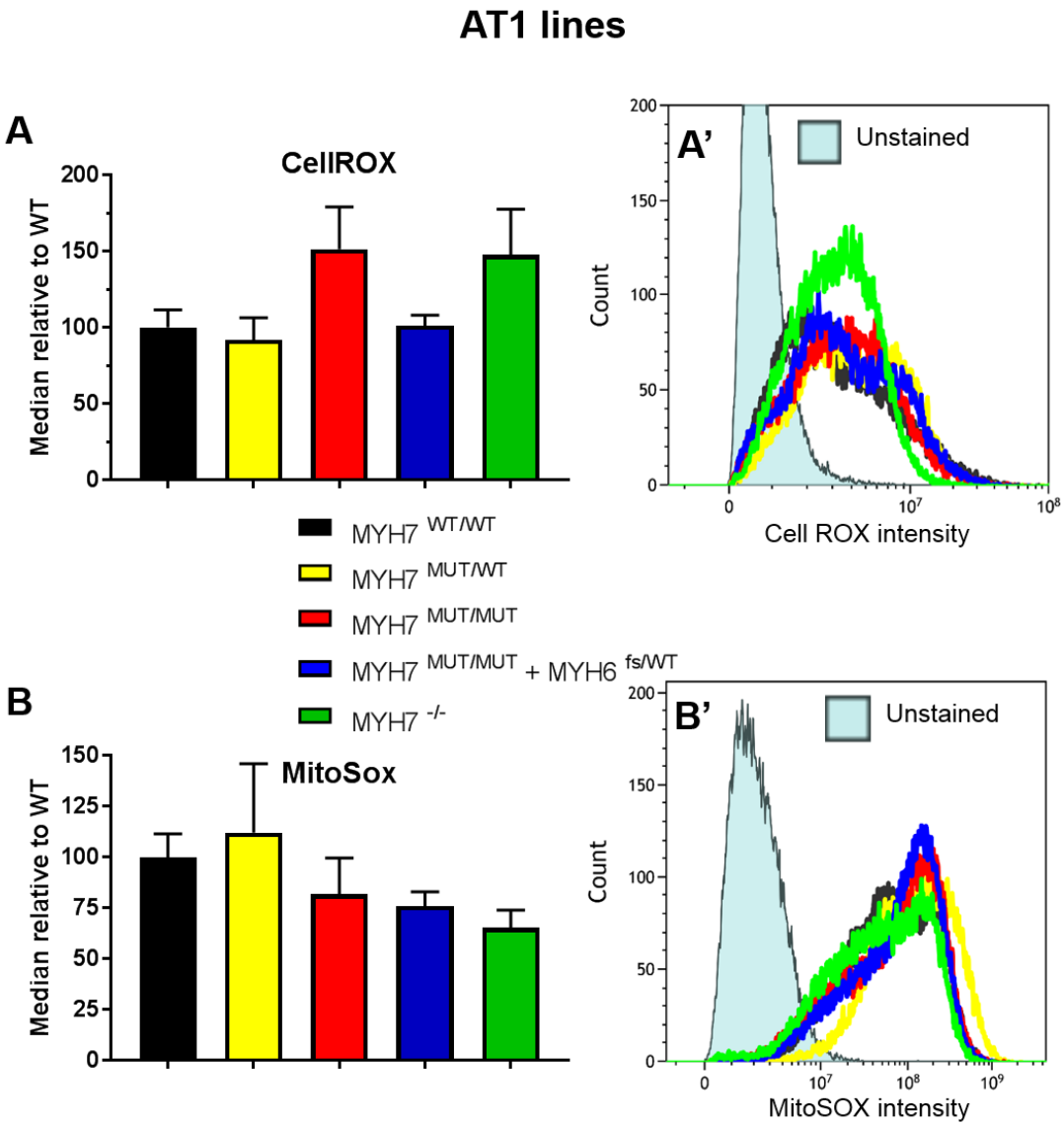


Figure 5.12 - Quantification of ROS production in HCM AT1 lines by flow cytometry. Signal intensity of CellROX **(A)** and MitoSOX **(B)** labelled cardiomyocytes did not show any statistically significant differences in AT1 lines (N=5). **A'-B'** show representative histograms of signal intensity of each sample/dye.

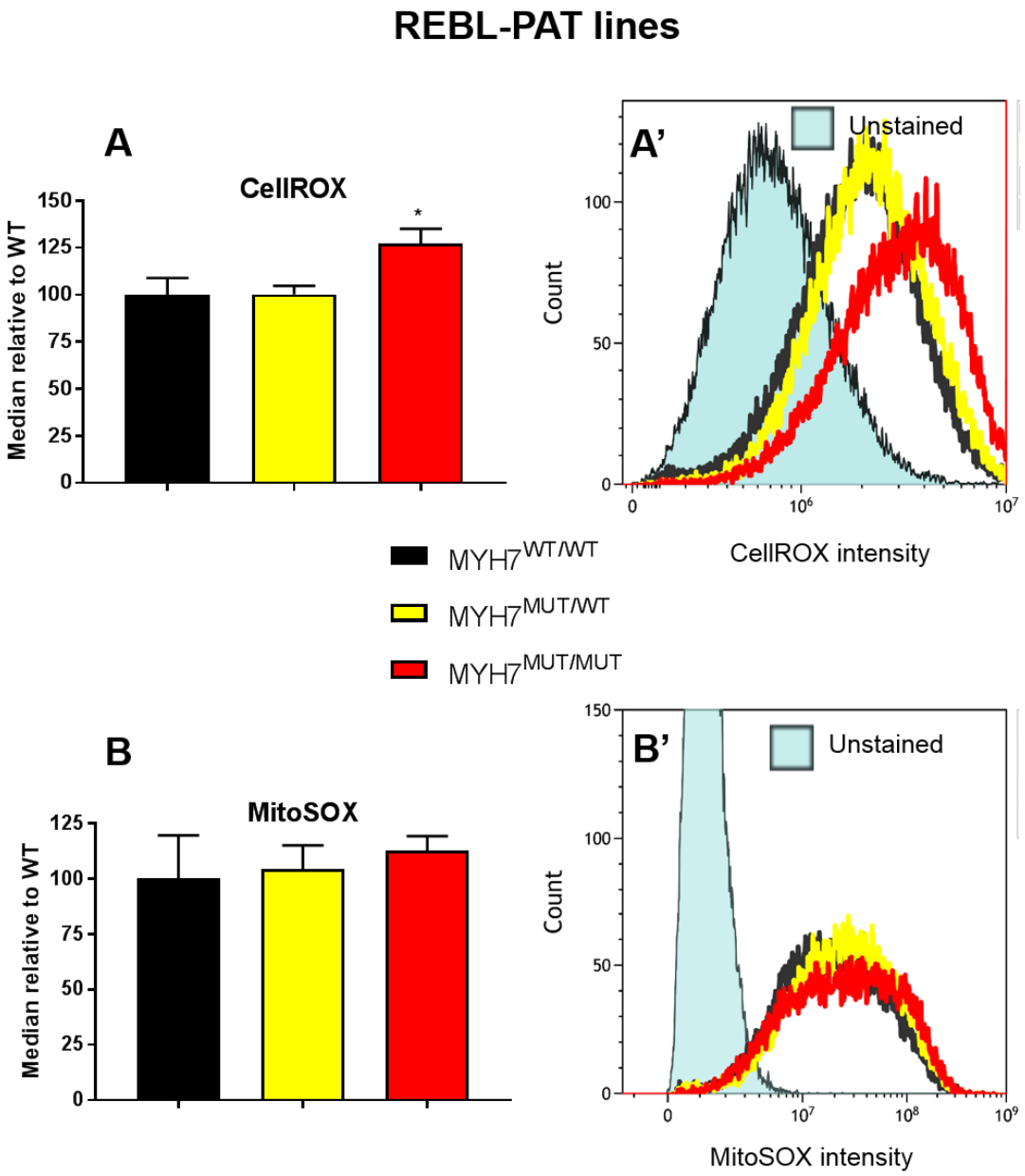


Figure 5.13 - Quantification of ROS production in HCM REBL-PAT lines by flow cytometry. Signal intensity of CellROX **(A)** and MitoSOX **(B)** labelled cardiomyocytes did not show any statistically significant differences in REBL-PAT lines (N=7) with the exception of homozygous R453C-MYH7 hPSC-CMs that showed an increase in CellROX signal intensity. **A'-B'** show representative histograms of signal intensity of each sample/dye.

5.2.4 Genome engineering of R-GECO in HCM lines

As calcium handling irregularities were consistently associated with HCM, calcium transient analysis was performed by precision targeting of a GECI into the safe harbour locus *AAVS1* using CRISPR/Cas9, followed by subsequent confocal line scan evaluation of gene-edited cardiomyocytes (courtesy of Jamie Bhagwan, PhD student). A plasmid-based nickase CRISPR/Cas9 approach was used to insert a CAG promoter-driven R-GECO1 intensiometric Ca^{2+} indicator in the *AAVS1* safe locus (**Fig5.14A**). PCR-genotyping of left and right homology arms (**Fig5.14B**) with further validation by sequencing joining regions with the targeting vector (**Fig5.14C**) confirmed successful gene editing in the previously generated REBL-PAT hiPSC lines (WT, R453C-heterozygote and R453C-homozygote). Determination of mono- vs bi-allelic targeting success was done by PCR-amplifying the *AAVS1* target locus, which is only possible in untargeted alleles (**Fig 5.15A,** due to the existence of highly repetitive sequences in the targeting construct). While monoallelic targeting efficiencies ranged from ~15-66% (**Fig 5.15C**) bi-allelic targeting (3.6% efficiency) was only achieved in WT line (**Fig 5.15B**, highlighted by yellow arrows). R-GECO protein expression in hPSC-CMs was then confirmed by ICC (**Figure 5.16**).

5.2.5 Calcium transient activity

Having confirmed successful gene targeting of the *AAVS1* locus and R-GECO protein expression in hPSC-CMs, confocal line scans were performed in REBL-PAT cardiomyocytes. **Figure 5.17** depicts representative line scans of each *MYH7* genotype, with each image being taken every 75ms for 300s in spontaneously beating REBL-PAT-cardiomyocytes, across a line drawn across fluorescence-emitting (mediated by R-GECO function) cardiomyocytes **(Fig5.17A)**. Broadly, R453C-MYH7 homozygous cardiomyocytes (**Fig5.17D**) showed smaller peaks between full peaks indicating DAD-like events (highlighted in red arrows).

The average fluorescence intensity of each line was calculated over time to generate a confocal line-scan trace. Traces were then filtered and automated quantification of median peak height analysis using ClampFit® and Excel™ softwares of confocal line scans was performed. Any calcium transient events that were below 75% of the peak height were considered ‘abnormal’ (DAD-like), including those that did not return to baseline and gave a ‘double peak’.

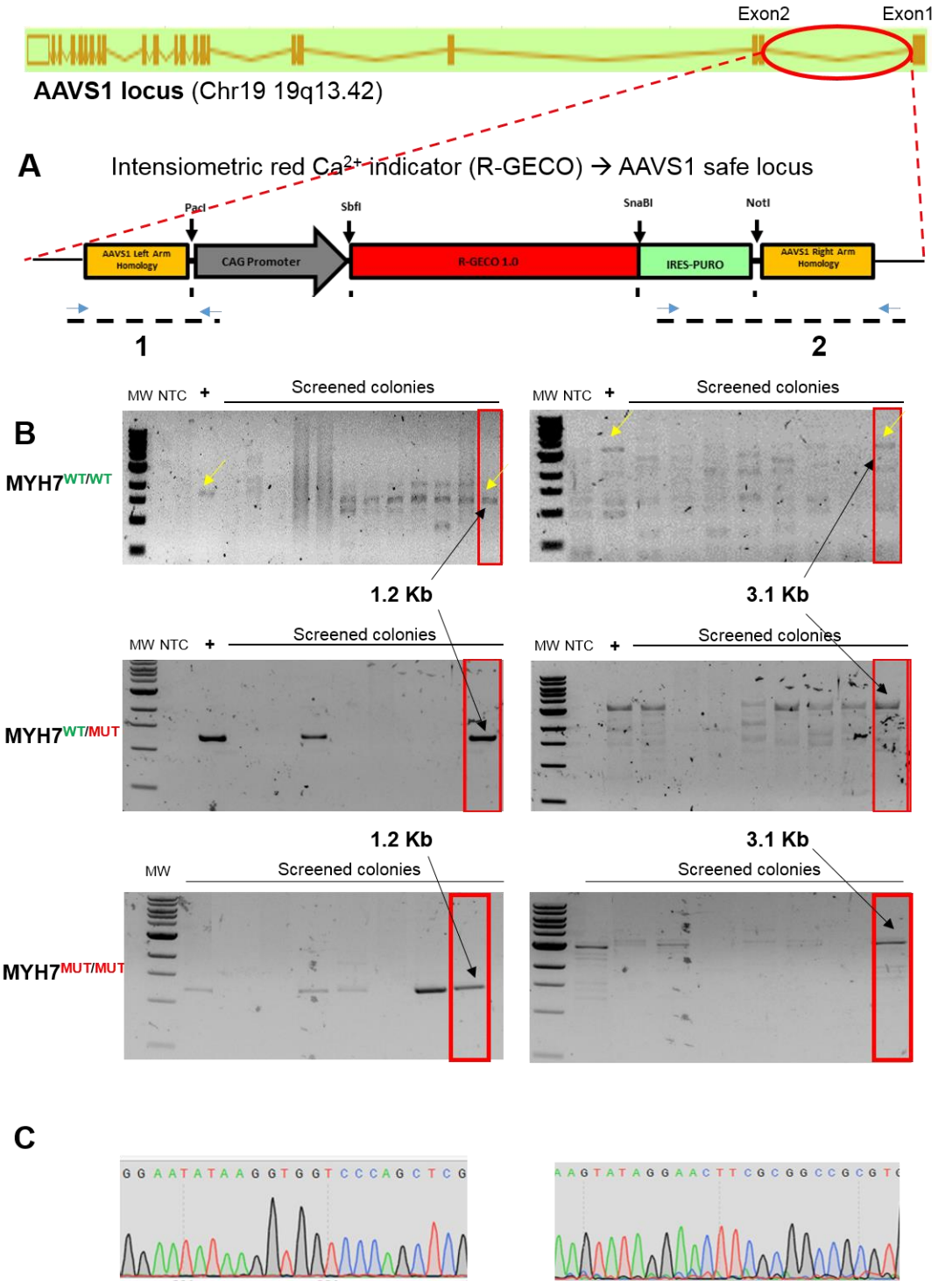
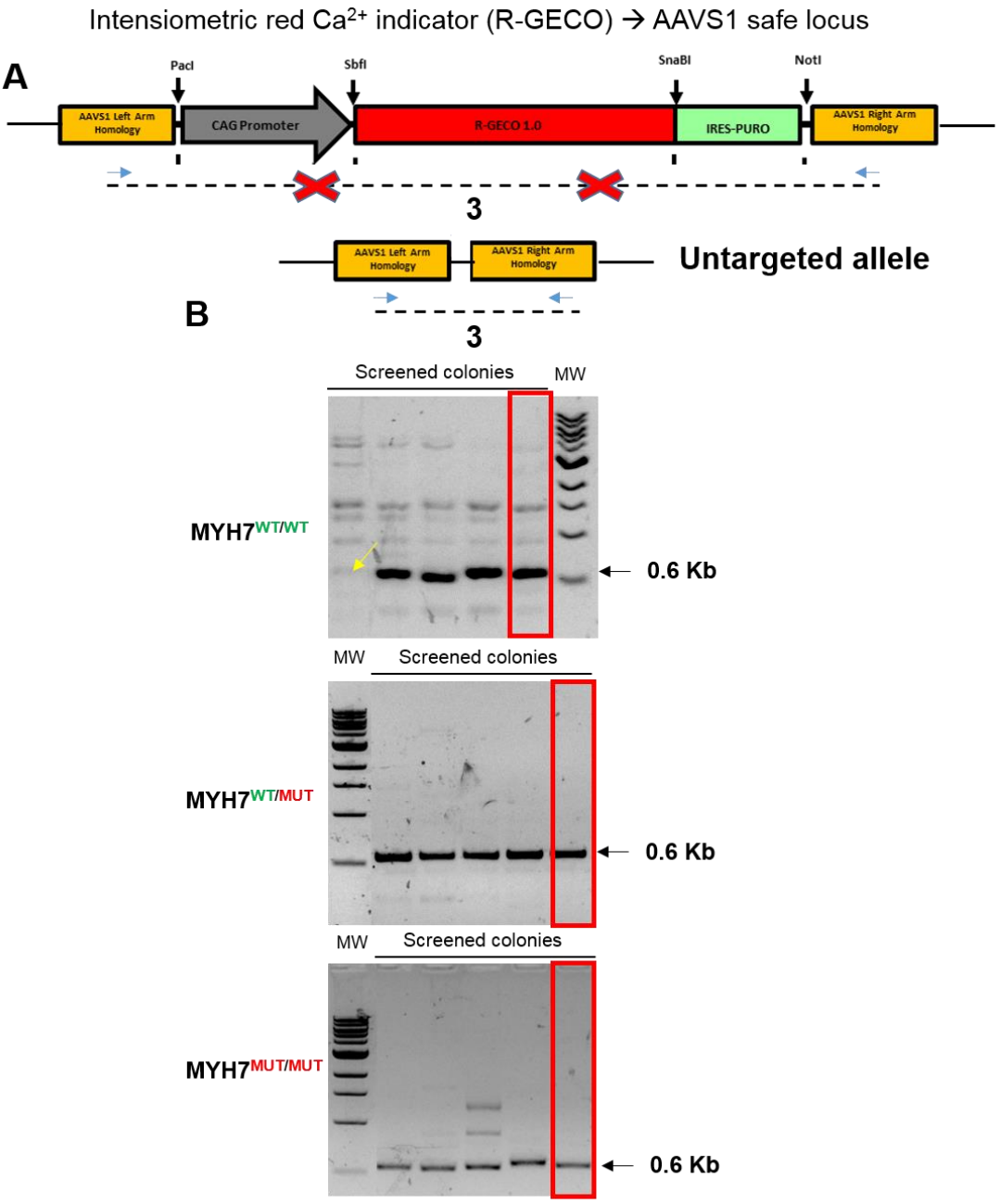


Figure 5.14 - Gene editing R-GECO calcium indicator into AAVS1 safe locus. A) DNA construct inserted in the AAVS1 locus via plasmid-based nickase CRISPR/Cas9 consisted on a CAG promoter-driven intensiometric R-GECO1. **B)** PCR-genotyping of left (1) and right (2) homology arms of targeted REBL-PAT iPSC confirmed successful gene editing in the isogenic trio (WT, R453C-MYH7 heterozygote, R453C-homozygote). **C)** Sanger sequencing of junction regions between homology arms and targeting construct confirms insertion of cassette into the *AAVS1* locus (courtesy of Jamie Bhagwan).



REBL PAT genotype	Positive colonies (% picked)	Bi-allelic (% positive)
MYH7WT/WT	6/28 (21.4%)	1/28 (3.6%)
MYH7WT/MUT	2/13 (15.4%)	0/13 (0%)
MYH7MUT/MUT	10/15 (66.3%)	0/15 (0%)

Figure 5.15 - Determination of successful mono- vs bi-allelic targeting of R-GECO1 in REBL-PAT lines. A) PCR-amplification of the whole targeting construct was only possible in untargeted alleles, enabling the distinction between mono- and bi-allelic targeted clones. **B)** Targeting both *MYH7*-mutant lines only resulted in monoallelic R-GECO-editing, whereas in the WT line one of the clones showed bi-allelic targeting (no band in region indicated by yellow arrow). **C)** Gene targeting efficiencies of *AAVS1*-editing towards R-GECO introduction (courtesy of Jamie Bhagwan).

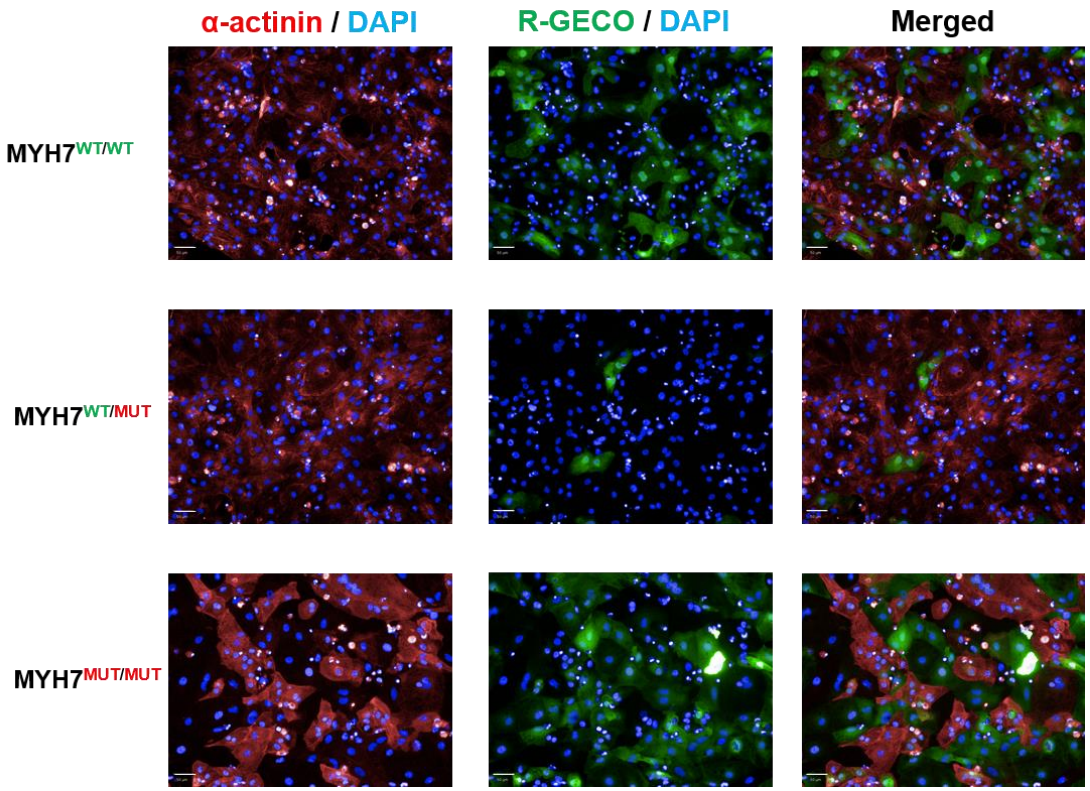


Figure 5.16 R-GECO protein expression detection by immunocytochemistry. Representative micrographs of hPSC-CMs of the REBL-PAT isogenic trio co-stained for α-actinin/ R-GECO and counterstained with DAPI confirm expression of the R-GECO sensor. Scale bar = 50µm. (courtesy of Jamie Bhagwan).

This analysis showed an increase in the frequency of DAD-like events in homozygous R453C-MYH7 line relative to isogenic control (9.1 vs 1.0%, **Fig5.18A**), as well as a 50% increase in the beat rate (**Fig5.18B**). A similar trend was shown in heterozygote lines but did not achieve statistical significance. Moreover, diseased hPSC-CMs displayed higher RGECO1 signal amplitude (F/F0) relative to WT controls (heterozygote ~1.72-fold increase, homozygote ~2.27-fold increase), indicating higher levels of resting calcium in the cytosol. In addition, further analysis of calcium transient kinetics showed a statistically significant ($p<0.01$) longer time to peak and time to decay between mutant lines and isogenic control (**Fig5.18C-E**).

In order to further test the observation that HCM lines displayed increased resting cytosolic calcium concentration, LTCC was blocked with Nifedipine, which impairs calcium influx into the hPSC-CMs, ultimately stopping cardiomyocyte contraction. Diseased hPSC-CMs should expectedly retain beating for longer upon LTCC blockage, due to a higher reserve cytosolic calcium concentration. Importantly, Nifedipine treatment exposed differences in the time of event detection failure in the line scans (**Figure 5.19**), with the R453C-MYH7 heterozygote and homozygoyte lines showing sustained beating for longer than the WT, either corroborating increased cytosolic calcium concentrations detected by higher signal amplitudes, or suggesting higher myofilament calcium sensitivity.

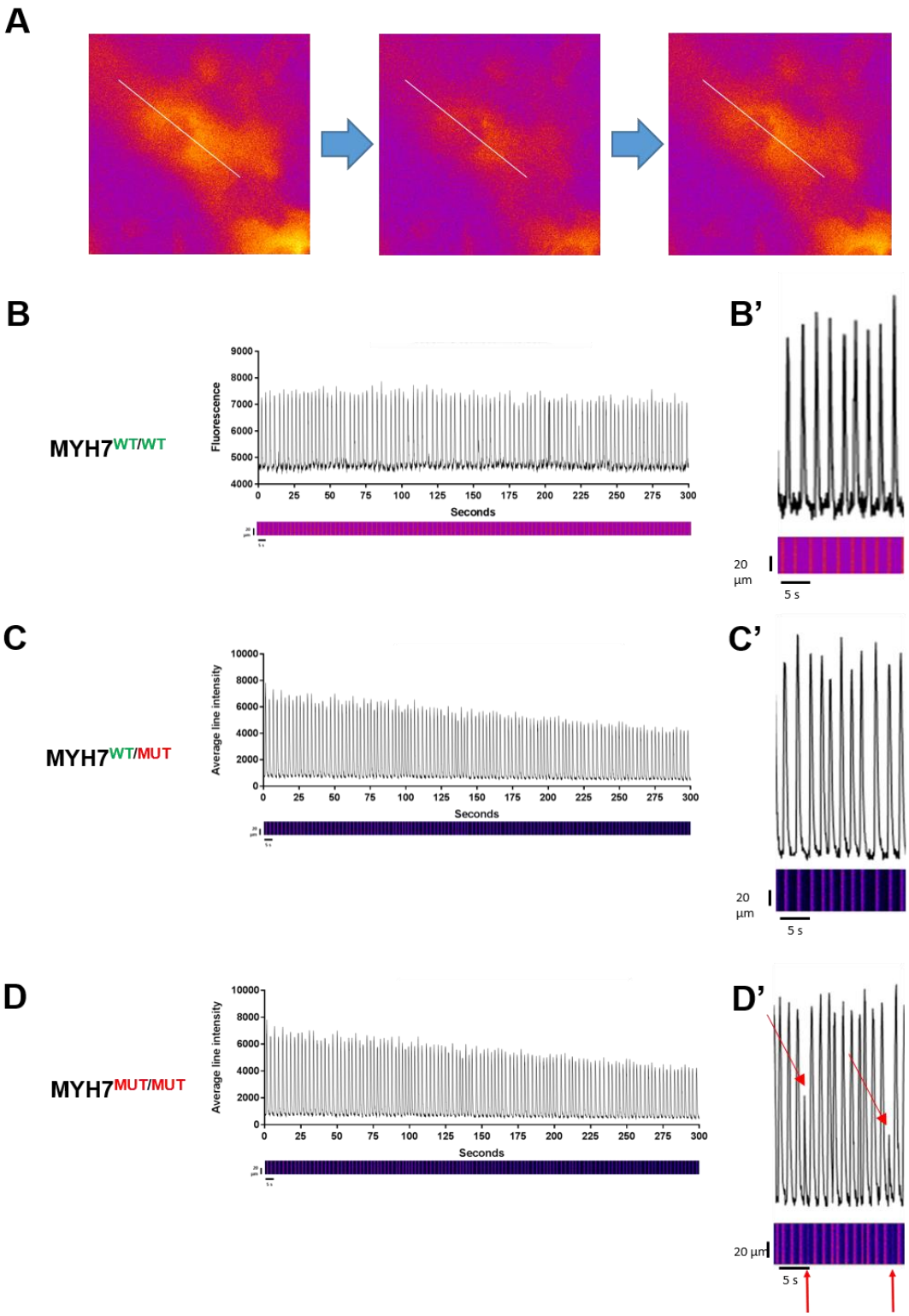


Figure 5.17 – Optical mapping of calcium transients in R453C-MYH7 REBL-PAT cardiomyocytes. A) Representative cardiomyocyte expressing-R-GECO and line path indicating scanned region by confocal microscopy. **B-D)** Representative line scans of spontaneously beating hPSC-CMs, where R-GECO signal intensity was plotted over time. The R453C-MYH7 homozygous hPSC-CM line exhibited delayed-after-depolarisation (DAD)-like events in (highlighted by red arrows, courtesy of Jamie Bhagwan).

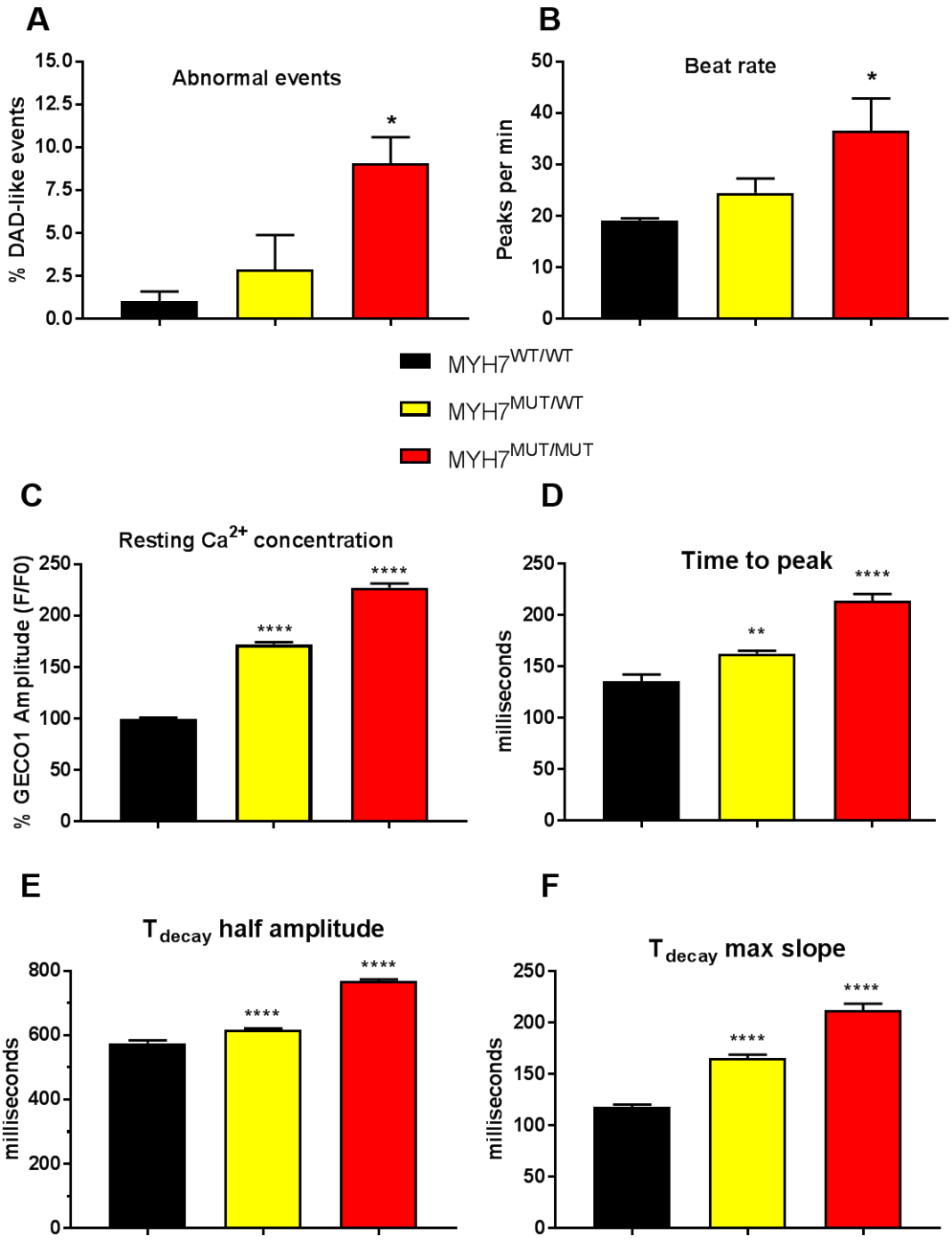


Figure 5.18 - Automated quantification of median peak height of calcium transients using ClampFit® and Excel™ softwares showed a ~10-fold increase in the frequency of DAD-like events in R453C-homozygous REBL-PAT cardiomyocytes relative to the WT control (**A**), associated to a 50% increase in the beat rate (**B**). Diseased cardiomyocytes displayed statistically significant higher GECO1 signal amplitude in comparison to healthy isogenic controls, indicative of increased resting calcium concentration, as well as longer time to peak and time to decay (**C-E**). ** p<0.01; ****p<0.0001 between groups indicated by lines. (courtesy of Jamie Bhagwan).

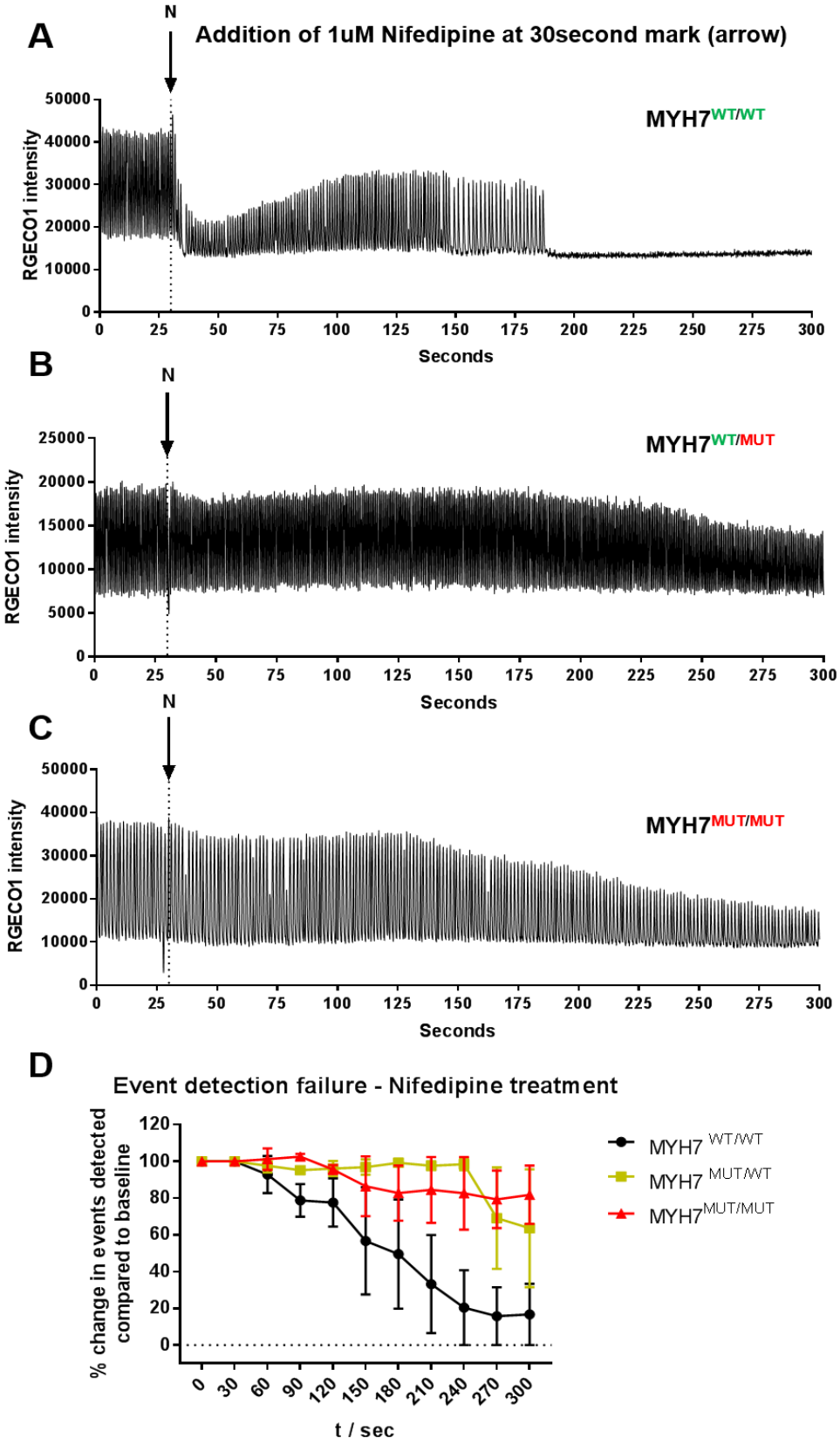


Figure 5.19 - Preliminary analysis of Nifedipine blockage of LTCC in REBL-PAT cardiomyocytes. Line scans of the different lines (**A-C**) showed that Nifedipine treatment led to event detection failure, with the heterozygote and homozygoyte lines sustaining beating for longer than the WT (**D**). N=3 (courtesy of Jamie Bhagwan).

5.2.6 Contractile force analysis in hEHT

Contractility evaluation was performed in the HCM lines by integrating gene edited hPSC-CMs in hEHTs (**Fig5.20A**), in collaboration with Dr. Ingra Mannhardt and Prof. Arne Hansen (Medical University of Hamburg-Eppendorf, Germany). After a period for formation and maturation of the hEHTs, three parameters were measured: contractile force (measurement of force generated); contraction time ($T1_{80\%}$) and relaxation time ($T2_{80\%}$) (**Fig5.20B**). Measurements were taken from hEHTs in both unpaced (spontaneous) and paced (2Hz) conditions.

Overall, the trends were similar to the assays performed above, with mutation load associating with poorer functional output. Specifically, unpaced hEHT made from R453C-MYH7 homozygote and $MYH7^{-/-}$ cardiomyocytes showed higher beat rate than WT controls ($p<0.001$, **Fig5.20C**). hEHTs paced at 2Hz has thus enabled comparison of contraction force between all lines, showing a hypocontractile and negative clinotropic (increased contraction time) phenotype of the mutant lines relative to the isogenic control (**Fig5.20D**). Quantification of contractile force in paced hEHTs revealed a progressive decrease in contractility as the extent of MYH7 mutation severed (**Fig5.20E**), with $MYH7^{-/-}$ displaying lower forces than R453C-MYH7 homozygotes which were in turn lower than R453C-MYH7 heterozygotes (0.0260±0.002mN vs 0.0580±0.003mN vs 0.1713±0.003mN, respectively, relative to 0.2045±0.005mN in WT). Interestingly, hEHTs bearing homozygous R453C-MYH7 + $MYH6^{fs/WT}$ genotype showed higher contractile force (0.0127±0.016mN) than the homozygous R453C-MYH7, but lower than the WT control. Analysis of the beating kinetics of paced hEHTs showed increased contraction times for mutant lines (**Fig5.20F**), except for the $MYH7^{-/-}$ ($p<0.001$). Relaxation times were not changed in mutant lines (**Fig5.20G**), except for the R453C-MYH7 + *MYH6*$^{fs/WT}$ genotype that showed a slight increase ($p<0.01$).

The same analysis was performed in REBL-PAT EHTs showing very similar phenotypes (**Figure 5.21**), with further histological analysis highlighting the alignment of hPSC-CMs within EHTs (**Fig5.21B**). Unpaced *MYH7*-mutant REBL-PAT EHTs exhibited an increase in beat rate (~20bpm) relative to healthy controls (**Fig5.21C**). Like AT1-EHTs, electrically-paced mutant lines showed a hypocontractile phenotype and a less pronounced negative clinotropy (**Fig5.21D**). Quantification of contraction force showed a progressive decrease in contractility in mutant lines relative to isogenic controls (0.037±0.003mN in homozygous vs 0.053±0.002mN in heterozygous relative to 0.070±0.003mN in WT, **Fig5.21E**). Analysis of the beating kinetics of paced EHTs showed a ~20% increase in the contraction time of homozygote line relative to WT (**Fig5.21F**), as well as increased relaxation time ($p<0.01$, **Fig5.21G**).

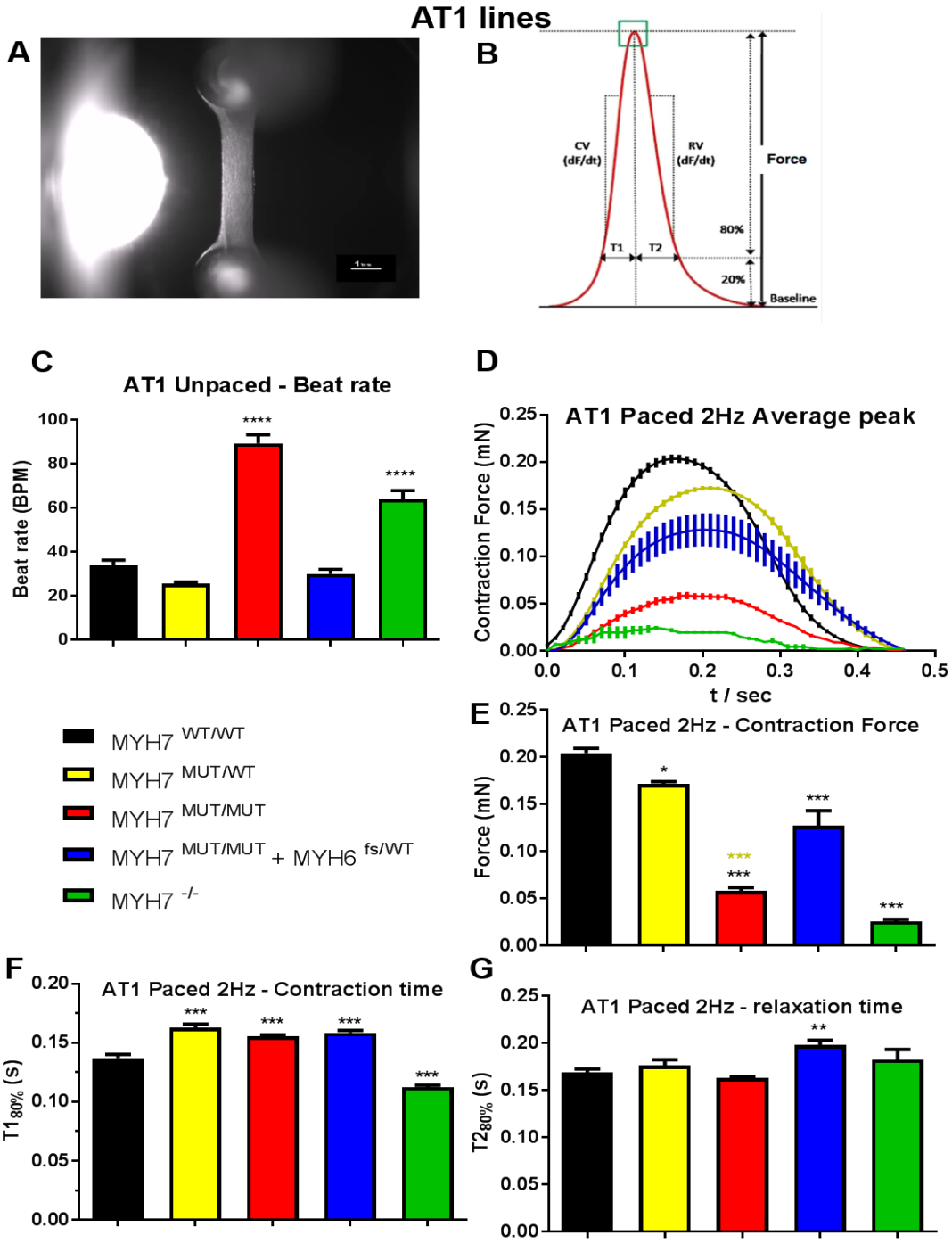


Figure 5.20 - Contractile force analysis in AT1-EHTs. A) Representative micrograph of an AT1-hEHT in a fibrin gel attached to two silicon posts (scale bar = 1mm). **B)** Representative contraction peak showing parameters analysed in EHT technology. **C)** Unpaced beat rate of AT1 EHTs showed statistically significant increase in homozygous R453C-MYH7 as well as the MYH7-knockout genotype relative to the WT line ($p<0.001$). **D)** Average contraction peaks of paced AT1-EHTs reveal a hypocontractile and negative clinotropic phenotype in the mutant lines relative to the healthy WT control. **E)** Quantification of contractile force in paced EHTs shows statistically significant decrease in contractility in all mutant lines in comparison to the isogenic control ($p<0.05$ for heterozygote, $p<0.001$ for the rest). Analysis of beating kinetics of paced EHTs revealed **(F)** longer contraction times in mutant lines (with the exception of the knockout line showing a decrease) and **(G)** no differences in the relaxation time (except for the homozygote MYH7 line + $MYH6^{fs/WT}$). N=4, * $p<0.05$; ** $p<0.01$; ***$p<0.005$; ****$p<0.0001$ between each genotype and its isogenic control (unless color-coded)

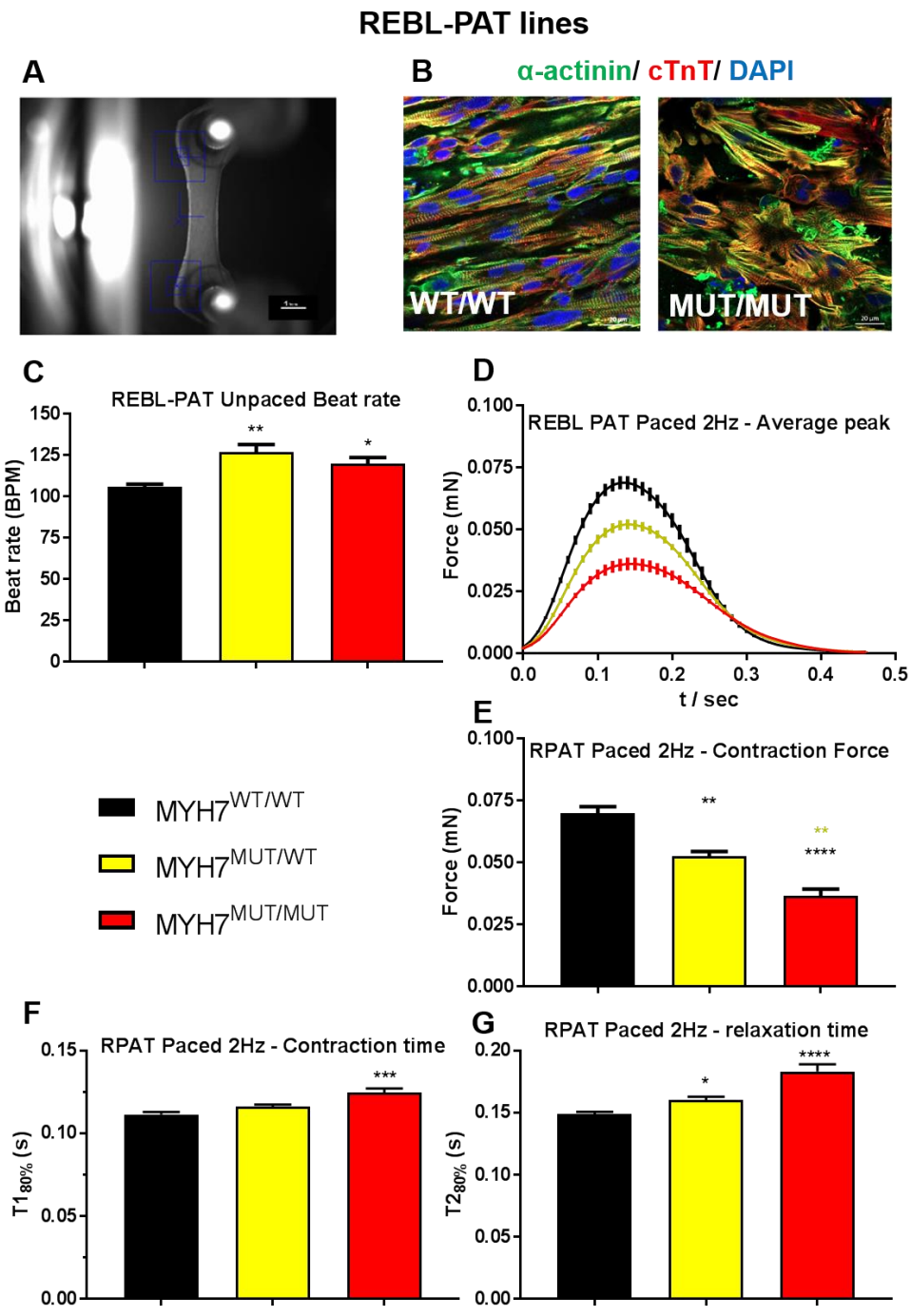


Figure 5.21 - Contractile force analysis in REBL-PAT-EHTs. A) Representative micrograph of a REBL-PAT hEHT in a fibrin gel attached to two silicon posts (scale bar = 1mm) **B)** Histological analysis of an EHT section reveals highly aligned cardiomyocytes in the fibrin gel (scale bar =20µm) **C)** Spontaneous beat rate of REBL-PAT EHTs showed statistically significant increase in mutant lines relative to the WT control ($p<0.01$ for heterozygote, $p<0.05$ for homozygote). **D)** Average contraction peaks of paced REBL-PAT-EHTs reveal a hypocontractile and marginally-negative clinotropic phenotype in all of the mutant lines vs the healthy WT control. **E)** Quantification of contractile force of paced EHTs shows statistically significant decrease in contractility in the mutant lines in comparison to the isogenic control ($p<0.01$ for heterozygote, $p<0.001$ for the homozygous). Analysis of beating kinetics of paced EHTs revealed longer contraction **(F)** and relaxation **(G)** time in homozygous R453C-MYH7 line relative to the healthy WT control. N=6, * $p<0.05$; ** $p<0.01$; ***$p<0.005$; ****$p<0.0001$ between each genotype and its isogenic control (unless color-coded)

Next, glucose consumption of hEHTs was performed by the analysis of hEHT medium 24h after medium replacement, using a blood glucose monitoring device. Results showed lower consumption rates per beat in heterozygote and homozygote mutants, in both isogenic lines (~60% lower in AT1-EHTs and ~40% lower for REBL-PAT-EHTs) (**Figure 5.22**).

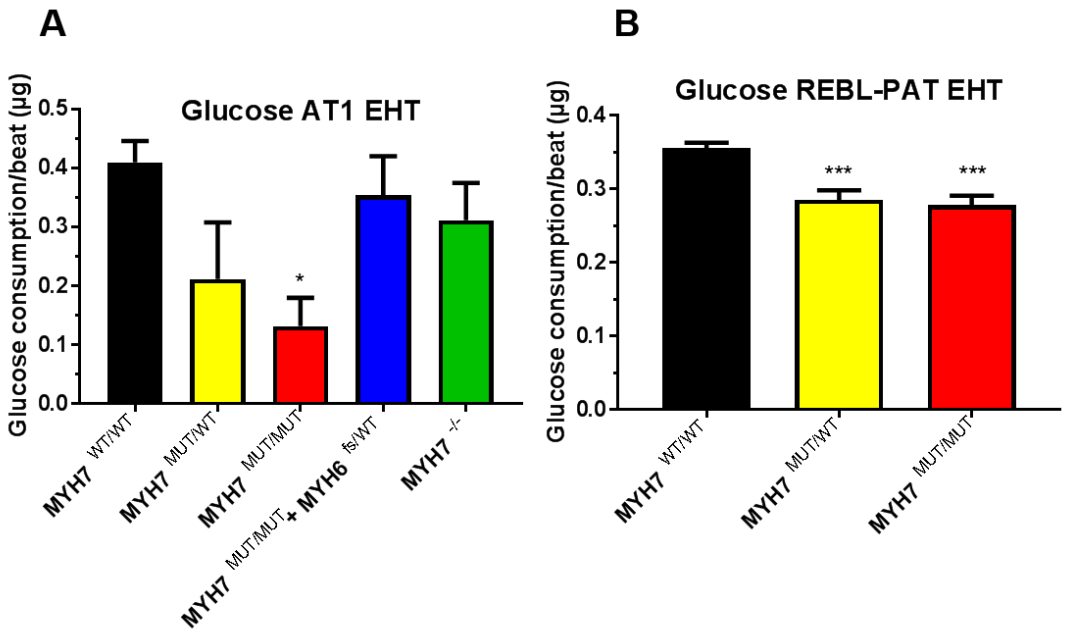


Figure 5.22 - Glucose consumption of hEHTs. *MYH7*-mutant EHTs showed a lower glucose consumption rate per beat in **(A)** AT1-EHTs (~60% decrease) and **(B)** REBL-PAT-EHTs (~40% reduction). N=4 for AT1-EHTs and N=6 for REBL-PAT EHTs * p<0.05; ***p<0.005.

5.2.7 Force-frequency relationship in HCM

Exercise-related SCD events are associated with an increased mechanical and energetic demand being placed in the cardiac tissue, which has dramatic consequences when HCM hearts cannot cope with the required efforts. This condition was simulated *in vitro* by pacing hEHTs. Increased pacing frequency coupled with analysis of contractile force showed a more pronounced negative force-frequency relationship in MYH7-mutant EHTs (**Fig5.23A2-4**) relative to the WT control (**Fig 5.23A,1**). This decrease showed statistical significance for heterozygous AT1-R453C-MYH7 EHTs and for homozygote AT1-R453C-MYH7 + $MYH6^{fs/WT}$, relative to the healthy control (**Fig5.23B**). Homozygote AT1-MYH7-R453C-EHTs did not respond to pacing at 1.5 and 2Hz (due to inherent higher beat rates) so could not be analysed. The same analysis was performed in REBL-PAT-EHTs but did not show statistically significant differences, although there is a slight trend for a more negative force-frequency relationship in the mutant lines (**Fig5.23C**).

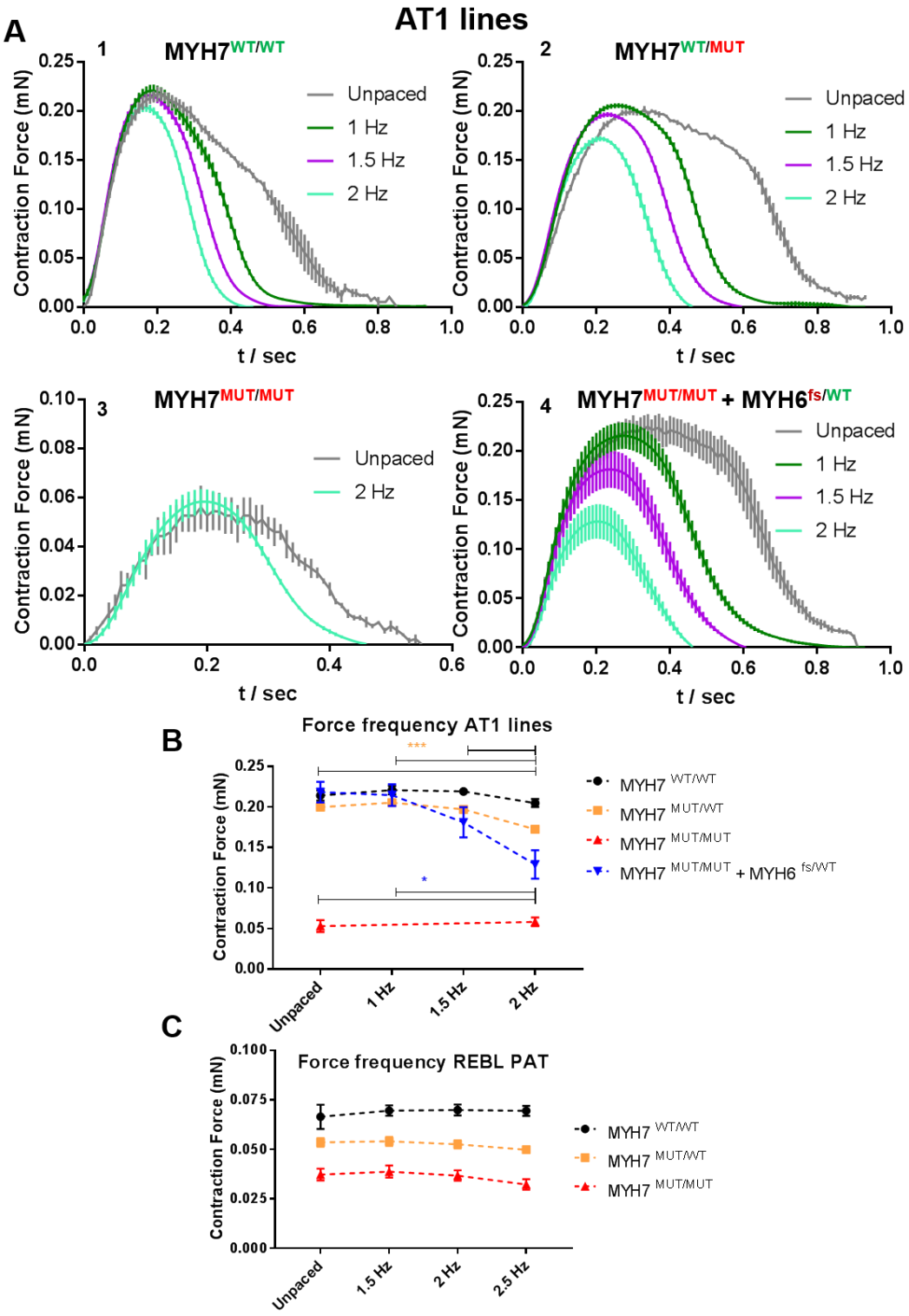


Figure 5.23 - Force-frequency relationship in *MYH7*-mutant EHTs. A) AT1-EHTs bearing *MYH7* mutations showed a more pronounced negative force-frequency relationship than the isogenic (WT) control, with the exception of the homozygous R453C-MYH7 mutant that could not be paced at lower frequencies due to a higher inherent beat rate. This decrease showed statistically significance for AT1-EHTs **(B)**, but not for REBL-PAT EHTs **(C)**. N=4 for AT1-EHTs and N=6 for REBL-PAT EHTs * p<0.05; ***p<0.005, between color-coded genotype and its isogenic control.

5.2.8 Pharmacological intervention in HCM-hEHTs

As R453C-MYH7 EHTs showed a hypocontractile phenotype, pharmacological intervention was attempted to rescue this phenotype, by treating with the cardiac myosin activator OM that acts by prolonging the actin-myosin interaction state[389].Treatment of AT1-EHTs with 1µM of OM under pacing at 1.25Hz resulted in a negative clinotropic effect (increase in contraction time) and a decrease in contractile force in all lines (**Fig5.24A**). Differences relative to untreated baseline conditions for each line varied, with homozygous R453C-MYH7 EHTs showing a more pronounced reduction in the contraction force than WT or heterozygous lines (**Fig5.24B,** $p<0.01$) and all mutant lines exhibiting a lower increase in the contraction time than the WT (~31% higher in mutant lines and ~76% higher in WT control, **Fig5.24C**). There was a trend for a less pronounced decrease in relaxation time in mutant lines vs healthy control upon OM treatment, but did not achieve statistical significance (**Fig5.24D**).

A similar pattern was observed in REBL-PAT-EHTs (**Fig5.25A**) paced at 1.7Hz, as homozygous R453C-MYH7-EHTs show a more pronounced decrease in force than WT ones (~50% lower vs 31% in WT, **Fig 5.25B**). Likewise, upon treatment, mutant lines showed a lower increase in the contraction time than WT controls (~13% increase in mutant lines vs ~50% increase in WT, **Fig5.25C**). Finally, OM treatment did not cause differences in relaxation time in the mutant lines whereas WT lines showed a ~25% decrease in this parameter (**Fig5.25D**).

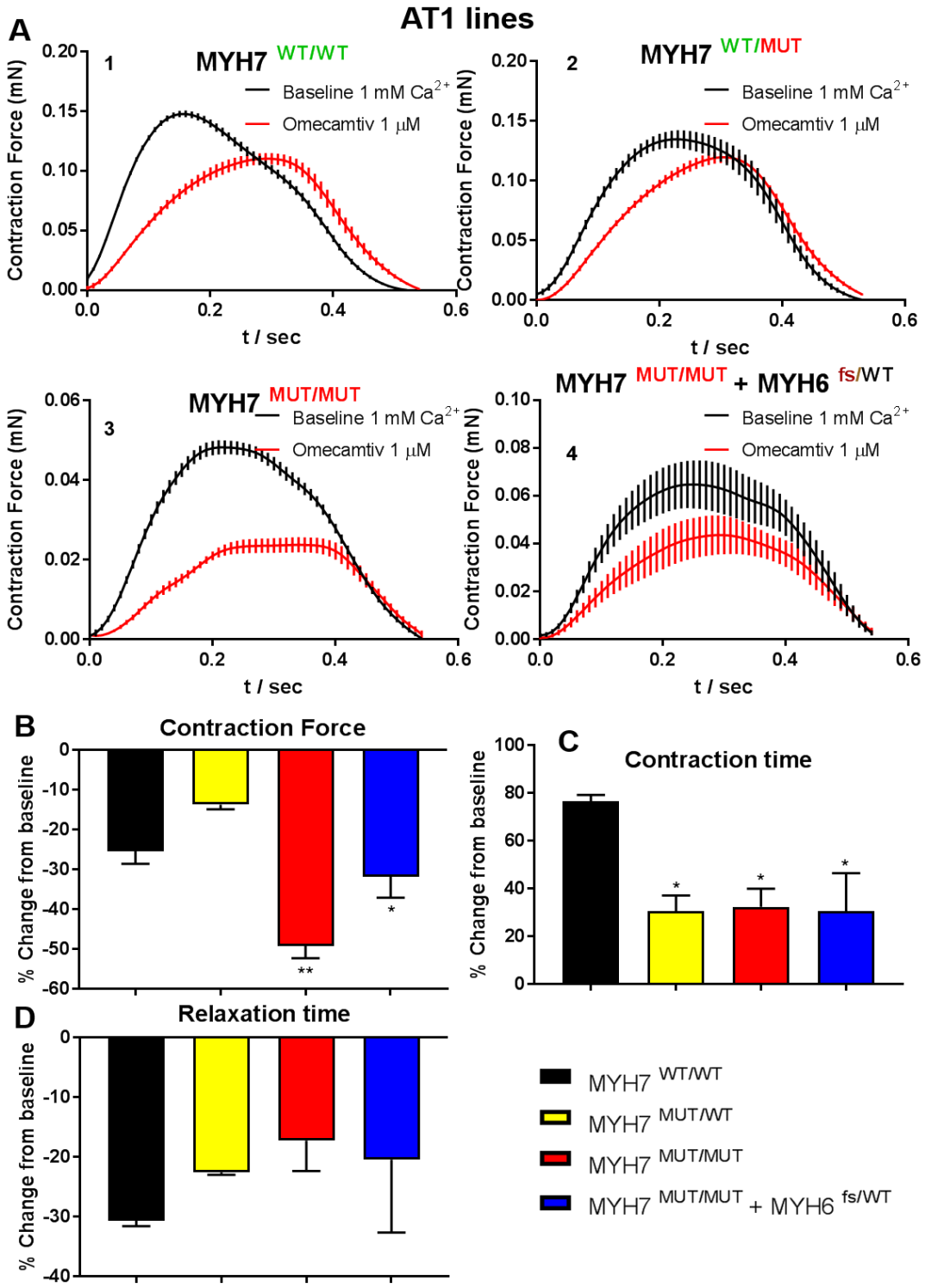


Figure 5.24 - Treatment of AT1-EHTs with Omecamtiv Mecarbil. A) Average contraction peaks (force over time) of AT1-EHTs in baseline conditions (black line) and upon OM tratment (red line) in the different genotypes (1-4). **B)** OM treatment caused a decrease in the contraction force in all lines, which was more pronounced in the R453C-MYH7 homozygote line relative to the WT control. **C)** Mutant lines had a less pronounced increase in the contraction time upon OM treatment, in comparison to healthy WT line. **D)** OM treatment resulted in a decrease in the relaxation time in all lines, with a trend towards a less pronounced effect in mutant lines, in comparison to the WT control. N=3, * p<0.05; **p<0.01, in differences upon treatment from baseline, between mutant lines and WT control.

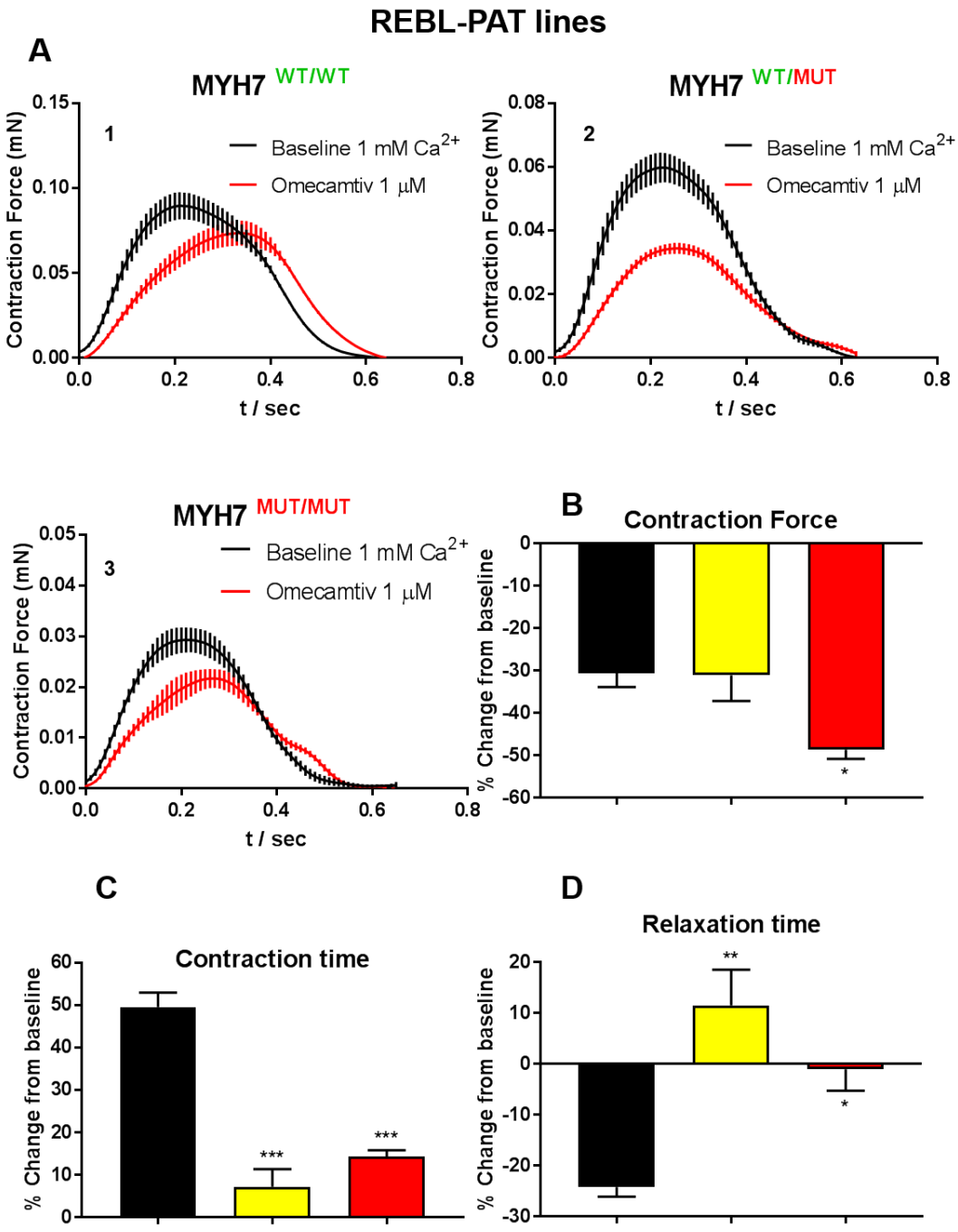


Figure 5.25 - Treatment of REBL-PAT-EHTs with Omecamtiv Mecarbil. A) Average contraction peaks of REBL-PAT EHTs in baseline conditions (black line) and upon OM tratment (red line) in the different genotypes (1-3). **B)** OM treatment caused a decrease in the contraction force in all lines, which was more pronounced in the R453C-MYH7 mutant line relative to the WT control. **C)** Mutant lines had a less pronounced increase in the contraction time upon OM treatment, in comparison to healthy WT line. **D)** OM treatment resulted in a decrease in the relaxation time in the WT line and slighter changes in mutant lines. N=3, * p<0.05; **p<0.01, ***p<0.001, in differences upon treatment from baseline, between mutant lines and WT control.

5.2.9 Transcriptomics of HCM lines

The data reported so far in this thesis has demonstrated several phenotypic changes of HCM lines, upon introduction of the R453C-MYH7 SNP in hPSC. In order to provide deeper mechanistic insight into the observed phenotypes, transcriptomics analysis of gene-edited hPSC-CMs from 2D and 3D culture systems was performed. While an in-depth RNA sequencing analysis is underway, a medium-scale (~50 genes) RNA chip analysis was done using nanoString nCounter Elements technology, in collaboration with Maksymilian Prondzynski and Prof. Lucie Carrier – Medical University of Hamburg-Eppendorf, Germany). This enabled a more focused analysis of expression of genes involved in archetypal HCM responses: **i)** fetal gene program, **ii)** hypertrophy, **iii**) Ca^{2+} handling machinery, **iv)** apoptosis, **v)** fibrosis and **vi)** autophagy. The results of the focused transcriptomics analysis are shown in **Figures 5.26 and 5.27**, where fold changes of gene expression of hPSC-CMs bearing the different MYH7 genotypes cultured in 2D or in 3D-EHTs are represented relative to isogenic controls, with fold SEM reported per each gene to provide an indication of the consistency of the data.

Gene expression analysis of 2D-REBL-PAT hPSC-CMs **(Fig5.26A**) overall shows an induction of genes involved in fetal gene program (e.g. *NPPA/B*), as well as increase in expression of most of the genes involved in hypertrophic response (*FHL1/2*), apoptosis (*CASP3*), fibrosis (*FN1*) and to a higher degree in the heterozygote line, in calcium handling (*PLN, ATP2A*) and autophagy (*NBR1, FYCO1, TFEB*). Interestingly, while some of these changes are sustained in hEHTs (mainly fibrosis and hypertrophy), others show opposing trends (**Fig5.26B**), such as the decrease in the genes involved in calcium handling machinery and less pronounced changes in apoptosis and autophagy.

Overall, data from AT1 lines show lower robustness, as evidenced by higher SEM values (likely due to lower replication - n=2), especially in homozygote R453C-MYH7 hEHTs (**Fig5.27**). Nevertheless, some trends are observed such as increased expression of apoptosis genes in all the mutant lines in 2D, induction of fetal gene program (*NPPB*) in the pure heterozygote and homozygote lines. Interestingly, the homozygote line (both in 2D and hEHT) showed some opposing trends relative to the heterozygote one in terms of changes in expression of genes involved in hypertrophy (*FHL1/2),* calcium handling (*ATP2A2)* – both categories upregulated in heterozygous and downregulated in homozygous. The same was true for fibrosis genes (decrease of *COL1A1* and *FN1* in heterozygous lines in 2D, slight increase to no change in 3D, whereas homozygous line showed an up-regulation in all conditions). In addition, genes involved in autophagy were upregulated in the heterozygote and knockout lines, particularly at the hEHT level, whereas both homozygote lines (with or without added *MYH6* frameshift) showed a downregulation. Nevertheless, data associated with homozygous R543C-MYH7 showed relatively high variation and so should be interpreted carefully.

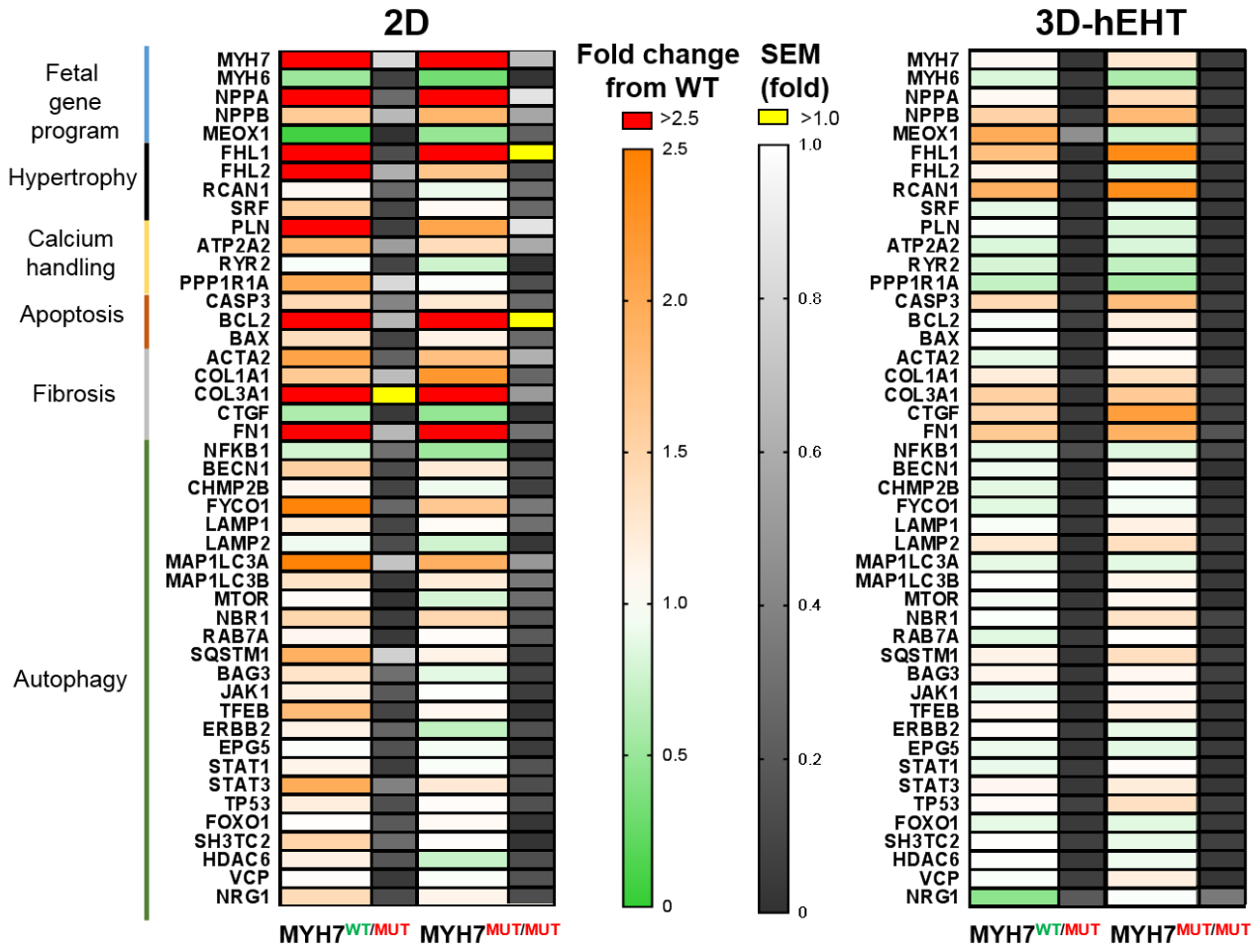


Figure 5.26 – Transcriptomics analysis of REBL-PAT hPSC-CMs either cultured in 2D **(A)** or integrated in 3D-EHTs **(B).**

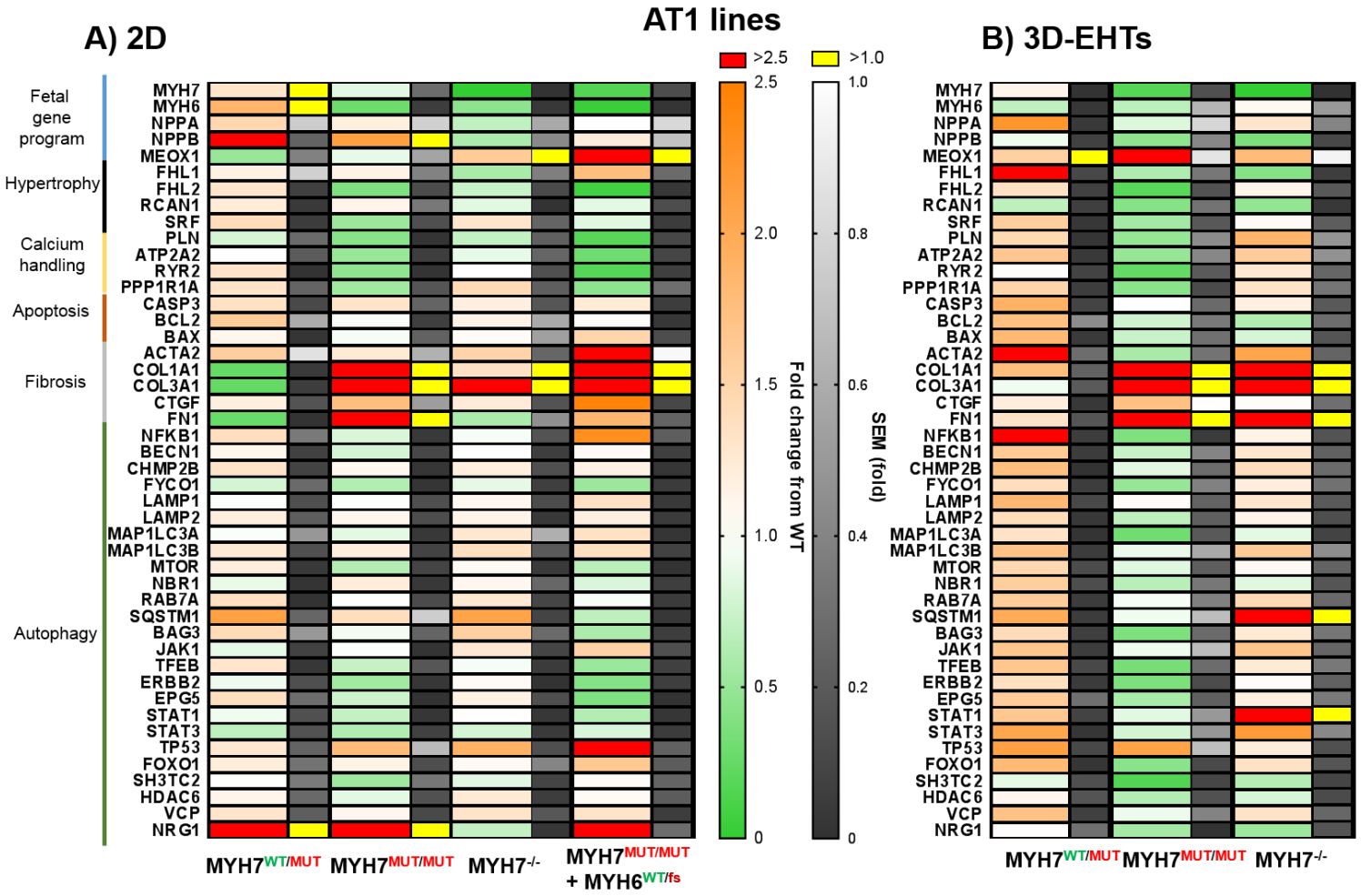


Figure 5.27 - Transcriptomics analysis of AT1 hPSC-CMs either cultured in 2D **(A)** or integrated in 3D-EHTs **(B)**.

When coupling the results from both REBL-PAT and AT1 lines several general tendencies are common: **i)** upregulation of genes involved in initiation of the fetal program and hypertrophy, particularly in the heterozygous variants; **ii)** increase in the expression of pro-apoptoptic (*CASP3*) and fibrotic (*COL1A1,* except for the AT1 heterozygote variant) genes; **iii)** increased up-regulation of *MYH7* isoform and concomitant down-regulation in *MYH6* (disabled in the MYH7$^{-/-}$ line), as detailed in **Figure 5.28.** While both lines show an increase in the *MYH7/MYH6* ratio in the WT controls from 2D to 3D cultures (an expected response to hEHT culture due to improved maturation), higher ratios are shown by *MYH7*-mutant lines and statistically validated in REBL-PAT lines (due to higher data repeats and consistency).

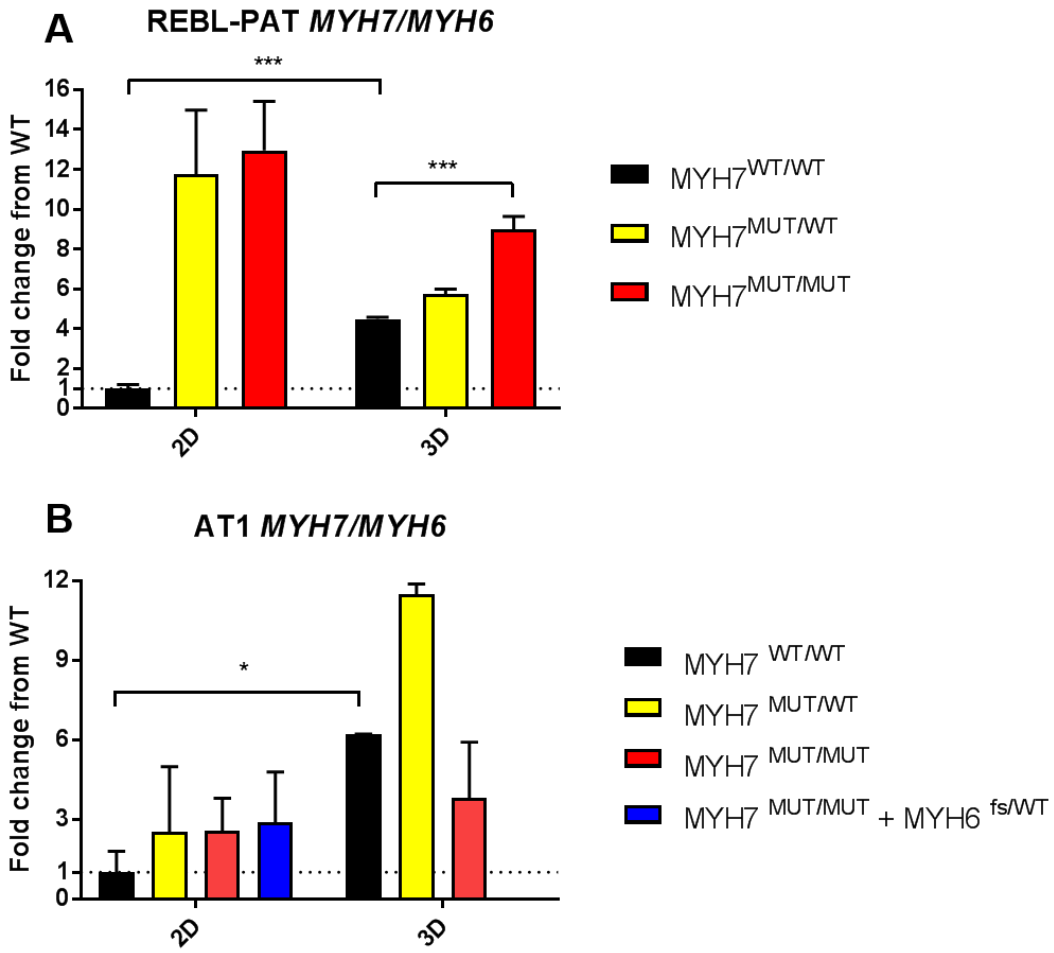


Figure 5.28 - Ratio of *MYH7/MYH6* expression in hPSC-CMs (**A**-REBL-PAT, **B**-AT1) cultured in 2D formats or in 3D-EHTs. *p<0.01, ***p<0.001

However, changes in expression of genes involved in calcium handling, autophagy and fibrosis were not robustly associated with a particular genotype and culture system (e.g. calcium handling genes were up-regulated in 2D REBL-PAT cardiomyocytes and down-regulated in 3D REBL-PAT-hEHTs, whereas no consistent trends are observed in AT1 lines). Nevertheless, these data indicates potential candidates that merit further validation for qPCR.

5.3 Discussion

In this chapter, functional evaluation of R453C-MYH7 hPSC-CMs generated by CRISPR/Cas9 genome editing technology was performed, in terms of **i)** cardiac bioenergetics, **ii)** calcium handling, **iii)** contractility and **iv)** molecular transcriptomics. These analyses revealed a general association between the mutation load and increased alterations of cardiomyocyte function, with homozygous variants resulting in more pronounced phenotypic changes than heterozygous lines. Striking changes in cardiomyocyte function between gene-edited and WT lines were detected towards higher energy production with the same mitochondrial content with potential implications due to the metabolic stress imposed in the cell. Calcium transient analysis revealed a higher prevalence of arrhythmias in R453C-MYH7 hPSC-CMs, increased beat rate and potentially higher resting calcium concentrations. Contractile force evaluation showed a hypocontractile and negative clinotropic phenotype of the diseased cell lines relative to healthy isogenic controls, with a more pronounced negative force-frequency relationship. These findings indicate that the energy depletion principle applies to the herein HCM model, as will be explained in this section.

5.3.1 Cardiac bioenergetics of genome-edited hPSC-CMs

The data reported herein using the Seahorse platform shows an increase in mitochondrial activity of *MYH7*-mutant cardiomyocytes in comparison to their isogenic controls, in terms of basal respiration (AT1 lines) and maximal respiration (both lines). Nevertheless, the values reported (1.75-3-fold increase in OCR, overall) are within the range of similar data obtained from explants of human hypertrophied hearts (~2-fold higher OCR)[333]. However, in a more recent report, the same analysis in skinned muscle bundles obtained from myocardium of failed explanted human hearts showed no differences in OCR relative to healthy controls[332]. Notably, none of these studies employed genetic profiling to determine the presence of known HCM-causing mutations. Additionally, the nature of the samples measured and their preparation is very distinct (*in vitro* cultured cardiomyocytes vs isolated mitochondria vs skinned cardiac muscle). Lastly, in these reports, healthy conditions are comprised by unrelated donors, whereas in the work developed in this thesis they are constituted by isogenic controls that enable a more precise determination of genotype-phenotype relationship.

It should be noted that this assay uses oxygen consumption and pH changes in the cardiomyocyte medium to calculate these metabolic parameters and therefore constitutes a broad estimation of mitochondrial energetic demands associated with HCM in cardiomyocytes. More kinetics-based in-depth studies assessing ATPase activity in HCM samples have shown variable results, due to the wide nature of sample sources and genotypes (human vs mouse cardiac explants, purified or heterologously produced). Even when considering work done in the same mutation (R403-MYH7), the use of different models leads to a variety of outcomes[370]. Specifically, the results obtained in rodents cannot be

directly extrapolated to human physiology, as rodents mostly express α-MHC in the ventricles whereas in humans the β-MHC isoform is predominant[423] (despite sharing ~92% sequence homology[424]). This was deemed clear in studies using transgenic R403Q-MYH7 mice which revealed a 30-40% increased actin-myosin sliding velocity and 30% actin-activated ATPase activity in the α-MHC background but not in the β-MHC background[425].
Particularly, cardiac explants obtained from a patient bearing homozygous R403W-MYH7 mutations (with the additional V896M-MYBPC3-SNP) showed higher sliding velocities and ATPase activity relative to healthy controls[349], in a model more representative of human physiology. It is worth reiterating that actin-myosin sliding assays and myosin ATPase assays represent an over-simplification of the ECC process as only those two sarcomeric proteins are present. For this, more complex cell and/or tissue experiments representing the full complexity of the sarcomere (and even clinical data) should be used to complement these evaluations, provided there is enough sensitivity and specificity in these assays to determine changes in cardiac function.

Analysis of mitochondrial content in the generated HCM lines was performed by quantifying the ratio between mitochondrial and nuclear DNA, as well as via quantification of Mitotracker-labeled cardiomyocyte signal intensity by flow cytometry, as previously done by other groups[352]. Collectively, data resulting from these assays were consistent: *MYH7*- mutant lines exhibit similar or lower mitochondrial content than isogenic controls. The extent of this change varies according to the line and to the method used. qPCR is based on the highly sensitive quantification of changes in DNA concentration whereas flow cytometry is useful for estimating differences in signal intensity in positively-labelled cardiomyocytes. As discussed in Chapter 4, cardiomyocyte cultures generated by most selection/purification-free differentiation protocols (such as that used in this thesis) result in heterogeneous populations (displaying >90% α-actinin purities). Although normalization to a cardiac marker such as α-actinin and cTnT by flow cytometry is feasible, staining protocols would require cell fixation and permeabilisation, which is incompatible with the live cell stains associated with Mitotracker, CellROX and MitoSOX dyes. Thus, flow cytometry analysis is partially limited to the extent of this heterogeneity between cardiomyocytes, which is known to be similar between lines analysed at the same time point (George and Hoang, manuscript in preparation).

Previous data from explanted failing hearts (not necessarily HCM) did not show an increase in mitochondrial content over healthy controls[352], which is corroborated by the herein observations in cultured HCM hPSC-cardiomyocytes. When taken together with oxygen consumption data (Seahorse platform), it becomes clear that HCM lines are producing more energy with the same or lower mitochondrial content. Although this shows a (predicted) adaptive response to HCM, likely due to inefficient ATP utilization in the sarcomere, it is conceivable that this additional workload imposed in mitochondria may result in metabolic stress, including but not restricted to ROS production.

In this regard, mouse models of deoxycorticosterone acetate-mediated induction of oxidative stress caused enhanced S-glutathionyation of cMyBP-C, leading to slower cross-bridge kinetics and increased Ca^{2+} sensitivity[426], thus exacerbating the HCM phenotype. Thus, it is likely that any other mechanism leading to an increased oxidative cellular state, such as that caused by the mismatch between cardiomyocyte energy supply and demand may result in aggravation of other HCM-associated phenotypes.

However, in some of the HCM lines analysed there was not a clear increase in ROS production, as analysed in the whole cell (via CellROX staining) and specifically in the mitochondria (through MitoSOX). This suggests that the cardiomyocytes are not producing high enough levels of ROS to cause the reported downstream detrimental effects such as mitochondrial damage and apoptosis[352]. Alternatively, the phenotypes were observed before the turning point where the sustained adaptive response becomes harmful to the cardiomyocyte physiology, i.e when metabolic stress is no longer supported by the same number of mitochondria and energy sources and thus ROS production is therefore enhanced towards apoptosis, as reported in [334]. At any rate, these results are in accordance with the data derived from cardiac explants sourced from cardiomyopathic patients which showed marginal (<25%) increase in NADPH-dependent superoxide production, whereas ROS levels in unstimulated conditions were below detection limit of Lucigenin Chemiluminescence[353]. However, data from a mouse model of Ang-II induction of HCM has showed increased ROS production[359], although the experimental setup is very distinct from the one used herein (mouse animal model vs hPSC-CMs, chemically stimulated HCM vs genetically-induced HCM), which could likely explain the phenotypic differences observed.

Interestingly, in contrast to HCM, MIC patients have showed increased mitochondrial proliferation and an exacerbated ROS production in the heart.[353]. This observation lends further aid in understanding HCM: phenotypic variability is greatly dependent on the primary genetic abnormality (mutations in sarcomeric vs non-sarcomeric genes) and to a lower extent on the specific gene and mutation belonging to each class (as evidenced by the distinct outcomes associated with diverse mutations in the same gene (e.g. *MYH7*, as explored in this chapter).

5.3.2 Calcium handling in HCM

Incorporation of stable calcium genetic indicators in the genome of *MYH7*-mutant hPSC via CRISPR/Cas9 was a novel approach resulting in a useful resource for investigating calcium handling properties of cardiomyocytes. In this work, R453C-MYH7 hPSC-CMs have shown more prevalent arrhythmogenic events in comparison to their isogenic controls (increase in frequency of DAD-like events), longer calcium transients and higher resting calcium concentration.

Contrarily to the other two topics of the functional analysis described in this thesis, analysis of calcium handling properties of HCM cardiomyocytes derived from hPSC-CMs is described more extensively in a few reports. In two of these reports, both the R663H-MYH7[161] and R442G-MYH7[162] genotypes were associated with arrhythmias and irregular calcium transients, related to higher resting calcium levels in the cytosol. Although these investigations were performed using fluorometric dyes, they show similar phenotypes as those displayed by the R453C-MYH7-GECI HCM lines developed in this thesis. Likewise, two other reports have used GECIs in Long QT syndrome (LQTS)[408] and CPVT2[409]-diseased hPSC-CMs showing increased prevalence of DADs in the diseased lines, relative to their respective isogenic controls. Although these represent channelopathies and not forms of HCM, the successful use of GECIs in hPSC-CMs further validates its application for the developed HCM model.

In the literature, only cTnT and cTnI mutations have consistently led to an increase in the calcium sensitivity in cardiomyocyte [427,428]. Work developed in *MYH7*-mutant samples has met variable outcomes such as increase, no difference or decrease in Ca^{2+} sensitivity, depending on the mutation[60]. Most of these reports rely on the tension models explored, using human tissue biopsies (from heart or *soleus* muscle). Therefore, besides the mutant locus (*TNNT2* vs *MYH7* vs *MYBPC3*), as well as the type (missense vs truncation/ knockout) and site (MYH7: R723, R719, I736, E848) of the mutations, methodological limitations may be causing such inconstant results. In the R453C-MYH7 HCM model developed in this thesis, the verified increase in time upon detection failure of calcium transient activity of diseased line upon Nifedipine treatment possibly indicates higher cytosolic calcium concentrations or myofilament sensitivity. Although this work needs further repeats to fully establish its significance, it may possibly validate another hallmark of HCM.

Notwithstanding, the use of GECIs in gene-edited lines may cause problems in terms of the (genomic) stability of the hPSCs. Effectively, the first round of gene editing (R453C-MYH7 introduction) already relies on a dual step of single cell culture for monoclonal passaging. Adding a similar process for the introduction of R-GECO has doubled this number, so there is a slight (yet significant) possibility that this has caused genetic abnormalities. Nonetheless, this was minimized by the use of initial REBL-PAT-iPSCs with a reduced number of population doublings (passage ~15, corresponding to approximately 50 population doublings, which by the end of the 2 rounds of targeting should double that number).

5.3.3 Contractility analysis in hEHTs

Overall, *MYH7*-mutant hEHTs displayed a hypocontractile and negative clinotropic phenotype relative to their isogenic healthy controls. While these differences were consistent between the two starting iPSC lines used, they were more striking in AT1-EHTs (especially regarding force-frequency relationship), which may be due to a higher proportion of the expression of

mutant allele relative to the WT (60% vs 35%, as further explored in Chapter 4). To the best of my knowledge this is the first report of *MYH7*-mutant-EHTs made from hPSC-CMs, and the second where gene-editing was performed to specifically modify a locus while maintaining the genetic background intact, which makes direct comparison with the literature a challenging task. Importantly, the R453C-MYH7 mutation has shown to cause sarcomeric disarray (detected via α-actinin staining, Chapter 4), which could be underlying the hypocontractile phenotype displayed, as was the case for R723G-MYH7 myofibers analysed in the tension model[307].

However, analysis of changes derived from mutation in *MYH7* gene previously performed using the tension model or the laser trap assay showed varying results, as explored in the introduction, due to varying sources of biological samples (human/mouse cardiac explants, multicellular cardiac myofibrils or purified protein extracts) as well as sample preparation differences. Previous reports using rodent-derived cardiomyocytes bearing mutations in HCM-causing genes (reviewed in the introduction) have shown variable outcomes in terms of contractility, with the majority of the studies where *MYH7*-mutant myofibers are employed exhibiting hypocontractile phenotypes. Notably, a recent report used for the first time myofibrils made from hPSC-CMs in a tension assay, showing that those bearing the E848G-MYH7 genotype displayed ~66% lower maximal isometric tension forces than healthy (non-isogenic) controls[342]. Although the mutation investigated herein is different and, as already explored, tension models differ considerably from 3D-based constructs, hEHTs made from R453C-MYH7 cardiomyocytes exhibited ~15-75% lower contractile forces relative to their isogenic controls, which is in line with those shown by R848-MYH7 myofibrils.

Surprisingly, murine models of HCM bearing R403Q or R453C mutations in *MYH7* have produced a gain in contractile function, showing an increase in force generation (50% in R403Q and 80% in R453C) by the laser trap assay when using α-MHC extracted from these animals[266]. Moreover, another study addressing the R453C-MYH7 mutation consisted on the heterologous expression of the human gene in C2C12 murine cell line and consequent protein purification towards contractile analysis via laser trap assay[372]. In this model, R453C-MYH7 showed a ~50% increase in the maximal force generated with changes in ATPase binding kinetics, although these observations were not fully corroborated by an independent group[373]. Moreover, the added concerns associated with species differences of α/β-MHC expression patterns (explored in the Discussion chapter), the use of heterologous expression systems, and the over-simplistic nature of the (forced) actin-myosin interaction associated with the laser trap assay render these results unclear.

Similarly, EHT models of HCM based on different animal sources and gene transfer strategies have reported distinct outcomes. Among the few examples available, it is worth highlighting the work done in mouse knock-in models of *Mybpc3*-mutants as it showed progressive phenotypic aggravation from heterozygote to homozygote variants (e.g. increase in calcium

sensitivity), with some phenotypes only emerging in the latter state (increased contraction and relaxation time[382]. This was also the case in the HCM lines generated in this report, where homozygous (or knock-out) mutants have shown more dramatic hypocontractility and negative clinotropy than their heterozygous counterparts.

Quite unexpectedly, glucose consumption per beat was lower in mutant lines in comparison to healthy counterparts. These differences are likely attributed to the substrate utilization by these cells. As an initial response to HCM, It has been reported that fatty acids are primarily used in (failing) hearts to cope with the high energetic demands associated with sustained cardiac function[334], after depletion of the phosphocreatine stores. It was previously observed in the Seahorse assay that R453C-MYH7 lines exhibit higher mitochondrial respiration rates. Therefore, it is conceivable that the *MYH7*-mutant hSPC-CMs integrated in the EHTs favour fatty acid usage (provided by the serum content of the medium[429]) as part of an adaptive response to the imposed metabolic stress. If this hypothesis is correct, it is expected that prolonged culture of hEHTs and/or aggravation of the imposed stress (e.g. by increasing the pacing frequency) may mimic the subsequent metabolic shift between fatty acids and glucose as an energy substrate, as seen in end-stage HCM[44].

Moreover, similarly to what was reported in Stöhr et al[382] with regards to isoprenaline and EMD50733 treatment of *Mybpc3*-mutant mice EHTs, pharmacological intervention in R453C-MYH7 hEHTs showed different responses relative to the isogenic control. OM treatment of healthy lines led to an increased contraction time, which is explained by its reported prolongation of systolic ejection time and consequent increase in LVEF [389] in (pre)-clinical trials. Moreover, due to the negative clinotropic phenotype showed by diseased lines (mainly AT1) relative to isogenic controls, OM treatment possibly exacerbates the diseased response by further stimulating an increase in contraction time. This observation is corroborated clinically, as HCM patients typically show higher LVEF[34], and thus pharmacological intervention to further boost that difference is potentially damaging.

However, although there was a marked increase in the contraction time in all lines, this was not reflected in increases in the contraction force. This is possibly due to the immaturity of the hPSC-CMs used in comparison to the adult CMs, as the lack of further regulatory mechanisms such as those conferred by T-tubules (which enable rapid electric excitation, initiation, and synchronous triggering of SR calcium release, and therefore, coordinated contraction throughout the entire cytoplasm[430]) preclude their full activation upon OM treatment. In addition, mutations in *MYH7* likely affect whole cardiac myosin dynamics (as evidenced by lower contractile force generations), which may possibly affect the outcome of OM treatment, as it is a specific myosin activator. Altogether, OM treatment did not rescue the hypocontractile phenotype showed by *MYH7*-mutant hEHTs, either due to limitations associated with hPSC-CM biology or related to primary HCM mechanisms (i.e the primary cause for the observed phenotypes may not be sarcomeric destabilization of cardiac myosin).

5.3.4. Transcriptomic analysis

The gene expression analysis performed herein corroborated most of the phenotypic data reported in separate assays. For instance, upregulation of genes involved in initiation of fetal program and hypertrophy in most of the lines had previously been shown by the increased proportion of cardiomyocytes expressing the hypertrophic marker BNP, resulting in higher cell volumes (Chapter 3). In addition, the increasing trend in *MYH7* expression previously detected by qPCR was validated in this transcriptomic study, with concomitant decrease in *MYH6* levels. In this regard, data from right ventricular endomyocardial biopsies reported differences in mRNA content of *MYH7* and *MYH6* upon HCM. While non-failing hearts showed a fraction of *MYH7* and *MYH6* relative to total MHCs to be 76.9% and 23.1%, respectively, hearts with HCM showed an increase in the relative *MYH7* fraction to 92.2% and a decrease in the *MYH6* to 7.8%[40]. Thus, the *MYH7/MYH6* ratio increased from 3.33 in healthy hearts to 12.1 in HCM, amounting to a 3.36-fold higher fraction. The ratios reported herein vary according to the lines, but the most reliable data from hEHTs made from *MYH7* heterozygous cardiomyocytes (REBL-PAT) show very similar values. Thus, these findings further demonstrate that several hallmarks of HCM are recapitulated in the generated disease models, validating them for further dissection of molecular mechanisms of disease progression as well as pharmacological intervention.

Moreover, other variations in gene expression in *MYH7*-edited lines indicate putative molecular mechanisms associated with some of the phenotypes reported in R453C-MYH7 lines. In this regard, upregulation of apoptotic genes may be closely linked with the increasing trend in ROS production (**Figures 5.13**, achieving statistical significance in the REBL-PAT homozygous line). This observation is supported by the literature as it was reported that exacerbated oxidative stress leads to programmed cell death, as shown in nitric oxide-induced apoptosis of NRVM[431].

In addition, the MYH7$^{-/-}$ line exhibited an interesting profile of gene expression, mostly pertaining higher upregulation of autophagic genes (both in 2D and 3D), which suggests that changes in sarcomeric structure and lower mitochondrial content (reported in Chapters 4 and 5, respectively) may lead to autophagy. Conceivably, this implies that an adaptive response aimed at degrading/recycling inefficient-mitochondria and sarcomeric apparatus in cardiomyocytes may result in further exacerbation of the energetic deficit and hypocontractility, as the functional stress is maintained without effective compensation, ultimately leading to HF.

Although data regarding the AT1 homozygous R453C-MYH7 + frameshift *MYH6* is limited to 2D conditions, it shows a clear difference in terms of initiation of fetal gene program and hypertrophy in comparison to heterozygous and homozygous lines (evidenced by the decrease in *MYH7*, *NPPB* and *FHL1/2* genes). This is in accordance with the observed phenotypic analysis of this line: no change in percentage of BNP-expressing cardiomyocytes,

and less pronounced sarcomeric disarray (Chapter 4) and hypocontractile phenotypes (Chapter 5). As further explored in the Discussion chapter, this is probably due to the effect of the *MYH6* frameshift mutation induced by CRISPR/Cas9 off-targeting, which may exert opposite responses to those featuring *MYH7* mutations.

Furthermore, when comparing gene expression changes between 2D vs 3D conditions, it appears that the referred variations are less pronounced in the latter system, particularly in REBL-PAT-CM samples (**Fig5.26**). Although integration of hPSC-CMs in EHTs enhances maturation to some extent (and therefore promotes *MYH7* expression as verified), this indicates that the 3D culture format (with continuous permanent auxotonic tension) may possibly attenuate the observed phenotypes. If further supported, this implies that 2D culture of more immature hPSC-CMs may result in overestimation of HCM disease mechanisms, with the underlying consequences in pharmacological testing of new compounds. Alternatively, culture of hPSC-CMs in a platform with added physiological-relevance such as the EHT-based 3D system may produce more efficient adaptive responses to HCM in comparison to 2D culture format.

Overall, the data resulting from the medium-scale gene expression analysis identifies main features of HCM in response to the R453C-MYH7 mutation, across the generated lines. Although further validation with qPCR is warranted, coupling these findings with the other more-focused phenotypic assays reported in this thesis strengthens their role in HCM disease. Finally, these results also point in new directions towards further elucidation of molecular mechanisms of HCM, namely pertaining apoptosis, fibrosis and autophagy. Expectedly, further support to these expression changes as well as identification of new molecular mechanisms involved in HCM will be provided upon completion of the ongoing RNA sequencing experiments.

5.3.5 Overall considerations

Collectively, the four topics evaluated in this chapter complement each other towards a better understanding of the HCM disease phenotype.

Notably, some of the observations in 2D culture of cardiomyocytes were reflected in 3D-EHTs, such as increased beat rate of R453C-MYH7 mutant cardiomyocytes as well as increased calcium transient duration (relatable to higher contraction and relaxation time in 3D-EHTs).

When coupling the data acquired in the Seahorse platform with the contractility analysis, it becomes clear that *MYH7*-mutant lines require more energy to produce lower contractile forces, in comparison to the healthy isogenic lines, resulting in much higher energy/force ratios. However, these investigations were made at a broad whole cell/tissue level, so tension models would be useful to further estimate tension costs of contraction, by dividing the force generated by the ATPase activity.

Taken together, the results presented in this chapter indicate that the energy depletion model applies to the HCM lines produced by CRISPR/Cas9, based on the following rationale:

1) Inefficient ATP utilization in the sarcomere leads to increased energy supply (which was partially met by developing a higher mitochondrial respiration rate, possibly leading to autophagy of impaired mitochondria)

2) Increased mitochondrial activity with unchanged mitochondrial content imposes a metabolic stress that may cause a harmful downstream response such as an increase in ROS production in later time points or in stimulated/aggravated conditions (potentially resulting in apoptosis)

3) Increased energetic demands of the sarcomere may lead to less energy available to the restoration of cytosolic calcium levels to relaxing state, resulting in higher concentrations in the cytoplasm;

4) hypo-contractile phenotype developed induces an adaptive response of the heart to compensate the less efficient cardiac output, resulting in higher beat rate, energy mobilization (maximal respiration rate) and, in critical conditions where these compensations are no longer sufficient, further reduction in the contractile force (more pronounced negative force-frequency relationship).

The functional analyses performed herein add clarity to the field, as data obtained from scarce human sources, animal models or non-isogenically controlled hPSC-CM are often variable and/or contradictory[6].

The impact of HCM on mitochondrial respiration is controversial. Explants of human hypertrophied hearts showed ~2-fold higher OCR[333], whereas skinned muscle bundles obtained from myocardium of explanted human hearts showed no difference relative to healthy controls[332]. The data reported herein on mitochondrial function/content, calcium handling and the transcriptome support the energy depletion model of HCM, which states disorganised sarcomere causes inefficient ATP usage and imposes increased energetic demands on the cardiomyocyte [325]. The generated isogenic sets of R453C-MYH7 hPSC-CMs supported the notion that mitochondrial content in failing hearts is not increased[352]. This compromises the energy available to reduce cytosolic calcium levels back to baseline, precipitating arrhythmogenesis, which corroborates the data from patient-derived *MYH7*-mutant hPSC-CM models[161,162].

The contractility data reported in this thesis is compatible with literature investigating HCM in human cells and tissues, but contradict rodent studies. In our R453C-βMHC hPSC-CM model, sarcomeric disarray and hypo-contractility were observed, despite increased metabolic demands. Force generation in R723G-βMHC human heart biopsies or E848-βMHC hPSC-CM myofibrils was 30%-66% lower[307,342]. Tension was ~35% lower in several βMHC-mutant tissues[366,368], whilst tension-cost was higher in R403Q-βMHC[370] and R403W-βMHC[349] variants. Contrastingly, murine C2C12 myoblasts expressing recombinant R453C-βMHC showed increased force generation and reduced maximum ATPase

activity[372]. Rodent cardiomyocyte-derived EHTs bearing missense mutations in sarcomeric genes (*FHL2*[380], *ANKRD1*[381], *MYBPC3*[382,383]) showed hyper-contractile phenotypes.

In summary, most HCM modelling studies have relied on animal models, analysing limited features[160] and/or lacked isogenic controls[161,162], resulting in incomplete understanding of the disease. In contrast, the holistic and comprehensive molecular and functional analyses developed in this thesis have added clarity to the field due to the use of an abundant and physiologically-relevant source of cardiomyocytes, across three independent cell lines of origin. The data generated also opens new avenues for further understanding HCM disease mechanisms and pharmacological management strategies.

6. General Discussion

The aim of this thesis was to generate new HCM models based on the introduction of the R453C-MYH7 mutation in hPSC lines, and subsequent phenotypic characterization in differentiated hPSC-CMs. In this section, the relevance of the generated models will be discussed in the context of HCM pathology. Moreover, experimental considerations and limitations will be drawn, and key findings of each chapter will be integrated towards establishing the model resulting from the generated cell lines. Contextualization of the work developed within the literature will be broadly performed, as more particular aspects were already explored in the respective Results chapters. Finally, methods for further investigation of the proposed models of HCM will be suggested.

6.1 Validity of generated HCM models

HCM is the most prevalent cardiomyopathy affecting 1:500 individuals which may develop SCD at particularly young age. As there is currently no effective cure for HCM, humanised physiologically-relevant models of HCM were developed in this thesis in order to further understand disease mechanisms and to accelerate drug discovery efforts.

6.1.1 Patient-derived vs genome-engineered cells

While it is clear that patient-derived cells constitute a prime source to generate *in vitro* hPSC-derived disease models for cardiomyopathies, these lack statistical power as the majority of mutations and associated genetic backgrounds are restricted to individual families, and even within families the complexity of HCM precludes drawing robust genotype-phenotype conclusions. As such, if patient history is not required to establish direct *in vitro-in vivo* correlations, the speed, flexibility, ease and low cost of gene targeting technologies is preferential to hiPSC reprogramming of each individual patient (and healthy relative) to capture specific genotypes[84]. However, in complex diseases such as HCM, characterized by genetic and phenotypic heterogeneity that is intrinsically associated to variable penetrance and expressivity, the introduction of the genetic element thought to cause the pathological response in otherwise healthy hPSC does not ensure full recapitulation of the whole spectrum of the disease phenotypes. Nevertheless, a few particular mutations have shown to be determinant in causing severe forms of HCM, such as R403Q and R453C in the *MYH7* gene, which have been linked to 100% penetrance[70]. This was reflected in the HCM model developed in this thesis, as all the R453C-MYH7 mutant hPSC-CMs (from 3 initial cell lines) showed clear phenotypes, with variations possibly being ascribed to differences in expression of mutant allele (higher expression correlated with more severe phenotypes), or due to the contribution of the (epi)genetic background inherent to each line.

Importantly, structural data shows that the R453 residue is found in a conserved surface loop of the upper 50-kDa domain of the myosin motor domain and lies between the nucleotide binding pocket and the actin binding site[373]. Thus, the observed changes in bioenergetics (energy depletion model) are expected in line with the amino acid location/ function. The R453C mutation changes the hydropathy of the aminoacid, from a hydrophilic to a hydrophobic side chain and is therefore in a position to hinder a wide range of myosin molecular activities, which deems it an important candidate to gene targeting approaches.

In order to further strengthen the premise that introduction of the R453C in hPSC and subsequent cardiac differentiation would result in observable phenotypes, a SNP prediction program (PolyPhen-2) was applied (**Figure 6.1**), showing that the R453C change is very likely to result in damaging effects, due to changes in the amino acid properties but also owing to its high residue conservation across species. Thus, the strategy used in this thesis to generate the model was corroborated by the (clinical) literature and validated by an SNP prediction algorithm. Remarkably, this was verified in the models generated in this thesis – despite (expected) differences in the degree of phenotypic changes, all the lines showed striking changes in hypertrophic responses.

6.1.2 hPSC-CM as model system

The core assumption associated with disease modeling *in vitro* is that at least some aspects of the (clinical) phenotype described in patients must be recapitulated in terms of pathological phenotypes in the models developed. While models portraying different degrees of complexity (intact heart muscle strips > extracted cardiomyocytes > purified actin-myosin proteins) and relevance (animal models < human sources) have been explored, hPSC offer the capacity to produce unlimited numbers of human cardiomyocytes for phenotypic studies, with the potential of genetic manipulation by the use of genome editing technologies such as CRISPR/Cas9.

In fact, the use of patient-derived or genome engineered hPSC-CMs entails several promises towards disease modeling and treatment, namely: **i)** establishing causality of disease, based on gene mutations; **ii)** determining disease mechanisms caused by such mutations; **iii)** testing of patient- or mutation-specific drug/gene therapies; **iv)** discovery of new disease mechanisms. In this thesis, all these avenues were explored: **i)** confirmation of R453C-MYH7 as critical determinant of HCM disease, **ii)** identification of genotype-phenotype responses associated with HCM, such as increased cardiomyocyte volume and multinucleation, expression of hypertrophic markers (e.g BNP), initiation of fetal gene program, energy-depletion status, calcium handling abnormalities and hypocontractility; **iii)** testing of bosentan and OM to rescue phenotypic changes; **iv)** exploration of the role of autophagy in exacerbating energy deficit by degradation of mitochondria. These findings further validate the use of hPSC-CM as useful disease models.

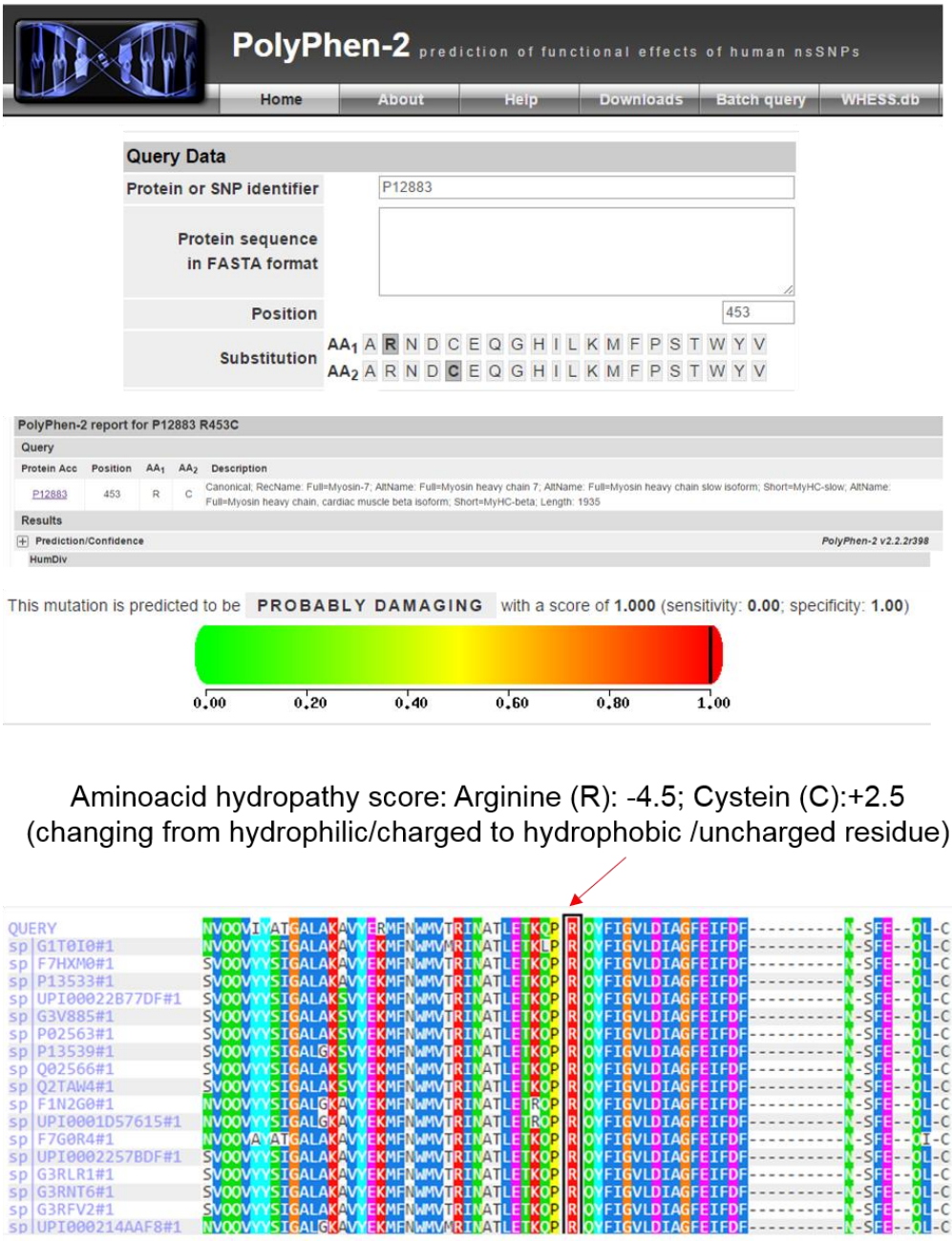


Figure 6.1 - In silico evaluation of the likelihood of the R453C-MYH7 SNP to cause damaging phenotypes. In the Poly-Phen2 algorithm, prediction of SNP-phenotype response relies on evaluating aminoacid hydropathy changes due to the mutation, as well as residue conservation across species. Adapted from http://genetics.bwh.harvard.edu/pph2/

However, the field of hPSC-CM has two main bottlenecks: phenotyping and maturation. In this thesis, the first hurdle was partially overcome by the use of high-throughput approaches to interrogate cardiomyocyte biology, mostly based on high-content imaging with its associated automated data analysis that confers additional confidence in the results generated due to its automated and unbiased nature. Moreover, adaptation of several assays from other fields was successfully done (flow cytometry to estimate cardiomyocyte volume, mitochondrial content and production of ROS, as well as line scan confocal imaging), extending the existing phenotyping toolbox. The second obstacle was partially addressed by integrating the hPSC-CMs in EHTs that more closely resemble the *in vivo* conditions, as cardiomyocytes are placed in a 3D environment under permanent auxotonic tension. Although this approach does not result in fully mature cardiomyocytes[174], it confers additional complexity and validity to the analyses performed.

Ultimately, it should be considered that HCM patients generally take over 20 years to develop a measurable phenotype whereas in the experiments performed in this thesis, hPSC-CMs were typically 1 month old (reaching 2 months in 3D-EHTs). Moreover, the full complexity of the heart as an organ or even the myocardium as a tissue is far from being recapitulated solely by hPSC-CMs. Although ventricular hPSC-CM comprise the main cell type affected by *MYH7* mutations, the heart is composed by other cardiomyocyte subtypes (atrial, nodal)[432], and even other non-cardiomyocyte cell types. Thus, cardiomyocyte-only (above 90% purities) models lack the complexity of cardiac tissue, which is multi-cellular (~30% cardiomyocytes; ~45% endothelial cells; ~15% cardiac fibroblasts; 10% smooth muscle cells)[433]. Therefore, it is expected that the complexity and severity of the observed phenotypes is being underestimated in the developed models. Nonetheless, their identification provides a tool to further elucidate molecular mechanisms associated with the disease and to identify therapeutic targets to direct drug discovery efforts.

6.2 Study limitations

6.2.1 CRISPR/Cas9 genome editing

The application of highly efficient genome editing technologies to hPSC resulted in the generation of isogenic pairs, which have added value for disease modeling as they only differ in the SNP of interest (the genetic background and all other factors associated with culture conditions and artefacts thereof presumably affect both diseased and healthy lines by the same extent). The field of gene targeting has evolved rapidly, especially with the advent of CRISPR/Cas9 discovery, with new variants and optimizations being published at an astonishing rate (over 450 publications per year, worldwide[434]). When this work was initiated (2014), the optimization of CRISPR/Cas9 gene editing in hPSC was ongoing, with most approaches relying in selection procedures to enhance the chances of obtaining colonies positive for the desired SNP. As explored in Chapter 3, this approach resulted in mono- and

bi-allelic variants of the R453C-MYH7 genotype in hPSC. However, only after excision of the resistance cassette is the *MYH7* expression restored. Although this observation proved to be advantageous in order to generate a MYH7$^{-/-}$ line (which proved to be a suitable control for most assays), the residual footprint left in the intron downstream the R453 location has unknown effects in regulation of gene expression. Importantly, developments in the field now enable footprint-free genome engineering (e.g. use of *Piggybac* transposon strategy[274]). The application of such methods to engineer new SNPs would therefore be advantageous relative to footprint-based techniques.

6.2.2 Phenotypic assays

The main drawback shared between the different methods used herein is the heterogeneity associated with hPSC-CM differentiation. In order to overcome this challenge, long-term culture[144] or metabolic selection methods[309] would possibly decrease the number of cell types present in the downstream analyses, although these two options could be biologically and/or logistically disadvantageous, as explored in Chapter 4. Conversely, culture conditions of cardiomyocytes were optimized in order to minimize the introduction of artefacts that would affect phenotypic readouts. For instance, hPSC-CMs were cultured in serum-free conditions in 2D experiments, as serum supplementation is a known hypertrophic inducer that can mask HCM phenotypes such as cell area[283]. Further limitations associated with the methodological approaches are described in this section.

6.2.2.1 High-content imaging

The phenotypes reported through high-content imaging analysis provide an unbiased interpretation of HCM responses. However, several issues associated with the automated algorithms developed for this thesis presented some challenges. Firstly, image segmentation (distinction between individual cardiomyocytes) is not fully optimized so the accuracy of the algorithms is not perfect, even though low background/ high resolution plates (CellCarrier Perkin Elmer) were used. In addition, as a considerable proportion of cardiomyocytes (>20%) is bi- or multinucleated, the software tended to identify them as multiple cells. This was corrected by the introduction of a building block in the image analysis that would group multinucleated cardiomyocytes based on the clustering of nuclei within an empirically-determined distance. An additional step was based on the elimination of non-relevant cell types by the exclusion of cell debris/ clusters and selection of cardiomyocyte populations among the (rare) non cardiomyocyte cells present, by the thresholding of α-actinin signal intensity to negative cell types (fibroblasts). Nevertheless, although resolved to some extent, these limitations are presumably similar in all conditions and as such should not skew the data presented.

6.2.2.2 Seahorse evaluation

Functional analysis based on Seahorse-assessment of mitochondrial respiration provided interesting data to test the energy depletion model. Still, this assay only provides a broad interpretation of the energetic state of cardiomyocytes seeded as a monolayer. Moreover, the normalisation done used cell nuclei is not flawless due to multinucleation, as mentioned above. This required the optimization of cell densities amenable for the assay to be developed with enough sensitivity whilst also enabling accurate determination of cell numbers in the wells. Alternatively, normalisation could have been performed using other methods such as DNA quantification via fluorometric methods such as Picogreen-labeling, or by protein quantification using standard Bradford assays. However, these methods also present obstacles due to different DNA content in multinucleated cells in the former and expectedly higher protein amounts in diseased lines (characteristic of HCM) in the latter. Thus, counting cell nuclei using an automated system (CellaVista) based on DAPI labelling was the method of choice, comprising a simple solution that is also the standard procedure done in previous experiments reported in the literature, including those using hPSC-CMs.[164,230].

6.2.2.3 Flow cytometry

The application of flow cytometry to determine mitochondrial content and ROS (as previously done[359]) resulted in high-throughput methods to assess changes in these parameters. However, the variations detected were mild which may be due to inherent biology (as unlike MIC, HCM do not cause drastic changes in ROS production[352]) or as a result of a lack of sensitivity of the method. In order to provide additional confidence to these assays, positive controls to maximize ROS production should have been used (such as H_2O_2 treatment), although these would require further optimization in order to generate a quantifiable response without causing extensive cell death that would result in abnormal signal patterns.

6.2.2.4 Confocal line scanning

The method used herein to detect changes in calcium handling properties of diseased lines resulted in the quantification of DAD-like events in hPSC-CMs as well as abnormal calcium peak kinetics and estimation of cytosolic calcium concentrations. Line scan experiments rely on the monolayer culture of cardiomyocytes followed by analysis of R-GECO1-expressing single cells over time. Importantly, not all the cardiomyocytes expressed R-GECO1, and even among positive cells, levels of the calcium indicator differ. Thus, cardiomyocytes had to be manually picked for the analysis, which may have introduced a bias in the results (only bright cells that had sufficient signal resolution were chosen). Notwithstanding, the same protocol was applied between cell lines, so its influence in the final results was minimized.

Furthermore, the R-GECO1 indicator is intensiometric and so the signal emitted in the calcium bound state is detected at a similar wavelength to that emitted in the calcium-free state (unlike ratiometric GECIs). Nevertheless, R-GECO1 is characterized by a 1600% intensity increase

in the presence of Ca^{2+}, with a K_d of 480nM[401], hence it is a very sensitive GECI with proven usefulness in calcium imaging.

Additionally, alternative methods for calcium imaging also have associated limitations (e.g. phototoxicity in fluorometric dyes[401]) which would potentially result in more serious changes in the signal intensities, hence distort reported phenotypes. Finally, all the experiments were performed in unpaced conditions, which may arguably result in differences in beating kinetics (affecting calcium peaks) that are not observed in vivo, as the heart beat is coordinated by the sino-atrial node conduction system[61].

6.2.2.5 Contractile force analysis in hEHTs

Integration of hPSC-CMs in fibrin gels under auxotonic tension (hEHTs) was the preferred methodology for evaluating contractile force, producing very consistent results. Notwithstanding, hEHT fabrication and analysis of contractile force were done in serum-supplemented environments, as these methods were historically optimized in such conditions[174]. In addition, the experiments employing OM were performed in Ca^{2+} concentrations lower than the physiological levels (1mM vs 1.8mM), as this drug was expected to enhance contractility and therefore providing maximum calcium concentrations in the baseline conditions would potentially limit the response observed. Ultimately, the treatment did not cause an increase in the magnitude of contractile force so this difference was not critical.

6.2.2.6 Transcriptomics analysis

The nanoString system enabled determination of expression changes between lines in about 50 genes, using only 50ng RNA as starting material. However, the data generated in this method had mixed consistency, partially due to the number of repeats done (3 for REBL-PAT lines, 2 for AT1 lines) and potentially due to RNA extraction procedures (particularly EHT disruption and homogenization) and logistics (shipment in dry ice to Germany). Thus, the results obtained by this experiment should be interpreted with caution and require further validation by gene-specific qPCR assays. Nevertheless, several trends are evident between samples and corroborate data obtained using different experiments (e.g. increase in *NPPB* expression vs BNP assay) which provide confidence in the results. Notwithstanding, an RNA sequencing study using the same lines is ongoing and should corroborate most of the results obtained herein as well as identify new pathways differentially regulated upon HCM (as this assay had a much wider gene coverage: ~30 million reads).

6.3 Proposed model of HCM

6.3.1 Disease phenotypes

The observed phenotypes of the R453C-MYH7 line reported in this thesis provide an overall understanding of the disease mechanisms. Collectively, there was an association with the mutation load and the severity of the phenotype.

All the mutant lines exhibited increased cardiomyocyte volume, which is a standard compensatory mechanism to HCM. In addition, all the AT1 mutant lines showed increased proportion of cardiomyocytes displaying disarrayed sarcomeres, with the MYH7$^{-/-}$ line bearing the most striking differences. Next, only the heterozygous and homozygous R453C-MYH7 lines displayed clear increased expression of hypertrophic marker BNP, which is regarded as a marker and regulator of HCM. Moreover, only the heterozygote lines in all the 3 cell types displayed increased proportion of bi- and multinucleated cardiomyocytes, which is a relevant finding as the heterozygote state is the most prevalent form of the disease.

Functional analysis showed that mutant lines had a higher mitochondrial respiration activity, mainly in terms of basal and maximal respiration rates. This increase in metabolism was associated with a similar or lower mitochondrial content, which led to an increasing trend in ROS production in cardiomyocytes, in accordance with the energy depletion model. Analysis of calcium handling analysis of R453C-MYH7 lines through the use of GECIs revealed higher frequency of DAD-like events, associated with increased beat rate, slower calcium kinetics and higher cytosolic calcium levels. Finally, contractile force analysis in hEHTs revealed a hypocontractile and a negative clinotropic response in R453C-MYH7 cardiomyocytes relative to their isogenic controls. This resulted in a more pronounced negative force-frequency relationship in the AT1 lines. These phenotypes were not rescued upon treatment with cardiac myosin activator OM.

Importantly, this work establishes a model of HCM and identifies possible targets for pharmacological intervention, as explored in the next section.

6.3.2 Potential molecular mechanisms and pharmacological intervention

Medium-scale transcriptomic analysis has further revealed other potential phenotypes as well as molecular mechanisms underlying the observed differences between healthy and diseased cardiomyocytes. All the cell lines showed upregulation of genes associated with fetal gene program (corroborating data from BNP assay), and hypertrophic response (e.g. *FHL1/2*). This analysis confirmed a previous trend of increased *MYH7* expression, also showing a concomitant *MYH6* downregulation, which validates the α to β MHC isoform switch reported in HCM hearts[40]. Moreover, upregulation of genes involved in fibrosis (e.g. *COL1A1*) in most cell lines indicate increased secretion of ECM proteins by cardiomyocytes which may be

recapitulating interstitial fibrosis reported *in vivo*. Furthermore, up-regulation of apoptosis genes (e.g *CASP3*) may be related to the metabolic stress associated with marginally higher ROS production. Finally, in the most severe variant of the engineered mutation (MYH7$^{-/-}$), an increase in genes involved in autophagy is possibly related to the decreased mitochondrial content: enhancement of autophagy to degrade inefficient mitochondria may contribute to further exacerbation of the energy deficit phenotype. However, it remains to be determined whether these gene expression changes are reflected in variations in protein levels.

Due to the high complexity of this disease, the potential candidates for therapeutic intervention should only be considered for disease forms as the one described in this thesis (other drugs/ candidates commonly associated with HCM exist that aim to cause the opposite effects)[435,436]. In this model, five main target mechanisms constitute promising targets to rescue HCM phenotypes: **i)** hypertrophy signalling pathways (such as BNP), **ii)** metabolic modulation and anti-oxidation, **iii)** anti-arrythmogenicity, **iv)** sarcomeric calcium concentration and **v)** cardiac myosin activity. These could be targeted by the drugs in **bold.**

Firstly, **bosentan** treatment of diseased lines generated herein rescued decreased levels of BNP expression to those of healthy lines. It thus stands to reason that inhibition of signalling pathways associated with other cardiac trophic factors including AngII and TGF-β in R453C-MYH7 lines could rescue the observed phenotypes, as further evidenced by the reported effect of **TGF-β neutralizing antibodies**[50] and **losartan**[437] (inhibiting Ang-II receptor) in attenuating cardiomyocyte hypertrophy and interstitial fibrosis.

Secondly, addressing the energy depletion phenotype with metabolic modulators such as **perhexiline**, that shift myocardial substrate utilization from fatty acids to more efficient carbohydrate sources such as lactate has shown significant improvement in the PCr/ATP ratio and increased exercise capacity[361], as reviewed in Chapter 5. Interestingly, data from hEHTs has showed lower glucose consumption from those made with R453C-MYH7 cardiomyocytes, suggesting the use of alternative energy substrates (such as fatty acids, present in the serum[429]) to compensate for the greater metabolic demand. Thus, any metabolic modulator that can re-direct metabolism for more efficient production of energy using simpler carbohydrates shows promise in attenuating the energy depletion phenotype.

Furthermore, worldwide use of beta-blockers such as **propranolol** is the gold standard for treating heart disease patients due to their anti-arrythmogenic activity, by competing with endogenous catecholamines (e.g. isoprenaline). In addition, stimulation of βARs activates pathways that can lead to production of ROS and ultimately cardiomyocyte apoptosis[362]. Thus, treatment with antioxidants such as **carvedilol** has shown in clinical trials to be superior to other beta-blockers (metoprolol) for the treatment of congestive heart failure[363]. Likewise, treatment of animal models of HCM such as E180G-tropomyosin mice with antioxidants such as **N-acetyl-cysteine** (NAC) has been led to a ~7-fold reduction of levels of glutathionylated myofilaments with reversal of increased myofilament calcium sensitivity (pCa_{50} of tension

decreased from 6.01 to 5.84), diastolic dysfunction, myocyte hypertrophy, and fibrosis[438]. Thus, treatment of HCM models with drugs with antioxidant activity is generally associated with beneficial prognosis.

Moreover, drugs targeting abnormal calcium sensitivity associated with HCM have been developed, such as levosimendan and EGCg to enhance or decrease calcium sensitivity, respectively. While in this model it is not clear whether myofilament sensitivity is altered, increased cytosolic calcium concentration is likely being triggered in response to energy depletion. In this regard, treatment of *MYBPC3*-mutant carriers with LTCC inhibitor **diltiazem** exhibited significantly ($p<0.05$) less increase in echocardiographic LV wall thickness and cardiac as well as improved LV filling pressures as represented by a decrease in ejection fraction[439]. However, this effect was not reproduced in *MYH7*-mutant patients, highlighting phenotypic differences between patient cohorts. For this, **ranolazine** might be a more promising drug as it inhibits late Na^+ channels, inhibiting sarcomeric Na^+ influx and increases Ca^{2+} efflux via NCX, potentially eliminating the excessive cytosolic calcium present in this HCM model. Interestingly, (non-genetically profiled) HCM patient-derived cardiomyocytes were treated with ranolazine leading to ~30% shortening of APD duration and 50% reduction in DAD events, ameliorating diastolic function[440]. As these phenotypes were also present in the R453C-MYH7 model developed herein, this drug is a promising candidate to test.

Finally, direct targeting of the contractile apparatus is another approach to consider for the treatment of HCM. Due to the hypocontractile phenotype exhibited by R453C-MYH7 hEHTs, **OM** was the drug of choice due to its known cardiac myosin activation effect[389]. However, OM treatment did not rescue the lower contractile forces associated with the mutation, either because the *MYH7* mutation likely causes severe changes in the cardiac myosin dynamics which are beyond myosin activators (like OM), or because it acts via prolongation of contraction time (systolic activity), which is already another pathological difference in the diseased cardiomyocytes (negative clinotropy). Paradoxically, treatment with **MYK-461**, a small-molecule inhibitor of myosin ATPase which prevents transition into the strongly bound state of the myosin cross-bridge cycle and thus results in decrease contractile action[388], might be considered. This is because the myosin ATPase may be over activated in the herein model (causing energetic deficit and prolonged contraction) and thus its direct inhibition may partially rescue some of the observed phenotypes.

Taken together, several candidates for functional rescue of the phenotypes associated with the R453C-MYH7 model generated herein are available, with promising drugs already showing pre-clinical (and in some cases clinical) validation. Therefore, pharmacological intervention with these drugs should be explored in the future. The observed phenotypes of the proposed HCM model and promising drugs to rescue them are illustrated in **Figure 6.2.**

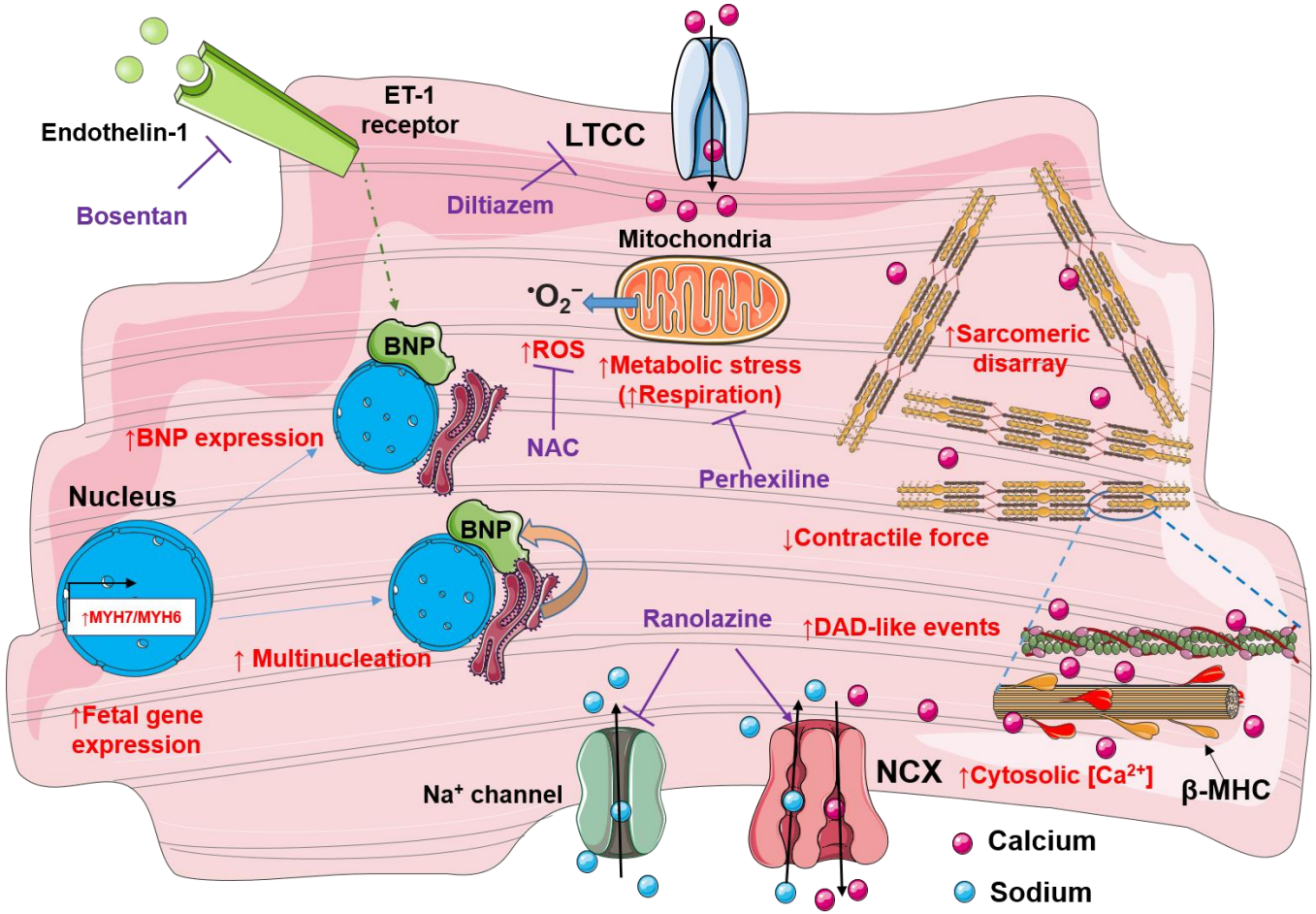


Figure 6.2 - Schematic of proposed HCM model. Phenotypes investigated in the R453C-βMHC hPSC-CM HCM model developed (red); putative rescue drugs (purple). The structural defect caused by the R453C change led to the pathological changes observed (hypertrophy, multi-nucleation, hypertrophic marker expression, sarcomeric disarray, hypo-contractility, energy depletion, abnormalities in calcium handling and arrhythmias). NAC, N-acetyl-cysteine; LTCC, L-type calcium channels; NCX, Sodium-calcium exchange pump, DAD, Delayed-after-depolarisation, ROS, reactive oxygen species, BNP, B-type natriuretic peptide, ET-1, endothelin 1.

6.3.2 Contextualization with literature

As explored throughout this thesis, most of the literature on HCM modelling consists of animal models and human cardiac tissue biopsies, with only a few examples featuring hPSC-CMs. Moreover, many different assays exist to interrogate the same aspects of the disease (e.g tension models, laser trap assays and hEHTs for assessing contractility). These wide range of models and methods result in often contradictory reports regarding particular genotype-phenotype relationships, which are further aggravated by the inherent complexity of the disease. Furthermore, the use of often inappropriate controls such as genetically-unrelated non-failing heart biopsies introduces further confounders in the analysis of HCM phenotypes.

In this regard, the work developed in this thesis is novel due to the inclusion of isogenic controls as healthy representatives of human cardiomyocytes. In addition, taking advantage of the efficiency of CRISPR/Cas9 genome editing system used, the use 3 cell type-based models developed showing similar phenotypes provides additional confidence in the results reported. Likewise, the establishment of homozygous variants of disease (rare) allowed additional degree of phenotyping by providing a gradual aggravation of the readouts measured. This approach surpasses the biological availability of human samples and thus contributed to further understanding disease mechanisms (for example, the MYH7$^{-/-}$ cell line showing the most severe sarcomeric disorganisation and induction of autophagy, shed light into underrepresented hallmarks of hypertrophy). Finally, the addition of GECIs to HCM hPSC-CMs increase the novelty of this work by extending the phenotyping assays that can be done. Taken together, this human physiologically-relevant model has resulted in a comprehensive characterization of HCM phenotypes, thus enhancing the understanding of this disease.

While the increased genetic tractability and methodological optimization of animal models offer advantages in recapitulating disease phenotypes, species differences often complicate interpretation of the results. This is particularly relevant in the α vs β-MHC dichotomy present between mice and humans. Firstly, the β-MHC isoform is predominantly expressed in the atria of mice hearts, whereas its expression in humans in mainly done in the ventricles. This difference occurs early in mice development as *MYH6* replaces *MYH7* as the predominant isoform in the ventricles 7 days post-birth, and remains constant throughout the life span of the animal[90]. Contrastingly, the β-MHC is always the main isoform expressed in the right and LV in humans[441] throughout development, with the ratio between *MYH7/MYH6* increasing even further upon HCM[279] (the latter also being verified in rodent models of the disease[278]). This difference results in striking effect of homozygous mutations in the *MYH7* gene: whereas these are typically neonatal-lethal in mice (as seen in R403Q mutants[442]), rare cases of patients showing homozygous mutations in these gene reaching adulthood have been documented[349]. Therefore, the differential expression patterns of *MYH7* and *MYH6* isoforms between mice and humans may lead to opposing phenotypes in HCM modelling,

which may further confound comparison between work done in mice and human models, despite sequence homology exceeding 90%[443].

Thus, the often hypercontractile phenotype associated with α-MHC mutations in mice [266,339] may cause opposing effects in the human ventricular counterpart (β-MHC) due to differences in expression patterns between species. This aspect may be reflected one of the "bonus" lines generated herein, the homozygous R453C-MYH7 + *MYH6*$^{fs/wt}$. Surprisingly, this line showed a higher contractile force than the (solely) homozygous R453C-MYH7 one, despite still being lower than the isogenic control. This difference may be ascribed to a hypercontractile phenotype of *MYH6* mutations in humans (in line with those of *MYH7* in mice), which is partially rescuing the *MYH7* mutations also presented by the same hPSC-CMs. Supporting this hypothesis is the observation that some of the phenotypes (multinucleation, BNP expression, initiation of fetal gene program and autophagy) were not exhibited by CMs bearing the additional *MYH6* mutation, while these were verified in the "clean" *MYH7*-mutant lines. These observations raise questions on the validity of extrapolation of contractility analysis between mice and human models. Importantly, hypocontractile phenotypes have been consistently reported in human *MYH7*-mutations in tension cost models[307,342,366,368-370], lending further aid to the human model developed herein.

Ultimately, it is challenging to pinpoint the exact mechanistic sequence that causes the observed phenotypes in the R453C-MYH7 models developed. In this regard, Marian, A. J. has postulated that hypocontractility itself was the cause (and not the consequence) of the of HCM phenotypes[36]. Accordingly, reduction in the contractile force of the myocardium leads to the production of stress-responsive trophic factors (including ET1, TGF-β and AngII) that act on cardiomyocytes to promote cellular responses that lead to increased fibrosis, hypertrophy and sarcomeric disarray, which in turn affect diastolic function (altering relaxation parameters). In addition, phenotypic diversity stems from the differential stress responses developed by the patients, whereby those showing the highest levels of trophic factors (due to more malignant mutations or because of the contribution of their genetic background, including gene modifiers) are likely to result in more severe phenotypes. Remarkably, this hypothesis is supported by the R453C-MYH7 model developed in this thesis. In order to provide further evidence of its validity, additional pharmacological intervention studies should be performed to rescue the observed phenotypes.

6.4 Future work

Although the work developed in this thesis has resulted in a disease model of HCM with considerable degree of validation, additional experiments should be performed to further elucidate molecular mechanisms associated with the disease and to maximize its potential for drug discovery efforts.

These include deep RNA sequencing between different lines to identify candidate signalling pathways differentially expressed between diseased and healthy conditions. This work is already underway in collaboration with Dr. Daniel Gaffney (Sanger Institute, UK), and should provide additional insight to the medium-scale transcriptomics study already performed (nanoString).

One of the priority areas of research entails the pharmacological modulation using drugs mentioned in the section above to address phenotype-rescuing potential. This can be done using the same assays developed for this thesis, as well as other high-throughput platforms that enable sequential measurement of calcium, voltage and contractility (such as CellOPTIQ[243]).

Challenging the established model with additional phenotypic assays is also another avenue to explore. For instance, tension cost evaluation can be performed by measuring the force produced by skinned myofibres isolated from hEHTs made from R453C-MYH7 cardiomyocytes, as well as estimating ATPase activity/ kinetics and calcium sensitivity simultaneously. This work is also ongoing, in collaboration with Dr. Paul Wijnker and Prof. Jolanda van der Velden (VU University Medical Centre, Amsterdam, The Netherlands).

Furthermore, the contribution of non-cardiomyocyte cell types and their interaction in the ECM for the HCM progression is another complex field of interest. In this regard, directed differentiation protocols could be applied to gene-edited hPSC (to generate smooth muscle and endothelial cells[444] as well as cardiac fibroblasts[445]) and secretome studies could be performed in these cells (e.g mass spectrometry). This would enable a deeper understanding of the crosstalk between cardiomyocytes and other cell types present in the heart, as well as their interaction with the underlying ECM. This work is the purpose of subsequent studies using these models (post-doctoral fellowship to be developed in Merry and Denning labs).

Finally, new *MYH6* and/or *MYH7* mutations (preferably highly penetrant) could also be engineered using CRISPR/Cas9 and the same experimental layouts could be applied, thus contributing to further understanding the contribution of α vs β-MHC domains to the development of HCM.

References

1. Maron B.J., Olivotto, I., Spirito, P.*, et al.* (2000). Epidemiology of Hypertrophic Cardiomyopathy–Related Death. Revisited in a Large Non–Referral-Based Patient Population. *Circulation*. **102**(8): 858-864.
2. Van Driest S.L., Jaeger, M.A., Ommen, S.R.*, et al.* (2004). Comprehensive Analysis of the Beta-Myosin Heavy Chain Gene in 389 Unrelated Patients With Hypertrophic Cardiomyopathy. *J Am Coll Cardiol*. **44**(3): 602-610.
3. Lopes L.R., Rahman, M.S., and Elliott, P.M. (2013). A systematic review and meta-analysis of genotype–phenotype associations in patients with hypertrophic cardiomyopathy caused by sarcomeric protein mutations. *Heart*. **99**(24): 1800-1811.
4. Ackerman M.J., VanDriest, S.L., Ommen, S.R.*, et al.* (2002). Prevalence and age-dependence of malignant mutations in the beta-myosin heavy chain and troponin t genes in hypertrophic cardiomyopathy. *J Am Coll Cardiol*. **39**(12): 2042-2048.
5. Milani-Nejad N. and Janssen, P.M.L. (2014). Small and large animal models in cardiac contraction research: Advantages and disadvantages. *Pharmacol Ther*. **141**(3): 235-249.
6. Eschenhagen T., Mummery, C., and Knollmann, B.C. (2015). Modelling sarcomeric cardiomyopathies in the dish: from human heart samples to iPSC cardiomyocytes. *Cardiovasc Res*. **105**(4): 424-438.
7. Heidenreich P.A., Albert, N.M., Allen, L.A.*, et al.* (2013). Forecasting the Impact of Heart Failure in the United States: A Policy Statement From the American Heart Association. *Circ Heart Fail*. **6**(3): 606-619.
8. Fuster V. and Kelly, B.B., Epidemiology of Cardiovascular Disease., in *Promoting Cardiovascular Health in the developing world: A critical challenge to achieve global health.* 2010, National Academies Press (US): Washington DC. p. 49-123.
9. Bui A.L., Horwich, T.B., and Fonarow, G.C. (2011). Epidemiology and risk profile of heart failure. *Nat Rev Cardiol*. **8**(1): 30-41.
10. Cook C., Cole, G., Asaria, P.*, et al.* (2014). The annual global economic burden of heart failure. *Int J Cardiol*. **171**(3): 368-376.
11. Lopes L.R. and Elliott, P.M. (2013). Genetics of heart failure. *Biochim Biophys Acta*. **1832**(12): 2451-2461.
12. Maron B.J., Towbin, J.A., Thiene, G.*, et al.* (2006). Contemporary Definitions and Classification of the Cardiomyopathies. An American Heart Association Scientific Statement From the Council on Clinical Cardiology, Heart Failure and Transplantation Committee; Quality of Care and Outcomes Research and Functional Genomics and Translational Biology Interdisciplinary Working Groups; and Council on Epidemiology and Prevention. *Circulation*. **113**(14): 1807-1816.
13. Towbin J.A. (2014). Inherited Cardiomyopathies. *Circ J*. **78**(10): 2347-2356.
14. Cahill T.J., Ashrafian, H., and Watkins, H. (2013). Genetic Cardiomyopathies Causing Heart Failure. *Circ Res*. **113**(6): 660-675.
15. Arbustini E., Pilotto, A., Repetto, A.*, et al.* (2002). Autosomal dominant dilated cardiomyopathy with atrioventricular block: a lamin A/C defect-related disease. *J Am Coll Cardiol*. **39**(6): 981-990.
16. Herman D.S., Lam , L., Taylor , M.R.G.*, et al.* (2012). Truncations of Titin Causing Dilated Cardiomyopathy. *N Engl J Med*. **366**(7): 619-628.
17. Peters S., Peters, H., and Thierfelder, L. (1999). Heart failure in arrhythmogenic right ventricular dysplasia-cardiomyopathy. *Int J Cardiol*. **71**(3): 251-256.
18. Basso C., Corrado, D., Marcus, F.I.*, et al.* (2009). Arrhythmogenic right ventricular cardiomyopathy. *The Lancet*. **373**(9671): 1289-1300.

19. Sen-Chowdhry S., Syrris, P., and McKenna, W.J. (2010). Genetics of Restrictive Cardiomyopathy. *Heart Fail Clin*. **6**(2): 179-186.
20. Jenni R., Oechslin, E., Schneider, J.*, et al.* (2001). Echocardiographic and pathoanatomical characteristics of isolated left ventricular non-compaction: a step towards classification as a distinct cardiomyopathy. *Heart*. **86**(6): 666-671.
21. Oechslin E.N., Attenhofer Jost, C.H., Rojas, J.R.*, et al.* (2000). Long-term follow-up of 34 adults with isolated left ventricular noncompaction: a distinct cardiomyopathy with poor prognosis. *J Am Coll Cardiol*. **36**(2): 493-500.
22. Towbin J.A. (2010). Left Ventricular Noncompaction: A New Form of Heart Failure. *Heart Fail Clin*. **6**(4): 453-469.
23. Semsarian C., Ingles, J., Maron, M.S.*, et al.* (2015). New Perspectives on the Prevalence of Hypertrophic Cardiomyopathy. *J Am Coll Cardiol*. **65**(12): 1249-1254.
24. Harris K.M., Spirito, P., Maron, M.S.*, et al.* (2006). Prevalence, Clinical Profile, and Significance of Left Ventricular Remodeling in the End-Stage Phase of Hypertrophic Cardiomyopathy. *Circulation*. **114**(3): 216-225.
25. Maron B.J., Spirito, P., Ackerman, M.J.*, et al.* (2013). Prevention of Sudden Cardiac Death With Implantable Cardioverter-Defibrillators in Children and Adolescents With Hypertrophic Cardiomyopathy. *J Am Coll Cardiol*. **61**(14): 1527-1535.
26. Murphy R.T., Mogensen, J., Shaw, A.*, et al.* (2004). Novel mutation in cardiac troponin I in recessive idiopathic dilated cardiomyopathy. *The Lancet*. **363**(9406): 371-372.
27. Mogensen J., Kubo, T., Duque, M.*, et al.* (2003). Idiopathic restrictive cardiomyopathy is part of the clinical expression of cardiac troponin I mutations. *J Clin Invest*. **111**(2): 209-216.
28. Kimura A., Harada, H., Park, J.-E.*, et al.* (1997). Mutations in the cardiac troponin I gene associated with hypertrophic cardiomyopathy. *Nat Genet*. **16**(4): 379-382.
29. Ingles J., Burns, C., Bagnall, R.D.*, et al.* (2017). Nonfamilial Hypertrophic Cardiomyopathy - Prevalence, Natural History, and Clinical Implications. *Circ Cardiovasc Genet*. **10**(2).
30. Sedaghat-Hamedani F., Kayvanpour, E., Tugrul, O.F.*, et al.* (2017). Clinical outcomes associated with sarcomere mutations in hypertrophic cardiomyopathy: a meta-analysis on 7675 individuals. *Clin Res Cardiol*. **107**(1): 30-41.
31. Melacini P., Basso, C., Angelini, A.*, et al.* (2010). Clinicopathological profiles of progressive heart failure in hypertrophic cardiomyopathy. *Eur Heart J*. **31**(17): 2111-2123.
32. Maron M.S., Olivotto , I., Betocchi , S.*, et al.* (2003). Effect of Left Ventricular Outflow Tract Obstruction on Clinical Outcome in Hypertrophic Cardiomyopathy. *N Engl J Med*. **348**(4): 295-303.
33. Sabater-Molina M., Pérez-Sánchez, I., Hernández del Rincón, J.P.*, et al.* (2017). Genetics of hypertrophic cardiomyopathy: A review of current state. *Clin Genet*.
34. Davies M.J. and McKenna, W.J. (1995). Hypertrophic cardiomyopathy — pathology and pathogenesis. *Histopathology*. **26**(6): 493-500.
35. Harvey P.A. and Leinwand, L.A. (2011). The cell biology of disease: Cellular mechanisms of cardiomyopathy. *J Cell Biol*. **194**(3): 355-365.
36. Marian A.J. (2000). Pathogenesis of diverse clinical and pathological phenotypes in hypertrophic cardiomyopathy. *The Lancet*. **355**(9197): 58-60.
37. Seidman J.G. and Seidman, C. (2001). The Genetic Basis for Cardiomyopathy. *Cell*. **104**(4): 557-567.
38. Kuwahara K., Saito, Y., Takano, M.*, et al.* (2003). NRSF regulates the fetal cardiac gene program and maintains normal cardiac structure and function. *EMBO J*. **22**(23): 6310-6321.
39. Dirkx E., da Costa Martins, P.A., and De Windt, L.J. (2013). Regulation of fetal gene expression in heart failure. *Biochim Biophys Acta*. **1832**(12): 2414-2424.

40. Lowes B.D., Minobe, W., Abraham, W.T.*, et al.* (1997). Changes in gene expression in the intact human heart. Downregulation of alpha-myosin heavy chain in hypertrophied, failing ventricular myocardium. *J Clin Invest*. **100**(9): 2315-2324.
41. Hajjar R.J. and Gwathmey, J.K. (1992). Cross-bridge dynamics in human ventricular myocardium. Regulation of contractility in the failing heart. *Circulation*. **86**(6): 1819-1826.
42. Smith C.S., Bottomley, P.A., Schulman, S.P.*, et al.* (2006). Altered Creatine Kinase Adenosine Triphosphate Kinetics in Failing Hypertrophied Human Myocardium. *Circulation*. **114**(11): 1151-1158.
43. Neubauer S. (2007). The Failing Heart — An Engine Out of Fuel. *N Engl J Med*. **356**(11): 1140-1151.
44. Dávila-Román V.G., Vedala, G., Herrero, P.*, et al.* (2002). Altered myocardial fatty acid and glucose metabolism in idiopathic dilated cardiomyopathy. *J Am Coll Cardiol*. **40**(2): 271-277.
45. Sack M.N., Rader, T.A., Park, S.*, et al.* (1996). Fatty Acid Oxidation Enzyme Gene Expression Is Downregulated in the Failing Heart. *Circulation*. **94**(11): 2837-2842.
46. Olivotto I., Girolami, F., Sciagrà, R.*, et al.* (2011). Microvascular Function Is Selectively Impaired in Patients With Hypertrophic Cardiomyopathy and Sarcomere Myofilament Gene Mutations. *J Am Coll Cardiol*. **58**(8): 839-848.
47. Weidemann F., Herrmann, S., Störk, S.*, et al.* (2009). Impact of Myocardial Fibrosis in Patients With Symptomatic Severe Aortic Stenosis. *Circulation*. **120**(7): 577-584.
48. Prinz C., Farr, M., Laser, K.T.*, et al.* (2013). Determining the role of fibrosis in hypertrophic cardiomyopathy. *Expert Rev Cardiovasc Ther*. **11**(4): 495-504.
49. Menon S.C., Eidem, B.W., Dearani, J.A.*, et al.* (2009). Diastolic Dysfunction and Its Histopathological Correlation in Obstructive Hypertrophic Cardiomyopathy in Children and Adolescents. *J Am Soc Echocardiogr*. **22**(12): 1327-1334.
50. Teekakirikul P., Eminaga, S., Toka, O.*, et al.* (2010). Cardiac fibrosis in mice with hypertrophic cardiomyopathy is mediated by non-myocyte proliferation and requires Tgf-β. *J Clin Invest*. **120**(10): 3520-3529.
51. Frey N., Luedde, M., and Katus, H.A. (2012). Mechanisms of disease: hypertrophic cardiomyopathy. *Nat Rev Cardiol*. **9**(2): 91-100.
52. Frank D. and Frey, N. (2011). Cardiac Z-disc Signaling Network. *J Biol Chem*. **286**(12): 9897-9904.
53. Siegert R., Perrot, A., Keller, S.*, et al.* (2011). A myomesin mutation associated with hypertrophic cardiomyopathy deteriorates dimerisation properties. *Biochem Biophys Res Commun*. **405**(3): 473-479.
54. Geier C., Perrot, A., Özcelik, C.*, et al.* (2003). Mutations in the Human Muscle LIM Protein Gene in Families With Hypertrophic Cardiomyopathy. *Circulation*. **107**(10): 1390-1395.
55. Heineke J. and Molkentin, J.D. (2006). Regulation of cardiac hypertrophy by intracellular signalling pathways. *Nat Rev Mol Cell Biol*. **7**(8): 589-600.
56. Frey N. and Olson, E.N. (2003). Cardiac Hypertrophy: The Good, the Bad, and the Ugly. *Annu Rev Physiol*. **65**(1): 45-79.
57. Molkentin J.D., Lu, J.-R., Antos, C.L.*, et al.* (1998). A Calcineurin-Dependent Transcriptional Pathway for Cardiac Hypertrophy. *Cell*. **93**(2): 215-228.
58. Naga Prasad S.V., Esposito, G., Mao, L.*, et al.* (2000). Gβγ-dependent Phosphoinositide 3-Kinase Activation in Hearts with in Vivo Pressure Overload Hypertrophy. *J Biol Chem*. **275**(7): 4693-4698.
59. Czubryt M.P. and Olson, E.N. (2004). Balancing contractility and energy production: the role of myocyte enhancer factor 2 (MEF2) in cardiac hypertrophy. *Recent Prog Horm Res*. **59**: 105-24.

60. Wehrens X.H. and Marks, A.R. (2004). Novel therapeutic approaches for heart failure by normalizing calcium cycling. *Nat Rev Drug Discov*. **3**(7): 565-73.
61. Kennedy A., Finlay, D.D., Guldenring, D.*, et al.* (2016). The Cardiac Conduction System. *Crit Care Nurs Clin North Am*. **28**(3): 269-279.
62. Anderson R.H., Ho, S.Y., Redmann, K.*, et al.* (2005). The anatomical arrangement of the myocardial cells making up the ventricular mass. *Eur J Cardiothorac Surg*. **28**(4): 517-525.
63. Frazier A.H., Ramirez-Correa, G.A., and Murphy, A.M. (2011). Molecular mechanisms of sarcomere dysfunction in dilated and hypertrophic cardiomyopathy. *Prog Pediatr Cardiol*. **31**(1): 29-33.
64. Stehle R. and Iorga, B. (2010). Kinetics of cardiac sarcomeric processes and rate-limiting steps in contraction and relaxation. *J Mol Cell Cardiol*. **48**(5): 843-850.
65. ter Keurs H.E., Bucx, J.J., de Tombe, P.P.*, et al.* (1988). The effects of sarcomere length and Ca2+ on force and velocity of shortening in cardiac muscle. *Adv Exp Med Biol*. **226**: 581-93.
66. Marston S.B. (2011). How Do Mutations in Contractile Proteins Cause the Primary Familial Cardiomyopathies? *J Cardiovasc Transl Res*. **4**(3): 245-255.
67. Keren A., Syrris, P., and McKenna, W.J. (2008). Hypertrophic cardiomyopathy: the genetic determinants of clinical disease expression. *Nat Clin Pract Cardiovasc Med*. **5**(3): 158-168.
68. Maron B.J., Maron, M.S., and Semsarian, C. (2012). Genetics of Hypertrophic Cardiomyopathy After 20 Years: Clinical Perspectives. *J Am Coll Cardiol*. **60**(8): 705-715.
69. Spirito P., Seidman , C.E., McKenna , W.J.*, et al.* (1997). The Management of Hypertrophic Cardiomyopathy. *N Engl J Med*. **336**(11): 775-785.
70. Watkins H., Rosenzweig , A., Hwang , D.-S.*, et al.* (1992). Characteristics and Prognostic Implications of Myosin Missense Mutations in Familial Hypertrophic Cardiomyopathy. *N Engl J Med*. **326**(17): 1108-1114.
71. Marian A.J. and Roberts, R. (2001). The Molecular Genetic Basis for Hypertrophic Cardiomyopathy. *J Mol Cell Cardiol*. **33**(4): 655-670.
72. Miroshnichenko N.S., Balanuk, I.V., and Nozdrenko, D.N. (2000). Packing of Myosin Molecules in Muscle Thick Filaments. *Cell Biol Int*. **24**(6): 327-333.
73. Walsh R., Rutland, C., Thomas, R.*, et al.* (2010). Cardiomyopathy: A Systematic Review of Disease-Causing Mutations in Myosin Heavy Chain 7 and Their Phenotypic Manifestations. *Cardiology*. **115**(1): 49-60.
74. Geisterfer-Lowrance A.A.T., Kass, S., Tanigawa, G.*, et al.* (1990). A molecular basis for familial hypertrophic cardiomyopathy: A β cardiac myosin heavy chain gene missense mutation. *Cell*. **62**(5): 999-1006.
75. Marian A.J. and Roberts, R. (1998). Molecular Genetic Basis of Hypertrophic Cardiomyopathy. *J Cardiovasc Electrophysiol*. **9**(1): 88-99.
76. Anan R., Greve, G., Thierfelder, L.*, et al.* (1994). Prognostic implications of novel beta cardiac myosin heavy chain gene mutations that cause familial hypertrophic cardiomyopathy. *J Clin Invest*. **93**(1): 280-285.
77. Bezzerides V.J., Zhang, D., and Pu, W.T. (2017). Modeling Inherited Arrhythmia Disorders Using Induced Pluripotent Stem Cell-Derived Cardiomyocytes. *Circ J*. **81**(1): 12-21.
78. Anderson C.L., Kuzmicki, C.E., Childs, R.R.*, et al.* (2014). Large-scale mutational analysis of Kv11.1 reveals molecular insights into type 2 long QT syndrome. *Nat Commun*. **5**(5535).
79. Romero L., Trenor, B., Yang, P.-C.*, et al.* (2015). In silico screening of the impact of hERG channel kinetic abnormalities on channel block and susceptibility to acquired long QT syndrome. *J Mol Cell Cardiol*. **87**: 271-282.

80. Duncker D.J., Bakkers, J., Brundel, B.J., *et al.* (2015). Animal and in silico models for the study of sarcomeric cardiomyopathies. *Cardiovasc Res*. **105**(4): 439-448.
81. Puckelwartz M. and McNally, E. (2014). Genetic Profiling for Risk Reduction in Human Cardiovascular Disease. *Genes*. **5**(1): 214.
82. Musunuru K., Domian, I.J., and Chien, K.R. (2010). Stem Cell Models of Cardiac Development and Disease. *Annu Rev Cell Dev Biol*. **26**(1): 667-687.
83. Leyton-Mange J.S. and Milan, D.J. (2014). Pluripotent Stem Cells as a Platform for Cardiac Arrhythmia Drug Screening. *Curr Treat Options Cardiovasc Med*. **16**(9): 334.
84. Denning C., Borgdorff, V., Crutchley, J., *et al.* (2016). Cardiomyocytes from human pluripotent stem cells: From laboratory curiosity to industrial biomedical platform. *Biochim Biophys Acta*. **1863**(7): 1728-1748.
85. May J.E., Xu, J., Morse, H.R., *et al.* (2009). Toxicity testing: the search for an in vitro alternative to animal testing. *Br J Biomed Sci*. **66**(3): 160-165.
86. Zebrowski D. and Engel, F., The Cardiomyocyte Cell Cycle in Hypertrophy, Tissue Homeostasis, and Regeneration., in *Reviews of Physiology, Biochemistry and Pharmacology*, B. Nilius, et al., Editors. 2013, Springer International Publishing. p. 67-96.
87. Skarnes W.C., Rosen, B., West, A.P., *et al.* (2011). A conditional knockout resource for the genome-wide study of mouse gene function. *Nature*. **474**(7351): 337-342.
88. Doevendans P.A., Daemen, M.J., de Muinck, E.D., *et al.* (1998). Cardiovascular phenotyping in mice. *Cardiovasc Res*. **39**(1): 34-49.
89. Morano I. (1999). Tuning the human heart molecular motors by myosin light chains. *J Mol Med*. **77**(7): 544-555.
90. Lyons G.E., Schiaffino, S., Sassoon, D., *et al.* (1990). Developmental regulation of myosin gene expression in mouse cardiac muscle. *J Cell Biol*. **111**(6): 2427-2436.
91. Qureshi Z.P., Seoane-Vazquez, E., Rodriguez-Monguio, R., *et al.* (2011). Market withdrawal of new molecular entities approved in the United States from 1980 to 2009. *Pharmacoepidemiol Drug Saf*. **20**(7): 772-777.
92. Gwathmey J.K., Tsaioun, K., and Hajjar, R.J. (2009). Cardionomics: a new integrative approach for screening cardiotoxicity of drug candidates. *Expert Opin Drug Metab Toxicol*. **5**(6): 647-660.
93. Thomson J.A., Itskovitz-Eldor, J., Shapiro, S.S., *et al.* (1998). Embryonic Stem Cell Lines Derived from Human Blastocysts. *Science*. **282**(5391): 1145-1147.
94. Takahashi K., Tanabe, K., Ohnuki, M., *et al.* (2007). Induction of Pluripotent Stem Cells from Adult Human Fibroblasts by Defined Factors. *Cell*. **131**(5): 861-872.
95. De Los Angeles A., Ferrari, F., Xi, R., *et al.* (2015). Hallmarks of pluripotency. *Nature*. **525**(7570): 469-478.
96. Somers A., Jean, J.-C., Sommer, C.A., *et al.* (2010). Generation of Transgene-Free Lung Disease-Specific Human Induced Pluripotent Stem Cells Using a Single Excisable Lentiviral Stem Cell Cassette. *Stem Cells*. **28**(10): 1728-1740.
97. McCormack M.P. and Rabbitts , T.H. (2004). Activation of the T-Cell Oncogene LMO2 after Gene Therapy for X-Linked Severe Combined Immunodeficiency. *N Engl J Med*. **350**(9): 913-922.
98. Fusaki N., Ban, H., Nishiyama, A., *et al.* (2009). Efficient induction of transgene-free human pluripotent stem cells using a vector based on Sendai virus, an RNA virus that does not integrate into the host genome. *Proc Jpn Acad Ser B Phys Biol Sci*. **85**.
99. Warren L., Manos, P.D., Ahfeldt, T., *et al.* (2010). Highly Efficient Reprogramming to Pluripotency and Directed Differentiation of Human Cells with Synthetic Modified mRNA. *Cell Stem Cell*. **7**(5): 618-630.
100. Drozd A.M., Walczak, M.P., Piaskowski, S., *et al.* (2015). Generation of human iPSCs from cells of fibroblastic and epithelial origin by means of the oriP/EBNA-1 episomal reprogramming system. *Stem Cell Res Ther*. **6**(1): 122.

101. Evans M.J. and Kaufman, M.H. (1981). Establishment in culture of pluripotential cells from mouse embryos. *Nature*. **292**(5819): 154-156.
102. Hongisto H., Vuoristo, S., Mikhailova, A.*, et al.* (2012). Laminin-511 expression is associated with the functionality of feeder cells in human embryonic stem cell culture. *Stem Cell Res*. **8**(1): 97-108.
103. Villa-Diaz L.G., Pacut, C., Slawny, N.A.*, et al.* (2009). Analysis of the Factors that Limit the Ability of Feeder Cells to Maintain the Undifferentiated State of Human Embryonic Stem Cells. *Stem Cells Dev*. **18**(4): 641-651.
104. Rottem S. and Barile, M.F. (1993). Beware of mycoplasmas. *Trends Biotechnol*. **11**(4): 143-151.
105. Xu C., Inokuma, M.S., Denham, J.*, et al.* (2001). Feeder-free growth of undifferentiated human embryonic stem cells. *Nat Biotech*. **19**(10): 971-974.
106. Kleinman H.K., McGarvey, M.L., Liotta, L.A.*, et al.* (1982). Isolation and characterization of type IV procollagen, laminin, and heparan sulfate proteoglycan from the EHS sarcoma. *Biochemistry*. **21**(24): 6188-6193.
107. Villa-Diaz L.G., Ross, A.M., Lahann, J.*, et al.* (2013). Concise Review: The Evolution of human pluripotent stem cell culture: From feeder cells to synthetic coatings. *Stem Cells*. **31**(1): 1-7.
108. Melkoumian Z., Weber, J.L., Weber, D.M.*, et al.* (2010). Synthetic peptide-acrylate surfaces for long-term self-renewal and cardiomyocyte differentiation of human embryonic stem cells. *Nat Biotech*. **28**(6): 606-610.
109. Chen G., Gulbranson, D.R., Hou, Z.*, et al.* (2011). Chemically defined conditions for human iPSC derivation and culture. *Nat Meth*. **8**(5): 424-429.
110. Beers J., Gulbranson, D.R., George, N.*, et al.* (2012). Passaging and colony expansion of human pluripotent stem cells by enzyme-free dissociation in chemically defined culture conditions. *Nat. Protocols*. **7**(11): 2029-2040.
111. Watanabe K., Ueno, M., Kamiya, D.*, et al.* (2007). A ROCK inhibitor permits survival of dissociated human embryonic stem cells. *Nat Biotech*. **25**(6): 681-686.
112. Amit M., Chebath, J., Margulets, V.*, et al.* (2010). Suspension Culture of Undifferentiated Human Embryonic and Induced Pluripotent Stem Cells. *Stem Cell Rev*. **6**(2): 248-259.
113. Olmer R., Haase, A., Merkert, S.*, et al.* (2010). Long term expansion of undifferentiated human iPS and ES cells in suspension culture using a defined medium. *Stem Cell Res*. **5**(1): 51-64.
114. Shiba Y., Fernandes, S., Zhu, W.-Z.*, et al.* (2012). Human ES-cell-derived cardiomyocytes electrically couple and suppress arrhythmias in injured hearts. *Nature*. **489**(7415): 322-325.
115. Chong J.J.H., Yang, X., Don, C.W.*, et al.* (2014). Human embryonic-stem-cell-derived cardiomyocytes regenerate non-human primate hearts. *Nature*. **510**(7504): 273-277.
116. Abu-Issa R. and Kirby, M.L. (2007). Heart Field: From Mesoderm to Heart Tube. *Annu Rev Cell Dev Biol*. **23**(1): 45-68.
117. Epstein J.A. (2010). Cardiac Development and Implications for Heart Disease. *N Engl J Med*. **363**(17): 1638-1647.
118. Wu S.M., Fujiwara, Y., Cibulsky, S.M.*, et al.* (2006). Developmental Origin of a Bipotential Myocardial and Smooth Muscle Cell Precursor in the Mammalian Heart. *Cell*. **127**(6): 1137-1150.
119. Zaffran S., Kelly, R.G., Meilhac, S.M.*, et al.* (2004). Right Ventricular Myocardium Derives From the Anterior Heart Field. *Circ Res*. **95**(3): 261-268.
120. Cai C.-L., Liang, X., Shi, Y.*, et al.* (2003). Isl1 Identifies a Cardiac Progenitor Population that Proliferates Prior to Differentiation and Contributes a Majority of Cells to the Heart. *Dev Cell*. **5**(6): 877-889.

121. Douglas Y.L., Jongbloed, M.R.M., DeRuiter, M.C., *et al.* (2011). Normal and abnormal development of pulmonary veins: State of the art and correlation with clinical entities. *Int J Cardiol*. **147**(1): 13-24.
122. Srivastava D. (2006). Making or Breaking the Heart: From Lineage Determination to Morphogenesis. *Cell*. **126**(6): 1037-1048.
123. Schleich J.-M., Abdulla, T., Summers, R., *et al.* (2013). An overview of cardiac morphogenesis. *Arch Cardiovasc Dis*. **106**(11): 612-623.
124. Später D., Hansson, E.M., Zangi, L., *et al.* (2014). How to make a cardiomyocyte. *Development*. **141**(23): 4418-4431.
125. Mummery C.L., Zhang, J., Ng, E.S., *et al.* (2012). Differentiation of Human Embryonic Stem Cells and Induced Pluripotent Stem Cells to Cardiomyocytes: A Methods Overview. *Circ Res*. **111**(3): 344-358.
126. Talkhabi M., Aghdami, N., and Baharvand, H. (2016). Human cardiomyocyte generation from pluripotent stem cells: A state-of-art. *Life Sci*. **145**: 98-113.
127. Anderson D., Self, T., Mellor, I.R., *et al.* (2007). Transgenic Enrichment of Cardiomyocytes From Human Embryonic Stem Cells. *Mol Ther*. **15**(11): 2027-2036.
128. He J.-Q., Ma, Y., Lee, Y., *et al.* (2003). Human Embryonic Stem Cells Develop Into Multiple Types of Cardiac Myocytes: Action Potential Characterization. *Circ Res*. **93**(1): 32-39.
129. Mummery C., Ward-van Oostwaard, D., Doevendans, P., *et al.* (2003). Differentiation of Human Embryonic Stem Cells to Cardiomyocytes: Role of Coculture With Visceral Endoderm-Like Cells. *Circulation*. **107**(21): 2733-2740.
130. Passier R., Oostwaard, D.W.-v., Snapper, J., *et al.* (2005). Increased Cardiomyocyte Differentiation from Human Embryonic Stem Cells in Serum-Free Cultures. *Stem Cells*. **23**(6): 772-780.
131. Laflamme M.A., Chen, K.Y., Naumova, A.V., *et al.* (2007). Cardiomyocytes derived from human embryonic stem cells in pro-survival factors enhance function of infarcted rat hearts. *Nat Biotech*. **25**(9): 1015-1024.
132. Zhang J., Klos, M., Wilson, G.F., *et al.* (2012). Extracellular Matrix Promotes Highly Efficient Cardiac Differentiation of Human Pluripotent Stem Cells. The Matrix Sandwich Method. *Circ Res*. **111**(9): 1125.
133. Lian X., Hsiao, C., Wilson, G., *et al.* (2012). Robust cardiomyocyte differentiation from human pluripotent stem cells via temporal modulation of canonical Wnt signaling. *Proc Natl Acad Sci U S A*. **109**(27): E1848–E1857.
134. Minami I., Yamada, K., Otsuji, Tomomi G., *et al.* (2012). A Small Molecule that Promotes Cardiac Differentiation of Human Pluripotent Stem Cells under Defined, Cytokine- and Xeno-free Conditions. *Cell Rep*. **2**(5): 1448-1460.
135. Burridge P.W., Matsa, E., Shukla, P., *et al.* (2014). Chemically defined generation of human cardiomyocytes. *Nat Meth*. **11**(8): 855-860.
136. Moretti A., Laugwitz, K.-L., Dorn, T., *et al.* (2013). Pluripotent Stem Cell Models of Human Heart Disease. *Cold Spring Harb Perspect Med*. **3**(11).
137. Ting S., Chen, A., Reuveny, S., *et al.* (2014). An intermittent rocking platform for integrated expansion and differentiation of human pluripotent stem cells to cardiomyocytes in suspended microcarrier cultures. *Stem Cell Res*. **13**(2): 202-213.
138. Fonoudi H., Ansari, H., Abbasalizadeh, S., *et al.* (2015). A Universal and Robust Integrated Platform for the Scalable Production of Human Cardiomyocytes From Pluripotent Stem Cells. *Stem Cell Transl Med*. **4**(12): 1482-1494.
139. Breckwoldt K., Letuffe-Breniere, D., Mannhardt, I., *et al.* (2017). Differentiation of cardiomyocytes and generation of human engineered heart tissue. *Nat. Protocols*. **12**(6): 1177-1197.
140. Yang X., Pabon, L., and Murry, C.E. (2014). Engineering Adolescence: maturation of human pluripotent stem cell-derived cardiomyocytes. *Circ Res*. **114**(3): 511.

141. Gerdes A.M., Kellerman, S.E., Moore, J.A., *et al.* (1992). Structural remodeling of cardiac myocytes in patients with ischemic cardiomyopathy. *Circulation*. **86**(2): 426-430.
142. Zhang J., Wilson, G.F., Soerens, A.G., *et al.* (2009). Functional Cardiomyocytes Derived From Human Induced Pluripotent Stem Cells. *Circ Res*. **104**(4): e30-e41.
143. Bird S.D., Doevendans, P.A., van Rooijen, M.A., *et al.* (2003). The human adult cardiomyocyte phenotype. *Cardiovasc Res*. **58**(2): 423-434.
144. Lundy S.D., Zhu, W.-Z., Regnier, M., *et al.* (2013). Structural and Functional Maturation of Cardiomyocytes Derived from Human Pluripotent Stem Cells. *Stem Cells Dev*. **22**(14): 1991-2002.
145. Bhavsar P.K., Dhoot, G.K., Cumming, D.V., *et al.* (1991). Developmental expression of troponin I isoforms in fetal human heart. *FEBS Lett*. **292**(1-2): 5-8.
146. Opitz C.A., Leake, M.C., Makarenko, I., *et al.* (2004). Developmentally Regulated Switching of Titin Size Alters Myofibrillar Stiffness in the Perinatal Heart. *Circ Res*. **94**(7): 967-975.
147. Saggin L., Gorza, L., Ausoni, S., *et al.* (1989). Troponin I switching in the developing heart. *J Biol Chem*. **264**(27): 16299-16302.
148. Mahdavi V., Lompre, A.M., Chambers, A.P., *et al.* (1984). Cardiac myosin heavy chain isozymic transitions during development and under pathological conditions are regulated at the level of mRNA availability. *Eur Heart J*. **5**: 181-191.
149. Xu X.Q., Soo, S.Y., Sun, W., *et al.* (2009). Global Expression Profile of Highly Enriched Cardiomyocytes Derived from Human Embryonic Stem Cells. *Stem Cells*. **27**(9): 2163-2174.
150. Ziman A.P., Gómez-Viquez, N.L., Bloch, R.J., *et al.* (2010). Excitation–contraction coupling changes during postnatal cardiac development. *J Mol Cell Cardiol*. **48**(2): 379-386.
151. Lopaschuk G.D. and Jaswal, J.S. (2010). Energy metabolic phenotype of the cardiomyocyte during development, differentiation, and postnatal maturation. *J Cardiovasc Pharmacol*. **56**(2): 130-140.
152. Schaper J., Meiser, E., and Stämmler, G. (1985). Ultrastructural morphometric analysis of myocardium from dogs, rats, hamsters, mice, and from human hearts. *Circ Res*. **56**(3): 377-391.
153. Gherghiceanu M., Barad, L., Novak, A., *et al.* (2011). Cardiomyocytes derived from human embryonic and induced pluripotent stem cells: comparative ultrastructure. *J Cell Mol Med*. **15**(11): 2539-2551.
154. Drouin E., Charpentier, F., Gauthier, C., *et al.* (1995). Electrophysiologic characteristics of cells spanning the left ventricular wall of human heart: Evidence for presence of M cells. *J Am Coll Cardiol*. **26**(1): 185-192.
155. Sartiani L., Bettiol, E., Stillitano, F., *et al.* (2007). Developmental Changes in Cardiomyocytes Differentiated from Human Embryonic Stem Cells: A Molecular and Electrophysiological Approach. *Stem Cells*. **25**(5): 1136-1144.
156. Chen H.S.V., Kim, C., and Mercola, M. (2009). Electrophysiological challenges of cell-based myocardial repair. *Circulation*. **120**(24): 2496-2508.
157. Angst B.D., Khan, L.U.R., Severs, N.J., *et al.* (1997). Dissociated Spatial Patterning of Gap Junctions and Cell Adhesion Junctions During Postnatal Differentiation of Ventricular Myocardium. *Circ Res*. **80**(1): 88-94.
158. Hasenfuss G., Mulieri, L.A., Blanchard, E.M., *et al.* (1991). Energetics of isometric force development in control and volume-overload human myocardium. Comparison with animal species. *Circ Res*. **68**(3): 836-846.
159. Mannhardt I., Breckwoldt, K., Letuffe-Brenière, D., *et al.* (2016). Human Engineered Heart Tissue: Analysis of Contractile Force. *Stem Cell Reports*. **7**(1): 29-42.

160. Tanaka A., Yuasa, S., Mearini, G.*, et al.* (2014). Endothelin-1 Induces Myofibrillar Disarray and Contractile Vector Variability in Hypertrophic Cardiomyopathy–Induced Pluripotent Stem Cell–Derived Cardiomyocytes. *J Am Heart Assoc*. **3**(6).
161. Lan F., Lee, Andrew S., Liang, P.*, et al.* (2013). Abnormal Calcium Handling Properties Underlie Familial Hypertrophic Cardiomyopathy Pathology in Patient-Specific Induced Pluripotent Stem Cells. *Cell Stem Cell*. **12**(1): 101-113.
162. Han L., Li, Y., Tchao, J.*, et al.* (2014). Study familial hypertrophic cardiomyopathy using patient-specific induced pluripotent stem cells. *Cardiovasc Res*. **104**(2): 258-269.
163. Peters N.S., Severs, N.J., Rothery, S.M.*, et al.* (1994). Spatiotemporal relation between gap junctions and fascia adherens junctions during postnatal development of human ventricular myocardium. *Circulation*. **90**(2): 713-725.
164. Yang X., Rodriguez, M., Pabon, L.*, et al.* (2014). Tri-iodo-l-thyronine promotes the maturation of human cardiomyocytes-derived from induced pluripotent stem cells. *J Mol Cell Cardiol*. **72**: 296-304.
165. White M.C., Pang, L., and Yang, X. (2016). MicroRNA-mediated maturation of human pluripotent stem cell-derived cardiomyocytes: Towards a better model for cardiotoxicity? *Food Chem Toxicol*. **98**: 17-24.
166. Taylor J.M., Rovin, J.D., and Parsons, J.T. (2000). A Role for Focal Adhesion Kinase in Phenylephrine-induced Hypertrophy of Rat Ventricular Cardiomyocytes. *J Biol Chem*. **275**(25): 19250-19257.
167. Opthof T. (1988). The mammalian sinoatrial node. *Cardiovasc Drugs Ther*. **1**(6): 573-97.
168. Radisic M., Park, H., Shing, H.*, et al.* (2004). Functional assembly of engineered myocardium by electrical stimulation of cardiac myocytes cultured on scaffolds. *Proc Natl Acad Sci U S A*. **101**(52): 18129-18134.
169. Mihic A., Li, J., Miyagi, Y.*, et al.* (2014). The effect of cyclic stretch on maturation and 3D tissue formation of human embryonic stem cell-derived cardiomyocytes. *Biomaterials*. **35**(9): 2798-2808.
170. Engler A.J., Carag-Krieger, C., Johnson, C.P.*, et al.* (2008). Embryonic cardiomyocytes beat best on a matrix with heart-like elasticity: scar-like rigidity inhibits beating. *J Cell Sci*. **121**(22): 3794-3802.
171. McCain M.L., Yuan, H., Pasqualini, F.S.*, et al.* (2014). Matrix elasticity regulates the optimal cardiac myocyte shape for contractility. *Am J Physiol Heart Circ Physiol*. **306**(11): H1525-H1539.
172. Rao C., Prodromakis, T., Kolker, L.*, et al.* (2013). The effect of microgrooved culture substrates on calcium cycling of cardiac myocytes derived from human induced pluripotent stem cells. *Biomaterials*. **34**(10): 2399-2411.
173. Palchesko R.N., Zhang, L., Sun, Y.*, et al.* (2012). Development of Polydimethylsiloxane Substrates with Tunable Elastic Modulus to Study Cell Mechanobiology in Muscle and Nerve. *PLoS One*. **7**(12): e51499.
174. Eder A., Vollert, I., Hansen, A.*, et al.* (2016). Human engineered heart tissue as a model system for drug testing. *Adv Drug Deliv Rev*. **96**: 214-224.
175. Nunes S.S., Miklas, J.W., Liu, J.*, et al.* (2013). Biowire: a platform for maturation of human pluripotent stem cell-derived cardiomyocytes. *Nat Meth*. **10**(8): 781-787.
176. Ruan J.-L., Tulloch, N.L., Razumova, M.V.*, et al.* (2016). Mechanical Stress Conditioning and Electrical Stimulation Promote Contractility and Force Maturation of Induced Pluripotent Stem Cell-Derived Human Cardiac Tissue. *Circulation*. **134**(20): 1557-1567.
177. Tiburcy M., Hudson, J.E., Balfanz, P.*, et al.* (2017). Defined Engineered Human Myocardium With Advanced Maturation for Applications in Heart Failure Modeling and Repair. *Circulation*. **135**(19): 1832-1847.

178. Robertson C., Tran, D.D., and George, S.C. (2013). Concise Review: Maturation Phases of Human Pluripotent Stem Cell-Derived Cardiomyocytes. *Stem Cells*. **31**(5): 829-837.
179. Pham H., Kearns, N.A., and Maehr, R., Transcriptional Regulation with CRISPR/Cas9 Effectors in Mammalian Cells, in *Post-Transcriptional Gene Regulation*, E. Dassi, Editor. 2016, Springer New York: New York, NY. p. 43-57.
180. Sala L., Bellin, M., and Mummery, C.L. (2017). Integrating cardiomyocytes from human pluripotent stem cells in safety pharmacology: has the time come? *Br J Pharmacol*. **174**(21): 3749-3765.
181. Takata M., Sasaki, M.S., Sonoda, E.*, et al.* (1998). Homologous recombination and non-homologous end-joining pathways of DNA double-strand break repair have overlapping roles in the maintenance of chromosomal integrity in vertebrate cells. *EMBO J*. **17**(18): 5497-5508.
182. Lieber M.R., Ma, Y., Pannicke, U.*, et al.* (2003). Mechanism and regulation of human non-homologous DNA end-joining. *Nat Rev Mol Cell Biol*. **4**(9): 712-720.
183. Ousterout D.G., Perez-Pinera, P., Thakore, P.I.*, et al.* (2013). Reading Frame Correction by Targeted Genome Editing Restores Dystrophin Expression in Cells From Duchenne Muscular Dystrophy Patients. *Mol Ther*. **21**(9): 1718-1726.
184. Holt N., Wang, J., Kim, K.*, et al.* (2010). Human hematopoietic stem/progenitor cells modified by zinc-finger nucleases targeted to CCR5 control HIV-1 in vivo. *Nat Biotechnol*. **28**(8): 839-47.
185. Canver M.C., Bauer, D.E., Dass, A.*, et al.* (2014). Characterization of Genomic Deletion Efficiency Mediated by Clustered Regularly Interspaced Palindromic Repeats (CRISPR)/Cas9 Nuclease System in Mammalian Cells. *J Biol Chem*. **289**(31): 21312-21324.
186. Canver M.C., Smith, E.C., Sher, F.*, et al.* (2015). BCL11A enhancer dissection by Cas9-mediated in situ saturating mutagenesis. *Nature*. **527**(7577): 192-197.
187. Moehle E.A., Rock, J.M., Lee, Y.-L.*, et al.* (2007). Targeted gene addition into a specified location in the human genome using designed zinc finger nucleases. *Proc Natl Acad Sci U S A*. **104**(9): 3055-3060.
188. Lombardo A., Cesana, D., Genovese, P.*, et al.* (2011). Site-specific integration and tailoring of cassette design for sustainable gene transfer. *Nat Meth*. **8**(10): 861-869.
189. Chen F., Pruett-Miller, S.M., Huang, Y.*, et al.* (2011). High-frequency genome editing using ssDNA oligonucleotides with zinc-finger nucleases. *Nat Meth*. **8**(9): 753-755.
190. Maeder M.L. and Gersbach, C.A. (2016). Genome-editing Technologies for Gene and Cell Therapy. *Mol Ther*. **24**(3): 430-46.
191. Urnov F.D., Rebar, E.J., Holmes, M.C.*, et al.* (2010). Genome editing with engineered zinc finger nucleases. *Nat Rev Genet*. **11**(9): 636-646.
192. Gabriel R., Lombardo, A., Arens, A.*, et al.* (2011). An unbiased genome-wide analysis of zinc-finger nuclease specificity. *Nat Biotech*. **29**(9): 816-823.
193. Ramirez C.L., Foley, J.E., Wright, D.A.*, et al.* (2008). Unexpected failure rates for modular assembly of engineered zinc fingers. *Nat Meth*. **5**(5): 374-375.
194. Boch J., Scholze, H., Schornack, S.*, et al.* (2009). Breaking the Code of DNA Binding Specificity of TAL-Type III Effectors. *Science*. **326**(5959): 1509-1512.
195. Mussolino C., Morbitzer, R., Lütge, F.*, et al.* (2011). A novel TALE nuclease scaffold enables high genome editing activity in combination with low toxicity. *Nucleic Acids Res*. **39**(21): 9283-9293.
196. Reyon D., Tsai, S.Q., Khayter, C.*, et al.* (2012). FLASH assembly of TALENs for high-throughput genome editing. *Nat Biotech*. **30**(5): 460-465.
197. Holkers M., Maggio, I., Liu, J.*, et al.* (2013). Differential integrity of TALE nuclease genes following adenoviral and lentiviral vector gene transfer into human cells. *Nucleic Acids Res*. **41**(5): e63-e63.

198. Barrangou R., Fremaux, C., Deveau, H., *et al.* (2007). CRISPR Provides Acquired Resistance Against Viruses in Prokaryotes. *Science*. **315**(5819): 1709-1712.
199. Mali P., Yang, L., Esvelt, K.M., *et al.* (2013). RNA-Guided Human Genome Engineering via Cas9. *Science*. **339**(6121): 823-826.
200. Cong L., Ran, F.A., Cox, D., *et al.* (2013). Multiplex Genome Engineering Using CRISPR/Cas Systems. *Science*. **339**(6121): 819-823.
201. Fonfara I., Le Rhun, A., Chylinski, K., *et al.* (2014). Phylogeny of Cas9 determines functional exchangeability of dual-RNA and Cas9 among orthologous type II CRISPR-Cas systems. *Nucleic Acids Res*. **42**(4): 2577-2590.
202. Ran F.A., Cong, L., Yan, W.X., *et al.* (2015). In vivo genome editing using Staphylococcus aureus Cas9. *Nature*. **520**(7546): 186-191.
203. Kleinstiver B.P., Prew, M.S., Tsai, S.Q., *et al.* (2015). Engineered CRISPR-Cas9 nucleases with altered PAM specificities. *Nature*. **523**(7561): 481-485.
204. Fu Y., Foden, J.A., Khayter, C., *et al.* (2013). High-frequency off-target mutagenesis induced by CRISPR-Cas nucleases in human cells. *Nat Biotech*. **31**(9): 822-826.
205. Hsu P.D., Scott, D.A., Weinstein, J.A., *et al.* (2013). DNA targeting specificity of RNA-guided Cas9 nucleases. *Nat Biotech*. **31**(9): 827-832.
206. Veres A., Gosis, Bridget S., Ding, Q., *et al.* (2014). Low Incidence of Off-Target Mutations in Individual CRISPR-Cas9 and TALEN Targeted Human Stem Cell Clones Detected by Whole-Genome Sequencing. *Cell Stem Cell*. **15**(1): 27-30.
207. Cradick T.J., Fine, E.J., Antico, C.J., *et al.* (2013). CRISPR/Cas9 systems targeting β-globin and CCR5 genes have substantial off-target activity. *Nucleic Acids Res*. **41**(20): 9584-9592.
208. Smith C., Abalde-Atristain, L., He, C., *et al.* (2015). Efficient and Allele-Specific Genome Editing of Disease Loci in Human iPSCs. *Mol Ther*. **23**(3): 570-577.
209. Kim S., Kim, D., Cho, S.W., *et al.* (2014). Highly efficient RNA-guided genome editing in human cells via delivery of purified Cas9 ribonucleoproteins. *Genome Res*. **24**(6): 1012-1019.
210. Ran F.A., Hsu, Patrick D., Lin, C.-Y., *et al.* (2013). Double Nicking by RNA-Guided CRISPR Cas9 for Enhanced Genome Editing Specificity. *Cell*. **154**(6): 1380-1389.
211. Kleinstiver B.P., Pattanayak, V., Prew, M.S., *et al.* (2016). High-fidelity CRISPR–Cas9 nucleases with no detectable genome-wide off-target effects. *Nature*. **529**(7587): 490-495.
212. Luo Y., Liu, C., Cerbini, T., *et al.* (2014). Stable Enhanced Green Fluorescent Protein Expression After Differentiation and Transplantation of Reporter Human Induced Pluripotent Stem Cells Generated by AAVS1 Transcription Activator-Like Effector Nucleases. *Stem Cell Transl Med*. **3**(7): 821-835.
213. Maeder M.L. and Gersbach, C.A. (2016). Genome-editing Technologies for Gene and Cell Therapy. *Molecular Therapy*. **24**(3): 430-446.
214. Yusa K., Rashid, S.T., Strick-Marchand, H., *et al.* (2011). Targeted gene correction of α(1)-antitrypsin deficiency in induced pluripotent stem cells. *Nature*. **478**(7369): 391-394.
215. Osborn M.J., Starker, C.G., McElroy, A.N., *et al.* (2013). TALEN-based Gene Correction for Epidermolysis Bullosa. *Mol Ther*. **21**(6): 1151-1159.
216. Karakikes I., Termglinchan, V., Cepeda, D.A., *et al.* (2017). A Comprehensive TALEN-Based Knockout Library for Generating Human-Induced Pluripotent Stem Cell–Based Models for Cardiovascular Diseases. *Circ Res*. **120**(10): 1561-1571.
217. Lattanzi A., Duguez, S., Moiani, A., *et al.* (2017). Correction of the Exon 2 Duplication in DMD Myoblasts by a Single CRISPR/Cas9 System. *Mol Ther Nucleic Acids*. **7**: 11-19.
218. Liang P., Xu, Y., Zhang, X., *et al.* (2015). CRISPR/Cas9-mediated gene editing in human tripronuclear zygotes. *Protein Cell*. **6**(5): 363-372.

219. Dever D.P., Bak, R.O., Reinisch, A.*, et al.* (2016). CRISPR/Cas9 β-globin gene targeting in human haematopoietic stem cells. *Nature*. **539**(7629): 384-389.
220. Ma H., Marti-Gutierrez, N., Park, S.-W.*, et al.* (2017). Correction of a pathogenic gene mutation in human embryos. *Nature*. **548**(7668): 413-419.
221. Cai M Fau - Yang Y. and Yang, Y. (2014). Targeted genome editing tools for disease modeling and gene therapy. *Curr Gene Ther*. **14**(1): 2-9.
222. Shaheen N., Shiti, A., and Gepstein, L. (2017). Pluripotent Stem Cell-Based Platforms in Cardiac Disease Modeling and Drug Testing. *Clin Pharmacol Ther*. **102**(2): 203-208.
223. Joseph M.Z. (2009). Applications of High Content Screening in Life Science Research. *Comb Chem High Throughput Screen*. **12**(9): 870-876.
224. Zanella F., Lorens, J.B., and Link, W. (2010). High content screening: seeing is believing. *Trends Biotechnol*. **28**(5): 237-245.
225. Földes G., Matsa, E., Kriston-Vizi, J.*, et al.* (2014). Aberrant α-Adrenergic Hypertrophic Response in Cardiomyocytes from Human Induced Pluripotent Cells. *Stem Cell Reports*. **3**(5): 905-914.
226. Pasqualini F.S., Sheehy, S.P., Agarwal, A.*, et al.* (2015). Structural Phenotyping of Stem Cell-Derived Cardiomyocytes. *Stem Cell Reports*. **4**(3): 340-347.
227. Mioulane M., Foldes, G., Ali, N.N.*, et al.* (2012). Development of High Content Imaging Methods for Cell Death Detection in Human Pluripotent Stem Cell-Derived Cardiomyocytes. *J Cardiovasc Transl Res*. **5**(5): 593-604.
228. Carlson C., Koonce, C., Aoyama, N.*, et al.* (2013). Phenotypic Screening with Human iPS Cell–Derived Cardiomyocytes. *J Biomol Screen*. **18**(10): 1203-1211.
229. Qian W. and Van Houten, B. (2010). Alterations in bioenergetics due to changes in mitochondrial DNA copy number. *Methods*. **51**(4): 452-457.
230. Correia C., Koshkin, A., Duarte, P.*, et al.* (2017). Distinct carbon sources affect structural and functional maturation of cardiomyocytes derived from human pluripotent stem cells. *Sci Rep*. **7**: 8590.
231. Kim C., Wong, J., Wen, J.*, et al.* (2013). Studying arrhythmogenic right ventricular dysplasia with patient-specific iPSCs. *Nature*. **494**(7435): 105-110.
232. Matsa E., Rajamohan, D., Dick, E.*, et al.* (2011). Drug evaluation in cardiomyocytes derived from human induced pluripotent stem cells carrying a long QT syndrome type 2 mutation. *Eur Heart J*. **32**(8): 952-962.
233. Brüggemann A., Farre, C., Haarmann, C.*, et al.*, Planar Patch Clamp: Advances in Electrophysiology, in *Potassium Channels: Methods and Protocols*, J.D. Lippiat, Editor. 2009, Humana Press: Totowa, NJ. p. 165-176.
234. Ma J., Guo, L., Fiene, S.J.*, et al.* (2011). High purity human-induced pluripotent stem cell-derived cardiomyocytes: electrophysiological properties of action potentials and ionic currents. *Am J Physiol Heart Circ Physiol*. **301**(5): H2006-H2017.
235. Scheel O., Frech, S., Amuzescu, B.*, et al.* (2014). Action potential characterization of human induced pluripotent stem cell-derived cardiomyocytes using automated patch-clamp technology. *Assay drug dev. technol.* **12**(8): 457-69.
236. Rajamohan D., Kalra, S., Duc Hoang, M.*, et al.* (2016). Automated Electrophysiological and Pharmacological Evaluation of Human Pluripotent Stem Cell-Derived Cardiomyocytes. *Stem Cells Dev*. **25**(6): 439-452.
237. Gilchrist K.H., Lewis, G.F., Gay, E.A.*, et al.* (2015). High-throughput cardiac safety evaluation and multi-parameter arrhythmia profiling of cardiomyocytes using microelectrode arrays. *Toxicol Appl Pharmacol*. **288**(2): 249-257.
238. Qu Y. and Vargas, H.M. (2015). Proarrhythmia Risk Assessment in Human Induced Pluripotent Stem Cell-Derived Cardiomyocytes Using the Maestro MEA Platform. *Toxicol Sci*. **147**(1): 286-295.

239. Spira M.E. and Hai, A. (2013). Multi-electrode array technologies for neuroscience and cardiology. *Nat Nano*. **8**(2): 83-94.
240. Loew L.M., Design and Use of Organic Voltage Sensitive Dyes, in *Membrane Potential Imaging in the Nervous System and Heart*, M. Canepari, D. Zecevic, and O. Bernus, Editors. 2015, Springer International Publishing: Cham. p. 27-53.
241. Bootman M.D., Rietdorf, K., Collins, T.*, et al.* (2013). Ca2+-Sensitive Fluorescent Dyes and Intracellular Ca2+ Imaging. *Cold Spring Harbor Protocols*. **2013**(2): 83-99.
242. Leyton-Mange Jordan S., Mills, Robert W., Macri, Vincenzo S.*, et al.* (2014). Rapid Cellular Phenotyping of Human Pluripotent Stem Cell-Derived Cardiomyocytes using a Genetically Encoded Fluorescent Voltage Sensor. *Stem Cell Reports*. **2**(2): 163-170.
243. Smith G., Craig, M.A., Anson, B.*, et al. Optical measurements of electrical activity from hiPSC-derived cardiomyocytes is a robust and high-throughput method for measuring NCE-effects on the cardiac action potential*. in *SOT Annual Meeting*. 2013.
244. Liu J., Sun, N., Bruce, M.A.*, et al.* (2012). Atomic Force Mechanobiology of Pluripotent Stem Cell-Derived Cardiomyocytes. *PLoS One*. **7**(5): e37559.
245. Hazeltine L.B., Simmons, C.S., Salick, M.R.*, et al.* (2012). Effects of Substrate Mechanics on Contractility of Cardiomyocytes Generated from Human Pluripotent Stem Cells. *Int J Cell Biol*. **2012**: 13.
246. Ribeiro M.C., Tertoolen, L.G., Guadix, J.A.*, et al.* (2015). Functional maturation of human pluripotent stem cell derived cardiomyocytes in vitro – Correlation between contraction force and electrophysiology. *Biomaterials*. **51**: 138-150.
247. Hayakawa T., Kunihiro, T., Ando, T.*, et al.* (2014). Image-based evaluation of contraction–relaxation kinetics of human-induced pluripotent stem cell-derived cardiomyocytes: Correlation and complementarity with extracellular electrophysiology. *J Mol Cell Cardiol*. **77**: 178-191.
248. Shim J., Grosberg, A., Nawroth, J.C.*, et al.* (2012). Modeling of cardiac muscle thin films: Pre-stretch, passive and active behavior. *J Biomech*. **45**(5): 832-841.
249. Colomo F., Nencini, S., Piroddi, N.*, et al.*, Calcium Dependence of the Apparent Rate of Force Generation in Single Striated Muscle Myofibrils Activated by Rapid Solution Changes, in *Mechanisms of Work Production and Work Absorption in Muscle*, H. Sugi and G.H. Pollack, Editors. 1998, Springer US: Boston, MA. p. 373-382.
250. Rodriguez M.L., Graham, B.T., Pabon, L.M.*, et al.* (2014). Measuring the Contractile Forces of Human Induced Pluripotent Stem Cell-Derived Cardiomyocytes With Arrays of Microposts. *J Biomech Eng*. **136**(5): 051005-051005-10.
251. Kensah G., Roa Lara, A., Dahlmann, J.*, et al.* (2013). Murine and human pluripotent stem cell-derived cardiac bodies form contractile myocardial tissue in vitro. *Eur Heart J*. **34**(15): 1134-1146.
252. Giaever I. and Keese, C.R. (1993). A morphological biosensor for mammalian cells. *Nature*. **366**(6455): 591-592.
253. Lamore S.D., Kamendi, H.W., Scott, C.W.*, et al.* (2013). Cellular Impedance Assays for Predictive Preclinical Drug Screening of Kinase Inhibitor Cardiovascular Toxicity. *Toxicol Sci*. **135**(2): 402-413.
254. Peters M.F., Lamore, S.D., Guo, L.*, et al.* (2015). Human Stem Cell-Derived Cardiomyocytes in Cellular Impedance Assays: Bringing Cardiotoxicity Screening to the Front Line. *Cardiovasc Toxicol*. **15**(2): 127-139.
255. Scott C.W., Zhang, X., Abi-Gerges, N.*, et al.* (2014). An Impedance-Based Cellular Assay Using Human iPSC-Derived Cardiomyocytes to Quantify Modulators of Cardiac Contractility. *Toxicol Sci*. **142**(2): 331-338.
256. Doerr L., Thomas, U., Guinot, D.R.*, et al.* (2014). New Easy-to-Use Hybrid System for Extracellular Potential and Impedance Recordings. *J Lab Autom*. **20**(2): 175-188.

257. Ran F.A., Hsu, P.D., Wright, J., *et al.* (2013). Genome engineering using the CRISPR-Cas9 system. *Nat. Protocols*. **8**(11): 2281-2308.
258. Burridge P.W., Anderson, D., Priddle, H., *et al.* (2007). Improved Human Embryonic Stem Cell Embryoid Body Homogeneity and Cardiomyocyte Differentiation from a Novel V-96 Plate Aggregation System Highlights Interline Variability. *Stem Cells*. **25**(4): 929-938.
259. Burkart A.M., Tan, K., Warren, L., *et al.* (2016). Insulin Resistance in Human iPS Cells Reduces Mitochondrial Size and Function. *Sci Rep*. **6**: 22788.
260. Schmittgen T.D. and Livak, K.J. (2008). Analyzing real-time PCR data by the comparative CT method. *Nat. Protocols*. **3**(6): 1101-1108.
261. Priddle H., Allegrucci, C., Burridge, P., *et al.* (2010). Derivation and characterisation of the human embryonic stem cell lines, NOTT1 and NOTT2. *In Vitro Cell Dev Biol Anim*. **46**(3): 367-375.
262. Gonzalez Garcia J.R. and Meza-Espinoza, J.P. (2006). Use of the International System for Human Cytogenetic Nomenclature (ISCN). *Blood*. **108**(12): 3952-3953.
263. Tzur A., Moore, J.K., Jorgensen, P., *et al.* (2011). Optimizing Optical Flow Cytometry for Cell Volume-Based Sorting and Analysis. *PLoS One*. **6**(1): e16053.
264. Schaaf S., Eder, A., Vollert, I., *et al.*, Generation of Strip-Format Fibrin-Based Engineered Heart Tissue (EHT), in *Cardiac Tissue Engineering: Methods and Protocols*, M. Radisic and L.D. Black Iii, Editors. 2014, Springer New York: New York, NY. p. 121-129.
265. Yazawa M., Hsueh, B., Jia, X., *et al.* (2011). Using induced pluripotent stem cells to investigate cardiac phenotypes in Timothy syndrome. *Nature*. **471**(7337): 230-234.
266. Debold E.P., Schmitt, J.P., Patlak, J.B., *et al.* (2007). Hypertrophic and dilated cardiomyopathy mutations differentially affect the molecular force generation of mouse α-cardiac myosin in the laser trap assay. *Am J Physiol Heart Circ Physiol*. **293**(1): H284-H291.
267. Li M., Suzuki, K., Kim, N.Y., *et al.* (2014). A Cut above the Rest: Targeted Genome Editing Technologies in Human Pluripotent Stem Cells. *J Biol Chem*. **289**(8): 4594-4599.
268. Shen B., Zhang, W., Zhang, J., *et al.* (2014). Efficient genome modification by CRISPR-Cas9 nickase with minimal off-target effects. *Nat Meth*. **11**(4): 399-402.
269. Harris N.L. and Senapathy, P. (1990). Distribution and consensus of branch point signals in eukaryotic genes: a computerized statistical analysis. *Nucleic Acids Res*. **18**(10): 3015-3019.
270. Byrne S.M., Mali, P., and Church, G.M. (2014). Genome Editing in Human Stem Cells. *Methods Enzymol*. **546**: 119-138.
271. Buzzard J.J., Gough, N.M., Crook, J.M., *et al.* (2004). Karyotype of human ES cells during extended culture. *Nat Biotech*. **22**(4): 381-382.
272. Das K., Eisel, D., Lenkl, C., *et al.* (2017). Generation of murine tumor cell lines deficient in MHC molecule surface expression using the CRISPR/Cas9 system. *PLoS One*. **12**(3): e0174077.
273. Hartley J.L., Temple, G.F., and Brasch, M.A. (2000). DNA Cloning Using In Vitro Site-Specific Recombination. *Genome Res*. **10**(11): 1788-1795.
274. Wang G., Yang, L., Grishin, D., *et al.* (2017). Efficient, footprint-free human iPSC genome editing by consolidation of Cas9/CRISPR and piggyBac technologies. *Nat. Protocols*. **12**(1): 88-103.
275. Jensen K.T., Fløe, L., Petersen, T.S., *et al.* (2017). Chromatin accessibility and guide sequence secondary structure affect CRISPR-Cas9 gene editing efficiency. *FEBS Lett*. **591**(13): 1892-1901.

276. Eggenschwiler R., Moslem, M., Fraguas, M.S., *et al.* (2016). Improved bi-allelic modification of a transcriptionally silent locus in patient-derived iPSC by Cas9 nickase. *Sci Rep*. **6**: 38198.
277. Tanigawa G., Jarcho, J.A., Kass, S., *et al.* (1990). A molecular basis for familial hypertrophic cardiomyopathy: An αβ cardiac myosin heavy chain hybrid gene. *Cell*. **62**(5): 991-998.
278. Wang J., Guo, X., and Dhalla, N.S. (2004). Modification of myosin protein and gene expression in failing hearts due to myocardial infarction by enalapril or losartan. *Biochim Biophys Acta*. **1690**(2): 177-184.
279. Miyata S., Minobe, W., Bristow, M.R., *et al.* (2000). Myosin Heavy Chain Isoform Expression in the Failing and Nonfailing Human Heart. *Circ Res*. **86**(4): 386-390.
280. Helms A.S., Davis, F.M., Coleman, D., *et al.* (2014). Sarcomere Mutation-Specific Expression Patterns in Human Hypertrophic Cardiomyopathy. *Circ Cardiovasc Genet*. **7**(4): 434.
281. Tripathi S., Schultz, I., Becker, E., *et al.* (2011). Unequal allelic expression of wild-type and mutated β-myosin in familial hypertrophic cardiomyopathy. *Basic Res Cardiol*. **106**(6): 1041-1055.
282. Bhana B., Iyer, R.K., Chen, W.L.K., *et al.* (2010). Influence of substrate stiffness on the phenotype of heart cells. *Biotechnol Bioeng*. **105**(6): 1148-1160.
283. Dambrot C., Braam, S.R., Tertoolen, L.G.J., *et al.* (2014). Serum supplemented culture medium masks hypertrophic phenotypes in human pluripotent stem cell derived cardiomyocytes. *J Cell Mol Med*. **18**(8): 1509-1518.
284. Földes G., Mioulane, M., Wright, J.S., *et al.* (2011). Modulation of human embryonic stem cell-derived cardiomyocyte growth: A testbed for studying human cardiac hypertrophy? *J Mol Cell Cardiol*. **50**(2): 367-376.
285. Bensley J.G., De Matteo, R., Harding, R., *et al.* (2016). Three-dimensional direct measurement of cardiomyocyte volume, nuclearity, and ploidy in thick histological sections. *Sci Rep*. **6**(23756).
286. Novak P., Li, C., Shevchuk, A.I., *et al.* (2009). Nanoscale live-cell imaging using hopping probe ion conductance microscopy. *Nat Meth*. **6**(4): 279-281.
287. Schneider R. and Pfitzer, P. (1972). Number of nuclei in isolated human myocardial cells. *Virchows Arch B Cell Pathol*. **12**(3): 238-58.
288. Vliegen H.W., van der Laarse, A., Cornelisse, C.J., *et al.* (1991). Myocardial changes in pressure overload-induced left ventricular hypertrophy. A study on tissue composition, polyploidization and multinucleation. *Eur Heart J*. **12**(4): 488-94.
289. Olivetti G., Cigola, E., Maestri, R., *et al.* (1996). Aging, Cardiac Hypertrophy and Ischemic Cardiomyopathy Do Not Affect the Proportion of Mononucleated and Multinucleated Myocytes in the Human Heart. *J Mol Cell Cardiol*. **28**(7): 1463-1477.
290. Brodsky V.Y., Arefyeva, A.M., Gvasava, I.G., *et al.* (1994). Polyploidy in cardiac myocytes of normal and hypertrophic human hearts; range of values. *Virchows Arch*. **424**(4): 429-435.
291. Herget G.W., Neuburger, M., Plagwitz, R., *et al.* (1997). DNA content, ploidy level and number of nuclei in the human heart after myocardial infarction. *Cardiovasc Res*. **36**(1): 45-51.
292. Bergmann O., Bhardwaj, R.D., Bernard, S., *et al.* (2009). Evidence for Cardiomyocyte Renewal in Humans. *Science*. **324**(5923): 98-102.
293. Liu Z., Yue, S., Chen, X., *et al.* (2010). Regulation of Cardiomyocyte Polyploidy and Multinucleation by CyclinG1. *Circ Res*. **106**(9): 1498-1506.
294. Anatskaya O.V. and Vinogradov, A.E. (2010). Somatic polyploidy promotes cell function under stress and energy depletion: evidence from tissue-specific mammal transcriptome. *Funct Integr Genomics*. **10**(4): 433-446.

295. Storchova Z. and Pellman, D. (2004). From polyploidy to aneuploidy, genome instability and cancer. *Nat Rev Mol Cell Biol*. **5**(1): 45-54.
296. H E Morgan, E E Gordon, Y Kira*, et al.* (1987). Biochemical Mechanisms of Cardiac Hypertrophy. *Annu Rev Physiol*. **49**(1): 533-543.
297. Chien K.R., Knowlton, K.U., Zhu, H.*, et al.* (1991). Regulation of cardiac gene expression during myocardial growth and hypertrophy: molecular studies of an adaptive physiologic response. *The FASEB Journal*. **5**(15): 3037-46.
298. Wei C.M., Heublein, D.M., Perrella, M.A.*, et al.* (1993). Natriuretic peptide system in human heart failure. *Circulation*. **88**(3): 1004-1009.
299. Gardner D.G. (2003). Natriuretic peptides: markers or modulators of cardiac hypertrophy? *Trends Endocrinol Metab*. **14**(9): 411-416.
300. Cao L. and Gardner, D.G. (1995). Natriuretic Peptides Inhibit DNA Synthesis in Cardiac Fibroblasts. *Hypertension*. **25**(2): 227-234.
301. Tamura N., Ogawa, Y., Chusho, H.*, et al.* (2000). Cardiac fibrosis in mice lacking brain natriuretic peptide. *Proc Natl Acad Sci U S A*. **97**(8): 4239-4244.
302. Tsuruda T., Boerrigter, G., Huntley, B.K.*, et al.* (2002). Brain Natriuretic Peptide Is Produced in Cardiac Fibroblasts and Induces Matrix Metalloproteinases. *Circ Res*. **91**(12): 1127-1134.
303. Kinnunen P., Vuolteenaho, O., and Ruskoaho, H. (1993). Mechanisms of atrial and brain natriuretic peptide release from rat ventricular myocardium: effect of stretching. *Endocrinology*. **132**(5): 1961-1970.
304. Macarthur H., Warner, T.D., Wood, E.G.*, et al.* (1994). Endothelin-1 Release from Endothelial Cells in Culture Is Elevated Both Acutely and Chronically by Short Periods of Mechanical Stretch. *Biochem Biophys Res Commun*. **200**(1): 395-400.
305. Harada M., Itoh, H., Nakagawa, O.*, et al.* (1997). Significance of Ventricular Myocytes and Nonmyocytes Interaction During Cardiocyte Hypertrophy: Evidence for Endothelin-1 as a Paracrine Hypertrophic Factor From Cardiac Nonmyocytes. *Circulation*. **96**(10): 3737-3744.
306. Tonne J.M., Campbell, J.M., Cataliotti, A.*, et al.* (2011). Secretion of Glycosylated Pro–B-Type Natriuretic Peptide from Normal Cardiomyocytes. *Clin Chem*. **57**(6): 864-873.
307. Kraft T., Witjas-Paalberends, E.R., Boontje, N.M.*, et al.* (2013). Familial hypertrophic cardiomyopathy: Functional effects of myosin mutation R723G in cardiomyocytes. *J Mol Cell Cardiol*. **57**: 13-22.
308. Massey A.J. (2015). Multiparametric Cell Cycle Analysis Using the Operetta High-Content Imager and Harmony Software with PhenoLOGIC. *PLoS One*. **10**(7): e0134306.
309. Tohyama S., Hattori, F., Sano, M.*, et al.* (2013). Distinct Metabolic Flow Enables Large-Scale Purification of Mouse and Human Pluripotent Stem Cell-Derived Cardiomyocytes. *Cell Stem Cell*. **12**(1): 127-137.
310. Lee J.H., Protze, S.I., Laksman, Z.*, et al.* (2017). Human Pluripotent Stem Cell-Derived Atrial and Ventricular Cardiomyocytes Develop from Distinct Mesoderm Populations. *Cell Stem Cell*. **21**(2): 179-194.e4.
311. Karakikes I., Senyei, G.D., Hansen, J.*, et al.* (2014). Small Molecule-Mediated Directed Differentiation of Human Embryonic Stem Cells Toward Ventricular Cardiomyocytes. *Stem Cell Transl Med*. **3**(1): 18-31.
312. Devalla H.D., Schwach, V., Ford, J.W.*, et al.* (2015). Atrial-like cardiomyocytes from human pluripotent stem cells are a robust preclinical model for assessing atrial-selective pharmacology. *EMBO Mol Med*. **7**(4): 394-410.
313. Birket Matthew J., Ribeiro, Marcelo C., Kosmidis, G.*, et al.* (2015). Contractile Defect Caused by Mutation in MYBPC3 Revealed under Conditions Optimized for Human PSC-Cardiomyocyte Function. *Cell Rep*. **13**(4): 733-745.

314. Pan Y., Zhang, L., Liu, Q.*, et al.* (2016). Insertion of a knockout-first cassette in Ampd1 gene leads to neonatal death by disruption of neighboring genes expression. *Sci Rep*. **6**(35970).
315. Lister R., Pelizzola, M., Kida, Y.S.*, et al.* (2011). Hotspots of aberrant epigenomic reprogramming in human induced pluripotent stem cells. *Nature*. **471**(7336): 68-73.
316. Bilic J. and Belmonte, J.C.I. (2012). Concise Review: Induced Pluripotent Stem Cells Versus Embryonic Stem Cells: Close Enough or Yet Too Far Apart? *Stem Cells*. **30**(1): 33-41.
317. Marian A.J. (2002). Modifier genes for hypertrophic cardiomyopathy. *Curr Opin Cardiol*. **17**(3): 242-252.
318. Fananapazir L., Dalakas, M.C., Cyran, F.*, et al.* (1993). Missense mutations in the beta-myosin heavy-chain gene cause central core disease in hypertrophic cardiomyopathy. *Proc Natl Acad Sci U S A*. **90**: 3993-3997.
319. Fananapazir L. and Epstein, N.D. (1994). Genotype-phenotype correlations in hypertrophic cardiomyopathy. Insights provided by comparisons of kindreds with distinct and identical beta-myosin heavy chain gene mutations. *Circulation*. **89**(1): 22-32.
320. Redwood C.S., Moolman-Smook, J.C., and Watkins, H. (1999). Properties of mutant contractile proteins that cause hypertrophic cardiomyopathy. *Circ Res*. **44**: 20-36.
321. The International Stem Cell I. (2011). Screening ethnically diverse human embryonic stem cells identifies a chromosome 20 minimal amplicon conferring growth advantage. *Nat Biotech*. **29**(12): 1132-1144.
322. Bers D.M. (2002). Cardiac excitation-contraction coupling. *Nature*. **415**(6868): 198-205.
323. Giordano F.J. (2005). Oxygen, oxidative stress, hypoxia, and heart failure. *J Clin Invest*. **115**(3): 500-508.
324. Rosca M.G., Vazquez, E.J., Kerner, J.*, et al.* (2008). Cardiac mitochondria in heart failure: decrease in respirasomes and oxidative phosphorylation. *Cardiovasc Res*. **80**(1): 30-39.
325. Ashrafian H., Redwood, C., Blair, E.*, et al.* (2003). Hypertrophic cardiomyopathy: a paradigm for myocardial energy depletion. *Trends Genet*. **19**(5): 263-268.
326. Lowey S. (2002). Functional Consequences of Mutations in the Myosin Heavy Chain at Sites Implicated in Familial Hypertrophic Cardiomyopathy. *Trends Cardiovasc Med*. **12**(8): 348-354.
327. Duke T.A.J. (1999). Molecular model of muscle contraction. *Proc Natl Acad Sci U S A*. **96**(6): 2770-2775.
328. Radda G. (1986). The use of NMR spectroscopy for the understanding of disease. *Science*. **233**(4764): 640-645.
329. Crilley J.G., Boehm, E.A., Blair, E.*, et al.* (2003). Hypertrophic cardiomyopathy due to sarcomeric gene mutations is characterized by impaired energy metabolism irrespective of the degree of hypertrophy. *J Am Coll Cardiol*. **41**(10): 1776-1782.
330. Spindler M., Saupe, K.W., Christe, M.E.*, et al.* (1998). Diastolic dysfunction and altered energetics in the alphaMHC403/+ mouse model of familial hypertrophic cardiomyopathy. *J Clin Invest*. **101**(8): 1775-1783.
331. Javadpour M.M., Tardiff, J.C., Pinz, I.*, et al.* (2003). Decreased energetics in murine hearts bearing the R92Q mutation in cardiac troponin T. *J Clin Invest*. **112**(5): 768-775.
332. Sharov V.G., Todor, A.V., Silverman, N.*, et al.* (2000). Abnormal Mitochondrial Respiration in Failed Human Myocardium. *J Mol Cell Cardiol*. **32**(12): 2361-2367.
333. Lindenmayer G.E., Sordahl, L.A., Harigaya, S.*, et al.* (1971). Some biochemical studies on subcellular systems isolated from fresh recipient human cardiac tissue obtained during transplantation. *Am J Cardiol*. **27**(3): 277-283.

334. Doenst T., Pytel, G., Schrepper, A.*, et al.* (2010). Decreased rates of substrate oxidation ex vivo predict the onset of heart failure and contractile dysfunction in rats with pressure overload. *Cardiovasc Res*. **86**(3): 461-470.
335. Hansson A., Hance, N., Dufour, E.*, et al.* (2004). A switch in metabolism precedes increased mitochondrial biogenesis in respiratory chain-deficient mouse hearts. *Proc Natl Acad Sci U S A*. **101**(9): 3136-3141.
336. Warshaw D.M. (1996). The in vitro motility assay: a window into the myosin molecular motor. *News Physio.l Sci.* **11**: 1-7.
337. Tesi C., Piroddi, N., Colomo, F.*, et al.* (2002). Relaxation Kinetics Following Sudden Ca2+ Reduction in Single Myofibrils from Skeletal Muscle. *Biophys J*. **83**(4): 2142-2151.
338. Sweeney H.L., Straceski, A.J., Leinwand, L.A.*, et al.* (1994). Heterologous expression of a cardiomyopathic myosin that is defective in its actin interaction. *J Biol Chem*. **269**(3): 1603-1605.
339. Tyska M.J., Hayes, E., Giewat, M.*, et al.* (2000). Single-Molecule Mechanics of R403Q Cardiac Myosin Isolated From the Mouse Model of Familial Hypertrophic Cardiomyopathy. *Circ Res*. **86**(7): 737-744.
340. Cuda G., Fananapazir, L., Epstein, N.D.*, et al.* (1997). The in vitro motility activity of beta-cardiac myosin depends on the nature of the beta-myosin heavy chain gene mutation in hypertrophic cardiomyopathy. *J Muscle Res Cell Motil*. **18**: 275-283.
341. Palmiter K.A., Tyska, M.J., Haeberle, J.R.*, et al.* (2000). R403Q and L908V mutant beta-cardiac myosin from patients with familial hypertrophic cardiomyopathy exhibit enhanced mechanical performance at the single molecule level. *J Muscle Res Cell Motil*. **21**(7): 609-620.
342. Pioner J.M., Racca, A.W., Klaiman, J.M.*, et al.* (2016). Isolation and Mechanical Measurements of Myofibrils from Human Induced Pluripotent Stem Cell-Derived Cardiomyocytes. *Stem Cell Reports*. **6**(6): 885-896.
343. Merante F., Tein, I., Benson, L.*, et al.* (1994). Maternally inherited hypertrophic cardiomyopathy due to a novel T-to-C transition at nucleotide 9997 in the mitochondrial tRNA(glycine) gene. *Am J Hum Genet*. **55**(3): 437-446.
344. Mayr J.A., Merkel, O., Kohlwein, S.D.*, et al.* (2007). Mitochondrial Phosphate–Carrier Deficiency: A Novel Disorder of Oxidative Phosphorylation. *Am J Hum Genet*. **80**(3): 478-484.
345. Smits P., Saada, A., Wortmann, S.B.*, et al.* (2011). Mutation in mitochondrial ribosomal protein MRPS22 leads to Cornelia de Lange-like phenotype, brain abnormalities and hypertrophic cardiomyopathy. *Eur J Hum Genet*. **19**(4): 394-399.
346. Tanaka T., Sohmiya, K., and Kawamura, K. (1997). Is CD36 Deficiency an Etiology of Hereditary Hypertrophic Cardiomyopathy? *J Mol Cell Cardiol*. **29**(1): 121-127.
347. Graham B.H., Waymire, G.W., Cottrell, B.*, et al.* (1997). A mouse model for mitochondrial myopathy and cardiomyopathy resulting from a deficiency in the heart/muscle isoform of the adenine nucleotide translocator. *Nat Genet*. **16**(3): 226-34.
348. Arbustini E., Fasani, R., Morbini, P.*, et al.* (1998). Coexistence of mitochondrial DNA and β myosin heavy chain mutations in hypertrophic cardiomyopathy with late congestive heart failure. *Heart*. **80**(6): 548-558.
349. Keller D.I., Coirault, C., Rau, T.*, et al.* (2004). Human homozygous R403W mutant cardiac myosin presents disproportionate enhancement of mechanical and enzymatic properties. *J Mol Cell Cardiol*. **36**(3): 355-362.
350. Hood D.A., Takahashi, M., Connor, M.K.*, et al.* (2000). Assembly of the cellular powerhouse: current issues in muscle mitochondrial biogenesis. *Exerc Sport Sci Rev*. **28**(2): 68-73.

351. Rosca M.G. and Hoppel, C.L. (2013). Mitochondrial dysfunction in heart failure. *Heart Fail Rev*. **18**(5): 607-622.
352. Scheubel R.J., Tostlebe, M., Simm, A.*, et al.* (2002). Dysfunction of mitochondrial respiratory chain complex I in human failing myocardium is not due to disturbed mitochondrial gene expression. *J Am Coll Cardiol*. **40**(12): 2174-2181.
353. Sebastiani M., Giordano, C., Nediani, C.*, et al.* (2007). Induction of Mitochondrial Biogenesis Is a Maladaptive Mechanism in Mitochondrial Cardiomyopathies. *J Am Coll Cardiol*. **50**(14): 1362-1369.
354. Davies K.J.A. (1995). Oxidative stress: the paradox of aerobic life. *Biochem Soc Symp*. **61**: 1-31.
355. Thollon C., Iliou, J.P., Cambarrat, C.*, et al.* (1995). Nature of the cardiomyocyte injury induced by lipid hydroperoxides. *Cardiovasc Res*. **30**(5): 648-55.
356. Hemnani T. and Parihar, M.S. (1998). Reactive oxygen species and oxidative DNA damage. *Indian J Physiol Pharmacol*. **42**(4): 440-52.
357. Stadtman E.R. and Levine, R.L. (2003). Free radical-mediated oxidation of free amino acids and amino acid residues in proteins. *Amino Acids*. **25**(3): 207-218.
358. Konat G.W. (2003). H2O2-induced higher order chromatin degradation: a novel mechanism of oxidative genotoxicity. *J Biosci*. **28**(1): 57-60.
359. Dai D.-F., Johnson, S.C., Villarin, J.J.*, et al.* (2011). Mitochondrial Oxidative Stress Mediates Angiotensin II–Induced Cardiac Hypertrophy and Gαq Overexpression–Induced Heart Failure. *Circ Res*. **108**(7): 837-846.
360. Izumiya Y., Kim, S., Izumi, Y.*, et al.* (2003). Apoptosis Signal-Regulating Kinase 1 Plays a Pivotal Role in Angiotensin II–Induced Cardiac Hypertrophy and Remodeling. *Circ Res*. **93**(9): 874-883.
361. Abozguia K., Elliott, P., McKenna, W.*, et al.* (2010). Metabolic Modulator Perhexiline Corrects Energy Deficiency and Improves Exercise Capacity in Symptomatic Hypertrophic Cardiomyopathy. *Circulation*. **122**(16): 1562-1569.
362. Remondino A., Kwon, S.H., Communal, C.*, et al.* (2003). β-Adrenergic Receptor–Stimulated Apoptosis in Cardiac Myocytes Is Mediated by Reactive Oxygen Species. c-Jun -Terminal Kinase–Dependent Activation of the Mitochondrial Pathway. *Circ Res*. **92**(2): 136-138.
363. Arumanayagam M., Chan, S., Tong, S.*, et al.* (2001). Antioxidant Properties of Carvedilol and Metoprolol in Heart Failure: A Double-Blind Randomized Controlled Trial. *J Cardiovasc Pharmacol*. **37**(1): 48-54.
364. van der Velden J., Klein, L.J., van der Bijl, M.*, et al.* (1999). Isometric tension development and its calcium sensitivity in skinned myocyte-sized preparations from different regions of the human heart. *Cardiovasc Res*. **42**(3): 706-19.
365. Yu Q.T., Ifegwu, J., Marian, A.J.*, et al.* (1993). Hypertrophic cardiomyopathy mutation is expressed in messenger RNA of skeletal as well as cardiac muscle. *Circulation*. **87**(2): 406.
366. Lankford E.B., Epstein, N.D., Fananapazir, L.*, et al.* (1995). Abnormal contractile properties of muscle fibers expressing beta-myosin heavy chain gene mutations in patients with hypertrophic cardiomyopathy. *J Clin Invest*. **95**(3): 1409-1414.
367. Enjuto M., Francino, A., Navarro-López, F.*, et al.* (2000). Malignant Hypertrophic Cardiomyopathy Caused by the Arg723Gly Mutation in β -Myosin Heavy Chain Gene. *J Mol Cell Cardiol*. **32**(12): 2307-2313.
368. Witjas-Paalberends E.R., Piroddi, N., Stam, K.*, et al.* (2013). Mutations in MYH7 reduce the force generating capacity of sarcomeres in human familial hypertrophic cardiomyopathy. *Cardiovasc Res*. **99**(3): 432-441.
369. Witjas-Paalberends E.R., Güçlü, A., Germans, T.*, et al.* (2014). Gene-specific increase in the energetic cost of contraction in hypertrophic cardiomyopathy caused by thick filament mutations. *Cardiovasc Res*. **103**(2): 248-257.

370. Witjas-Paalberends E.R., Ferrara, C., Scellini, B.*, et al.* (2014). Faster cross-bridge detachment and increased tension cost in human hypertrophic cardiomyopathy with the R403Q MYH7 mutation. *J Physiol*. **592**(15): 3257-3272.
371. Finer J.T., Simmons, R.M., and Spudich, J.A. (1994). Single myosin molecule mechanics: piconewton forces and nanometre steps. *Nature*. **368**(6467): 113-119.
372. Sommese R.F., Sung, J., Nag, S.*, et al.* (2013). Molecular consequences of the R453C hypertrophic cardiomyopathy mutation on human β-cardiac myosin motor function. *Proc Natl Acad Sci U S A*. **110**(31): 12607-12612.
373. Bloemink M., Deacon, J., Langer, S.*, et al.* (2014). The Hypertrophic Cardiomyopathy Myosin Mutation R453C Alters ATP Binding and Hydrolysis of Human Cardiac β-Myosin. *J Biol Chem*. **289**(8): 5158-5167.
374. Boudou T., Legant, W.R., Mu, A.*, et al.* (2012). A Microfabricated Platform to Measure and Manipulate the Mechanics of Engineered Cardiac Microtissues. *Tissue Engineering. Part A*. **18**(9-10): 910-919.
375. Eschenhagen T., Fink, C., Remmers, U.*, et al.* (1997). Three-dimensional reconstitution of embryonic cardiomyocytes in a collagen matrix: a new heart muscle model system. *The FASEB Journal*. **11**(8): 683-94.
376. Schaaf S., Shibamiya, A., Mewe, M.*, et al.* (2011). Human Engineered Heart Tissue as a Versatile Tool in Basic Research and Preclinical Toxicology. *PLoS One*. **6**(10): e26397.
377. Stoehr A., Neuber, C., Baldauf, C.*, et al.* (2014). Automated analysis of contractile force and Ca2+ transients in engineered heart tissue. *Am J Physiol Heart Circ Physiol*. **306**(9): H1353-H1363.
378. Eder A., Hansen, A., Uebeler, J.*, et al.* (2014). Effects of proarrhythmic drugs on relaxation time and beating pattern in rat engineered heart tissue. *Basic Res Cardiol*. **109**(6): 436.
379. Friedrich F.W., Wilding, B.R., Reischmann, S.*, et al.* (2012). Evidence for FHL1 as a novel disease gene for isolated hypertrophic cardiomyopathy. *Hum Mol Genet*. **21**(14): 3237-3254.
380. Friedrich F.W., Reischmann, S., Schwalm, A.*, et al.* (2014). FHL2 expression and variants in hypertrophic cardiomyopathy. *Basic Res Cardiol*. **109**(6): 451.
381. Crocini C., Arimura, T., Reischmann, S.*, et al.* (2013). Impact of ANKRD1 mutations associated with hypertrophic cardiomyopathy on contraction parameters of engineered heart tissue. *Basic Res Cardiol*. **108**(3): 349.
382. Stöhr A., Friedrich, F.W., Flenner, F.*, et al.* (2013). Contractile abnormalities and altered drug response in engineered heart tissue from Mybpc3-targeted knock-in mice. *J Mol Cell Cardiol*. **63**: 189-198.
383. Wijnker P.J.M., Friedrich, F.W., Dutsch, A.*, et al.* (2016). Comparison of the effects of a truncating and a missense MYBPC3 mutation on contractile parameters of engineered heart tissue. *J Mol Cell Cardiol*. **97**: 82-92.
384. Cashman T.J., Josowitz, R., Johnson, B.V.*, et al.* (2016). Human Engineered Cardiac Tissues Created Using Induced Pluripotent Stem Cells Reveal Functional Characteristics of BRAF-Mediated Hypertrophic Cardiomyopathy. *PLoS One*. **11**(1): e0146697.
385. Stillitano F., Turnbull, I.C., Karakikes, I.*, et al.* (2016). Genomic correction of familial cardiomyopathy in human engineered cardiac tissues. *Eur Heart J*. **37**(43): 3282-3284.
386. Katz D.H., Beussink, L., Sauer, A.J.*, et al.* (2013). Prevalence, Clinical Characteristics, and Outcomes Associated With Eccentric Versus Concentric Left Ventricular Hypertrophy in Heart Failure With Preserved Ejection Fraction. *Am J Cardiol*. **112**(8): 1158-1164.

387. Ho C.Y., Sweitzer, N.K., McDonough, B.*, et al.* (2002). Assessment of Diastolic Function With Doppler Tissue Imaging to Predict Genotype in Preclinical Hypertrophic Cardiomyopathy. *Circulation*. **105**(25): 2992-2997.
388. Green E.M., Wakimoto, H., Anderson, R.L.*, et al.* (2016). A small-molecule inhibitor of sarcomere contractility suppresses hypertrophic cardiomyopathy in mice. *Science*. **351**(6273): 617-621.
389. Liu L.C.Y., Dorhout, B., van der Meer, P.*, et al.* (2016). Omecamtiv mecarbil: a new cardiac myosin activator for the treatment of heart failure. *Expert Opin Investig Drugs*. **25**(1): 117-127.
390. Rockman H.A., Koch, W.J., and Lefkowitz, R.J. (2002). Seven-transmembrane-spanning receptors and heart function. *Nature*. **415**(6868): 206-212.
391. Jones L.R., Simmerman, H.K., Wilson, W.W.*, et al.* (1985). Purification and characterization of phospholamban from canine cardiac sarcoplasmic reticulum. *J Biol Chem*. **260**(12): 7721-30.
392. Knollmann B.C., Kirchhof, P., Sirenko, S.G.*, et al.* (2003). Familial Hypertrophic Cardiomyopathy-Linked Mutant Troponin T Causes Stress-Induced Ventricular Tachycardia and Ca²⁺-Dependent Action Potential Remodeling. *Circ Res*. **92**(4): 428-436.
393. Priori S.G., Napolitano, C., Tiso, N.*, et al.* (2001). Mutations in the Cardiac Ryanodine Receptor Gene (hRyR2) Underlie Catecholaminergic Polymorphic Ventricular Tachycardia. *Circulation*. **103**(2): 196-200.
394. Baudenbacher F., Schober, T., Pinto, J.R.*, et al.* (2008). Myofilament Ca2+ sensitization causes susceptibility to cardiac arrhythmia in mice. *J Clin Invest*. **118**(12): 3893-3903.
395. Kirschner S.E., Becker, E., Antognozzi, M.*, et al.* (2005). Hypertrophic cardiomyopathy-related β-myosin mutations cause highly variable calcium sensitivity with functional imbalances among individual muscle cells. *Am J Physiol Heart Circ Physiol*. **288**(3): H1242-H1251.
396. Rosevear P.R. and Finley, N. (2003). Molecular mechanism of levosimendan action: an update. *J Mol Cell Cardiol*. **35**(9): 1011-1015.
397. Kass D.A. and Solaro, R.J. (2006). Mechanisms and Use of Calcium-Sensitizing Agents in the Failing Heart. *Circulation*. **113**(2): 305-315.
398. Kivikko M., Lehtonen, L., and Colucci, W.S. (2003). Sustained Hemodynamic Effects of Intravenous Levosimendan. *Circulation*. **107**(1): 81-86.
399. Tadano N., Du, C.-K., Yumoto, F.*, et al.* (2010). Biological actions of green tea catechins on cardiac troponin C. *Br J Pharmacol*. **161**(5): 1034-1043.
400. Zhang L., Nan, C., Chen, Y.*, et al.* (2015). Calcium desensitizer catechin reverses diastolic dysfunction in mice with restrictive cardiomyopathy. *Arch Biochem Biophys*. **573**: 69-76.
401. Zhao Y., Araki, S., Wu, J.*, et al.* (2011). An Expanded Palette of Genetically Encoded Ca2+Indicators. *Science*. **333**(6051): 1888-1891.
402. Thomas D., Tovey, S.C., Collins, T.J.*, et al.* (2000). A comparison of fluorescent Ca2+indicator properties and their use in measuring elementary and global Ca2+signals. *Cell Calcium*. **28**(4): 213-223.
403. Berlin J.R., Bassani, J.W., and Bers, D.M. (1994). Intrinsic cytosolic calcium buffering properties of single rat cardiac myocytes. *Biophys J*. **67**(4): 1775-1787.
404. Kaestner L., Scholz, A., Tian, Q.*, et al.* (2014). Genetically Encoded Ca2+ Indicators in Cardiac Myocytes. *Circ Res*. **114**(10): 1623-1639.
405. El-Armouche A., Singh, J., Naito, H.*, et al.* (2007). Adenovirus-delivered short hairpin RNA targeting PKCα improves contractile function in reconstituted heart tissue. *J Mol Cell Cardiol*. **43**(3): 371-376.

406. Dull T., Zufferey, R., Kelly, M.*, et al.* (1998). A Third-Generation Lentivirus Vector with a Conditional Packaging System. *J Virol*. **72**(11): 8463-8471.
407. Viero C., Kraushaar, U., Ruppenthal, S.*, et al.* (2008). A primary culture system for sustained expression of a calcium sensor in preserved adult rat ventricular myocytes. *Cell Calcium*. **43**(1): 59-71.
408. Song L., Awari, D.W., Han, E.Y.*, et al.* (2015). Dual Optical Recordings for Action Potentials and Calcium Handling in Induced Pluripotent Stem Cell Models of Cardiac Arrhythmias Using Genetically Encoded Fluorescent Indicators. *Stem Cell Transl Med*. **4**(5): 468-475.
409. Shinnawi R., Huber, I., Maizels, L.*, et al.* (2015). Monitoring Human-Induced Pluripotent Stem Cell-Derived Cardiomyocytes with Genetically Encoded Calcium and Voltage Fluorescent Reporters. *Stem Cell Reports*. **5**(4): 582-596.
410. Schlossarek S., Frey, N., and Carrier, L. (2014). Ubiquitin-proteasome system and hereditary cardiomyopathies. *J Mol Cell Cardiol*. **71**: 25-31.
411. Collins G.A. and Goldberg, A.L. (2017). The Logic of the 26S Proteasome. *Cell*. **169**(5): 792-806.
412. Glick D., Barth, S., and Macleod, K.F. (2010). Autophagy: cellular and molecular mechanisms. *J Physiol*. **221**(1): 3-12.
413. Zheng Q. and Wang, X. (2010). Autophagy and the ubiquitin-proteasome system in cardiac dysfunction. *Panminerva Med*. **52**(1): 9-25.
414. Mearini G., Schlossarek, S., Willis, M.S.*, et al.* (2008). The ubiquitin–proteasome system in cardiac dysfunction. *Biochim Biophys Acta*. **1782**(12): 749-763.
415. Sarikas A., Carrier, L., Schenke, C.*, et al.* (2005). Impairment of the ubiquitin–proteasome system by truncated cardiac myosin binding protein C mutants. *Cardiovasc Res*. **66**(1): 33-44.
416. Bahrudin U., Morisaki, H., Morisaki, T.*, et al.* (2008). Ubiquitin-Proteasome System Impairment Caused by a Missense Cardiac Myosin-binding Protein C Mutation and Associated with Cardiac Dysfunction in Hypertrophic Cardiomyopathy. *J Mol Biol*. **384**(4): 896-907.
417. Predmore J.M., Wang, P., Davis, F.*, et al.* (2010). Ubiquitin Proteasome Dysfunction in Human Hypertrophic and Dilated Cardiomyopathies. *Circulation*. **121**(8): 997-1004.
418. De Meyer G.R.Y., De Keulenaer, G.W., and Martinet, W. (2010). Role of autophagy in heart failure associated with aging. *Heart Fail Rev*. **15**(5): 423-430.
419. Fidziańska A., Bilińska, Z.T., Walczak, E.*, et al.* (2010). Autophagy in transition from hypertrophic cardiomyopathy to heart failure. *J Electron Microsc (Tokyo)*. **59**(2): 181-183.
420. Saijo M., Takemura, G., Koda, M.*, et al.* (2004). Cardiomyopathy with Prominent Autophagic Degeneration, Accompanied by an Elevated Plasma Brain Natriuretic Peptide Level Despite the Lack of Overt Heart Failure. *Intern Med*. **43**(8): 700-703.
421. Eskelinen E.-L., Illert, A.L., Tanaka, Y.*, et al.* (2002). Role of LAMP-2 in Lysosome Biogenesis and Autophagy. *Mol Biol Cell*. **13**(9): 3355-3368.
422. Endo Y., Furuta, A., and Nishino, I. (2015). Danon disease: a phenotypic expression of LAMP-2 deficiency. *Acta Neuropathol*. **129**(3): 391-398.
423. Mercadier J.J., Bouveret, P., Gorza, L.*, et al.* (1983). Myosin isoenzymes in normal and hypertrophied human ventricular myocardium. *Circ Res*. **53**(1): 52-62.
424. Gulick J., Subramaniam, A., Neumann, J.*, et al.* (1991). Isolation and characterization of the mouse cardiac myosin heavy chain genes. *J Biol Chem*. **266**(14): 9180-9185.
425. Lowey S., Lesko, L.M., Rovner, A.S.*, et al.* (2008). Functional Effects of the Hypertrophic Cardiomyopathy R403Q Mutation Are Different in an α- or β-Myosin Heavy Chain Backbone. *J Biol Chem*. **283**(29): 20579-20589.

426. Lovelock J.D., Monasky, M.M., Jeong, E.-M., *et al.* (2012). Ranolazine Improves Cardiac Diastolic Dysfunction Through Modulation of Myofilament Calcium Sensitivity. *Circ Res*. **110**(6): 841-850.
427. Miller T., Szczesna, D., Housmans, P.R., *et al.* (2001). Abnormal Contractile Function in Transgenic Mice Expressing a Familial Hypertrophic Cardiomyopathy-linked Troponin T (I79N) Mutation. *J Biol Chem*. **276**(6): 3743-3755.
428. Alves M.L., Dias, F.A.L., Gaffin, R.D., *et al.* (2014). Desensitization of Myofilaments to Ca2+ as a Therapeutic Target for Hypertrophic Cardiomyopathy With Mutations in Thin Filament Proteins. *Circ Cardiovasc Genet*. **7**(2): 132-143.
429. Stoll L.L. and Spector, A.A. (1984). Changes in serum influence the fatty acid composition of established cell lines. *In Vitro*. **20**(9): 732-8.
430. Hong T. and Shaw, R.M. (2017). Cardiac T-Tubule Microanatomy and Function. *Physiol Rev*. **97**(1): 227-252.
431. Andreka P., Tran, T., Webster, K.A., *et al.* (2004). Nitric oxide and promotion of cardiac myocyte apoptosis. *Mol Cell Biochem*. **263**(1-2): 35-53.
432. David R. and Franz, W.-M. (2012). From Pluripotency to Distinct Cardiomyocyte Subtypes. *Physiology*. **27**(3): 119-129.
433. Pinto A.R., Ilinykh, A., Ivey, M.J., *et al.* (2016). Revisiting Cardiac Cellular Composition. *Circ Res*. **118**(3): 400-409.
434. Lin J., Zhou, Y., Liu, J., *et al.* (2017). Progress and Application of CRISPR/Cas Technology in Biological and Biomedical Investigation. *J Cell Biochem*. **118**(10): 3061-3071.
435. Marian A.J. and Braunwald, E. Hypertrophic Cardiomyopathy: Genetics, Pathogenesis, Clinical Manifestations, Diagnosis, and Therapy. *Circ Res*. **121**(7): 749-770.
436. Philipson D.J., DePasquale, E.C., Yang, E.H., *et al.* (2017). Emerging pharmacologic and structural therapies for hypertrophic cardiomyopathy. *Heart Fail Rev*.
437. Yamazaki T., Suzuki, J.-i., Shimamoto, R., *et al.* (2007). A New Therapeutic Strategy for Hypertrophic Nonobstructive Cardiomyopathy in Humans. Randomized and Prospective Study With an Angiotensin II Receptor Blocker. *Int Heart J*. **48**(6): 715-724.
438. Wilder T., Ryba, D.M., Wieczorek, D.F., *et al.* (2015). N-acetylcysteine reverses diastolic dysfunction and hypertrophy in familial hypertrophic cardiomyopathy. *Am J Physiol Heart Circ Physiol*. **309**(10): H1720-H1730.
439. Ho C.Y., Lakdawala, N.K., Cirino, A.L., *et al.* (2015). Diltiazem Treatment for Pre-Clinical Hypertrophic Cardiomyopathy Sarcomere Mutation Carriers: A Pilot Randomized Trial to Modify Disease Expression. *JACC Heart Fail*. **3**(2): 180-188.
440. Coppini R., Ferrantini, C., Yao, L., *et al.* (2013). Late Sodium Current Inhibition Reverses Electromechanical Dysfunction in Human Hypertrophic Cardiomyopathy. *Circulation*. **127**(5): 575-584.
441. Reiser P.J., Portman, M.A., Ning, X.-H., *et al.* (2001). Human cardiac myosin heavy chain isoforms in fetal and failing adult atria and ventricles. *Am J Physiol Heart Circ Physiol*. **280**(4): H1814-H1820.
442. Fatkin D., Christe, M.E., Aristizabal, O., *et al.* (1999). Neonatal cardiomyopathy in mice homozygous for the Arg403Gln mutation in the α cardiac myosin heavy chain gene. *J Clin Invest*. **103**(1): 147-153.
443. Matsuoka R., Beisel, K.W., Furutani, M., *et al.* (1991). Complete sequence of human cardiac alpha-myosin heavy chain gene and amino acid comparison to other myosins based on structural and functional differences. *Am J Med Genet*. **41**(4): 537-47.
444. Iyer D., Gambardella, L., Bernard, W.G., *et al.* (2016). Robust derivation of epicardium and its differentiated smooth muscle cell progeny from human pluripotent stem cells. *Development*. **143**(5): 904-904.

445. Bao X., Lian, X., Qian, T.*, et al.* (2017). Directed differentiation and long-term maintenance of epicardial cells derived from human pluripotent stem cells under fully defined conditions. *Nat. Protocols*. **12**(9): 1890-1900.

Appendix I – Publication Documents

1- Denning C, Borgdorff V, Crutchley J, Firth KS, George V, Kalra S, Kondrashov A, Hoang MD, **Mosqueira D**, Patel A, Prodanov L, Rajamohan D, Skarnes WC, Smith JG, Young LE. "Cardiomyocytes from human pluripotent stem cells: From laboratory curiosity to industrial biomedical platform." Biochimica et Biophysica acta – Molecular Cell Research (**2016**) 1863 (7PtB).

2- Santos JM*,Camões SP*, Filipe E, Cipriano M, Barcia RN, Filipe M, Teixeira M, Simões S, Gaspar M, **Mosqueira D**, Nascimento DS, Pinto-do-Ó P, Cruz P, Cruz, H, Castro M, Miranda JP. "Three-dimensional spheroid cell culture of umbilical cord tissue-derived mesenchymal stromal cells leads to enhanced paracrine induction of wound healing." Stem Cell Research and Therapy (**2015**) 6:90.

3- Mosqueira D*, Pagliari S*, Uto K, Ebara M, Romanazzo S, Escobedo-Lucea C, Nakanishi J, Taniguchi A, Di Nardo P, Goumans MJ, Pinto-do-Ó P, Aoyagi T*, Forte G*. "Hippo pathway effectors control cardiac progenitor cell fate by acting as dynamic sensors of substrate mechanics and nanostructure." ACS Nano (**2014**) 25; 8(3): 2033-47.

4- Nascimento DS*, **Mosqueira D***, Sousa LM, Teixeira M, Filipe M, Resende TP, Araújo AF, Valente M, Almeida J, Martins JP, Santos JM, Barcia RN, Cruz P, Cruz H, Pinto-do-Ó P. "Human umbilical cord tissue-derived mesenchymal stromal cells attenuate remodeling following myocardial infarction by pro-angiogenic, anti- apoptotic and endogenous cell activation mechanisms." Stem Cell Research and Therapy (**2013**) 5(1):5.

5- Pagliari S, Romanazzo S, **Mosqueira D**, Pinto-do-Ó P, Aoyagi T, Forte G. "Adult stem cells and biocompatible scaffolds as smart delivery tools for cardiac tissue repair". Current Medicinal Chemistry (**2013**) 20(28):3429-47.

6- Lindberg S*, Muñoz-Alarcón A*, Helmfors H, **Mosqueira D**, Gyllborg D, Tudoran O, Langel U "PepFect15, a novel endosomolytic cell-penetrating peptide for oligonucleotide delivery via scavenger receptors". International Journal of Pharmaceutics, (**2013**) 441(1-2):242-7.

7- Tavares JM; Vieira LM; **Mosqueira D**; Amaral IF; Granja PL; Pinto-do-Ó P; Lima R; Garcia V; Mendes A; Almeida S. "Chapter 10 - Physical Chemistry of Life" in Magalhães AB; Santos AD; Cunha JF (Eds.), Introduction to Mechanical Engineering (p352-411). Publindústria, Porto, Portugal (**2013**). (original text in Portuguese)

Appendix II – Other scientific contributions

Patents

Santos JM, Filipe E, Filipe M, Teixeira M, Cipriano M, Barcia R, Cruz P, **Mosqueira D**, Nascimento DS, Pinto-do-Ó P, Cruz H, Castro M, Miranda JP (2013). Method for priming umbilical cord tissue-derived mesenchymal stromal cells (UC-MSCs) towards a higher therapeutic potential and applications thereof. Portugal: ECBio; [INPI, Provisional Patent: 107148 T].

Honors and awards

Mar 2017: Full bursary to present at conference The Biology of Regenerative Medicine – Wellcome Genome Campus, Cambridge, UK.

Jun 2015: Best peer-nominated e-poster during the Medicine & Health Sciences Faculty Postgraduate Research Forum 2015, University Of Nottingham, UK.

Sep 2012: 1st prize Ex-aequo of plenary oral presentation for the work: "Mechanotransduction in cardiac stem cells: Role of YAP/TAZ in the cellular response to the microenvironment", during the 7th edition of Young European Scientist meeting, held at Faculty of Medicine of University of Porto, Portugal.

Jul 2011: The Scholarship Merit Award concerning year 2009/2010, by Public or Private Education System, conferred to students with exceptional academic records.

Oral Presentations in Scientific Meetings

Apr 2017: The Biology of Regenerative Medicine, Wellcome Genome Campus, Cambridge UK. Presentation title: "Disease Modeling Hypertrophic Cardiomyopathy using genome-edited human pluripotent stem cell-derived cardiomyocytes"

Jan 2016: Winter Divisional Meeting, University of Nottingham, UK. Presentation title: "Addressing prevalent cardiomyopathies through disease modelling in a dish".

Dec 2015: British Heart Foundation – Annual Post Doc meeting, Imperial College, London, UK. Presentation title: "Modeling hypertrophic cardiomyopathy using CRISPR/Cas9 genome editing technology in human pluripotent stem cell-derived cardiomyocytes".

Sep 2012: 7th Young European Scientist meeting, Faculty of Medicine of University of Porto, Portugal. Presentation title: "Mechanotransduction in cardiac stem cells: Role of YAP/TAZ in the cellular response to the microenvironment.